Dottorato di Ricerca in Ingegneria Civile
Graduate School in Civil Engineering
Sede: Facoltà di Ingegneria - Università di Pavia - Via Ferrata 1 - 27100 Pavia - Italy

☐ Dipartimento di Meccanica Strutturale Tel. 0382-505450 - Fax 0382-528422
☐ Dipartimento di Ingegneria Idraulica e Ambientale Tel. 0382-505300 - Fax 0382-505589

Sail Modelling for Maximal Speed Optimum Design

PhD student
Roberto Nascimbene

Supervisor
Prof. Armando Gobetti

Revisor
Prof. Fabio Casciati

Dottorato di Ricerca in Ingegneria Civile XV Ciclo

To Serenella and Paolo

Ph.D. in Civil Engineering

Settore:	Ingegneria
Sede Amministrativa non consortile:	Università degli Studi di Pavia
Durata del dottorato in anni:	3
Periodo formativo estero in mesi:	come previsto dal regolamento del Dottorato di Ricerca
Numero minimo di corsi	6

Description of the Ph.D. course

Il dottorato di ricerca in *Ingegneria Civile* è stato istituito presso la Facoltà di Ingegneria dell'Università degli Studi di Pavia nell'anno accademico 1994/95 (X Ciclo).
Il corso, sino alla sua ridefinizione in concomitanza con il XVI Ciclo, consentiva al dottorando di scegliere tra due curricula: idraulico o strutturale. Egli svolge la propria attività di ricerca rispettivamente presso il Dipartimento di Ingegneria Idraulica e Ambientale o quello di Meccanica Strutturale.
Durante i primi due anni sono previsti almeno sei corsi, seguiti dai rispettivi esami, che il dottorando è tenuto a sostenere. Il Collegio dei Docenti, composto da professori dei due Dipartimenti, organizza i corsi con lo scopo di fornire allo studente di dottorato opportunità di approfondimento in alcune delle discipline di base per entrambe le componenti, idraulica e strutturale. Corsi e seminari vengono tenuti da docenti di Università nazionali e estere.
Il Collegio dei Docenti, cui spetta la pianificazione della didattica, si è orientato ad attivare ad anni alterni corsi sui seguenti temi:

- Meccanica dei solidi e dei fluidi
- Metodi numerici per la meccanica dei solidi e dei fluidi
- Rischio strutturale e ambientale
- Metodi sperimentali per la meccanica dei solidi e dei fluidi
- Intelligenza artificiale

a questi si aggiungono corsi specifici di indirizzo.
Al termine dei corsi del primo anno il Collegio dei Docenti assegna al dottorando un tema di ricerca da sviluppare, sotto forma di tesina, entro la fine del secondo anno; il tema, non necessariamente legato all'argomento della tesi finale, è di norma coerente con il curriculum, scelto dal dottorando (idraulico o strutturale).
All'inizio del secondo anno il dottorando discute con il Coordinatore l'argomento della tesi di dottorato, la cui assegnazione definitiva viene deliberata dal Collegio

dei Docenti.
Alla fine di ogni anno i dottorandi devono presentare una relazione particolareggiata (scritta e orale) sull'attività svolta. Sulla base di tale relazione il Collegio dei Docenti, "previa valutazione della assiduità e dell'operosità dimostrata dall'iscritto", ne propone al Rettore l'esclusione dal corso o il passaggio all'anno successivo.
Il dottorando può svolgere attività di ricerca sia di tipo teorico che sperimentale, grazie ai laboratori di cui entrambi i Dipartimenti dispongono, nonchè al Laboratorio Numerico di Ingegneria delle Infrastrutture.
Il "Laboratorio didattico sperimentale" del Dipartimento di Meccanica Strutturale dispone di:

1. una tavola vibrante che consente di effettuare prove dinamiche su prototipi strutturali;
2. opportuni sensori e un sistema di acquisizione dati per la misura della risposta strutturale;
3. strumentazione per la progettazione di sistemi di controllo attivo e loro verifica sperimentale;
4. strumentazione per la caratterizzazione dei materiali (macchina di prova universale biassiale), attraverso prove statiche e dinamiche.

Il laboratorio del Dipartimento di Ingegneria Idraulica e Ambientale dispone di:

1. un circuito in pressione che consente di effettuare simulazioni di moto vario;
2. un tunnel idrodinamico per lo studio di problemi di cavitazione;
3. canalette per lo studio delle correnti a pelo libero.

The Graduate School in *Civil Engineering* at Department of Structural Mechanics, University of Pavia, was established in 1994/95 (X Ciclo).
Two different type of curricula are available for students: hydraulic and structural engineering. The student works either at the Department of Structural Mechanics or at the Department of Hydraulics and Environmental Engineering.
Each student must select at least six courses with homeworks and final exams. The Teaching Council, compounded by professors coming from both departments, organise the courses with the aim to give the student the opportunity of improving his basic knowledge in the field of structural and hydraulic engineering. The courses and the seminars are held by national and international lecturers.
The following courses are organised every two years:

- Continuum Mechanics (Fluids and Solids)

- Computational Solids and Fluids Mechanics
- Structural and Environmental Risk Analysis
- Experimental Methods for Solids and Fluids Mechanics
- Artificial Intelligence

At the end of the first year, the Teaching Council assigns a homework covering one the above themes. This homework is not necessarily related to the final topic of the thesis.
During the second year the student will start his PhD thesis often discussing it with the Course Coordinator. The Teaching Council assigns the task.
At the end of each year the student has to present a detailed report regarding his research activity. The Teaching Council will decide, after a detailed revision of this report, to admit the student to the next year course.
A number of numerical and experimental laboratory can be used by all the students to improve their skill in civil engineering.
At the "Experimental and Teaching Laboratory" of the Department of Structural Mechanics the following equipment is available:

1. a shaking table for dynamic and control testing on small scale prototypes;
2. sensors and acquisition systems for measuring the structural response;
3. instrumentation for the design of active and semi-active control and their experimental validation;
4. instrumentation for material characterisation (bi–axial universal testing machine) with static and dynamic tests.

At the laboratory of the Department of Hydraulics and Environmental Engineering one has available:

1. a circuit in pressure able to model the unsteady motion of fluids;
2. a hydrodynamic tunnel to simulate cavitation problems;
3. a small scale model of channel.

Ph.D. Theses

Dottorandi del X Ciclo:

Marco Battaini	Sistemi strutturali controllati: progettazione e affidabilità (Febbraio 1998).
Claudia Mariani	Problemi di ottimizzazione per strutture bidimensionali anisotrope (Febbraio 1998).
Antonella Negri	Stima delle perdite idrologiche nei bacini di drenaggio urbani (Febbraio 1999).

Dottorandi XI Ciclo:

Aurora Angela Pisano	Structural system identification: advanced approaches and applications (Febbraio 1999).
Carla Saltalippi	Preannuncio delle piene in tempo reale nei corsi d'acqua naturali (Febbraio 1999).
Eugenio Barbieri	Thermofluid dynamics and topology optimization of an active thermal insulation structure (Ottobre 1999).

Dottorandi XII Ciclo:

Massimiliano Barbolini	Dense snow avalanches: computational models, hazard mapping and related uncertainties (Ottobre 1999).

Paolo Espa	Moti atmosferici generati da forze di galleggiamento: simulazioni numeriche e studio su modello fisico (Ottobre 1999).
Lorenza Petrini	Shape memory alloys: modelling the martensitic phase behavior for structural engineering exploitation (Ottobre 1999).

Dottorandi XIV Ciclo:

Stefano Podestà	Risposta sismica di antichi edifici religiosi in muratura: sviluppo di nuovi modelli per l'analisi di vulnerabilità (Ottobre 2001).

Acknowledgments

I owe a debt of gratitude to Prof. Armando Gobetti, who has coached me during the last three years.
I wish to acknowledge here, the warm friendship of Prof. Paolo Venini who introduced me to the wonderfull world of computational mechanics. I feel privileged to have worked with such a teacher, whose knowledge, skill and creativity continue to amaze me, and I hope to continue to work with him for the next future.
My heart–felt gratitude goes out to Prof. Fabio Casciati, his wife Prof. Lucia Faravelli and their daughter M.Sc. Ph.D. Sara Casciati for their continuous support.
I feel indebted to Prof. Carlo Cinquini for his precious support during my investigation in the huge field of structural optimization.
A similar acknowledgement is due to Prof. Antonio Tiano for his advices during my research in the area of sail and yacht design.
I thank the members of the DISTART, University of Bologna, in the person of Prof. Francesco Ubertini for his encouragement to persist.
Thanks to Ing. Juri Brunoro for positive provoking questions and discussions and to Ing. Roberto Franzolin for having realized all the beautifull designs used to illustrate this thesis.
My gratitude goes out to Dott. Dario Papoff for his *informatic* help in preparing all the codes used in this thesis.
I wish to acknowledge here the exceptional friendship of Ing. Dacarro Filippo, Ing. Guarnaschelli Roberto, *Next Ing.* Luca Torretta and Ing. Bergamaschi Manuel: thanks for their support through thick and thin; furthermore, I wish to thank the rest of the band: Antonio Bernini, Tito Caffi and the lost *souls* of the last floor of Collegio Fraccaro.
To Don Gianluca Vernetti, the only one who was able to bring me up during the last ten yaers and I also hope for the rest of my life.
At least, but not last, my gratitude goes out to my girlfriend Sara for her patience through the late nights and non–existent weekends. Don't worry, be happy ... *eternally forever*!

Sommario esteso

La maggior parte delle conoscenze teoriche sul moto di una barca a vela deriva dalla ricerca aeronautica, nella quale la spinta principale è sempre stata fornita dagli enormi interessi economici in gioco, se si esclude il caso dei pionieri dell'aria per i quali lo stimolo fondamentale era senz'altro costituito dal desiderio di vincere l'antica sfida del volo.
La forza trainante che ci porta alla conoscenza della natura delle azioni sulle vele è molto simile a quella che animava i pionieri dell'aeronautica e consiste probabilmente nel desiderio di trovare il modo per estrarre la massima energia possibile dalla natura.
Ci sono molti modi per descrivere le forze che agiscono sulle vele e in generale su superfici in movimento. Il più semplice consiste nel dividere le forze in *portanza* e *resistenza*. La portanza è, per definizione, perpendicolare alla direzione del vento apparente; la resistenza è parallela ad essa (**Capitolo 1**).
La circolazione o portanza di una vela dipende da tre fattori: l'angolo di incidenza del vento, la forma della vela e la lunghezza della corda. In generale queste tre quantità variano se ci si sposta lungo la vela, oltre a variare con l'intensità e la direzione del vento, con la situazione di sforzo della vela e con la flessione dell'albero. Per ogni andatura esiste senz'altro una distribuzione ottimale della portanza, ma i modi per ottenere una medesima distribuzione sono probabilmente molti. Si tenga inoltre conto che un problema arduo e in continua evoluzione è che la forza della pressione del vento cambia continuamente e viene influenzata dalla forma della vela, mentre accade che la forma della vela, attraverso lo stiramento del tessuto e la flessione, è influenzata dalla pressione del vento.
Due modi principali consentono di ottenere maggiore portanza: il primo è incrementare l'angolo di incidenza della vela. Per esempio si può cazzarla oppure poggiare senza lascare la vela. Il secondo modo è rendere la vela più *grassa*: regolando la sua curvatura, ghindando meno la drizza, lascando il tesabugne, incrementando la flessione dello strallo e così via.
Per una vela, una forma ottimale e una curvatura corretta forniscono un ingresso facilitato dei flussi d'aria. Quindi dato un certo angolo di incidenza, una vela opportunamente grassa, facilita l'ingresso dei filetti fluidi, e può fornire una portanza

maggiore.
Obiettivo di questo primo capitolo è quindi quello di determinare, sotto opportune ipotesi semplificative, la forma aerodinamicamente ottimale di una vela. Il problema di ottimo verrà impostato cercando come obiettivo la massima forza propulsiva e imponendo due vincoli: uno sulla portanza e uno sullo sbandamento laterale.

Una progettazione ottimale che controlli la forma migliore di una vela non può prescindere da considerazioni di tipo strutturale che si basino anche su un attento studio della natura del tipo di carico applicato (vento) (**Capitolo 2**). L'estrema complessità di questo aspetto, influenzata notevolmente anche dalla stretta e mutua correlazione tra vento e forma della vela assunta durante l'esercizio, ci porta a semplificare il problema trasferendolo in campo completamente statico, congelando idealmente l'applicazione del campo di pressioni ad un generico istante. Inoltre in questo capitolo verranno evidenziate alcune delle principali tattiche usate nel campo di regata. Questo perchè, come sempre accade in ogni settore, ricordiamo che, come il migliore strumento musicale non fa del possessore il migliore dei musicisti, così la migliore vela non sempre è associata allo skipper migliore!

Dopo avere ottenuto una forma ottimale della vela (**Capitolo 1**) per una data condizione di regata e per un assegnato vento (**Capitolo 2**), si passa a considerare un secondo aspetto, non meno importante del precedente (**Capitolo 3**): il materiale con cui è realizzata!
Un famoso detto popolare vuole gli italiani come ... *popolo di santi, poeti e navigatori* ... In effetti, tralasciando le prime due definizioni, poco consone all'ambiente ingegneristico, stiamo assitendo in questi ultimi anni ad una rinnovata rinascita della passione per la vela. Complici le affascinanti imprese sportive delle imbarcazioni italiane impegnate nelle più recenti edizioni della *Coppa America*, come *Il Moro di Venezia*, *Luna Rossa* e *Mascalzone Latino*, molti italiani hanno passato più di una nottata a seguire incollati allo schermo le gesta dei nostri portacolori.
Tali imprese sportive, anche se ci piacerebbe pensarle come frutto esclusivo di cuore e passione, derivano dalle più innovative rivoluzioni tecnologiche introdotte negli ultimi decenni. L'industria navale fa ormai uso delle più ardite soluzioni tecnologiche, sfruttando in modo massiccio i benefici introdotti dall'uso dei materiali compositi e dei laminati fibrorinforzati. Tali materiali vengono impiegati con successo sia per la costruzione degli scafi e di tutte le parti strutturali delle imbarcazioni quali alberi e timoni, sia per il confezionamento delle vele.
Il progetto, la fabbricazione e l'utilizzo delle nuove vele, oltre a fare tesoro della vastissima tradizione velaia, fatta più di esperienza pratica e di sensibilità personale dei velai piuttosto che da precise e codificate regole tecniche, si affida anche alle collaborazioni con l'industria tessile e con l'industria meccanica. In un'era domi-

nata ormai dall'elettronica, diffusa in ogni settore, anche un campo artigianale per tradizione come quello dell'industria delle vele stà subendo l'influenza delle più moderne analisi fluido-strutturali eseguite dai potenti codici di calcolo ad elementi finiti di ultima generazione, spesso appositamente concepiti ex–novo parzialmente modificati da sofisticate routine.
Nel corso degli ultimi due secoli lo sviluppo di questo settore è stato frenetico: abbiamo assistito dapprima al passaggio del confezionamento delle vele a mano a quello fabbricato in larga scala grazie ad appositi macchinari, e poi siamo passati da rudimentali vele in fibra naturale (tipicamente cotone) a vele costruite con fibre sintetiche (come il *nylon*, a partire dai primi anni trenta), per passare ai più recenti prodotti dell'industria chimica come *poliestere*, *dacron*, *spectra* e *mylar* (a partire dagli anni cinquanta e sessanta). Lo sviluppo è stato continuo e nel giro di qualche anno si è arrivati ai giorni nostri dove ormai è indispensabile l'uso dei materiali compositi fibrorinforzati.
Come è naturale ed ovvio aspettarsi, nelle imbarcazioni a vela è proprio l'interazione di quest'ultimo strumento con l'azione del vento ad assicurare la spinta necessaria all'avanzamento della barca. Lo scopo delle vele è dunque quello di intercettare una porzione del campo di pressioni *disordinate* del vento e di convertirle in una più ordinata causa di moto facilmente governabile, incanalando l'energia eolica nella direzione più favorevole. E' facile allora intuire come una vela progettata in modo ottimale possa assicurare prestazioni più elevate e risparmi in termini di tempo dell'ordine di qualche secondo (che spesso decidono l'esito di una competizione). Non solo, per chi non ha velleità sportive, una vela adeguata comporta benefici effetti in termini di durata e di affidabilità.
Un materiale composito è ottenuto dall'associazione di due o più materiali diversi, rinforzati da orditi di fibre opportunamente intessuti ed orientati, annegati in un altro materiale, detto *matrice*, che conferisce la forma definitiva alla vela nelle sue diverse configurazioni di esercizio, quando sottoposta all'azione dinamica del vento. Oggetto di questo terzo capitolo, una volta affrontata e ottenuta la forma ottimale della vela nel primo capitolo, è sostanzialmente un problema di ottimizzazione il cui scopo è quello di trovare, mediante lo sviluppo di un opportuno codice di calcolo in linguaggio *FORTRAN 77*, la configurazione e l'orientamento ottimale delle fibre all'interno della matrice delle vele in modo che, quando la vela è investita dal vento, la direzione delle fibre stesse sia tale da far sì che in esse lo sforzo sia il minore possibile e sia distribuito il più uniformemente possibile, compatibilmente con le loro caratteristiche meccaniche di resistenza.
Anticipiamo fin da ora che il metodo da noi impiegato, nonchè il modo più efficiente di orientare le fibre è quello che le costringe a seguire le linee isostatiche di sforzo di trazione che si diffondono nelle vele quando vengono caricate. Alla luce di questo fatto, quindi, il primo passo sarà quello della ricerca di tali linee. In seguito, si disporranno le fibre e se ne ottimizzerà la distribuzione di area trasversale.

Nell'ottica della elevata spesa computazionale che comporta un algoritmo di ottimizzazione e tenendo inoltre presente l'inadeguatezza dei modelli tessili usati in letteratura per descrivere le vele, si è preferito introdurre un nuovo modello matrice–fibra capace di coniugare insieme la snellezza computazionale (pochi gradi di libertà) con l'efficenza applicativa (ottimo riscontro con i dati sperimentali). In definitiva, come meglio verrà descritto nel **Capitolo 5**, si discretizzeranno le fibre con elementi finiti corda e la matrice con elementi finiti membrana concepiti appositamente per queste simulazione e rivelatosi successivamente capaci di essere estese alla modellazione di casistiche assolutamente più generali.

Una progettazione ottimale che controlli l'orientamento di queste fibre all'interno di una vela non può prescindere da due fondamentali considerazioni di tipo strutturale–geometrico riguardanti la modellazione della superficie velica (**Capitolo 4**) e l'introduzione, come detto prima, di opportuni elementi finiti capaci di descrivere contemporaneamente le corde (utilizzate per modellare le fibre) e le membrane (impiegate per modellare la matrice–guscio) (**Capitolo 5**).
L'estrema complessità del primo aspetto, influenzata notevolmente anche dalla stretta e mutua correlazione tra vento applicato e conseguente cambio di forma della vela, ci porta a studiare il problema in campo altamente non lineare introducendo l'ipotesi di grandissimi spostamenti il tutto in opportuni sistemi di riferimento curvilinei locali (**Capitolo 4**).
Inoltre per sopperire alle carenze in letterature di elementi finiti capaci di arrivare a modellare, sia nel monodimensionale (fili) sia nel bidimensionale (membrane–gusci), spessori dell'ordine del decimo di millimetro, si è dovuto introdurre nuovi modelli ad interpolazione mista allo scopo di risolvere questo problema.
In definitiva si è scelto di modellare la vela con una mesh di membrane su cui si sovrappone una mesh di corde, che modella l'andamento delle fibre di rinforzo (**Capitolo 5**).

La vela, nel **Capitolo 6**, ormai ottimizzata nella forma e nel materiale, verrà investita da una raffica di vento (in una virata!) capace di farle cambiare concavità. Verranno quindi presentati i risultati delle simulazioni in grandissimi spostamenti ottenuti utilizzando i codici di calcolo implementati in *FORTRAN 77* seguendo le direttive dei precedenti capitoli.

Contents

List of Figures

[1] 1 oz. (ounce) = 28.35 g.

List of Tables

Chapter 1

How fast is fast?

Both men and ships live in an unstable element, are subject to subtle and powerful influences and want to have their merits understood rather than their faults found out.
Joseph Conrad, *The Mirror of the Sea*

1.1 Speed performance

Sailing has grown enormously in popularity as a means of sport (America's Cup) and recreation in the last three decades. Most recent major developments, resulting in a large variety of types of contemporary sailing craft, have been inspired by desire for greater speed. It appears that the fascination with speed for speed's sake has more of a hold today than ever before. *Unthinkable* futuristic shapes, some resembling aeroplanes more than boats, and the speed records achieved, have captured the public attention and attracted almost unlimited financial sponsorship, without which such creations could not have appeared and proliferated so rapidly. Speed fever, which has descended recently on a large part of the sailing population, is well reflected in Table 1.1 that illustrates the increase in speed recorded by a variety of sailing craft during their west–east transatlantic passages over the last 100 years or so. The increase in speed listed against time in Table 1.1 is expressed in terms of *relative speed*, that is speed–length ratio $V_s/\sqrt{\mathrm{LWL}}$ (see Appendix A). These terms refer to the fact that simply increasing the size of the vessel, with no change in basic design philosophy, will increase its sailing speed roughly in proportion to the square root of the increase in the waterline lenght of the hull. Thus, for instance, if the size of the hull is increased twofold, all other things being equal, its potential speed should increase roughly in proportion to $\sqrt{2} = 1.4 \approx 40$ %. There-

Year	Name of Yacht	Type	LWL (Ft)	BDR (Miles)	V_s/LWL
1851	*America*	mono	90	284	1.25
1866	*Henrietta*	mono	84	280	1.27
1866	*Alice*	mono	48	207	1.24
1869	*Sappho*	mono	121	315	1.19
1887	*Coronet*	mono	124	291	1.09
1905	*Atlantic*	mono	135	342	1.23
1928	*Elena*	mono	96	282	1.20
1931	*Dorade*	mono	37	210	1.44
1935	*Vamarie*	mono	54	222	1.26
1952	*Caribbee*	mono	44	212	1.33
1977	*But*	mono	70	298	1.48
1980	*Desperado*	ULDB[a]	47	245	1.49
1981	*Kriter VIII*	ULDB	62	304	1.61
1983	*La Vie Clare*	ULDB	213	447	1.28
1988	*Phocea*	ULDB	213	490	1.42
1979	*Kriter IV*	tri	66	340	1.74
1980	*Paul Ricard*	tri	46	357	2.19
1981	*Elf Aquitaine*	cat	62	370	1.96
1981	*Sidinox*	proa	52	350	2.02
1981	*FMV*	cat	60	361	1.94
1981	*Le Turnesol*	tri	46	312	192
1981	*Fleury Michon IV*	cat	42	301	1.94
1981	*Dict Robert*	tri	50	301	1.77
1981	*Gautier II*	tri	43	250	1.59
1981	*Brittany Ferries*	tri	60	400	2.15
1982	*Gauliosis IV*	tri	42	325	2.09
1984	*Jet Services II*	cat	60	433	2.33
1984	*Formula Tag*	cat	74	420	2.03
1984	*William Saurin*	tri	80	447	2.08
1986	*Royale II*	cat	80	468	2.18
1990	*Jet Services V*	cat	75	454	2.18

Table 1.1: Relative speeds $V_s/\sqrt{\text{LWL}}$ achieved by some outstanding mono and multihulls when sailing across the Atlantic west–east.

[a] ULDB stands for ultra light displacemet boat

fore when comparing the speeds of different types of sailing craft *size for size*, it is not speed alone that should be used as a yardstick of the design excellence or the crew achievement, but speed in relation to the length of the craft. In other words, in order to compare objectively the speed potential of boats of different length, one must reduce them to the same *corrected* length. It has been understood for a long time that one cannot hope to continue indefinitely the speed improvements of the displacement type of yacht (in which the lateral stability needed to carry sails is provided by heavy metal keels), but, for no immediately reasons, this interest in high speed sailing has driven people to discuss new concepts of high performance sailing machines, build them and finally sail almost unthinkable, spider–like sea monsters bordering on pure fantasy.
Filippo Tommaso Marinetti, the founder and leader of Italian Futurism, in his *Futurist Manifesto* published in 1916, developed his idea of the new religion of speed. The following extract is evidence of the remarkable sensitivity of Marinetti as an artist who was capable of giving expression to a powerful trend that was hardly discernible at his time:

> La velocità, avendo per essenza la sintesi intuitiva di tutte le forze in movimento, è naturalmente pura. La lentezza, avendo per essenza l'analisi razionale di tutte le stanchezze in riposo, è naturalmente immonda. Dopo la distruzione dell'antico bene e dell'antico male, noi creiamo un nuovo bene: la velocità, e un nuovo male: la lentezza. Velocità = sintesi di tutti i coraggi in azione. Aggressiva e guerresca. Lentezza = analisi di tutte le prudenze stagnanti. Passiva e pacifista. Velocità = disprezzo degli ostacoli, desiderio di nuovo e d'inesplorato. Modernità, igiene. Lentezza = arresto, estasi, adorazione immobile degli ostacoli, nostalgia del già visto, idealizzazione della stanchezza e del riposo, pessimismo circa l'inesplorato.....L'ebbrezza delle grandi velocità in automobile non è che la gioia di sentirsi fusi con l'unica divinità. Gli sportsmen sono i primi catecumeni di questa religione. Prossima distruzione delle case e delle città, per formare dei grandi ritrovi di automobili e di aeroplani.

No doubt the peculiar fascination and exhilaration of high speed under sail was, and still is, a powerful emotive drive to stir man's creative imagination and desire to build and sail faster and faster craft. Progress towards higher speed is not always, however, a continuous process, and has been achieved in a rather spasmodic fashion through the last 100 years (see Table 1.1). Right now the majority of sailing men seem inspired by dreams of ultimate speed under sail: the Transatlantic Single Handed Race and the JohnPlayer World Sailing Speed Record are just two extreme examples of the competitive spirit which dominates the sailing scene.
Concentrating on the competitive and high speed aspect of sailing boats, we may divide existing and anticipated sailing craft into five categories, as follows:

1. Light, flat bottomed *skimming* forms (dinghies, scows, maxi–raters, etc).

2. Heavy displacement forms (heavy conventional ballasted yachts).

3. Multihulls (catamarans, trimarans, proas).

4. Sailing hydrofoils.

5. Other, various, craft, using sail for propulsion (land yachts, ice boats, surfboards, skimmers).

We will focus our attention on a typical International America's Cup Class Yacht (Fallow 1996; Richards, Johnson, and Stanton 2001) that we can insert in the point 1. To explore ways and means of sailing faster, we shall review the basic factors and underlying principles that govern the behaviour and limit the performance of a variety of sailing crafts. Since sailing boats are not constant cruising speed vehicles such as aircraft, but operate in a variety of wind velocities, ranging from calm to gale (see Appendix C), and on various courses relative to the wind, one should not expect that any simple set of criteria can succesfully be applied to judge the merits of rigs or hulls.
The choice of a rig or the concept of a hull to match it, must necessarily be a compromise, depending largely on what one is trying to achieve: to improve a boat's performance on a triangular course, or on an arbitrary course when racing offshore, to beat some absolute speed record in sheltered water or to cross the Atlantic in the shortest time singlehanded.
However crude and difficult to determine, a set of evaluation criteria must be established or agreed upon, in order to estimate the quality of a sailing boat and the eventual progress made. With no criteria it is difficult to make any sensible judgement concerning the excellence of a design or development. The criteria by which the merits of a particular type of boat are evaluated will of course change with the particular design aims of the vessel.
Taking into account the opinion expressed by the late Lord Brabazon of Tara at one time British Minister of Aircraft Production and also member of the Advisory comittee for Yacht Research

> ....the designing of aircraft is child's play compared with difficulties of the sailing craft.

in order to understand the *not–so–easy* fundamental factors governing yacht performance one may reasonably look at the sailing yacht as:

1. a combination of two distinct systems: one of which is the *aerodynamic* (rig), and the other the *hydrodynamic* (hull with appendages), whose performances can be considered and measured separately, or

2. a complex dynamic system consisting of two interdependet parts, aerodynamic ans hydrodynamic, in which case each part is the cause and effect of the other part, and of the whole system; and the system itself is the cause and effect of its parts. In other words, the whole system's characteristic are more than just the sum of the characteristics of its parts. Hence, the

resulting performance cannot be estimated directly from model results by a simple, straightforward process.

The first approach is more tempting than the second, since it suggests the possibility of relatively uncomplicated, direct comparison between different rigs, or different hulls that, for example, can be developed and measured separately in the wind tunnel and towing tank respectively. An immediate practical purpose of such method is in a optimal design process in order to determine whether one proposed design is better than another, either proposed, or already constructed. As mentioned earlier, the essence of the second alternative approach to the estimate of sailing yacht performance is that the craft is regarded as one complex aero–hydrodynamic machine, so that the boat speed cannot be determined from the characteristic of its aerodynamic and hydrodynamic components alone. As might be expected, to achieve a goal in this design a great deal of sail and hull data are required.

1.2 The symmetry of sailing

Whether you sail well or poorly, Nature sees to it that the forces between wind and boat are always precisely balanced by the forces between water and boat. This symmetry of sailing is happening all the time:

> I have become an avid symmetry fan, addicted beyond cure, utterly convinced of the fertility of symmetry in scientific study and research as a unifying and simplifying factor.
> Joe Rosen, *Simmetry Discovered*

Because the aerodynamic of yacht sails is complex, and because its application to yachts differs in fundamental ways from aeronautical applications, it is essential to begin by focussing on the objectives of a study on sail aerodynamics. This requires a basic understanding of the overall equilibrium of forces and moments on a yacht. The words *drag* and *lift*, borrowed from aeronautics, refer to key concepts in understanding sailing. Aspects of sailing which depend primarly on drag, namely *downwind sailing*, are discussed in Section 1.2.1; both lift and drag, or more specifically their relationship, form the kernel of understanding *windward* or *upwind sailing* in Section 1.2.2.

1.2.1 Downwind sailing

The key concept associated with downwind sailing is fluid drag even if:

> It is deplorable fact that no theory of drag yet exist which even approximately does justice to the experimental results.
> Prandtl and Tientjens, *Fundamentals of Aero and Hydrodynamic*

and, although this quotation dates 1934 it is still true. We would like to minimize the hydrodynamic drag of the hull through the water and maximize the aerodynamic drag of the sails originated entirely from the pressure distribution over the sails. Drag is defined as the net force in the direction of the undisturbed flow. Fluid drag is not brought about a single mechanism but, it is the combination of several effects. These can be divided into two main categories (Marchaj 1979):

1. surface friction drag

2. normal pressure drag that consists of three distinct parts:

   - boundary layer pressure drag
   - vortex drag or induced drag
   - wave drag.

1.2.1.1 Surface friction drag

The way in which these various forms of drag manifest themselves, is best seen by looking carefully at the fluid flow close to the surface of a keel (Cebeci 1999). This flow will be close to the ideal, unlike that around the mainsail, for instance, which is disturbed by the mast. What we would like to study here, is the flow close to the surface because it is in this region that the drag–producing effects mainly operate.
The nature of the flow at a particular point on the keel depends on the history of events leading up to that point. Air (sail) or water (hull and keel) flowing uniformily in the absence of any obstruction will continue to flow without turbulence, but in the presence of some object like a sail or keel the nature of the flow will change as one moves from the *leading edge* to the *trailing edge*. The change does not occur immediately on encountering the obstruction but in three fairly discrete steps as we move back along the surface. Figure 1.1 shows the extent of a flow regime known as the *boundary layer*, a region near the surface where the flow velocity is changing rapidly with distance out from the surface (Thwaites 1960). Within the boundary layer the flow speed varies from zero at the surface to that of the external flow. In this Section, we will be looking only at the flow within the boundary layer, since it is here that the effects of viscosity are manifested and where most of the drag has its own origins. The character of the *external* flow, or separation region, will be discussed in Section 1.2.2.2 because of its greater importance for lift than for drag.
There are three kinds of boundary layer: a laminar one, a turbulent one and a transition region.

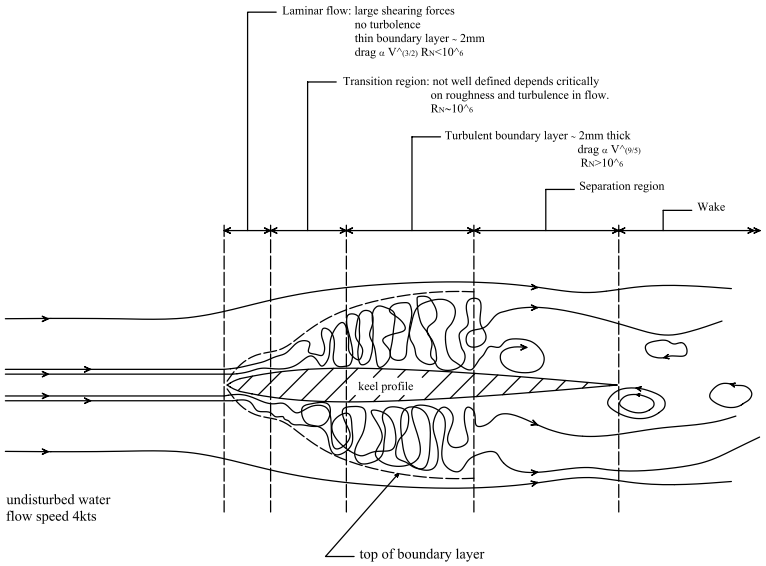

Figure 1.1: The general nature of the flow which is always found when fluid moves past an obstacle. Figure given here is for water flow at 4 knots past a fin keel.

Laminar flow region: in order to understand the formation of the boundary layer and also the fundamental origin of nearly all drag forces, one must understand clearly what is meant by viscosity. We consider two smooth flat plates of area A with a fluid filling the space between them. To move the plates at a constant speed, it requires a force F which is found by experiment to depend exactly on the following parameters: it increases in proportion to the area A and to the velocity v and is inversely proportional to the thickness of the fluid t; clearly F will be greater for a high viscosity than a low one, so we can write:

$$F = \frac{\eta v A}{t}, \tag{1.1}$$

where η is called the coefficient of viscosity and is a measure of the resistance to sliding of one surface over another when they are separated by a thickness of fluid. In order to see how this relates to the boundary layer and fluid drag in general there is one more important ingredient that must be added: intermolecular forces. The ultimate origin of fluid viscosity lies in the forces between molecules; such forces exist between all molecules of whatever kind, but taking into account that a molecule feels an attraction only for those others immediately surrounding it. It is now easy to see what must happen very close to the surface of a hull or sail when the water or the air is flowing past without any turbolence. The layer of fluid

molecules next to the solid interact strongly with its molecules and also with the adjacent fluid molecules, but not to any significant extent with any others. So the first layer moves hardly at all with respect to the solid. The second layer, being held by the first one, moves slowly with respect to it but therefore a bit faster with respect to the solid. As one continues out through millions of such layers a point is reached where the speed of flow is the same as that of the external flow at some distance from the surface. It is therefore clear that the velocity of flow increases smoothly as one moves away from the surface. Thus the frictional drag of the laminar boundary layers brought about by the forces that have to be applied to make these layers move with respect to one another against the intermolecular attraction.

The man who first investigated the characteristic of laminar and turbulent flow was Osborne Reynolds in 1883, using an apparatus in which the flow of a stream of coloured fluid was observed. More will be said later about the onset of turbulence, which is such an important part of the fluid flows which power all boats. For the moment we are concerned only with the fact discovered by Reynolds that the onset of turbulence in an otherwise non–turbulent flow depends on three quantities: the speed of the flow, the viscosity (actually the kinematic viscosity) of the fluid and the *length of the flow* which refers to the distance along the flow direction from the leading edge of the sail or keel. It is assumed that the air is moving without turbulence, a pretty crude approximation, of course, and it is simply the introduction of a sail (or keel) into this stable state that produces turbulence in the flow. This doesn't happen immediately, but only after the air has been in contact with the sail (or keel) over a distance which we call L. Reynolds discovered that the turbulence always occurs when the product of L and the speed divided by the kinematic viscosity, has a numerical value equal to about one million, or:

$$\frac{Lv}{\nu} = 10^6 \quad \Longrightarrow \quad L = \frac{10^6 \nu}{v}, \tag{1.2}$$

where v is the velocity, $\nu = \mu/\rho$ is the kinematic viscosity ($\nu_{\text{air}} = 1.5\,10^{-5}\text{m}^2/\text{sec}$; $\nu_{\text{water}} = 1.0\,10^{-6}\text{m}^2/\text{sec}$), ρ is the air density $\rho_{\text{air}} = 1.20\text{kg}/\text{m}^3$ or water density $\rho_{\text{water}} = 1000\text{kg}/\text{m}^3$. We have two results for the maximum length of the laminar flow region (Garrett 1990), depending on whether we are looking at sails or hulls as shown in Table 1.2.

So because of the physically simple circumstances of laminar flow we are able to calculate quite precisely the friction drag due to the laminar part of the flow. The first step is to calculate the velocity distribution through the boundary layer and then the rate of growth of the thickness of the laminar boundary layer. To get the total flow these contributions are mathematically added and we find that the

	Water (Keel)	Air (Sail)
L (metres)	$\dfrac{1}{v \text{ metres per sec}}$	$\dfrac{15}{v \text{ metres per sec}}$
L (metres)	$\dfrac{2}{v \text{ knots}}$	$\dfrac{30}{v \text{ knots}}$

Table 1.2: Length of the laminar flow region.

friction drag force in purely laminar flow is (Thwaites 1960):

$$\boxed{\text{laminar–frictional boundary layer drag force}} \quad \overset{\text{is proportional to}}{\propto} \quad v^{3/2} \times \text{wetted area}, \tag{1.3}$$

here v is the hull speed (for a keel) or apparent wind speed for a sail. Of course it also depends on the viscosity, but this is not a variable over which we have much control.

Transition to turbulence: Figure 1.1 shows the location of the transition region between the laminar boundary layer and the turbulent boundary layer. As has already been said, fluids which are initially non–turbulent soon get tired of this state of orderliness and turbulence sets in. It is part of the grand scheme of things in Nature, where it is known that the total amount of disorder in the Universe is constantly increasing. In summary, the characteristics of the transition region are as follows:

- sources of turbulence appear randomly in time and position as spots in the laminar flow which grow as they move downstream;
- the frequency of appearance of these source spots depends on the turbulence in the incident flow;
- transition can be triggered by a particle of dust which acts as a continuous source spot.

Turbulent boundary layer: two important differences between laminar and turbulent boundary layer flow are evident: first, the turbulent boundary layer is nearly five times as thick as the laminar one, and second, the rate of increase of

velocity, as we move away from the surface, is much greater in the turbulence case. This means that near the surface the shear forces within the fluid are greater, and hence a greater drag is expected. Also, because the turbulent boundary layer is so much thicker, a greater mass of fluid is affected by these shearing forces. It is clear that laminar flow, over as much of the hull or sail surface as possible, should be maintained in order to minimize the surface friction drag. Unfortunately, in sailing, laminar flow is the exception rather than the rule, because laminar flow is a rather unstable condition compared with turbulent flow. Any turbulence in the incident flow will quickly destroy the laminar condition so that only when we are sailing in very smooth water with a steady but not too strong wind, is it likely that there will be regions of laminar flow on the sails and hull. Thus in practice most of the surface friction drag has its origins in the region of turbulent boundary layer flow. As we saw for laminar flow, the friction drag force in turbulent flow is also determined entirely by the shape of the velocity gradient curve and the boundary layer thickness. When the calculation is carried through in the same ways as in the laminar case we find:

$$\boxed{\text{turbulent–frictional boundary layer drag force}} \quad \overset{\text{is proportional to}}{\propto} \quad v^{9/5} \times \text{wetted area.} \tag{1.4}$$

Thus the surface friction drag increases almost as the square of the speed. If the speed is doubled the drag increases by nearly 4 times.

1.2.1.2 Normal pressure drag

In Section 1.2.1 it was pointed out that the phenomenon of drag could be divided into two broad categories. The first, surface friction drag, has already been discussed; the second, normal pressure drag, will occupy the remainder of this section. The drag associated with lift or vortex drag or induced drag will be treated in Section 1.2.2.2. If we were able to determine the total drag force on a small area of hull, say 1 cm^2, it might have a magnitude and direction represented by the arrow in Figure 1.2(a). The component of the total drag force which is parallel to the hull or sail is of course the surface friction drag already discussed in Section 1.2.1.1. The component perpendicular to the hull or sail is the normal pressure drag. Any object immersed in water or air has pressure forces on it. These come from the fluid and are always perpendicular to the surface. The situation is also the same for an object moving in a non–viscous fluid. This is an idealisation which is of course not true, as all fluids under normal conditions have viscosity, but we discuss this case first because it helps in understanding normal pressure drag. For a simple shape like a cylinder, it is easy to calculate the fluid flow if there is no viscosity

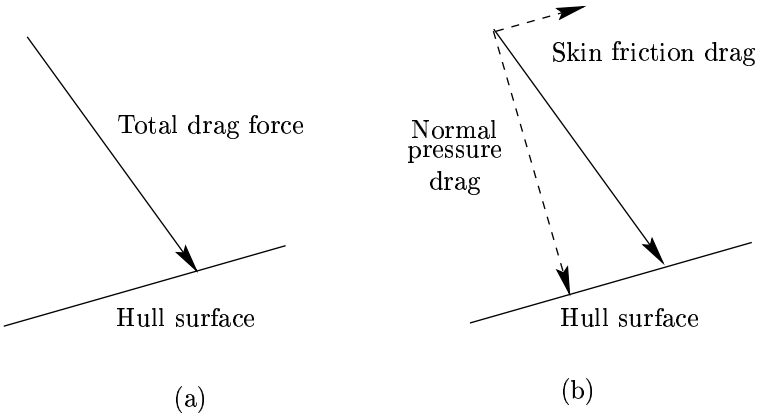

Figure 1.2: A small section of a hull and a measure of the drag on it.

(Figure 1.3). From such a flow pattern, one can deduce the pressure distribution: since the flow pattern is symmetrical, so must be the pressure distribution. Diametrically opposite pressures are the same so the net force on the cylinder is zero. Thus in this case of no viscosity there is certainly no surface friction drag, but also no normal pressure drag either. This state of affairs is known as d'Alembert's *paradox* (Thwaites 1960). Like all paradoxes, it is only a paradox if one doesn't know enough. Its resolution is simple: no real fluids are completely non–viscous. What is interesting, however, is the fact that when viscosity disappears, not only does the surface friction drag (Section 1.2.1.1), which depends directly on viscosity, disappear, but so also does the normal pressure drag.

Boundary layer normal pressure drag: This is also known as *form drag*. It arises from the dissipation of energy within the boundary layer, which modifies the symmetrical pressure distribution that would be obtained in a non–viscous fluid.

Vortex drag: we will consider the induced drag or vortex drag in Section 1.2.2.2.

Wave drag: That the formation of waves in the wake of a boat gives rise to drag is well known. That immutable law of Nature, the conservation of the energy, is basically responsible. The production of waves requires energy, supplied by the moving hull. If the hull did not have to produce such large waves, as for instance when planing, more energy would be available for overcoming other forms of resistance, so that the hull would go faster. So we reach the somewhat obvious qualitative conclusion that the bigger the bow and stern waves, the greater the

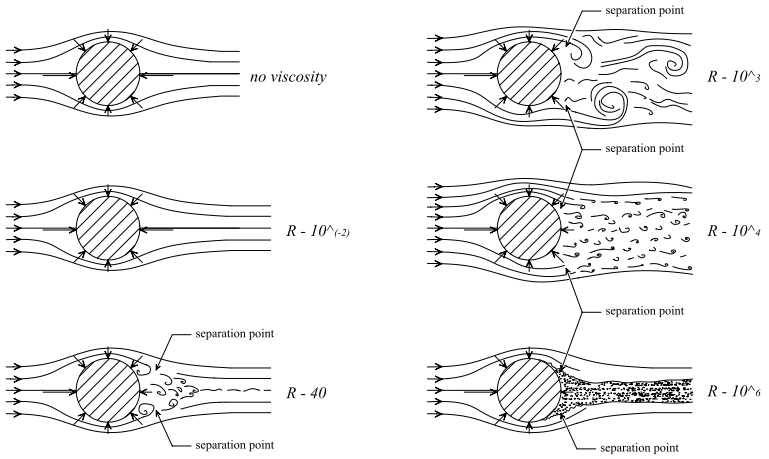

Figure 1.3: Flow distributions around a cylinder, such as mast or a shroud, under different conditions.

wave resistance. Furthermore, the size of these waves (and hence the resistance) depends upon the speed and shape of the hull. At low speed the bow and stern waves are more or less independent and have a wavelength λ (distance from crest to crest) much less than the waterline length of the boat LWL. As the boat speeds up, the height of the bow and stern waves increases and, as the stability of a water wave requires, the wavelength increases. Eventually the wavelength is such that the second crest of the bow wave coincides with the stern wave: this magnifies the size of the stern wave and hence also the wave drag. At this point we have the *hull speed* at which resistance is increasing rapidly so that in order to raise the speed over, much more power is needed. In the case of water waves this hull speed is given by (Prandtl 1952):

$$V_s = \sqrt{\frac{g\lambda}{2\pi}}, \tag{1.5}$$

where g is the acceleration due to gravity. Because of the way in which the bow and stern waves are produced, the maximum wavelength for the combination wave is going to be approximately equal to the waterline length LWL of the hull. Since the bow and stern are stationary with respect to the boat they must be moving across the water at the same speed as it is. For waves there is a unique relationship between their speed and their wavelength (Eq. (1.5)), and since their wavelength is just the waterline length of the boat we get from this the well known value for

hull speed (Claughton, Wellicome, and Shenoi 1998):

$$V_s = \underbrace{\sqrt{\frac{g\lambda}{2\pi}}}_{\text{speed of water waves}} = \overbrace{\sqrt{\frac{g\ \mathrm{LWL}}{2\pi}}}^{\text{speed of boat}} = 1.25\sqrt{\mathrm{LWL}}, \tag{1.6}$$

where V_s is in metres/sec and LWL in metres. If V_s is in knots and LWL in metres, then $V_s = 2.4\sqrt{\mathrm{LWL}}$. When V_s is in knots and LWL in feet, the equation is $V_s = 1.34\sqrt{\mathrm{LWL}}$.
The generation of lift (see Section 1.2.2.2) will in general alter the magnitudes of the boundary layer normal pressure drag and wave drag, and in addition give rise to a trailing vortex system. It should be emphasised that these drag concepts are not independent of one other.

1.2.2 Upwind sailing

The idea of symmetry in Section 1.2 is also present in the much more complex situation of windward sailing. The verses of Samuel T. Coleridge from *The Rime of the Ancient Mariner*:

> At length did cross an Albatros.
> through the fog it came;
> As if it had been a Christian soul.
> We hailed it in God's name.

are one of the most preferred works to yachtsmen an lovers of the sea because it is a story of the age of sail and human dependence on the elements. Sailors struggling to beat to windward in an inefficient square–rigger (Tilley 1994), easily believed in the supernatural powers of the incredible Wandering Albatross or *Toroa* as it is known to the Polynesian navigators of the South Pacific, which could effortlessly follow them to windward with never the slightest movement of its wing, by simply flying in great tilted circles about their ships. The question is: how could it fly to windward without flapping its wings as any other bird would? It was not until 1883 that the albatross's secret was laid bare (Roberts 1995). The first person to understand this was the englishman John William Strutt who later became Baron Rayleigh. He lived in a period of time in which it was thought that all phenomena of Nature were explanable in terms of the laws of classical physics. Understanding the flight of the albatross was a problem which he solved in terms of the fundamental laws of physics, years before a practical airplane was built. Friction slows the wind at sea level and just above, with the result that the wind

speed increases from zero to its full value in the first 30 or so metres above the waves. It is from this gradient in velocity that the albatross extracts the energy for its flight. The bird glides downward, converting potential energy to kinetic energy and picking up air speed as well as ground speed. Just above the waves it wheels into the wind, acquiring initial lifting acceleration from an abrupt increase in wing incidence or angle of attack. As the bird rises it encounters ever higher wind speeds and, with its air speed thereby maintained, is able to rise again without any expenditure of its own energy to the altitude from which it first descended. In a similar way but with a slight change of path, it can proceed to windward again without expending its own energy. Thus it is not correct to say that is the *relative* speed of air and water that enables boats to sail to windward; now we see, using a similitude with the Nature, that we don't need to media, just a *velocity gradient* within one will do.

1.2.2.1 Balance of air and water forces on a yacht going to windward

Because the aerodynamic of yacht sails is complex, and because its application to yachts differs in fundamental ways from aeronautical applications, it is essential to begin by focussing on the objectives of a study on sail aerodynamics. In turn, this requires a basic understanding of the overall equilibrium of forces and moments on a yacht (Marchaj 1979; Claughton, Wellicome, and Shenoi 1998). Figure 1.4 illustrate the hull of a yacht sailing upright at a constant speed with the *centre of effort* (CE) of the sail and the *centre of lateral resistance* (CLR) of the submerged hull coincident at the point O. These simplifications do not affect the geometrical relationships (1.7) we shall derive (Marchaj 1990). In Figure 1.4 we use the following notations:

- for the velocity field:

  V_{mg} speed made good to windward or velocity made good;

  V_a apparent wind velocity;

  V_t true wind velocity;

  V_s boat speed through the water;

- for the angles:

  λ leeway angle;

  β angle between apparent wind and course or course angle; it is

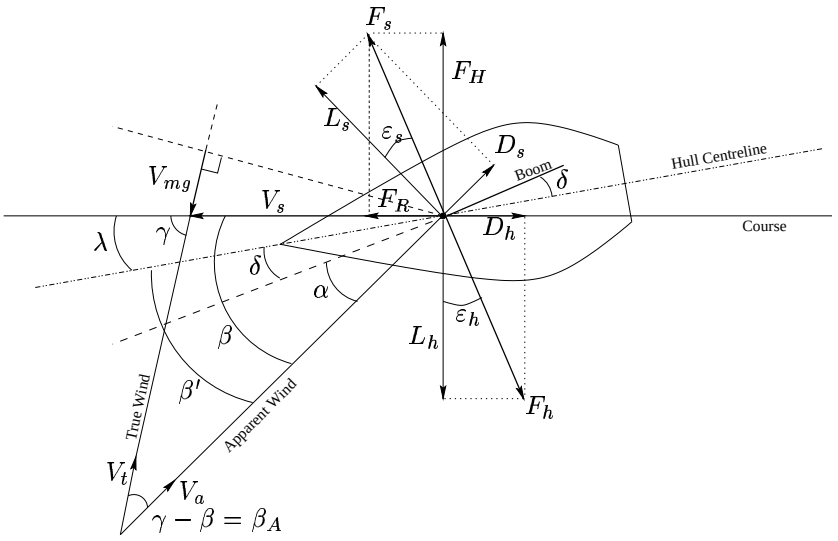

Figure 1.4: Velocity triangle and forces on a boat in the water plane with heeling angle $\phi = 0$.

obviously a measure of how high the boat is pointing;

$\beta' = \beta - \lambda$ measured apparent wind angle between apparent wind and heading; angle measured by on–board instruments;

γ angle between true wind and course or true wind angle;

δ sheeting angle or angle between boom and centreline;

α angle of incidence of wind on the sail or geometric angle of attack.

The geometrical relationships between the six quantities, apparent wind speed V_a, apparent wind angle β, boat speed V_s, true wind speed V_t, true wind angle γ and speed made good to windward V_{mg} are fundamental and applicable to any boat on any point of sailing. Even without any reference to the details of hull and sail characteristics, these relationships impose severe restriction on the range of possible performance of a sail boat. The following useful formulae are simply algebraic statements of the geometry of Figure 1.4

or 1.6:

$$V_{mg} = V_s \cos\gamma \tag{1.7a}$$
$$V_t \sin\gamma = V_a \sin\beta \tag{1.7b}$$
$$V_s \sin\gamma = V_a \sin(\gamma - \beta) \tag{1.7c}$$
$$(V_t + V_{mg})^2 + (V_{mg}\tan\gamma)^2 = V_a^2 = (V_s + V_t\cos\gamma)^2 + (V_t\sin\gamma)^2 \tag{1.7d}$$

where from Equation (1.7d) we may write:

$$\frac{V_t}{V_a} = -\frac{V_{mg}}{V_a} + \sqrt{1 - \left(\frac{V_{mg}}{V_a}\tan\gamma\right)^2}. \tag{1.8}$$

- for the forces acting on the hull:

  F_h total hull force;

  L_h hull lift force perpendicular to fluid (water) flow direction;

  D_h hull drag force along fluid (water) flow direction;

- for the forces acting on the sail:

  F_s total sail forces or driving force;

  L_s sail lift force perpendicular to fluid (apparent wind air) flow direction;

  D_s sail drag force along fluid (apparent wind air) flow direction;

  F_H heeling force of sails where (see Figure 1.8):

  $H = F_H \cos\phi$ sideforce in horizontal plane;

  $F_V = F_H \sin\phi$ vertical force of sail;

  F_R driving force of sails along course direction or propulsion or thrust force

The geometry of sailing windward: the sailing yacht operates at the interface between two fluids: the immersed part of the hull moves through water along the

yacht's track, the above water part of the hull, the mast and sails move through the air, experiencing an incident wind field that is the vector sum of the natural or true wind V_t and the wind arising from the yacht's motion through the air. The true wind, vectorially added to the wind produced by the boat's motion, creates the apparent wind V_a as *felt* by the sails. It is obvious that if one sails dead downwind at 8 knots (V_s) in a 15 knot wind (V_t), the apparent wind (V_a) over the deck will be only 7 knots. It is not, however, so obvious that after turning back and now moving through the water at 6 knots with the wind direction indicator showing $\beta = 33°$, the wind over the deck will now be 19.7 knots (V_a). In Figure 1.4 the arrow marked V_t specifies the magnitude and direction of the true wind, that is measured by an observer fixed with respect to the sea; V_s is the speed of the boat with respect to the water and is therefore measured directly from the knotmeter providing the leeway is not extremely large; V_a is the apparent wind speed and can be measured directly on board. This three quantities, V_s, V_t and V_a form what is usually called a vector triangle. The other quantities are: the angle β, which is the angle between the direction of the apparent wind and the course sailed; the angle γ which is the angle between the true wind and the course sailed, and finally the important quantity V_{mg} which is the speed made good to windward. This latter quantity is the component of the boat speed which is directly opposite to the true wind. Given any three of the six quantities V_a, V_t, V_s, V_{mg}, β and γ it is possible to determine the other three from the Equations (1.7) and (1.8). It should further be remembered that the crew has direct control over only two variables: the apparent wind angle via the helm (rudder) and the angle of incidence of wind on sails via the sheets. Of course a number of adjustments are possible, mainly concerned with sail shape.

In windward sailing it is the ratio of lift to drag that is substantially important in determining the characteristics of the boat. A description of windward sailing is somewhat like an exercise in geometry, so you will not be surprised to learn that lift/drag ratio can be represented by an angle, the *drag angle*$= \varepsilon$. In Figure 1.5 we show that the total forces F_s and F_h acting on a object in a fluid flow (air/water respectively) are generally at some angles to the undisturbed flow direction. If these forces slopes aft a long way, the drag component is large compared to the lift, whereas if it is near to the perpendicular at the apparent wind, the lift component is relatively larger than the drag. The drag angle ε is therefore defined as the angle between the direction of the lift force and the total force. Clearly a large drag angle implies a larger drag or to be more precise a large drag/lift ratio. When we refer to the sail, ε_s is the drag angle between F_s and L_s; whereas with reference to the hull, ε_h is the angle between F_h and L_h. Since we will more often be speaking of the ratio of lift to drag rather than drag to lift we define drag angle by:

$$\frac{L}{D} = \frac{1}{\tan\varepsilon} \quad \text{or} \quad \varepsilon = \arctan\frac{D}{L}. \tag{1.9}$$

From Figure 1.4 it is easy to write the relation:

$$\beta = \varepsilon_s + \varepsilon_h, \tag{1.10}$$

moving from which we can write the following theorem:

Theorem 1 (Beta Theorem or Course Theorem) *The angle β between the apparent wind and the course actually sailed is equal to the sum of the sail ε_s and hull ε_h drag angles.*

This simple geometrical relationship was first identified by Lanchester in (1907) and it is of fundamental importance in understanding principles which control the performance of any sailing boat. The apparent simplicity of the Theorem 1 tends to obscure the complex interactions of physical effects which are involved when a boat sails to windward, as we shall see later in Section 1.2.2.3.

Aerodynamic and hydrodynamic forces: let us limit our attention to the windward leg, generally regarded as the most important sailing course. This course, more than any other, intensifies the conflict between the aerodynamic efficiency of a rig and the hydrodynamic efficiency of a hull, together with its resistance and stability. The most obvious manifestation of this conflict in the traditional monohull yachts is that between resistance against stability (i.e. narrowness and lightness, giving an easily driven hull) and beam and weight (giving power to stand up to the sail forces). Yacht performance, particularly when sailing to windward, is in fact a complicated game of hull resistance, the driving power of the sail and stability. Figures 1.5, 1.6 and 1.9 show a yacht sailing at a steady speed in calm water: in this quasi static equilibrium condition the net forces and moments acting on the vessel are zero. The forces acting on the above water part of the yacht F_s, propel underwater part, which produce an equal and opposite force F_h. By adjustement of the sails (sheets) and rudder, the yacht can be made to hold a steady course. The waterplane in Figures 1.5 and 1.6 is conventionally treated as the divide between the aerodynamic and the hydrodynamic forces. The behaviour of the yacht can be viewed as a balancing of the forces in these two domains. As we can see in Figure 1.5, hydrodynamic and aerodynamic characteristics are usually presented on *track axes*, that is a right–hand orthogonal axis system in the vertical and horizontal water plane with X_0 axis aligned with the yacht's direction of motion, Y_0 is positive to port and Z_0 positive upwards. On the contrary, structurally based characteristics are generally considered in a coordinate system that moves together with the body of the yacht. It is another right–hand orthogonal system based on the centre plane of the yacht, aligned with the hull centreline and mast: X forward along the yacht centre line, Y normal to the centreline of the yacht in the plane of the deck and Z vertical in the plane of the mast.

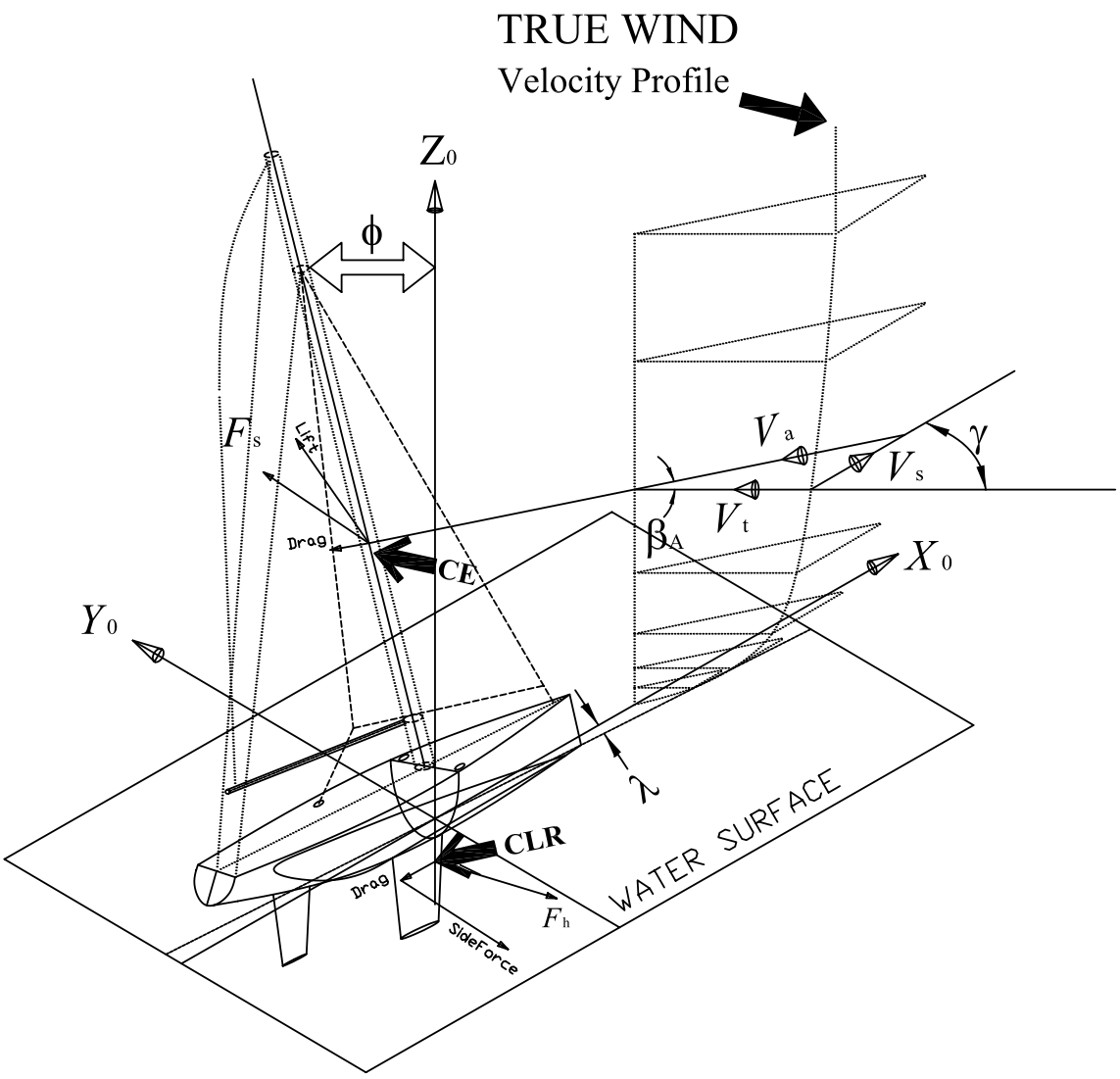

Figure 1.5: Forces acting on a sailing yacht.

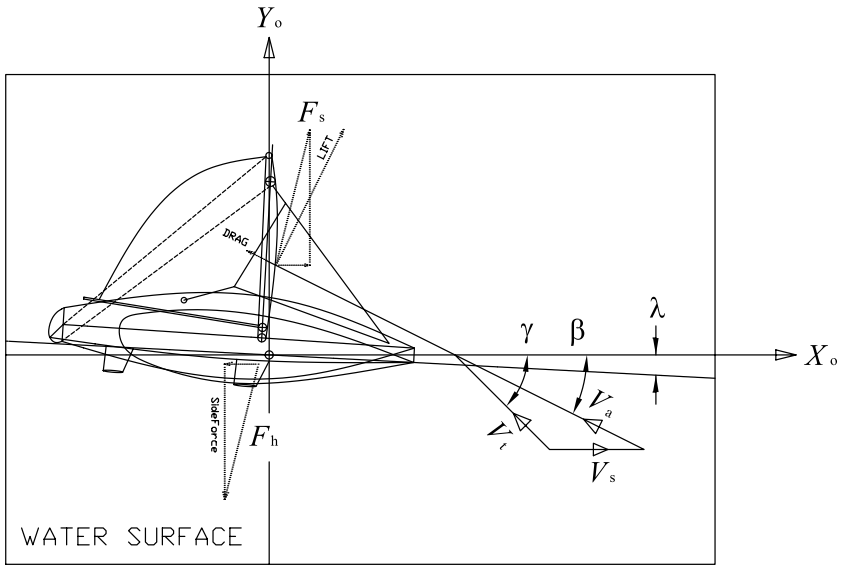

Figure 1.6: Components of forces acting on a sailing yacht in the plane of the water surface.

The total resultant aerodynamic force, F_s, generated by sails, can be resolved into two components in a plane passing through the centre of effort (CE), as shown in Figure 1.4 and 1.5. These components are:

- a driving force F_R acting along the direction of the course sailed;
- a heeling force F_H acting perpendicular to both the course and the mast. This force can be further resolved into two components, whose magnitudes will depend on the angle of heel ϕ:
  - $H = F_H \cos\phi$ horizontal or lateral force,
  - $F_V = F_H \sin\phi$ vertical force.

When beating against the wind, we should like to have the maximum possible driving force F_R and simultaneously a minimum heeling force F_H so that we may sail at high speed with neglegible heel and drift. It will be seen from the following trigonometrical relationship that the magnitudes of F_R and F_H depend on the angle β between the course and the apparent wind, and on the lift L_s and drag D_s that are assumed to act normal to the centre plane of the hull and mast, and may be resolved into the space axis system (X_0, Y_0, Z_0) by the following relations:

$$F_R = L_s \sin\beta - D_s \cos\beta \tag{1.11a}$$
$$H = F_H \cos\phi = (L_s \cos\beta + D_s \sin\beta)\cos\phi. \tag{1.11b}$$

It is evident from relations (1.11) that the drag not only decreases the driving force F_R (Equation (1.11a)), but also increases the harmful heeling force F_H (Equation (1.11b)). It is not difficult to see that if the aerodynamic force on the sails, F_s, and the hydrodynamic force on the hull, F_h, are equal and opposite, as shown in Figure 1.4, then the components of these forces, if taken along the same directions, must also be equal and opposite. This is shown in Figure 1.4 where F_R is the component of F_s along the course sailed; for this reason it is called the driving force of the sails. This is exactly opposed by the hull drag force D_h, measured along the direction of undisturbed water flow, which is simply the direction of the course sailed. At right angles to these are the two indipendent force components F_H and L_h which are also equal and opposite. They are at right angles to the boat's direction of motion and so do not contribute to its speed but only to its tendency to heel. As well as forces the boat is subject to torques or moments (Figures 1.7, 1.8 and 1.9). If the boat is sailing with a constant angle of heel ϕ, the clockwise torque or heeling moment M_H produced by F_H and L_h must be exactly opposed by a counterclockwise moment, or righting moment M_R, produced by W, the total weight of the boat plus crew and B, the buoyancy force resulting from the displaced water (see Figures 1.7 and 1.8). Obviously W and B are equal and opposite, otherwise the boat would either rise up out of the water or sink farther into it.

1.2.2.2 What about lift? Two–dimensional effects.

Although we saw in Section 1.2.2.1 that there are only two prime forces acting on a boat moving through the water F_s and F_h, it is useful to decompose these into components such as lift and drag. Drag is the component of the total force which is along the direction of motion and was discussed in detail in Section 1.2.1. We have a strong intuitive notion about drag but the situation is completely reversed in the case of lift. It is not so easy to understand why there can be such large component of force at right angles to the direction of flow. For this reason, classically (Prandtl and Tietjens 1934; Garrett 1990; Vinh 1993), the lift, which is so important in sailing, can be explained in three different ways:

1. flow line method,
2. momentum change approach,
3. mathematical approach.

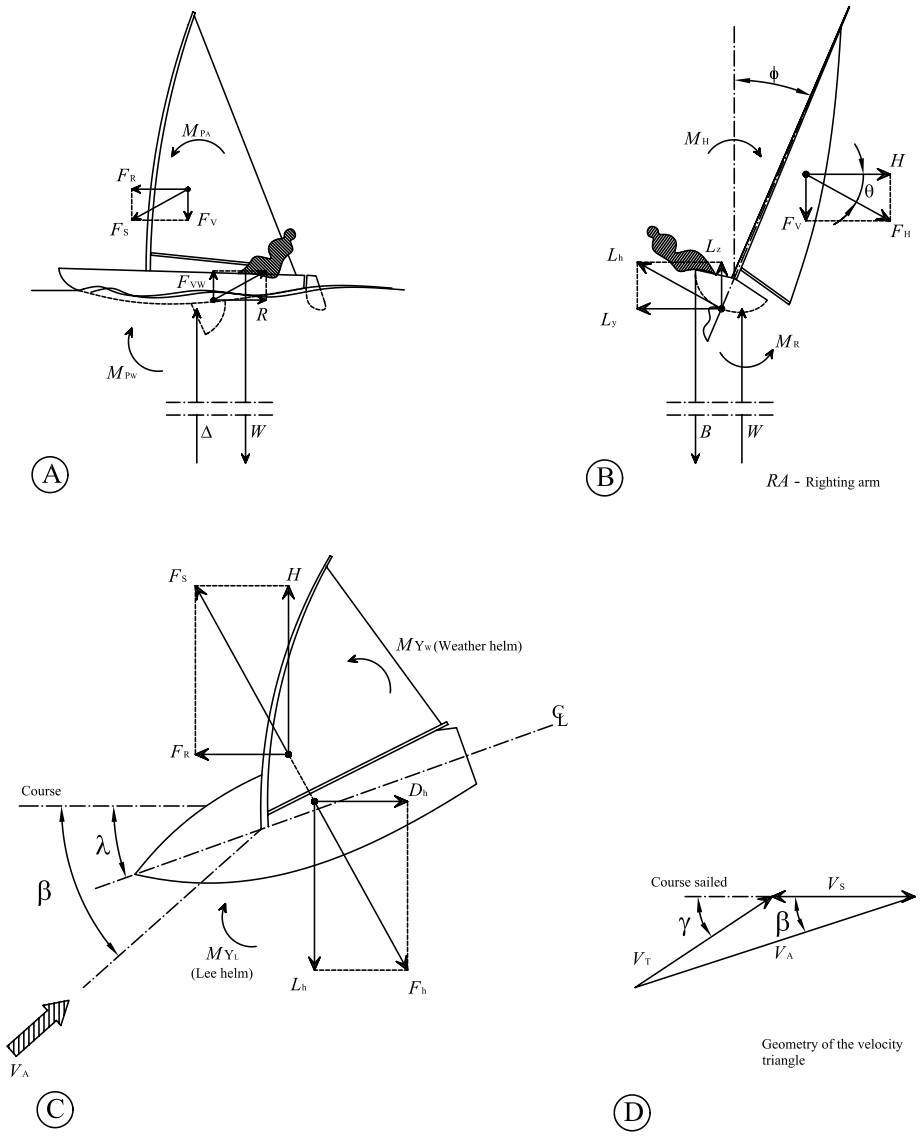

Figure 1.7: Fundamental relations.

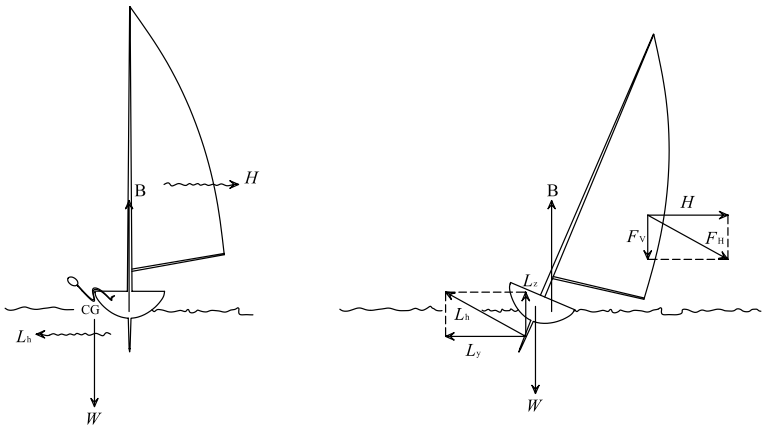

Figure 1.8: Torques or moments on a boat.

Flow line method: this is perhaps the standard method for explaining lift in books about sailing (Glènans 1975). We begin by drawing a diagram of the flow lines, called streamlines, around a sail without a mast, as shown in Figure 1.10. The result is the *potential flow*, or *ideal flow*, around an object. It gives the correct flow distribution in situations where separation does not occur. Since this is what is desired with sails and can be accomplished in many real sailing situations, the distribution of the flow shown in Figure 1.10 can then be regarded as qualitatively correct. We notice that at the left of the diagram the streamlines are equally spaced, indicating that there is no variation in flow rate from top to bottom along the left hand edge. For practical reasons we limit the extent of the flow into a region where the sail is placed in the centre. All the streamlines which pass to leeward of the sail, go through the area A_L, and all those passing to windward of the sail go through A_W. About eight streamlines flow through the small area A_L: if we follow them back to the region in front of the sail we see all of them pass through an area A which is much larger than A_L. In other words, the flow around the leeward side of a sail is such as to constrict the streamlines; on the other hand, on the windward side of the sail, the streamlines open out from a small area to a larger one A_W. This means that flow over the leeward side is faster than in front and over the windward side slower than in front (see Figure 2.18 and example at pag. 85). To make a connection between speed of flow and lift, we must introduce another law of Nature: the Law of Conservation of Energy. In incompressible fluid flow, the sailing's case, we are concerned only with two forms of mechanical energy: kinetic and potential. If the system is purely mechanical and there is no exchange of energy to other forms, then conservation of energy requires that the sum of

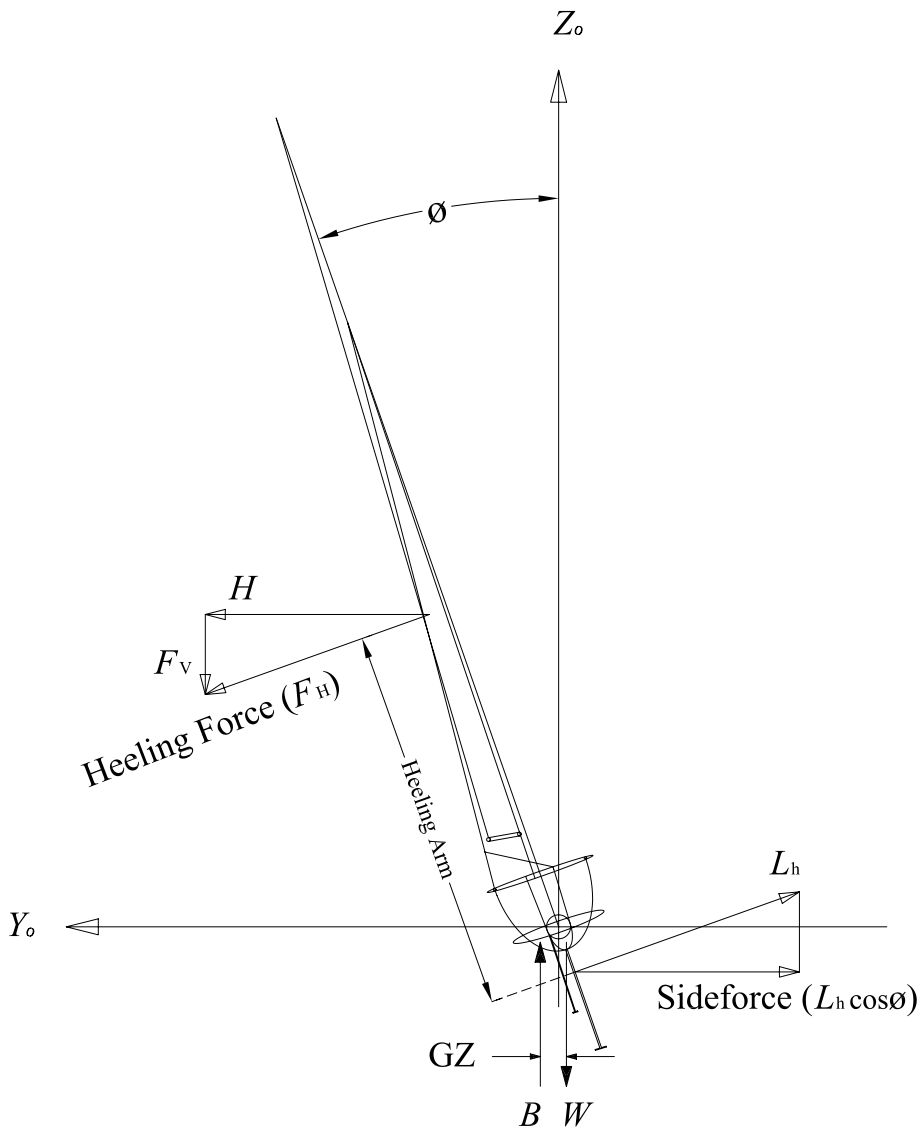

Figure 1.9: Roll moment equilibrium.

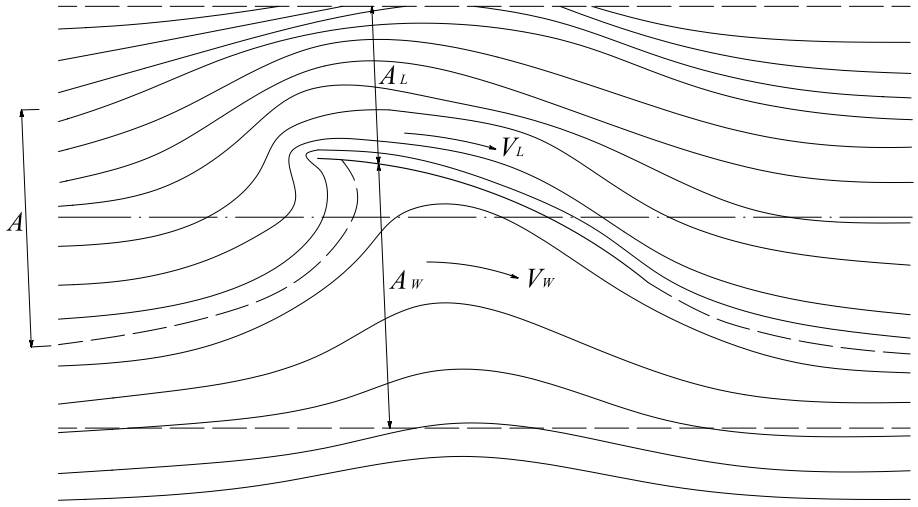

Figure 1.10: The flow around a sail under conditions where no separation is occurring. All the streamlines that flow through the area A ahead of the sail also flow through the smaller area A_L.

the kinetic and potential energies remains constant. It is only approximately true because in all systems, friction is present giving a change of energy to heat. Think now of a particle of fluid in a region of flow. If it finds itself in a region of high pressure and there exists nearby a region of low pressure, then the particle will be compelled to flow to the point of lower pressure. As a result of moving from the high pressure to the low pressure area the particle of fluid has speeded up. Thus we can associate high pressure with large potential energy and low pressure with large kinetic energy. We are now able to write the fluid form of the Conservation of Energy (Prandtl and Tietjens 1934):

$$\frac{w^2}{2} + \frac{p}{\rho} = \text{const.}, \tag{1.12}$$

where ρ is the density, w is the velocity of a fluid particle and p the difference between the actual pressure and the pressure which would exist if the fluid were at rest. This result (Equation (1.12)) usually goes under the name of Bernoulli's Law, formulated in 1738. What we find for a sail, applying the Bernoulli's Law, is something like that shown in Figure 1.11 (a), where the length and direction of the arrows give the magnitude and direction of the pressure, respectively. As expected, the arrows are longer on the windward side, indicating that the pressure there is greater than to leeward. The vector sum of all these forces gives the total

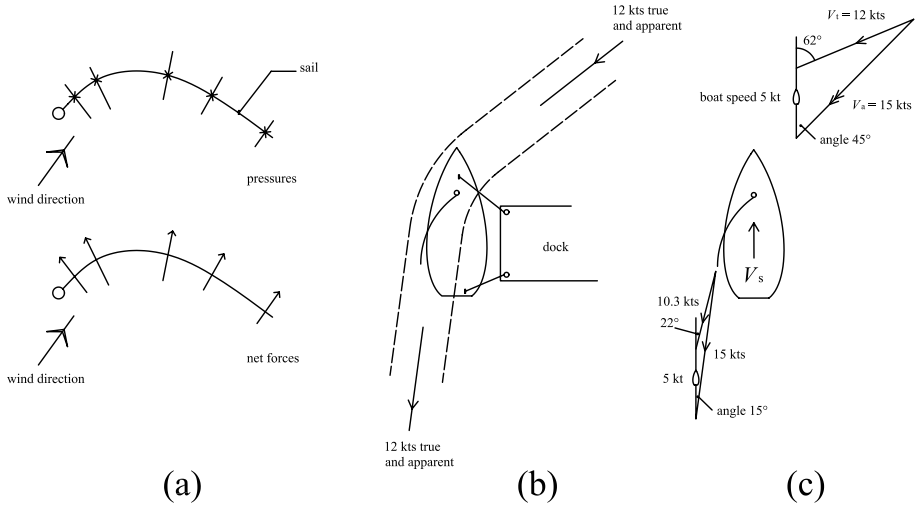

Figure 1.11: (a) Distribution of pressure for the flow shown in Figure 1.10. (b) The air flow around a fixed sail is equivalent to a deflection of the air stream. (c) If the boat is allowed to move forward energy is extracted from the air flow.

sail force which has a component perpendicular to the wind direction: this is the lift.

The momentum change approach: we use here the concept of the sail as an *air deflector*, see Figure 1.11 (b). It is a rather strange kind of deflector because the air is deflected not just from the windward side, but from the leeward side as well. The objective in sailing is to extract as much energy as possible from the air and water flow. If energy is to be taken from the wind, the wind speed will be reduced. To see just how this comes about, we consider in Figure 1.11 (c) a boat moving forward at 5 knots. In the absence of any true wind, the apparent wind felt on board would be 5 knots from dead ahead. If we add to this a true wind of 12 knots at 62° to the yacht's heading, using relations (1.7), we find that the apparent wind is 15 knots at 45°. After the wind leaves the sail it will still have an apparent speed of 15 knots. This is because apparent wind is measured with respect to the boat. However, an observer in an anchored boat would measure a true wind speed of 12 knots just ahead of the sail and a speed of 10.3 knots downwind of the leech. This reduction of true wind speed by 1.7 knots represents a loss of energy by the wind which has been transferred to the yacht. We now have to examine the physics of what is happening. The magnitude of the momentum, or quantity of motion, is simply the product of mass and velocity. One of the most fundamental

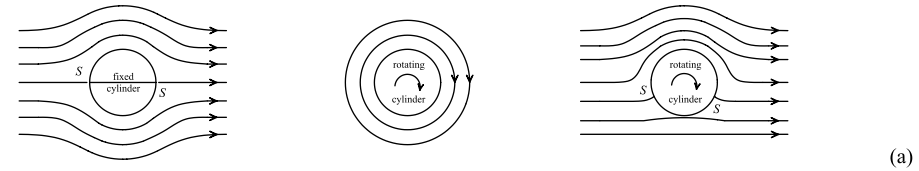

(a)

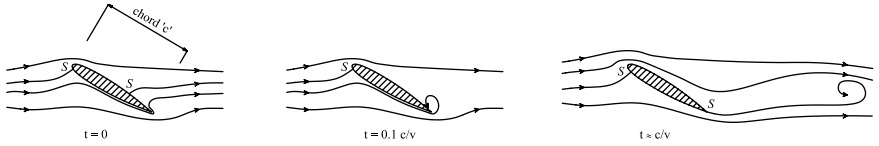

(b)

Figure 1.12: (a) Ideal potential flow around a fixed cylinder. (b) How the streamlines change with time around a symmetrical keel section at a fixed angle of leeway.

laws of classical mechanics concerns the relationship between force and change of momentum described by Sir Isaac Newton (1642–1727). The proper understanding of mechanics that Newton accomplished represents perhaps the greatest single leap forward in human understanding of Nature. Known nowdays as Newton's Second Law of Motion, it states that:

> ...**the rate of change of momentum of an object is equal to the net external force applied to it**...

Rate of change refers to a change with time, and since the mass of an object is usually fixed, rate of change of momentum refers to a change in its velocity, or direction, or both. If the speed is moored, (Figure 1.11 (b)) the speed of the air flow after it leaves the sail is unchanged: only its direction is changed. This amounts to a change in momentum of the air which gives rise to a force on the sail. In this way, the apparent wind in Figure 1.11 (c) is turned, but its speed remains unchanged. The symmetry of the situation suggests that the resultant force on the sail makes equal angles between the direction of the incident wind and the wind leaving the sail: this is of course the total sail force. The lift is the component perpendicular to the incident wind direction. The momentum change approach in order to understanding lift is a macroscopic theory: it can tell nothing about how a sail deflects the wind, but simply that if one knows the approaching and leaving wind directions and speeds then one can determine the resultant magnitude and direction of the total sail force. To be able to understand how the wind *works*, one must read the mathematical approach to understanding lift.

The mathematical approach: the ideal fluid flow, where viscosity is unimportant, is called *potential* flow because the equations involved are the same as those describing the potential in an electric field. In the 18^{th} century mathematics developed a theory able to describe situations where viscosity effects can be neglected.
Figure 1.12 (b) shows the sequence of events for the flow around a keel section when a boat starts to move forward at a constant leeway angle. The movement begins at time $t = 0$: initially the streamlines are exactly as potential theory would have them (Ashley and Landahl 1965). A short time later $t = 0.1c/v$, when the water has moved about a tenth of a chord length, it is already having trouble rounding the trailing edge and is separating from the surface forming a vortex. After the keel has moved forward to a distance about equal to its own chord, the vortex formed has been left astern and the flow over the keel is now smooth and attached at time $t \approx c/v$. The vortex, which is left behind, is known as the *starting vortex.* The crucial point here is that because of the inability of the water to flow around the trailing edge, a vortex has formed. Now, before proceeding with the final step of the argument explaining lift, something has to be said about the behaviour of these vortices.
Our understanding of vortex behaviour comes mainly from the work of Hermann Ludwig Ferdinand von Helmholtz (1821–1894) whose three Theorems are usually enunciated as follows (Ashley and Landahl 1965):

Theorem 2 (First Vortex Theorem) *The circulation around a given vortex tube (*strength *of the vortex) is the same everywhere along its length.*

Theorem 3 (Second Vortex Theorem) *A vortex tube can never end in the fluid, but must close onto itself, end at a boundary, or go to infinity.*

Theorem 4 (Third Vortex Theorem) *Vortices are preserved as time passes and they cannot decay or dissapear except through the action of viscosity or some other dissipative mechanism. So circulation or vortex motion in a fluid can neither be created nor destroyed.*

Such Theorems require a little explanation. The amount of circulation, or vortex strength, is equal to the line integral of the tangential component of the velocity along any closed curve surrounding a general airfoil (Batchelor 1967). Of these three Theorems of vortex behaviour, the one that concern us here is Theorem 4. We apply this Theorem to a situation of sailing in clear air and smooth water, when the apparent flow approaching the boat will normally contain no vortex strength: no eddies, just translational flow. If we now start sailing in this idyllic situation, we know that the first thing that happens is that a starting vortex is created in the water. According to Theorem 4 the total amount of vorticity cannot change. The only way this is possible is that there must exist an equal

and opposite vorticity called *bound vortex* or *circulation* around the keel section as depicted in Figure 1.12 (a). This circulation when added to the potential flow of Figure 1.12 (b) is precisely that needed to modify the flow near the trailing edge to produce the situation in Figure 1.12 (b) where the stagnation point has moved to the sharp trailing edge and flow over this point of the keel is free of discontinuities. Now, at last, the true origin of the lift should be appearing out of the mist: the key to the generation of the lift is the presence of circulation in the flow (in aeronautical parlance (Vinh 1993) the circulation around the wing is known as the bound vortex as opposed to the starting vortex which is left behind on the airfield) and if the circulation is known then lift can be calculated. Thus in order to summarize the mathematical theory of lift:

1. A fundamental feature of the flow around a lifting section is that the downstream stagnation line comes smoothly off the sharp trailing edge (Ashley and Landahl 1965).

2. The price for the production of this type of flow is the production of a starting vortex in the fluid. A physical role of the starting vortex is to shift the rear stagnation point towards the trailing edge, so that the velocity of the flow leaving the upper surface at the tailing edge is equal to that of the flow leaving the lower surface. This assumpton is called the Kutta–Joukowski condition (Marchaj 1979; Garrett 1990).

3. The fundamental Theorem 4 of fluid flow tells us that the existence of one vortex must be associated with the presence somewhere in the flow of an equal and opposite vorticity. This is the bound vortex or circulation around the lifting section. It has been understood from points 2 and 3 that the generation of circulation round an airfoil (see Figure 1.12 (b)) is necessarly accompained by a starting vortex (Whidden and Levitt 1993).

4. Just as a spinning ball, Figure 1.12 (a), produces circulation and has lift, so a lifting section has lift by virtues of its circulation although it does not have to physically rotate to produce it. The magnitude of the lift L per unit span b (cutting out from the infinitely long wing) perpendicular to the flow, applicable to two–dimensional flow, is given by:

$$\frac{L}{b} = \rho v_0 \Gamma, \tag{1.13}$$

where Γ being, of course, the circulation round any circuit enclosing the aerofoil; v_0 is the undisturbed tangential flow velocity of an infinite extent of fluid and ρ the fluid density as defined in pag. 8. This results constitutes what is known as Kutta–Joukowski theorem of lift. This is an extremely important results in fluid flow theory and forms the basis for the *lifting line theory* of sail and wing forces (Tanner 1967; Guermond 1989).

1.2.2.3 Three–dimensional lift effects.

The kind of ships referred to by William Shakespeare in *The life of King Henry V*, Act. III, Prologue:

> ...behold the threaden sails
> Borne with the invisible and creeping wind
> Draw the huge bottoms through the furrow'd sea
> Breasting the lofty surge...

could not go to windward. Only drag forces, as explained in Section 1.2.1, were involved in determining the driving force of the sails and the resistance of the hull. In Section 1.2.2.2 we saw that fluid flow, as well as generating drag, can also generate lift. The origin of lift which acts at right angles to the flow was fully explained in Section 1.2.2.2, however entirely in terms of two–dimensional flow. This is the kind usually measured in a wind tunnel (Wang, Plate, Rau, and Keiser 1996; Diana, DePonte, Falco, and Zasso 1998) where the effects of the ends of the foils are eliminated. For yachts, these three–dimensional effects are very important indeed, both under the water and especially in the air (Flay, Locke, and Mallinson 1996). End effects, or three–dimensional effects, arise simply because there is a difference in pressure between the two sides of a sail or keel (Garrett 1990). Fluid always wants to flow from a region of high pressure to a region of low pressure. If a sail is porous, air will flow straight through it from windward to the leeward side. Good sail cloth doesn't allow this (Whidden and Levitt 1993) so that the only other open course for the air is to flow under the boom or over the head of the sail in order to equalise the pressure difference. This gives rise to an additional form of drag, as we saw in Section 1.2.1 and as we shall see right now. As a general rule, the farther the ends are from the main body of the sail, the less is this extra drag: a tall sail (high aspect–ratio=AR) is aerodynamically more efficient than a short one (low aspect–ratio) (Marchaj 1990). Let us now look at the physics of this in more detail considering, as shown in Figure 1.13, a sail set so close to a flat deck that there is a hermetic seal between it and the deck. This means that the air flow near the foot of the sail is going to be close to the two–dimensional ideal one. So, the theory of Section 1.2.2.2 is directly applicable in this lower region of the sail. Because of the sail's shape and the geometric angle of incidence α of the undisturbed flow mesured between the direction of the flow at a distance from the sail and the sail chord, a circulation or bound vortex is set up aroun it. The lift produced in this region is directly proportional to the strength of the circulation as given by the Kutta–Joukowski relation (1.13). If we imagine the sail as being divided into a series of horizontal strips, then we expect the circulation and hence the local lift to decrease with height; the main reason for this is simply that the sail chord and also the area of each strip is decreasing. So the picture we have of the sail is a system in which the strength of the circulation is decreasing with height. Thus when the circulation decreases from one region to the adjacent

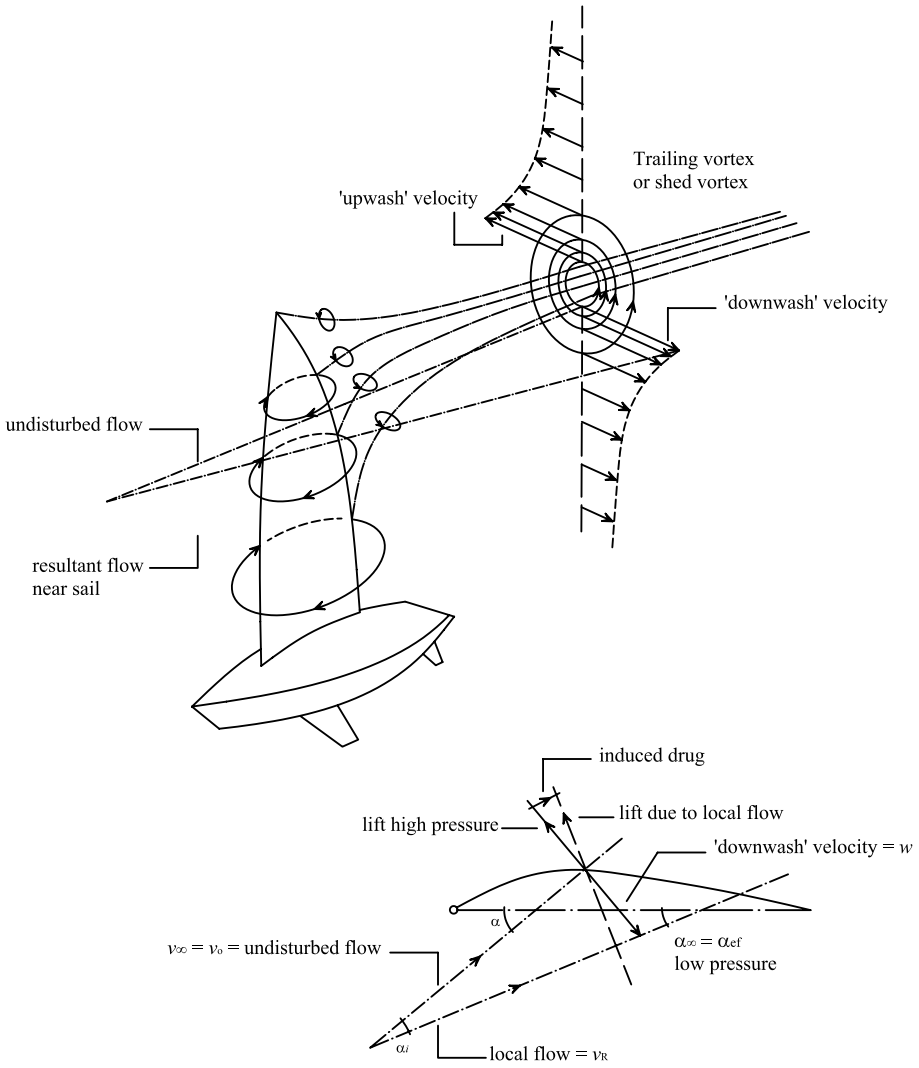

Figure 1.13: The flow of air around a sail results in circulation which is directly responsible for its lift.

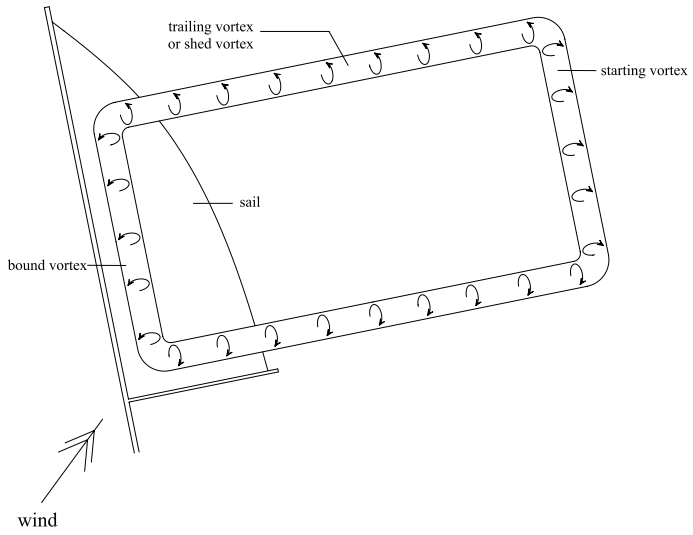

Figure 1.14: How the bound vortex and the starting vortex shown in Figure 1.12 are connected by the trailing vortices to form a closed loop, as demanded by the Theorem 3.

region of a sail, the difference in vorticity, as shown in Figure 1.15, must appear somewhere as a consequence of the Theorem 4. It does so in the form of a *shed vortex* from the leech of the sail (see Figure 1.14). Of course, the process is not dicontinuous as implied by the Figure 1.13 but it consists of an infinite number of infinitesimal vortices which all add up to a finite amount. At the top of the mast, there is a component of flow from the high pressure side over to the low pressure side which is just part of the overall system of shed vortices. That these shed vortices combine downwind to form one large vortex appearing emanate from the tip of the sail is beautifully demonstrated by vapour trails from high–flying aircraft in Figure 1.16. The variation of the circulation and lift with height is often referrred to as *distribution of loading*; this term comes from aeronautics where the wing lift must support the weight of the plane (Vinh 1993).
The consequence of this trailing vortex will now be looked at. The flow in a vortex is, of course, circular and the tangential speed of the flow varies inversely as the distance out from the center. This vortex motion is now imposed on the incoming flow, modifying it in the region of the sail. If we concentrate our attention on the velocities near the plane of the sail (Figure 1.13) we see that the contribution of the trailing vortex is the tangential velocity distribution at the bottom of the vortex flow. This velocity, w, is perependicular to the oncoming flow v_0, and falls

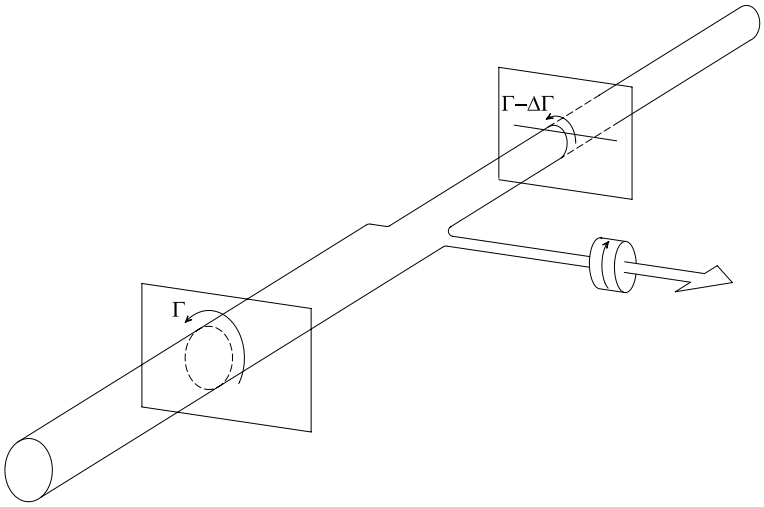

Figure 1.15: According to the Theorem 4 the total vorticity or circulation within a fluid must remain fixed and the vortex must be a continuous loop unless there is a solid surface for it to end on.

off with distance from the centre of the vortex. For aeronautical reason (Vinh 1993) w is referred to as *downwash velocity.* Looking now Figure 1.13 at a cross section part way up the sail, the downwash velocity w is vectorially added to the undisturbed oncoming velocity flow v_0 giving the resultant local flow velocity v_R, as graphically shown. If we add, as vectors, the downwash velocity w at the foil to the oncoming flow velocity v_0, we find that the resultant local velocity v_R is deflected downwards through an angle α_i whose tangent is w/v_0. This angle is usually called the induced angle. The downwash reduces the effective angle of incidence and it can be seen in Figure 1.13 that:

$$\alpha_{\text{ef}} = \alpha - \alpha_i = \alpha - \frac{w}{v_0}. \tag{1.14}$$

Hence, the lift generated at the effective incidence (α_{ef} in (Marchaj 1979) and α_∞ in (Garrett 1990; Claughton, Wellicome, and Shenoi 1998)) is smaller than would be expected from the geometric angle of incidence α. For a foil of infinite aspect–ratio (two–dimensional flow as in Section 1.2.2.2), the induced angle of incidence α_i is zero. Therefore the effective angle of incidence α_{ef} is equal to the geometric incidence α so that:

$$\alpha_{\text{ef}} = \alpha. \tag{1.15}$$

Figure 1.16: Tip vortex of an airplane performing agricultural spraying.

Therefore, for finite span foils (three–dimensional effects), the geometric angle of incidence is the sum of α_{ef} and α_i:

$$\alpha = \alpha_{\text{ef}} + \alpha_i. \tag{1.16}$$

Thus, in order to produce the same lift L, as is produced in the two–dimensional flow condition, the finite span foil must be set at the geometric angle of incidence α which is larger by α_i than the effective incidence α_{ef} for the foil of infinite aspect–ratio. But there is a more serious effect. Lift is the component of the total force (i.e. F_s) which is perpendicular to the direction of the undisturbed flow. Because of the downwash velocity, the perpendicular to the local flow direction is angled downwind. From the point of view of the undisturbed flow, the local lift has a component parallel to the flow. As we have seen in Section 1.2.1, such a component is a contribution to the drag. Since this drag has its own origin in lift, it is often referred to as *induced drag* or *vortex drag*. The vortex drag depends on the vorticity shed from the leech, which in turns depends on the change in circulation with height up the sail, so it should be not surprising to discover that the overall vortex drag depends on the sail form and shape. It is natural then to ask ourself what kind of sail shape will give the minimum vortex drag for a given lift. Perhaps surprisingly, there is no unique answer to this, though that is because it is not a good question. We must ask ourself a slightly more fundamental one:

what loading distribution will result in minimum vortex drag?

This refers to the way in which the lift varies with height. Since lift is related to circulation by expression (1.13), we are concerned with the variation of circulation with height. We will try to answer the question in Section 1.3 after having defined a good relation between the most important quantities previously introduced: lift L, drag D and geometric angle of attack α.

1.2.2.4 Lifting line theory: wings and sails of large aspect ratio

A calculation of the lift and induced drag forces exerted on a wing of given shape and attitude may employ the methods of inviscid fluid theory when the wing is sharp–tailed and boundary layer separation does not occur upstream of the sharp trailing edge (Batchelor 1967). The main difficulty lies in the determination of the strength and position of the vortices which trail downstream from the wing and which influence the flow near the wing. A theory which enables the trailing vortex system and the lift and the induced drag forces on the wing to be calculated under certain conditions was initiated by Lanchester (1907) and Prandtl (1952) in the early days of aeronautics and then was extended to sail by Tanner (1967), Milgram (1968) and Wood and Tan (1978).
This theory, the *lifting line theory*, is still of considerable value in the design and testing of aeroplane wings intended for use at sub–sonic flight speeds (Vinh 1993), and a brief account of it will now be given. The theory rests on two main assumptions about the wing under consideration:

1. the first is that the trailing votices are straight and parallel to the direction of flight, with consequent simplification of the expression for the velocity field induced by the trailing sheet vortex;

2. the second main assumption is that the ratio of the span $2s$ to the mean chord c, known as the aspect ratio of the wing (AR), is large and that as a consequence (for a wing which is not extensively swept back[1]) the flow in the neighbourhood of any one section of the wing is approximately two–dimensional.

Figure 1.17 shows the coordinate system and the notation to be used. The axes are fixed relative to the wing, and at infinity the fluid has uniform speed v_0 in the direction of the negative X-axis. The wing is assumed to be symmetrical about the central vertical plane on which $Z = 0$. The chord c, the geometrical angle of incidence α between the chord line and the direction of flight of the wing, and the cross–sectional shape of the wing (all shown in Figure 1.17) may all vary with the spanwise coordinate Z. Now when AR $\gg 1$ (Assumption 2), the planform of a

[1]Foils such as sails, keels and rudders are frequently raked bodily backward or, much more rarely, forward, through some angle called sweep–back or sweep–forward respectively.

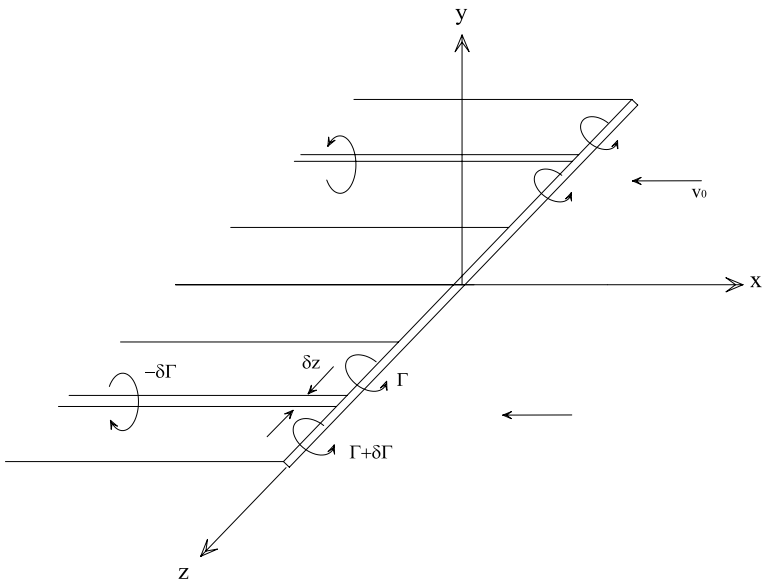

Figure 1.17: Coordinate system for a wing with the Y-axis vertical. Furthermore, the trailing vortex system from a lifting line.

wing without sweep–back (see footnote (1)) reduces to a straight line[2] The only relevant property of this *lifting line* is the circulation Γ round a circuit enclosing the wing in a plane normal to the Z-axis. Γ may vary across the span of the wing, and the variation in $\Gamma(Z)$ gives rise to a trailing vortex sheet of strength $\gamma_T(Z)$. The sign convention chosen for $\Gamma(Z)$ and $\gamma_T(Z)$ is the right–handed screw convention, so that $\gamma_T(Z)$ is given by:

$$\gamma_T(Z) = -\frac{d\Gamma(Z)}{dZ} = -\dot{\Gamma}(Z). \tag{1.17}$$

A quantity which we have already introduced in pag. 33 is the downwash velocity induced at position $(0, 0, \bar{Z})$ on the lifting line by the whole vortex system. It is evident from the geometry that this induced velocity is vertical and reads:

$$w(\bar{Z}) = -\frac{1}{4\pi}\int_{-s}^{s} \frac{d\Gamma(Z)}{dZ}\frac{dZ}{Z-\bar{Z}} = -\frac{1}{4\pi}\ \fint_{-s}^{s} \frac{d\Gamma(Z)}{dZ}\frac{dZ}{Z-\bar{Z}}, \tag{1.18}$$

[2]A wing with a small degree of sweep–back would be represented by a curved line making a small angle with the Z-axis everywhere and can be brought within the scope of this theory (Batchelor 1967).

where s is the semispan and since the integral becomes indeterminate at $Z = \bar{Z}$ on account of the integrand $f(Z)$ becoming infinitely large, it is necessary to take the so called *Cauchy principal value* (Tricomi 1957) of it, defined by:

$$\barint_{-s}^{s} f(Z)dZ = \lim_{\varepsilon \to 0} \left(\int_{-s}^{\bar{Z}-\varepsilon} + \int_{\bar{Z}+\varepsilon}^{s} \right) f(Z)dZ. \tag{1.19}$$

where

$$0 < \varepsilon \leq \min(s + \bar{Z}, s - \bar{Z})$$

The definition (1.19) is such that the value of $\bar{Z}$ has to be approached from both

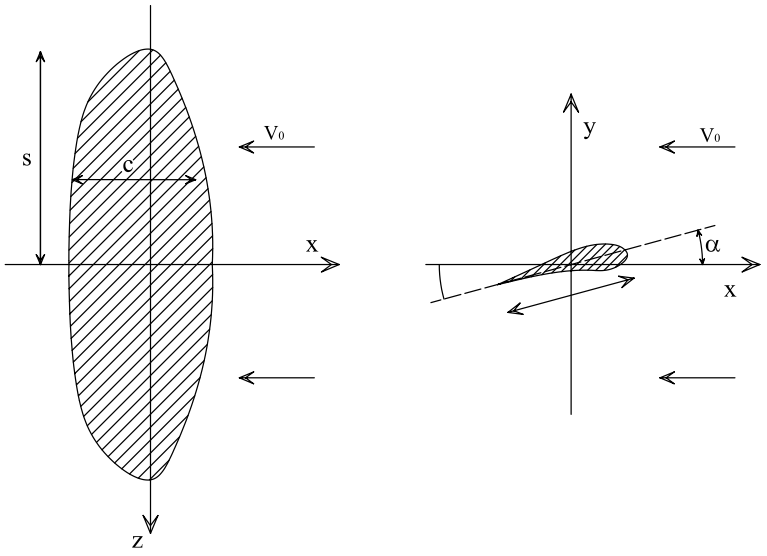

Figure 1.18: Coordinate system and notation to be used for a wing with the Y-axis vertical.

sides at the same rate. We shall denote this integral by placing a bar over the usual integration symbol.
The key point of the theory is that under the conditions stated above the induced vertical velocity w due to the trailing vortex system associated with the wing is approximately uniform over the neighbourhood of any section of the wing and is therefore equivalent in its effect on the flow past this section to a small change in the direction of the undisturbed stream velocity v_0. We see then that the two–dimensional flow near a section of the wing at station $\bar{Z}$ is that due to an aerofoil

immersed in a uniform stream of speed v_0 and working at an effective angle of attack α_{ef} calculated by subtracting from the geometrical angle α (measured from zero–lift attitude), the contribution of the downwash velocity w:

$$\text{Eq. (1.14)} \quad \Rightarrow \quad \alpha_{\text{ef}} = \alpha - \frac{w}{v_0} = \alpha - \frac{1}{4\pi v_0} \int_{-s}^{s} \frac{d\Gamma(Z)}{dZ} \frac{dZ}{\bar{Z} - Z}. \tag{1.20}$$

The foregoing results may be interpreted physically as follows: the influence of finite span on the flow over a wing is to reduce the local incidence at any station $\bar{Z}$ by an induced angle of attack:

$$\alpha_i = \frac{1}{4\pi v_0} \int_{-s}^{s} \frac{d\Gamma(Z)}{dZ} \frac{dZ}{\bar{Z} - Z}. \tag{1.21}$$

The resultant forces in the fluid, by what has been said above, have two components: the lift L and the induced drag D_i:

$$L = \rho v_0 \int_{-s}^{s} \Gamma(Z)\, dZ \tag{1.22}$$

$$D_i = \rho \int_{-s}^{s} w \Gamma(Z)\, dZ, \tag{1.23}$$

where equation (1.22) is none other than the Kutta–Joukowski Theorem applied to the finite aerofoil (see pag. 29 and Equation (1.13)).
The extension of lifting line theory to a sail has been done by Tanner (1967) and Milgram (1968). We consider in Figure 1.18, the same right–handed coordinate system of Figure 1.17, in which the $X - Y$ plane coincides with the water surface, with the X-axis aligned parallel to the centreline of the yacht hull and facing forwards. The Z-axis is vertically upwards at the position of the sail which is replaced by one lifting line of variable strength $\Gamma(Z)$ on the Z-axis. First of all, it brings to light the salient difference between aerodynamic theories for sails and for wings in a free stream:

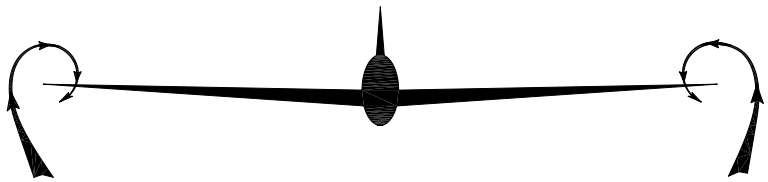

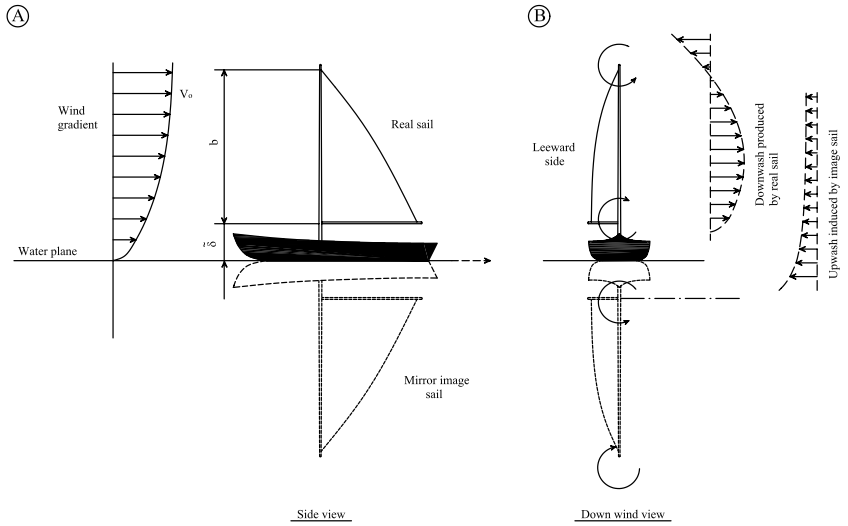

Figure 1.19: Mirror image concept makes easier to grasp the distinction between the hidden essentials and delusive appearance. For the sake of simplicity, the downwash and upwash velocity are drawn qualitatively.

> We know *nothing* of how the vastly important wing tip vortices (so important in aviation) affect our sails. Here is an aircraft approaching: Our sails is *one* of these wings. There is a small vortex up aloft and there must be a big one, greatly modified by the hull and the sea, low down at the foot and, in a sharply heeled keel yacht, what happens? Does the sea's surface act like the top wing of a bi–plane and give the same adverse effect on the lower wing, the sail?
> Gen. H. J. Parham, *Yachts and Yachting*, 1956

No doubt that the salient difference is the proximity of the sea that will have an effect on the flow round the sail, and therefore on loading distribution, and of course on the associated phenomena, induced drag and induced angle of incidence. In order to obtain a picture of the influence of the water plane on the flow round the sail and in order to satisfy the boundary condition of no flow normal to the horizontal plane (Assumption 1), the best way is to introduce the so–called *mirror image method*. By using this method, the effect of sea presence can be obtained by replacing the water plane by an inverted mirror image of the boat as shown in Figure 1.19 and considering the new but easier problem of interacting of flow around the two sails, or rather two boats since the hull below the sail should not be ignored. So, the flow pattern and interactions resulting from a combination of a real and a mirror image boat symmetrically placed on the other side of the boundary, will be identical with the flow pattern on a real boat over a flat plane.

1.3 Optimal sail design

Although sails have been used as a means of propulsion for thousands of years, no method for the design of sail shape based on fundamental aerodynamics (Munk 1923c) has come into use until the work of Milgram (1968). There are numerous reasons for this; not the least significant being that:

> We cannot raise the winds. But each of us can put up a sail, so that when the wind comes, we can catch it.
> E.F. Schumacher in *Small is Beautiful*

This to say that a sail of almost any shape can be attached to the spars of a vessel and provide a motive force in the presence of wind. Although such a sail will move the vessel, there is only a very small probability that the driving force will be close to its optimum value. Within the framework of existing classical aerodynamic theory (Ashley and Landahl 1965; Cebeci 1999), it is now possible to take an almost completely analytical or numerical approach to the optimal design of sails. The purpose of Section 1.3.1 is to provide the state of the art in optimum design of yacht sails during the last century. It's important to underline, as is the case with almost all fields of design engineering, that the best results can be obtained only by the proper blending of analytical methods with practical experience of generations of sailors:

> When the wind shifts against the sun,
> Trust it not, for back it will run.
>
> The clouds look black, and the glass is low;
> Last night the sun went pale to bed;
> The halved moon now hides her head.
>
> Look out, my lads! A wicked gale
> With heavy rain will soon prevail.
>
> First rise after low
> Foretells stronger blow.
>
> Evening red and morning gray,
> Two sure signs of one fine day.

1.3.1 State of the art

In this Section a variety of approaches to sail optimization are reviewed. As with any optimization problem, there are two major decisions to be made before a systematic optimization study of sails may be effected: the choice of the parameters defining the sail which are to be optimized, and the choice of objective or merit function, which effectively determines the aspect of performance to be maximized or minimized.

The first of these is apparently the easier decision to make: the designer would, in an ideal world, like to know the three–dimensional geometry of the sails which will give the best performance. One difficulty immediately encountered with the optimization of sail geometry is that the flying shape of the sails and spars is likely in many cases to be substantially different from the shape generated by the rig pre–tension alone. If the problem is tackled using a purely aerodynamic approach, only the flying shape may be optimized; the designer, however, is required to know the unloaded shape. The inclusion of a structural model of the sails, spars and rigging is thus desirable, but adds a substantial degree of complexity and computational cost (Day 1996). Even if is accepted that the geometry to be optimized is that of the flying shape, a full three–dimensional model is somewhat complex: around thirty parameters would probably be necessary for each sail in order to allow realistic variation in both the:

planform parameters: such as luff, leech, foot length, roach shapes (on both the leech and in some cases, the foot) and mast bend;

sectional shape parameters: such as the magnitude and position of the maximal camber and the entry and exit angles.

This is likely to lead to unmanageably large numbers of parameters even for simple sloop rigs. Much of the published work has rejected this geometrical full three–dimensional approach and opted instead to examine the spanwise distribution of lift (see Section 1.2.2.3). This type of approach allows the use of simple and computationally cheap lifting line type models (Munk 1923a; Thwaites 1960), at least for high aspect ratio rigs. Some research, predominantely experimental, has been carried out to investigate the effect of varying the sectional shape on the flow around two–dimensional sails, both with and without the presence of a mast, though little appears to have been published on systematic optimization in this regard. This presumably reflects the difficulties of predicting the effects of flow separation on the leeward side of the sail particularly aft of the mast and near the trailing edge. Here, we think that the approach offering most potential for guiding designers is a compromise in which the sectional shape parameters are assumed fixed (at values chosen from experience as being typical of those representing flying shapes) and the basis planform parameters are optimized.

The choice of objective function is rather harder than the choice of parameters. In the case of a *cruising yacht* for example, a very wide variety of factors must be taken into account: speed both on and off wind will certainly be important in terms of the ability to sail away from hazards; reliability and structural integrity; cost will always be of some relevance and may in some cases provide active constraints on the options available. Here we consider an *out and out racing yacht* where the decision is, at least superficially, somewhat easier: it might be argued

that the best yacht is the yacht which would win the most races if all the crews were of equal ability. However, this by no means leads to a simple criterion for an optimal rig. The type of racing for which the yacht is intended is of obvious importance: match racing (Richards, Johnson, and Stanton 2001), for example, will place a higher premium on maneuvrability than short handed offshore racing. The likely windspeeds in the area or areas where the yacht is to be raced will affect the optimal rig size; the choice of the course type for which the yacht is intended, either inshore or offshore, will influence the relative importance of speed on various points of sailing (see Section 2.3). Reliability and structural integrity will still be important factors: as has been said many times, in order to win, it is first necessary to finish. Cost will in many cases still provide some constraints (Fallow 1996). A final difficulty faced in the design of yachts intended for racing under a handicapping rule such as (Offshore Racing Council 2002) is that outright speed is often less important than speed relative to the yacht rating. Given the wide range of factors to be considered, it is necessary to attempt to simplify the criteria in order to make some progress.
A simple criterion, already seen in Section 1.2.2.1, often discussed for lifting surface is the maximization of lift to drag ratio (Garrett 1990), though it is arguably more convenient in the context of yacht rigs to deal with drive force F_R and sideforce H.

As a consequence, a more sophisticated criterion is the maximization of drive force with or without constraint on forces and/or moments (Sparenberg 1984) taking into account that the simple optimization of the lift/drag ratio has therefore not yielded maximum performance. To introduce this advanced criterion of thrust force optimization we move from an age far removed from our own, exactly 1923b, when Max Munk, a German scientist, who later emigrated to the USA to work for the National Committee for Aeronautics (NACA) proved mathematically that, for a single wing, minimum induced drag (see Section 1.2.2.2) occurs when the airstreams are deflected with the same downwash velocity all along the trailing edge. The elliptic wing of the famous Spitfire aircraft (Figure 1.20) has exactly this property, and in this sense might be considered as an ideal planform. Munk used the lifting line theory and the variational principle to minimize the induced drag of wings with finite spans, and obtained the optimum circulation that is the elliptic circulation (Munk 1923b). Several authors, Prandtl and Tietjens (1934), Jones (1950) and Klein and Viswanathan (1973) have extended the problem of minimizing the drag to take account of practical constraints. These studies have revealed the fact that the elliptic circulation is largely dependent on constraints. So it should be emphasized that the elliptic circulation is not always optimum. Extensions to sail aerodynamics and analyses on it have been conducted, at first, by Tanner (1967) and Milgram (1968) using the lifting line theory. They approximated sails as horseshoe vortex systems (see Figure 1.14) with mirror images

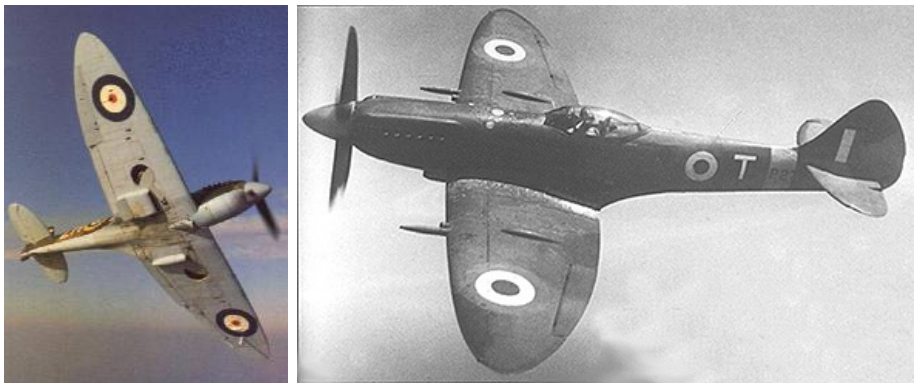

Figure 1.20: The Supermarine Spitfire first flew in 1936. Some of its Second World War success was due to its elliptic wing form.

reflected by the sea surface (see Figurefig:specular)in order to neglect the hull effect and at the same time taking into account the sea effect. One of the key parameters in their analises, is the gap between the sail foot and the flat sea surface. The Fourier series expansion is used to obtain numerical solutions. They concluded unanimously that sail designers should trade off drag reduction against the heeling moment constraint, and that the gap between the sail foot and the sea surface enhances the induced drag considerably. Sparenberg and Wiersma (1976) have treated this *trade off* problem by introducing Munk's variational principle to analysis of sails (Munk 1923b). They presented asymptotic and numerical solutions for the optimum circulation which maximize the thrust with a given side force and a given heeling moment. Wood and Tan (1978) also computed the optimum circulation about sails having the maximum thrust and a given heeling moment through trial-and-error procedure; whereas Sugimoto (1993) computed the optimum sail under more practical constraints on forces and moments with the aid of the classical lifting line theory. Furthermore Sugimoto extended earlier work to take into account effects due to the heel of sailing craft (Sugimoto 1995) and the wind shear ((Sneyd and Sugimoto 1997) and Figure 2.5(b)) and some other wind conditions (Sugimoto 1999). Wohlfahrt (1988) has analyzed sail aerodynamics based on the extended lifting line theory called Weissinger's method (Weissinger 1947; Weissinger 1949). He postulates that the elliptic circulation is optimum, ang gives the optimum sail geometry. His analysis, in comparison with the previous ones, takes into account of deformation of elastic leech. In order to avoid the hull–deficiency, it is necessary to model the underwater body of the yacht in some way (Wiersma 1978), avoiding the use of the mirror images reflected by the sea surface. This immediately complicates the problem somewhat whilst simulta-

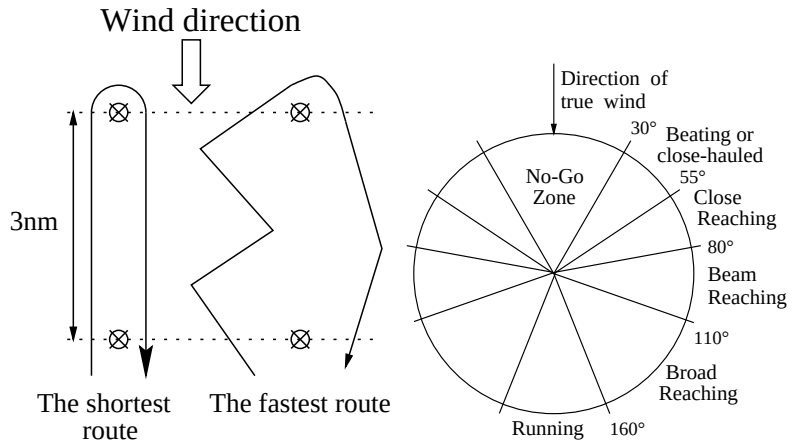

(a) Windward/leeward legs. (b) Wind polar diagram.

Figure 1.21: Knowing the direction from which the wind is blowing is fundamental to the art of sailing.

neously restricting the applicability of the results obtained to the particular hull form chosen, or, at best, to similar hull forms. The lack of generality of results thus obtained make it somewhat harder to establish trends or guidelines for designers. One manner in which this may be achieved is to represent the hull as a thin upright lifting surface, thus neglecting viscous and wavemaking resistance (Wiersma 1979). This allows a relatively simple model of the hull induced drag to be incorporated in an optimization based on maximization of drive force, effectively resulting in a constraint on hydrodynamic sideforce as well as heeling moment, but inevitably lacks a degree of realism.

1.3.2 Design procedure

The art of knowing what can be safely ignored in scientific analysis is often difficult, but vitally important. The analysis of sailboats requires understanding of complex interactions among aerodynamic and hydrodynamic forces (see Section 1.2.2.1)and structural stresses. Though it might be possible to approach the complex problems directly, we believe that it is valuable to study, as a starting point, a simplified analytical model which reveals skeletal structures of relations between function and shape. We assume that:

1. the air is steady, inviscid and incompressible;

2. because it is a hard task to sail to windward in lighter winds, we shall optimize the sail performance in lightwinds;

3. as a consequence of point 2 we may neglect the effects of the boundary layer on waters and the surface wave in the first approximation. So we assume that the sea surface is flat;

4. for the driving force F_s created by the relative motion of sails and air, it is important that the resistance forces be small. These may be listed, according to the definitions in Section 1.2.1, as induced drag, friction drag, form drag and additional resistance of rigging. Here we will consider only the induced drag D_i, which, as discussed by Milgram (1968), is a substantial part of the total drag of the rig;

5. since upright single mainsails produce large thrust than heeled ones, we design sails to trim at zero heel angle ($\phi = 0$). Furthermore, the function of jib sails is to prevent separation on mainsails. As it is inconsistent to consider viscous effects due to jib sails by the inviscid theory, we confine ourselves to the mainsail design;

6. we neglect sail flexibility in the first approximation. When we will study sail mechanics in detail, it is going to be necessary to combine aerodynamic and structural analyses (Bisplinghoff, Ashley, and Halfman 1955). Deformation of sails is caused by their elasticity and leech slackness that has the effect of causing twist and reducing the effective angle of attack (α). We should avoid unfavorable effect by neglecting the chamber effect due to the elasticity of fabric sails;

7. we postulate that sail is set flat;

8. we neglect the effect of the hull. The flow around the sail will be affected by the close proximity of the sea and the presence of the hull, but if we neglect the latter entirely a reasonable estimation of the sea effect when the sail is in vertical attitute ($\Rightarrow \phi = 0$, zero heel angle, point 5) can be made by assuming that the surface acts as a reflecting plane so that an exact image of the real sail appears below the surface as shown in Figure 1.19 (Marchaj 1979; Prandtl and Tietjens 1934);

9. America's Cup and Louis Vuitton Cup yacht races (the challenger series) are simply a series of windward and leeward legs as shown in Figure 1.21(a). Because the most important performance of a yacht is its ability to sail to windward (see Section 2.3.2), we will study a single mainsail assumed to be set close–hauled (see Figure 1.21(b)).

To resume: we consider a single mainsail assumed to be set close–hauled in uniform wind and upright on the flat sea surface.

1.3.2.1 Optimization procedure: windward performance

The most important performance of a yacht is its ability to sail to windward. As Marchaj (1979) points out:

> At the present time it is commonly agreed that the performance of a sailing yacht in close–hauled conditions is ultimately measured by the distance it has travelled directly to windward in a given time.

This is usually referred to as the speed made good to windward V_{mg} which should be a maximum at each true wind velocity V_t. Whatever the hull form and rig size of the boat, all yachts experience the following three modes when sailing upwind. These can be termed: *under–powered*, *powered up* and *overpowered*. Each mode is defined by the actual V_{mg}^{boat} to windward relative to the maximum $V_{mg}^{\max}$ of the yacht. The maximum hull speed can be determined by the following empirical relationship (Fallow 1996):

$$V_{mg}^{\max} = (\text{water length in feet})^{0.5}. \tag{1.24}$$

If the $V_{mg}^{\text{boat}} < V_{mg}^{\max}$ then the boat is said to be underpowered. In this situation, the primary consideration is to develop the maximum possible force from the sails. This is achieved by increasing the camber of the sails, at the expense of skin friction drag. If the $V_{mg}^{\text{boat}} = V_{mg}^{\max}$ at the minimum possible wind speed then the boat is powered up. Here the boat is sailing in its most efficient mode; hence the most efficient yacht should have the largest V_{mg}:

$$V_{mg} = V_s \cos\gamma \qquad \Leftarrow \quad \text{Equation (1.7a)}, \tag{1.25}$$

where V_s and γ denote the yacht speed and the angle of the true sailing course, that is the angle between true wind and course directions. We can deduce from Equation (1.25) that the optimum V_{mg} is attained by larger V_s and smaller γ.

1.3.2.2 Optimal design concept

The question that we are going to answer in this section is: how can we obtain in our sail–boat system the larger V_s and smaller γ?

1. Since the square of V_s is in direct proportion to the boat drag D_h (Garrett 1990) and the boat drag is in equilibrium with the sail thrust F_R in steady–state sailing, hence the largest V_s is obtained by maximizing the thrust.

Furthermore, the smaller γ is also obtained by maximizing the thrust. Indeed, the following relation holds:

$$V_s \cos\gamma \approx \sqrt{F_R}\cos\gamma, \tag{1.26}$$

where the optimum γ is given from the condition:

$$\frac{\partial\left(\sqrt{F_R}\cos\gamma\right)}{\partial\gamma} = 0 \quad \Rightarrow \quad \gamma_{\text{opt}} = \cot\left[\frac{1}{2F_R}\frac{\partial F_R}{\partial\gamma}\right]. \tag{1.27}$$

It is a hard task the optimization of $\partial F_R/\partial\gamma$, because it depends on equilibrium between hydrodynamic and aerodynamic forces; however, Equation (1.27) implies that the larger F_R makes γ_{opt} smaller.
Though the windward performance of sailing yachts can be optimized by maximizing the thrust F_R, it is evident that aerodynamic and hydrodynamic forces and moments have their maxima, so we need to consider that the lift L_s and the heeling moment M_H are constrained.

2. In steady state close–hauled sailing (Hypothesis 9) with $\phi = 0$ (Hypothesis 5), aerodynamic and hydrodynamic forces are in equilibrium; using Equations (1.11) we can write:

Hydro

$$D_h = \overbrace{L_s\sin\beta - D_s\cos\beta}^{F_R\ \text{Aero}} \underset{\text{Hypothesis 4}}{\approx} L_s\sin\beta - D_i\cos\beta \underset{\text{Hypothesis 9}}{\approx} L_s\beta - D_s \tag{1.28a}$$

$$L_h = \underbrace{L_s\cos\beta + D_s\sin\beta}_{F_H\ \text{Aero}} \overset{\uparrow}{\approx} L_s\cos\beta + D_i\sin\beta \overset{\uparrow}{\approx} L_s + D_s\beta \approx L_s \tag{1.28b}$$

According to the conventional wing theory (Ashley and Landahl 1965, pag.137, Eq.7-48), D_h can be approximated as a quadratic function of $L_h \Rightarrow L_h \approx L_s$. Therefore, D_h reaches its maximum as L_h reaches its maximum and also as L_s reaches its maximum.

3. The bending moment at the mast root is closely related to the strength of the mast, and corresponds to the heeling moment of yachts. If the heeling moment M_H and the righting moment M_R are not in equilibrium, the boat will turn over (see Figure 1.9). The righting moment is produced by helmsmen's weights and by the weight of the boat. Hence the righting moment has its upper limit. Therefore, either the mast strength or the righting moment constraints the heeling moment.

To summarize, our design goal is the maximization of the aerodynamic thrust F_R (Point 1) under the equality constraint on the lift L_s (Point 2)and the heeling moment M_H (Point 3).
Once the goal of our design concept is established we describe this goal as a requirement of boundary conditions by using the variational principle (Yang and Botkin 1986; Mróz 1986) and the conventional wing theory.
The first step is the definition of the aerodynamic forces and heeling moment on the basis of the lifting line theory, as introduced in Section 1.2.2.4:

$$L_s = \rho {V_a}^2 h^2 \int_{\tilde{\delta}}^{1} \tilde{\gamma}(z) dz \quad \Leftarrow \quad \text{Eq. (1.22)}, \tag{1.29a}$$

$$D_i = \rho {V_a}^2 h^2 \int_{\tilde{\delta}}^{1} \tilde{\gamma}(z) \alpha_i(z) dz \quad \Leftarrow \quad \text{Eqs. (1.14) and (1.23)}, \tag{1.29b}$$

$$M_H = \rho {V_a}^2 h^3 \int_{\tilde{\delta}}^{1} \left[\tilde{\gamma}(z) \cos\beta + \tilde{\gamma}(z) \alpha_i(z) \sin\beta\right] z dz \approx \tag{1.29c}$$

$$\approx \rho {V_a}^2 h^3 \int_{\tilde{\delta}}^{1} \tilde{\gamma}(z) z dz \quad \Leftarrow \quad \text{Eq. (1.28b)}, \tag{1.29d}$$

where using the same notation previously introduced, we can define:

- L_s = sail lift force (see Figure 1.4);
- D_i = induced drag (Section 1.2.2.4);
- M_H = heeling moment (see Figure 1.7);
- V_a = apparent wind velocity (Equations (1.7));
- h = mast height (see Figure 1.19);
- $\tilde{\gamma}(z) = \dfrac{\Gamma(Z)}{V_a h}$ = dimensionless circulation (Wood and Tan 1978);
- $\tilde{\delta}$ = dimensionless gap between the sail foot and the sea surface (see Figure 1.19);
- $z = \dfrac{Z}{h}$ = dimensionless mast–coordinate axis.
- α_i = induced angle of attack (Equation (1.21)).

This angle (α_i) represents the reduction of the effective incidence (α_{ef}) induced by the circulation and is given using the lifting line integral Equation (1.21) with a

mirror image of the vortex system (see Figure 1.19):

$$\alpha_i(z) = -\frac{1}{4\pi} \int_{\tilde{\delta}}^{1} \tilde{\gamma}'(\zeta) \left(\frac{1}{\zeta - z} + \frac{1}{\zeta + z} \right) d\zeta. \tag{1.30}$$

By using a change of variables:

$$z^2 = (1 - \tilde{\delta}^2)\eta + \tilde{\delta}^2, \tag{1.31}$$

$$\zeta^2 = (1 - \tilde{\delta}^2)u + \tilde{\delta}^2, \tag{1.32}$$

Equation (1.30) becomes the *finite Hilbert transformation*:

$$\alpha_i(z(\eta)) = -\frac{1}{4\pi} \int_{0}^{1} \tilde{\gamma}'(\zeta) \frac{du}{u - \eta} \quad \Leftarrow \quad \text{Equation (1.21).} \tag{1.33}$$

Once we invert Equation (1.33) above by using the formula of the finite Hilbert transformation (Tricomi 1957, pag.175, Eq.12), then through reversion of variables we have:

$$\frac{d\tilde{\gamma}(z)}{dz} = \frac{4}{\pi\sqrt{(z^2 - \tilde{\delta}^2)(1 - z^2)}} \int_{\tilde{\delta}}^{1} \left[\sqrt{(\zeta^2 - \tilde{\delta}^2)(1 - \zeta^2)}\alpha_i(\zeta) \left(\frac{1}{\zeta - z} + \frac{1}{\zeta + z} \right) \right] d\zeta + \frac{C}{\pi\sqrt{(z^2 - \tilde{\delta}^2)(1 - z^2)}}, \tag{1.34}$$

where C is a constant to be given so that $\tilde{\gamma}(z)$ satisfies the boundary conditions $\tilde{\gamma}(\tilde{\delta}) = \tilde{\gamma}(1) = 0$.

1.3.2.3 The variational problem

Our optimum goal is to seek the maximum F_R with the inequality constraint on M_H and the equality constraint on L_s, accompained by Equation (1.30). Using Equations (1.29a) and (1.29d), the constraints are written in the form:

$$l_{\max} = \int_{\tilde{\delta}}^{1} \tilde{\gamma}(z) dz, \tag{1.35a}$$

$$m_{\max} \geq \int_{\tilde{\delta}}^{1} \tilde{\gamma}(z) z dz, \tag{1.35b}$$

where definite integrals correspond to the nondimensional lift L_s and moment M_H. As a reference, we shall make use of the *elliptic sails* without gap between the sail foot and the sea surface ($\tilde{\delta} = 0$), then we have:

$$l_{\max} = \frac{\pi\tilde{\gamma}_R}{4\mu^2}, \qquad m_{\max} = \frac{\tilde{\gamma}_R}{3\mu^3}, \tag{1.36}$$

where μ is the mast height ratio defined by h/h_e; $\tilde{\gamma}_R$ is the value of the elliptic circulation at $z = 0$ for the elliptically loaded sail (Glauert 1926, pag.143):

$$\tilde{\gamma}_e(z) = \tilde{\gamma}_R\sqrt{1-z^2}, \tag{1.37a}$$

$$L_e = \frac{1}{4}\pi\rho V_a^2 h_e^2 \tilde{\gamma}_R \quad \Leftarrow \text{ Eq. (1.29a)}, \tag{1.37b}$$

$$D_e = \frac{1}{16}\pi\rho V_a^2 h_e^2 \tilde{\gamma}_R^2 \quad \Leftarrow \text{ Eq. (1.29b)}, \tag{1.37c}$$

$$F_{Re} = L_e\beta - D_e \quad \Leftarrow \text{ Eq. (1.28a)}, \tag{1.37d}$$

$$M_{He} = \frac{1}{3}\rho V_a^2 h_e^3 \tilde{\gamma}_R \quad \Leftarrow \text{ Eq. (1.29d)}, \tag{1.37e}$$

where quantities with subscript e denote those attributed to the elliptic loading. The inequality constraint (1.35b) can be written as an equality constraint by introducing the *slack variable* ξ_m (Fletcher 1987, pag.146); hence the constraints (1.35) can be rewritten by:

$$l_{\max} - \int_{\tilde{\delta}}^{1} \tilde{\gamma}(z)dz = 0, \tag{1.38a}$$

$$m_{\max} - \int_{\tilde{\delta}}^{1} \tilde{\gamma}(z)zdz - \xi_m^2 = 0. \tag{1.38b}$$

Furthermore, the definite integral functional $\tilde{\gamma}(z)[\beta - \alpha_i(z)]$ of z from $\tilde{\delta}$ to 1, corresponds to the sail thrust F_R:

$$\overbrace{F_R = L_s\beta - D_s}^{\text{Dimensional}} = \overbrace{\int_{\tilde{\delta}}^{1} \tilde{\gamma}(z)\beta dz - \int_{\tilde{\delta}}^{1} \tilde{\gamma}(z)\alpha_i(z)dz}^{\text{Adimensional}} = \int_{\tilde{\delta}}^{1} \tilde{\gamma}(z)[\beta - \alpha_i(z)]dz. \tag{1.39}$$

Using Equations (1.30), (1.38) and (1.39) and introducing the Lagrange multipliers λ_a, λ_l and λ_m, the final form of our problem becomes maximization of the extended functional given by:

$$\int_{\tilde{\delta}}^{1} \{\tilde{\gamma}(z)[\beta - \alpha_i(z)] + \lambda_a[\alpha_i(z) - f(\tilde{\gamma}, z)]\}\, dz + \lambda_l\left(l_{\max} - \int_{\tilde{\delta}}^{1} \tilde{\gamma}(z)dz\right) + \lambda_m\left(m_{\max} - \int_{\tilde{\delta}}^{1} \tilde{\gamma}(z)zdz - \xi_m^2\right), \tag{1.40}$$

where $f(\tilde{\gamma}, z)$ denotes the right–hand side of Equation (1.30). Taking the first variation of the functional (1.40) with respect to λ_a, λ_l, λ_m, ξ_m, α_i and $\tilde{\gamma}(z)$, we

obtain six stationary conditions:

$$\alpha_i(z) = -\frac{1}{4\pi} \oint_{\tilde{\delta}}^{1} \tilde{\gamma}'(\zeta) \left(\frac{1}{\zeta - z} + \frac{1}{\zeta + z} \right) d\zeta, \tag{1.41a}$$

$$l_{\max} - \int_{\tilde{\delta}}^{1} \tilde{\gamma}(z) dz = 0, \tag{1.41b}$$

$$m_{\max} - \int_{\tilde{\delta}}^{1} \tilde{\gamma}(z) z dz - \xi_m^2 = 0, \tag{1.41c}$$

$$\lambda_m \xi_m = 0 \quad \Rightarrow \quad \lambda_m = 0 \quad \text{or} \quad \xi_m = 0, \tag{1.41d}$$

$$\lambda_a = \tilde{\gamma}(z), \tag{1.41e}$$

$$\alpha_i(z) = \frac{\beta - \lambda_l - \lambda_m z}{2}. \tag{1.41f}$$

Substituting Equation (1.41f) into Equation (1.34) and using conditions $\tilde{\gamma}(\tilde{\delta}) = \tilde{\gamma}(1) = 0$, we have:

$$\frac{d\tilde{\gamma}(z)}{dz} = \frac{2}{\pi\sqrt{(z^2 - \tilde{\delta}^2)(1 - z^2)}} \left[\left(\frac{E}{K} - z^2 \right) (\pi(\beta - \lambda_l) - 2E\lambda_m) + \right.$$
$$\left. + \lambda_m \left(\frac{E^2}{K} - \tilde{\delta}^2 K \right) - 2\lambda_m (z^2 - \tilde{\delta}^2)(1 - z^2) \oint_0^1 \frac{1}{1 - z^2 - k^2 u^2} \sqrt{\frac{1 - k^2 u^2}{1 - u^2}} du \right], \tag{1.42}$$

where K, E and k denote the *complete elliptic integrals of the first* and *second kind* and the *modulus*, respectively:

$$K = \int_0^1 \frac{du}{\sqrt{(1 - u^2)(1 - k^2 u^2)}}, \tag{1.43a}$$

$$E = \int_0^1 \sqrt{\frac{1 - k^2 u^2}{1 - u^2}} du, \tag{1.43b}$$

$$k = \sqrt{1 - \tilde{\delta}^2}. \tag{1.43c}$$

Equation (1.42) yields the nondimensional lift and moment, previously introduced in Equations (1.35a) and (1.35b), as

$$\int_{\tilde{\delta}}^{1} \tilde{\gamma}(z) dz = \frac{\pi}{2} \left(1 + \tilde{\delta}^2 - 2\frac{E}{K} \right) (\beta - \lambda_l) -$$
$$- \frac{2}{3} \left((1 + \tilde{\delta}^2) E - \tilde{\delta}^2 \frac{K}{2} - \frac{3E^2}{2K} \right) \lambda_m, \tag{1.44}$$

$$\int_{\tilde{\delta}}^{1} \tilde{\gamma}(z) z dz = \frac{2}{3}\left((1+\tilde{\delta}^2) - \tilde{\delta}^2\frac{K}{2} - \frac{3E^2}{2K}\right)(\beta - \lambda_l) - \\ - \frac{E}{\pi}\left((1+\tilde{\delta}^2)E - \tilde{\delta}^{"}K - \frac{E^2}{K}\right)\lambda_m. \quad (1.45)$$

Let us introduce a nondimensional thrust coefficient:

$$C_{F_R} = \frac{F_R}{\frac{1}{2}\rho V_a^2 h_e^2 \mu^2} \quad \Rightarrow \quad \mu^2 C_{F_R} = \frac{F_R}{\frac{1}{2}\rho V_a^2 h_e^2}. \quad (1.46)$$

Using Equations (1.28a), (1.29a), (1.29b) and (1.41f), we obtain a convenient expression of C_{F_R} as:

$$C_{F_R} = (\beta + \lambda_l)\int_{\tilde{\delta}}^{1} \tilde{\gamma}(z) dz + \lambda_m \int_{\tilde{\delta}}^{1} \tilde{\gamma}(z) z dz. \quad (1.47)$$

Now let us study two possible optimum cases (see Equation (1.41d)):

Case 1 : $\xi_m = 0$. When the slack variable ξ_m is equal zero, Equation (1.41c) implies that the moment is equal to the given value. Equating Equations (1.44) and (1.45) to their maximum values $l_{\max}$ and $m_{\max}$ respectively (Equations (1.36)), we obtain a system of two simulatneous equations in λ_l and λ_m, from which we obtain:

$$\lambda_l^{\mathrm{I}} = \beta - \frac{A\tilde{\gamma}_R}{2\mu^3}(\mu - \mu_l), \quad (1.48)$$

$$\lambda_m^{\mathrm{I}} = -\frac{3\pi A\tilde{\gamma}_R}{8\mu^3}\mu_l(\mu_m - \mu), \quad (1.49)$$

where:

$$A = \frac{9E\left[(1+\tilde{\delta}^2)E - \tilde{\delta}^2 K - \frac{E^2}{K}\right]}{\left[(1+\tilde{\delta}^2)E - 2\tilde{\delta}^2 K\right]\left[(1+\tilde{\delta}^2)E + \tilde{\delta}^2 K - 3\frac{E^2}{K}\right]}, \quad (1.50a)$$

$$\mu_l = \frac{8\left[(1+\tilde{\delta}^2)E - \frac{1}{2}\tilde{\delta}^2 K - 3\frac{E^2}{2K}\right]}{9E\left[(1+\tilde{\delta}^2)E - \tilde{\delta}^2 K - \frac{E^2}{K}\right]}, \quad (1.50b)$$

$$\mu_m = \frac{1 + \tilde{\delta}^2 - 2\frac{E}{K}}{(1+\tilde{\delta}^2)E - \frac{1}{2}\tilde{\delta}^2 K - 3\frac{E^2}{2K}}, \quad (1.50c)$$

and the superscript $^{\mathrm{I}}$ denotes **Case 1**. Between Equations (1.50b) and (1.50c), the following inequalities hold:

$$\mu_m - \mu_l = \frac{1}{A} \geq 0 \;\Rightarrow\; \boxed{\mu_m \geq \mu_l} \text{ where } \mu_m \geq 0 \text{ and } \mu_l \geq 0. \quad (1.51)$$

Using Equation (1.47), the thrust coefficient is given by:

$$C^{\mathrm{I}}_{F_R} = l_{\max}(\beta + \lambda^{\mathrm{I}}_l) + m_{\max}\lambda^{\mathrm{I}}_m = \frac{\pi\tilde{\gamma}_R}{4\mu^2}\left[2\beta - \left(\frac{A\tilde{\gamma}_R}{2\mu^4}\right)(\mu^2 - 2\mu_l\mu + \mu_l\mu_m)\right]. \tag{1.52}$$

Equation (1.52) implies that the thrust, in proportion to $\mu^2 C^{\mathrm{I}}_{F_R}$, globally becomes larger toward the limiting value $\frac{\pi\tilde{\gamma}_R\beta}{2}$, as μ tends to infinity.

Case 2 : $\lambda_m = 0$. When the Lagrange multiplier λ_m is zero, equating Equations (1.44) to his maximum value $l_{\max}$ (Equation $(1.36)_1$), we obtain:

$$\lambda^{\mathrm{II}}_l = \beta - \frac{\tilde{\gamma}_R}{2\mu^2\left(1 + \tilde{\delta}^2 - 2\frac{E}{K}\right)}, \tag{1.53}$$

where the superscript $^{\mathrm{II}}$ denotes **Case 2**. Because the slack variable is different from zero, the moment must be smaller than the reference value; using Equations $(1.36)_2$ and (1.45), this condition is given by:

$$\mu \leq \mu_m. \tag{1.54}$$

In this second case, the thrust coefficient is given by:

$$C^{\mathrm{II}}_{F_R} = l_{\max}(\beta + \lambda^{\mathrm{II}}_l) = \frac{\pi\tilde{\gamma}_R}{4\mu^2}\left(\beta - \frac{\tilde{\gamma}_R}{2\mu^2\left(1 + \tilde{\delta}^2 - 2\frac{E}{K}\right)}\right). \tag{1.55}$$

From Equations (1.52) and (1.55) we have the inequality:

$$C^{\mathrm{I}}_{F_R} - C^{\mathrm{II}}_{F_R} = \frac{\tilde{\gamma}_R}{3\mu^2}\left(\frac{1}{\mu} - \frac{1}{\mu_m}\right)\lambda^{\mathrm{I}}_m \leq 0, \tag{1.56}$$

because of Equation (1.54), and $\lambda^{\mathrm{I}}_m \leq 0$ (Equation (1.49)). Therefore $C^{\mathrm{II}}_{F_R}$ prevails over $C^{\mathrm{I}}_{F_R}$ for smaller μ than μ_m. However, Equations (1.48)–(1.53) and (1.55), imply that the maximum thrust $\mu^2 C^{\mathrm{II}}_{F_R}$ is obtained and equal to $\mu^2 C^{\mathrm{I}}_{F_R}$ at $\mu = \mu_m$ from Equation (1.52). So **Case 1** represents the optimum circulations. As a consequence further discussion is confined to **Case 1** that, obviously, becomes optimum when μ is no less than μ_m, so that:

$$\boxed{\mu \geq \mu_m \geq \mu_l}, \tag{1.57}$$

and from Equations (1.48) and (1.49), respectively:

$$\beta - \lambda_l \geq 0, \tag{1.58}$$

$$\lambda_m \geq 0. \tag{1.59}$$

Let us study Equation (1.42) to see the behaviour of circulations; in doing these we need to take into account that *feasible* solution (domain) must satisfy the obvious constraint on the chord:

$$c(z) = \frac{\tilde{\gamma}(z)}{\pi[\alpha - \alpha_i(z)]} = \frac{\tilde{\gamma}(z)}{\pi\alpha_{\text{ef}}} \geq 0, \tag{1.60}$$

where $c(z)$ is the dimensionless chord; α the geometrical angle of attack (see Figure 1.4) and the difference in brackets, $\alpha - \alpha_i(z)$, is the effective angle of attack α_{ef} (Equation (1.16)). Equation (1.60) has been obtained from the Kutta–Joukowski condition (1.13) (Thwaites 1960, pag.115, Eq.9).
Let us study the behaviour of circulation; Equation (1.42) can be also written in a more convenient way as :

$$\frac{d\tilde{\gamma}(z)}{dz} = \frac{2}{\pi\sqrt{(z^2 - \tilde{\delta}^2)(1 - z^2)}} \Big[(\pi(\beta - \lambda_l) - 2E\lambda_m) g_1(z) + \\ + \lambda_m \left(\frac{E^2}{K} - \tilde{\delta}^2 K \right) - 2\lambda_m g_2(z) \Big], \tag{1.61}$$

where:

$$g_1(z) = \frac{E}{K} - z^2, \tag{1.62}$$

$$g_2(z) = \underbrace{(z^2 - \tilde{\delta}^2)(1 - z^2)}_{g_2'(z)} \underbrace{\int_0^1 \frac{1}{1 - z^2 - k^2u^2} \sqrt{\frac{1 - k^2u^2}{1 - u^2}} du}_{g_2''(z)}. \tag{1.63}$$

The function $g_1(z)$ is a *monotone decreasing* function, because:

$$\frac{dg_1(z)}{dz} = -2z \leq 0.$$

The function $g_2(z)$ is the product of $g_2'(z)$ and the integral term $g_2''(z)$. In the segment $z \in [\tilde{\delta}, 1]$, the former term is *positive convex* with one peak at $z = \sqrt{(1 + \tilde{\delta}^2)/2}$ and two zeros at $z = \tilde{\delta}$ and $z = 1$. The latter integral $g_2''(z)$ can be formally rewritten by using Neville's theta function, to show that this term is *positive* and *monotone increasing*. The product of a positive convex function with one peak ($g_2'(z)$), with a monotone increasing positive function ($g_2''(z)$) yields a positive function with two zeros at $z = \tilde{\delta}$ and $z = 1$ and, at most, one peak.
So the very last term on the right hand side of Equation (1.61) is a concave function with one peak and two zeros at $z = \tilde{\delta}$ and $z = 1$. The rest of the terms in the square brackets may become monotone, constant, increasing or decreasing, depending on the sign of the term $\pi(\beta - \lambda_l) - 2E\lambda_m$. We have two possibilities:

1. suppose $\pi(\beta - \lambda_l) - 2E\lambda_m$ to be negative:

$$\lim_{z\to 1}\frac{d\tilde{\gamma}(z)}{dz} = \frac{2}{\pi\sqrt{(z^2-\tilde{\delta}^2)}}\left[\left(\frac{E}{K}-1\right)[\pi(\beta-\lambda_l)-2E\lambda_m]+\right.$$
$$\left.+\lambda_m\left(\frac{E^2}{K}-\tilde{\delta}^2K\right)\right]\lim_{z\to 1}\frac{1}{\sqrt{1-z^2}} > 0, \quad (1.64)$$

because of the inequality properties of the elliptic functions. The inequality (1.64) implies that $\tilde{\gamma}$ becomes negative in the vicinity of the mast top!! Therefore this situation will not produce positive lift and is not feasible;

2. now we find that $\pi(\beta - \lambda_l) - 2E\lambda_m$ should be positive; so the condition for $\tilde{\gamma}'(1)$ is needed and given by:

$$\left(\frac{E}{K}-1\right)[\pi(\beta-\lambda_l)-2E\lambda_m]+\lambda_m\left(\frac{E^2}{K}-\tilde{\delta}^2K\right)\leq 0,$$

or concisely using Equations (1.48), (1.49) and (1.50):

$$\mu \leq \mu_c \quad \Rightarrow \quad \boxed{\mu_c \geq \mu \geq \mu_m \geq \mu_l}, \quad (1.65)$$

where:

$$\mu_c = \frac{4}{3}\frac{(1+3\tilde{\delta}^2)E-\tilde{\delta}^2(1+3\tilde{\delta}^2)\frac{K}{2}-(5-\tilde{\delta}^2)\frac{E^2}{2K}}{(1+\tilde{\delta}^2)E^2-\tilde{\delta}^2(1+2\tilde{\delta}^2)EK+\tilde{\delta}^4K^2-(2+\tilde{\delta}^2)\frac{E^3}{K}}. \quad (1.66)$$

When the inequality (1.65) holds, the terms:

$$(\pi(\beta-\lambda_l)-2E\lambda_m)g_1(z)+\lambda_m\left(\frac{E^2}{K}-\tilde{\delta}^2K\right),$$

of Equation (1.61) constitutes a *monotone decreasing positive function.* Summing this function and the last concave function:

$$-2\lambda_m g_2(z),$$

we have a function with one zero for $z \in [\tilde{\delta}, 1]$.
Table 1.3 shows the behaviour of $\frac{d\tilde{\gamma}(z)}{dz}$ when Equation (1.65) holds and therefore $\tilde{\gamma}(z)$ is always positive. If $\tilde{\gamma}(z)$ is positive, the effective angle of attack α_{ef} must also be positive as a consequence of Equation (1.60) and due to Equation (1.41f) it increases toward the mast top because $\beta - \lambda_l$ and λ_m are positive.

z	$\frac{d\tilde{\gamma}(z)}{dz}$	$\tilde{\gamma}(z)$
$\tilde{\delta}$	$+\infty$	0
$\vdots$	Positive	Increasing
$\downarrow$	0	Maximum
$\vdots$	Negative	Decreasing
1	$-\infty$ or 0	0

Table 1.3: Behaviour of circulation $\tilde{\gamma}(z)$ with respect to z.

To summarize, feasible solutions must satisfy the condition (1.65).
The last task of our design is to optimize the mast height and the gap. Using Equation (1.52), the first derivative of the nondimensional thrust:

$$\frac{d}{d\mu}\left(C^{\mathrm{I}}_{F_R}\right) = \frac{\pi A\tilde{\gamma}_R^2}{4\mu^5}(\mu^2 - 3\mu_l\mu + 2\mu_l\mu_m), \tag{1.67}$$

tell us that in the interval $[\mu_m, \mu_c]$ we have one μ, which gives the extremum of $\mu^2 C^{\mathrm{I}}_{F_R}$. Let μ_{opt} denote this μ:

$$\mu_{\mathrm{opt}} = \frac{4}{3}\frac{1 + \tilde{\delta}^2 - 2\frac{E}{K}}{(1+\tilde{\delta}^2)E - \tilde{\delta}^2 K - \frac{E^2}{K}}. \tag{1.68}$$

The nondimensional thrust behaves with respect to μ as is shown in Table 1.4. Hence μ_{opt} maximizes the thrust.
Furthermore Equation (1.68) shows that the optimum mast height decreases as the gap increases; otherwise the heeling moment will become greater than the constrained value for larger $\tilde{\delta}$. Due to the properties of the elliptic integral, the following inequality, coming from Equation (1.68), holds:

$$(1+\tilde{\delta}^2)E - \tilde{\delta}^2 K\frac{E^2}{K} \geq 1 + \tilde{\delta}^2 - 2\frac{E}{K}. \tag{1.69}$$

Therefore, μ_{opt} is not larger than 4/3. The equality in Equation (1.69) holds if and only if $\tilde{\delta}$ is zero. When $\tilde{\delta}$ is zero, μ_{opt} coincides with μ_c at $\mu = 4/3$. Therefore, the gap should be as small as possible.

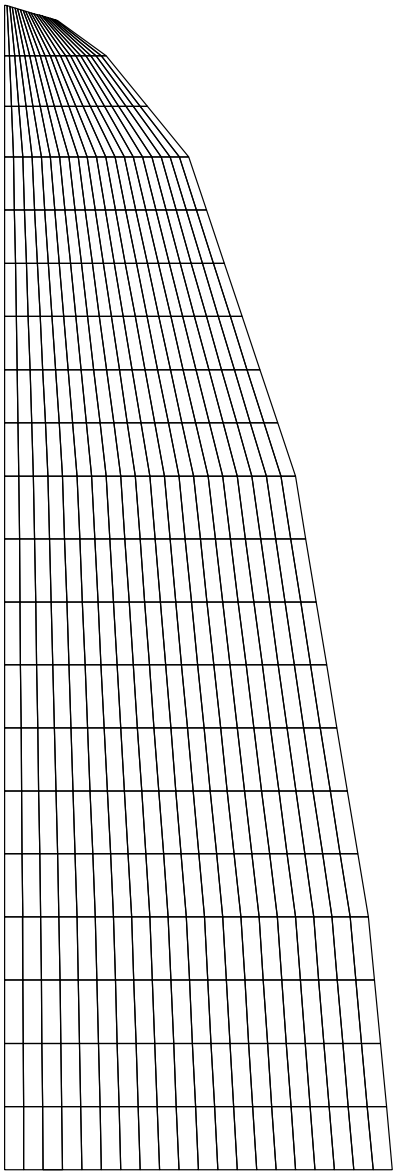

Figure 1.22: The optimum sail geometry.

μ	$d^2(\mu^2 C^{\mathrm{I}}_{F_R})/d\mu^2$	$d(\mu^2 C^{\mathrm{I}}_{F_R})/d\mu$	$\mu^2 C^{\mathrm{I}}_{F_R}$
μ_m	Negative	Positive	
$\downarrow$	Negative	Positive	Increasing
μ_{opt}	Negative	0	Maximum
$\downarrow$	Negative	Negative	Decreasing
μ_c	Negative	Negative	

Table 1.4: Behaviour of nondimensional thrust $\mu^2 C^{\mathrm{I}}_{F_R}$ with respect to μ.

Our formulation implies that the maximization of the thrust and the reduction of the induced drag is achieved by using a high aspect ratio for zero $\tilde{\delta}$, and the rest of the solutions ($\tilde{\delta} \neq 0$) have patterns of distribution closer to the elliptic loading. Equation (1.60) implies that the chord is in direct proportion to the circulation and in inverse proportion to the effective angle of attack. The chord is much greater in the vicinity of the sail foot, partly because the optimum circulation is greater in the lower portion, and partly because the effective angle of attack increases toward the mast top. This result implies that constraint on the heeling moment plays a decisive role in the sail design.
Using Equations (1.50) and (1.52) with no gap ($\tilde{\delta} = 0, \mu_{\mathrm{opt}} = 4/3$), we have the maximum thrust coefficient:

$$\boxed{C^{\max}_{F_R} = \frac{9\pi\tilde{\gamma}_R}{32}\left(\beta - \frac{81\tilde{\gamma}_R}{256}\right)}. \tag{1.70}$$

Using Equations (1.47)–(1.50) and (1.70) with no gap, the optimum circulation coincides with:

$$\boxed{\tilde{\gamma}_{\mathrm{opt}} = \frac{27\tilde{\gamma}_R}{32}\left(\sqrt{1-z^2} + \frac{z^2}{2}\ln\left|\frac{1-\sqrt{1-z^2}}{1+\sqrt{1-z^2}}\right|\right)}. \tag{1.71}$$

Then using Equations (1.41f), (1.48)–(1.50), (1.60) and (1.71), we have the geometry of the ultimately optimum sail with no gap:

$$\boxed{c(z) = \frac{\sqrt{1-z^2} + \frac{1}{2}z^2 \ln\left|\frac{1-\sqrt{1-z^2}}{1+\sqrt{1-z^2}}\right|}{\pi\left(\frac{32\alpha}{27\tilde{\gamma}_R} - \frac{1}{2} + \frac{1}{4}\pi z\right)}}. \tag{1.72}$$

Figure 1.22 shows the geometry of the optimum sail when $\tilde{\delta} = 0$.

Chapter 2

Wind load

No laws for a wind, an eagle, or a maiden's heart.
Pushkin.

2.1 Introduction

The development of modern materials and construction techniques has resulted in the emergence of a new generation of structures that are often remarkably flexible, low in damping and light in weight (i.e. tall buildings, cable–supported bridges, suspended–span bridges, membrane roofs, antennas, sails). It is the task of the engineer to ensure that the performance of structures subjected to the action of wind will be adequate during their life from the standpoint of both structural safety and serviceability. To achieve this goal, we need some information regarding the wind climate in general (Section 2.2); then, in more detail, some concerning about wind's direction and strength in the case of a long offshore race as well as during racing in sheltered waters (Section 2.3); and the relation between that wind and the forces it induces on the structures (Section 2.4) (for more details see (Ubertini 1994)).

2.2 Wind environment

Some knowledge of meteorology and micrometeorology, is needed for a realistic prediction of wind load on structures (Simiu and Scanlan 1986). Meteorology provides a description and explanation of the basic features of atmospheric flows. Such features may be of considerable significance, because wind arises as a result of pressure differences in the atmosphere. For the earth, as a whole, there

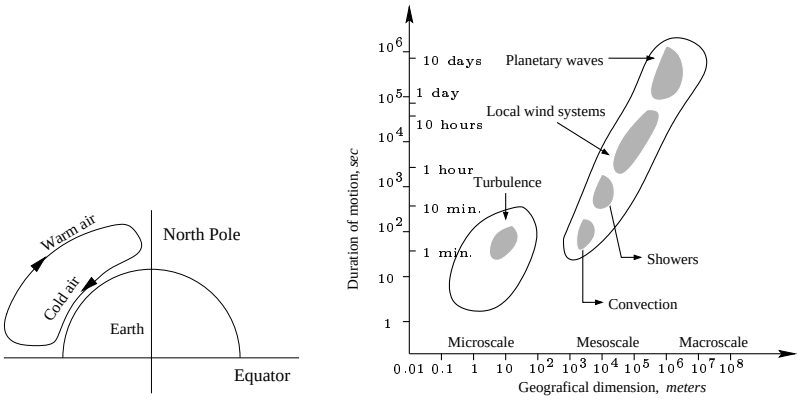

(a) (b)

Figure 2.1: Simplified model of atmospheric circulation and qualitatively order of magnitude in space and time of atmospheric scales.

is equilibrium between the energy received from the sun and the energy which is radiated from the earth into space. There is a surplus on energy near the equator and a deficiency near the poles. At the equator, ground–level air is heated, it expands, rises and flows away, leaving low pressure. Similarly, at the poles, ground–level air cools and contracts, so at higher levels, air flows in and high pressure results (see Figure 2.1(a)). Atmospheric motions may be described as superpositions of interdependent flows characterized by scales ranging from approximately a few centimeters to thousands of kilometers. For our purpose, it is convenient to classify them according to a space–time scale (Dyrbye and Hansen 1997). From Figure 2.1(b) three main groups of atmospheric scales are commonly defined: *microscale* including motions with characteristic dimensions of less than 20 Km or so in space and time scales of less than one hour; *synoptic scale or macroscale* including motions with characteristic dimensions exceeding 500 Km. or so and time scales of two days or more. The *mesoscale* is defined by dimensions and periods between those characteristic of microscale and synoptic scale.
This chapter is devoted to the study of microscale spects of the flow that are of interest in structural design. The Earth's surface exerts on the moving air a horizontal drag force, the effect of which is to retard the flow. The effect of this drag force upon the flow decreases as the height above ground increases and become neglegible above a height of a region referred to as atmospheric boundary layer. The depth of the boundary layer normally ranges from a few hundred meters to

several kilometers, depending upon wind intensity, roughness of terrain and angle of latitude. Within the boundary layer, the wind speed increases with elevation; its magnitude at the top of the boundary layer is often referred to as the gradient speed. Above the boundary layer, inside the free atmosphere, the frictionless wind balance, is established and the wind flows approximately with the gradient speed. It is the wind regime within the boundary layer of the atmosphere that is of direct interest to the designer of structures.

2.2.1 The atmospheric boundary layer

This section is devoted to the study of aspects of atmospheric boundary layer flow: the theoretical results presented, include descriptions of geostrophic and gradient wind velocity, mean wind profiles and the relation between wind speeds in different roughness regimes. The motion of an elementary mass of air is determined by Newton's second law (pag.27), the vector expression of which is:

$$\mathbf{f} = m\mathbf{a}, \tag{2.1}$$

where m is the mass of a particle. It is the purpose of this section to briefly describe the forces and some of their effects on the motion of air; infact wind speed and direction of the wind itself depends only on the horizontal pressure gradient $\mathbf{P}$, on the Coriolis force $\mathbf{F}_c$ and the centrifugal force $\mathbf{C}$, that we are going to define (see Appendix B).
We consider an infinitesimal volume of air $dx\,dy\,dz$ and the pressures acting on the lower and upper faces to be p and $p + \frac{\partial p}{\partial z}dz$, respectively. The net vertical force acting on the volume $dx\,dy\,dz$ will be $-\frac{\partial p}{\partial z}dx\,dy\,dz$ or $-\frac{\partial p}{\partial z}$ per unit volume. Similarly the net forces per unit volume acting in the x and y direction will be denoted $-\frac{\partial p}{\partial x}$ and $-\frac{\partial p}{\partial y}$, respectively. The resultant of these forces is called *horizontal pressure gradient* and is denoted $-\frac{\partial p}{\partial n}$ where n is the normal to the isobars[1]. The net force per unit mass exerted by the horizontal pressure gradient, $\left(\frac{1}{\rho}\right)\frac{\partial p}{\partial n}$ is often referred to as the *pressure gradient force* (ρ is the air density in pag.8). The horizontal pressure gradient is the driving force which initiates the horizontal motion of air. Air subjected only to the action of pressure gradient forces will move from regions of high pressure to regions of low pressure. If we define the motion of an air particle, not subjected to the action of an external force, with respect to an absolute frame of reference, it will follow a straight line. To an observer on a rotating frame (the Earth), the path described by the particle will appear curved. The deviation of the particle motion from a straight line fixed with respect to the rotating Earth, may be attribuited to an apparent force, the Coriolis force, the

[1]Lines contained in the same horizontal plane and connecting points of equal pressure.

vector expression of which is (see Equation (B.1.9)):

$$\mathbf{F}_c = 2m\,(\mathbf{v} \times \boldsymbol{\omega})\,, \tag{2.2}$$

where $\boldsymbol{\omega}$ is the angular velocity of the Earth and $\mathbf{v}$ is the velocity of the particle relative to a coordinate system rotating with the Earth. Following the right–handed multiplication rule $\times$, $\mathbf{F}_c$ is perpendicular to $\boldsymbol{\omega}$ and $\mathbf{v}$. As we told before, the effect on the wind due to friction along the ground become negligible and the horizontal motion of air relative to the surface of the Earth is determined, in unaccelerated flow, by the balance among the pressure gradient, the Coriolis and the centrifugal force.

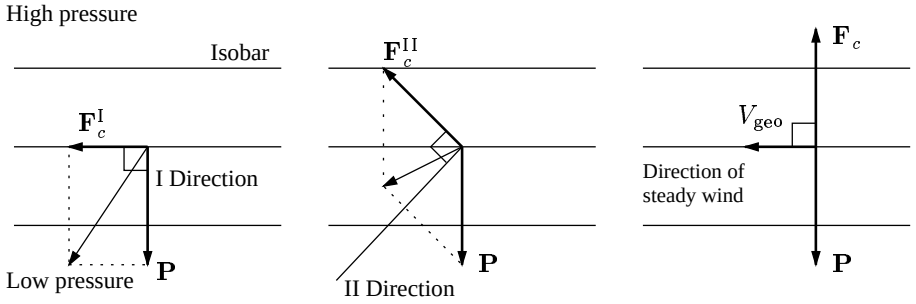

Figure 2.2: Wind balance in geostrophic flow in the Northern Hemisphere: a air particle is accelerated towards the low pressure area, due to the pressure gradient $\mathbf{P}$ and its path will be diverted, due to the Coriolis force $\mathbf{F}_c$.

At first we consider the isobar straight: this means no centrifugal force. In this case, the pressure gradient towards a low–pressure zone causes a mass of air to accelerate along a curve, until a state of equilibrium between the pressure gradient and the Coriolis force per unit of air volume is reached, as depicted in Figure 2.2. The steady velocity for which this balance occurs is called the *geostrophic wind velocity* V_{geo} and using Equation (B.1.9) is related to the pressure gradient by the equation:

$$2\omega V_{\mathrm{geo}} \sin\phi = P = \frac{1}{\rho}\frac{dp}{dn} \quad \Rightarrow \quad V_{\mathrm{geo}} = \frac{1}{\rho f}\frac{dp}{dn}, \tag{2.3}$$

where P is the magnitude of the pressure gradient force vector $\mathbf{P}$, f is the Coriolis parameter, ω is the angular velocity of the Earth ($2\pi/24$ hours $= 7.27 \cdot 10^{-5}$ rad/s) and ϕ is the latitude[2]. This wind, parallel to the isobars, is called *geostrophic wind*. If the isobars are curved (see Figure 2.3), wind velocity and direction not only

[2]For example at Greenwich latitude (51°), $f = 1.13 \cdot 10^{-4}$ s^{-1}.

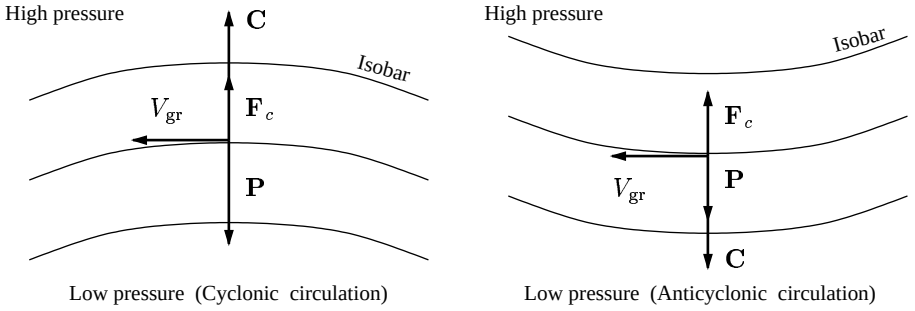

Figure 2.3: Gradient wind with constant speed but following a curved path: wind balance in cyclonic and anticyclonic flow in the Northern Hemisphere.

depend on the pressure gradient and the Coriolis force but also on the centrifugal force of the curved path. The wind in question is called the *gradient wind* and the equation of motion is:

$$\pm\frac{V_{gr}^2}{r} + fV_{gr} = P = \frac{1}{\rho}\frac{dp}{dn}, \tag{2.4}$$

where, if the mass of air is in the Northern Hemisphere, the positive or the negative sign correspond to cyclonic (around a low pressure center) and anticyclonic (around a high pressure center); r is the radius of curvature of the isobars; V_{gr} is called the *gradient wind velocity* and it is equal to V_{geo} in the case of straight isobars. The solution of Equation (2.4), in the Northern Hemisphere is:

$$V_{gr} = -\frac{fr}{2} + \sqrt{\left(\frac{fr}{2}\right)^2 + \frac{r}{\rho}\frac{dp}{dn}} \qquad \text{for cyclonic winds,} \tag{2.5}$$

$$V_{gr} = +\frac{fr}{2} - \sqrt{\left(\frac{fr}{2}\right)^2 - \frac{r}{\rho}\frac{dp}{dn}} \qquad \text{for anticyclonic winds} \tag{2.6}$$

With reference to Figure 2.5(a), close to the ground, in the boundary layer, wind velocity and direction varies as a function of height. This is because the ground tends to reduce wind velocity and this effect spreads upwards. The equilibrium of forces in the boundary layer is illustrated in Figure 2.4. If the point A (Figure 2.4) is at a higher level than B (Figure 2.4), its speed and its Coriolis force will be larger than those of point B. The deviation angle ι between the wind direction and the isobars will therefore be smaller for the higher and faster particle. The angle ι will be zero at the gradient level and will reach its maximum value ι_0 near the ground. The wind velocity in the boundary layer may thus be represented by a spiral, as in Figure 2.5(b).

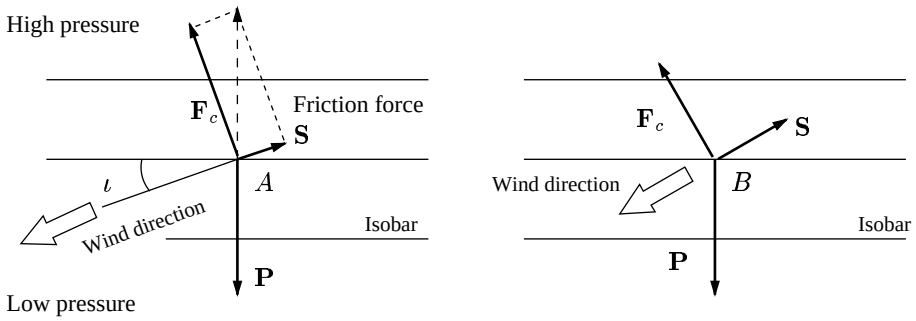

Figure 2.4: There is equilibrium between the forces due to the pressure gradient $\mathbf{P}$, the Coriolis force $\mathbf{F}_c$ and the friction generated $\mathbf{S}$ in the atmospheric boundary layer.

2.2.2 Equations of mean motion

The motion of a particle in the atmospheric boundary layer is governed by the fundamental equation of continuum mechanics that include the equation of continuum (conservation of mass) (Schlichting 1979, pag.47) and the equations of motion (conservation of momentum or Newton's second law of motion, Equation (2.1)) (Schlichting 1979, pag.65). These equations must be supplemented by the constitutive relations (Schlichting 1979, pag.58), that are empirical relations able to describe the specific response to external effects of the continuous medium considered.
If the equation of continuity (2.7d) and the equations of motion (2.7a)–(2.7c) are evaluated at constant ρ, for an incompressible and steady fluid flow (hypothesis 1, pag.45), and if terms that can be shown to be negligible are dropped, the following Navier–Stokes equations describing the mean motion in the boundary layer of the atmosphere are obtained (Sherman 1990):

$$U\frac{\partial U}{\partial x} + V\frac{\partial U}{\partial y} + W\frac{\partial U}{\partial z} + \frac{1}{\rho}\frac{\partial p}{\partial x} - fV - \frac{1}{\rho}\frac{\partial \tau_x}{\partial z} = 0, \tag{2.7a}$$

$$U\frac{\partial V}{\partial x} + V\frac{\partial V}{\partial y} + W\frac{\partial V}{\partial z} + \frac{1}{\rho}\frac{\partial p}{\partial y} - fU - \frac{1}{\rho}\frac{\partial \tau_y}{\partial z} = 0, \tag{2.7b}$$

$$\frac{1}{\rho}\frac{\partial p}{\partial z} + g = 0, \tag{2.7c}$$

$$\frac{\partial U}{\partial x} + \frac{\partial V}{\partial y} + \frac{\partial W}{\partial z} = 0, \tag{2.7d}$$

where U, V and W are the mean velocity components along the axes x, y and z of a right–handed cartesian system of coordinates, the z axis of which is vertical; p,

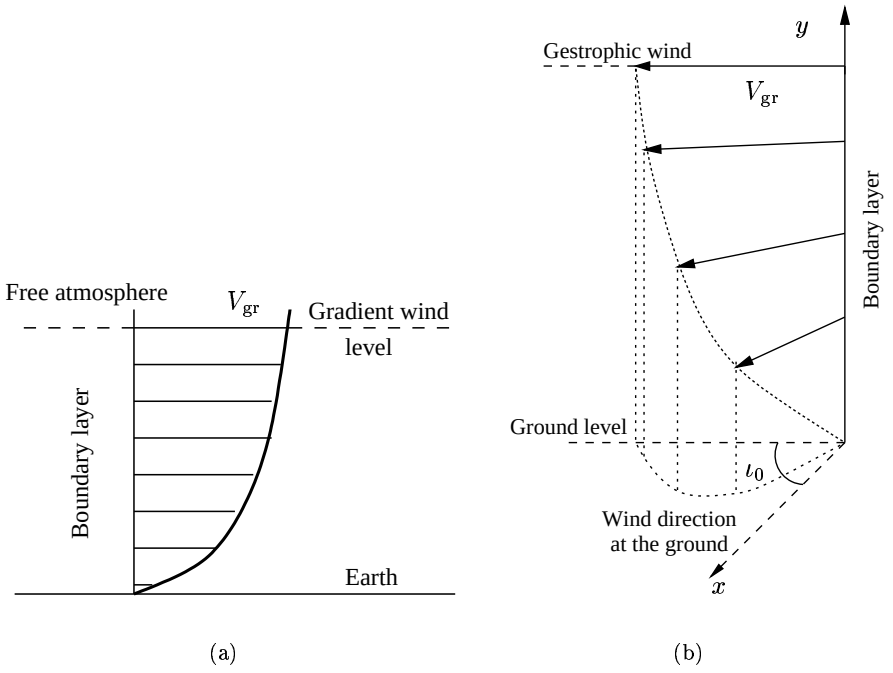

Figure 2.5: Wind velocity spiral in the atmospheric boundary layer.

ρ, f and g are the mean pressure, the air density, the Coriolis parameter (Equation (2.3)) and the acceleration of gravity, respectively; and τ_x and τ_y are shear stresses in the x and y directions, respectively. The x and z axes are selected, for convenience, as shown in Figure 2.5(b). The shear stress at the surface is denoted by τ_0.

In a gradient wind condition, with a horizontal density gradient negligible (barotropic flows), by differentiating Equation (2.7c) with respect to x or y, we can see that the horizontal pressure gradient does not vary with height and thus has, throughout the boundary layer, the same magnitude as at the top of the boundary layer:

$$\frac{dp}{dn} = \rho \left[f V_{gr} \pm \frac{V_{gr}^2}{r} \right] \quad \Leftarrow \quad \text{Equation (2.4).} \tag{2.8}$$

In a geostrophic wind condition, it follows from Equation (2.3) that:

$$\frac{1}{\rho}\frac{\partial p}{\partial x} = fV_{\text{y–geo}}, \tag{2.9a}$$

$$\frac{1}{\rho}\frac{\partial p}{\partial y} = -fV_{\text{x–geo}}, \tag{2.9b}$$

where $V_{\text{x–geo}}$ and $V_{\text{y–geo}}$ are the components of the geostrophic velocity V_{geo} along the x and y axes.
To solve the equations of mean motion (2.7a)–(2.7d) of mean motion, it is necessary that constitutive or *closure* relations be assumed, defining the shear stresses τ_x and τ_y. A well consolidated assumption (Prandtl 1952, pag.118) is that an *eddy viscosity* A_τ and a *mixing length* l may be defined such that:

$$\tau_x = \rho A_\tau(x,y,z)\frac{\partial U}{\partial z}, \tag{2.10a}$$

$$\tau_y = \rho A_\tau(x,y,z)\frac{\partial V}{\partial z}, \tag{2.10b}$$

$$A_\tau = l^2(x,y,z)\sqrt{\left[\left(\frac{\partial U}{\partial z}\right)^2 + \left(\frac{\partial V}{\partial z}\right)^2\right]}. \tag{2.11}$$

The use of Equations (2.10)–(2.11) in conjunction with Equations (2.7a)–(2.7d) is referred to as the *mean velocity field closure.*
It may be assumed that, within a horizontal site of uniform roughness over a sufficiently large extent, a region exists over which the flow is horizontally homogeneous. Under this condition, Equations (2.7a)–(2.7b), in which Equations (2.9) are used, become:

$$V_{\text{y–geo}} - V = \frac{1}{\rho f}\frac{\partial \tau_x}{\partial z}, \tag{2.12a}$$

$$V_{\text{x–geo}} - U = -\frac{1}{\rho f}\frac{\partial \tau_y}{\partial z}. \tag{2.12b}$$

If in the above model, the shear stresses are represented by Equations (2.10) and if, in addition, it is assumed that A_τ is constant, the model obtained is called the *Ekman spiral* (Simiu and Scanlan 1986). With the boundary conditions $U = V = 0$ at $z = 0$ and $U = V_{\text{x–geo}}$ and $V = V_{\text{y–geo}}$ at $z = 0$, the solution of the system (2.12) is:

$$U = \frac{1}{\sqrt{2}}V_{\text{geo}}\left[1 - e^{-az}(\cos az - \sin az)\right], \tag{2.13a}$$

$$V = \frac{1}{\sqrt{2}}V_{\text{geo}}\left[1 - e^{-az}(\cos az + \sin az)\right], \tag{2.13b}$$

where $a = \sqrt{\frac{f}{2A_\tau}}$. Equations (2.13), which describe the Ekman spiral, are represented schematically and qualitatively in Figure 2.5(b). More refined theories are obtained assuming an eddy viscosity that does depend on height (Simiu and Scanlan 1986).
A different type of approach gives the more classical *logarithmic law*. In this approach, two characteristic length scales are applied in the boundary layer. In the lower part of the boundary layer, the *surface layer*, the dominant length scale is the *roughness length* z_0 that is a measure of surface roughness. In the upper part of the boundary layer (*outer layer*) close to the free regime, the boundary layer height is an important length scale.
In deriving the logarithmic profile, only surface roughness is taken into account, so the profile applies close to the ground, up to 50–100 meters above terrain. Close to the ground, the velocity gradient V_{gr} depends upon τ_0, ρ and the height z from the ground. Based upon a dimensional analysis (Dyrbye and Hansen 1997), a differential equation for the mean wind velocities can be formulated, and if there is a long, flat terrain upstream, its solution leads to the following expression for the logarithmic profile:

$$U(z) = \frac{1}{\kappa} u_\star \ln \frac{z}{z_0}, \tag{2.14}$$

where κ is the Von Karman's constant ($\kappa \approx 0.4$) and $u_\star$ the *friction* or *shear velocity* of the flow:

$$u_\star = \sqrt{\frac{\tau_0}{\rho}} \tag{2.15}$$

2.3 Wind and water

Every sailor, no matter whether he be racing or cruising, tries to get a forecast of the wind's direction and strength before setting the sails. A correct *weather oracle* can often influence the crew's efforts to complete their task. Before a long *offshore race*, most attention will be given to getting a synoptic picture of the weather over a broad area, while for *racing in sheltered waters* an intimate knowledge of local wind conditions will be more useful.

2.3.1 Weather conditions: global wind and offshore sailing

Weather conditions, and therefore *global winds*, over large areas come under the influence of *lows* (depressions or cyclones[3]), and *highs* (anticyclones[4]), moving

[3]Circulation around a center of low pressure.
[4]Circulation around a center of high pressure.

generally from west to east (see Figure 2.6 from (Marchaj 1964, pag.364)). The mean speed of the depression centre is about 20 knots or even more, whereas the winds within a depression, moving inward in a spiral, may reach speeds of 135 knots (250 km/h). In the northern hemisphere, winds rotate anticlockwise round the *lows* (Figure 2.6). As Figure 2.7 shows, the winds in a cyclone may aid or hinder the progress of a sailing craft, depending on the position of the yacht in a particular quadrant. For example, if a yacht follows the course AB (Figure 2.7) which cuts through the depression system, then in position 1 she will be reaching on the port tack. In position 2 she is forced to sail close–hauled, still on the port tack. When the yacht passes to quadrant II, however, she is forced to go on to a starboard tack.
Clearly, therefore, the art of offshore sailing involves not only a skilfull use of the

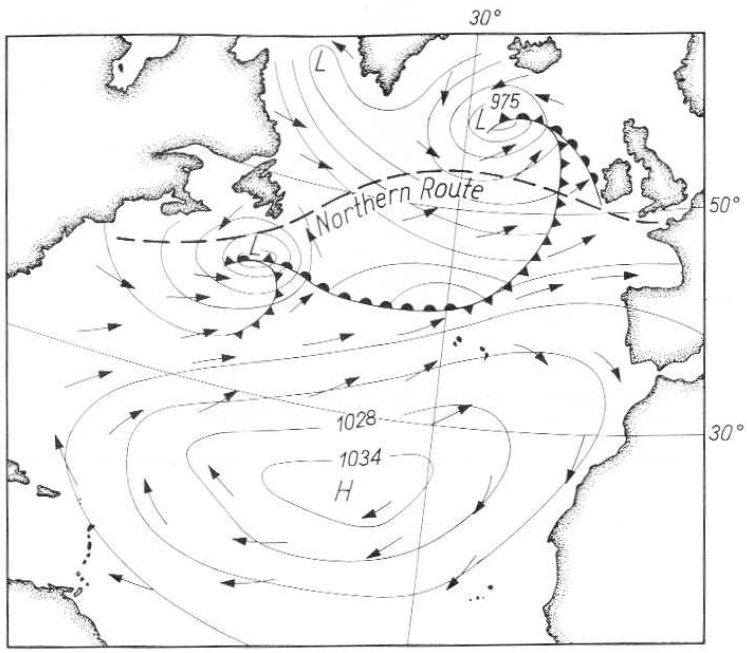

Figure 2.6: Typical pressure and wind distribution in the North Atlantic; wind changes within a depression (low) in the northern hemisphere.

possibilities offered by the yacht's aerodynamic and hydrodynamic efficiency, but also a knowledge of how to take advantage of the meteorological conditions met with. This is most striking in the somewhat longer offshore races.
As an example, let us consider the transatlantic race, which is run along the north-

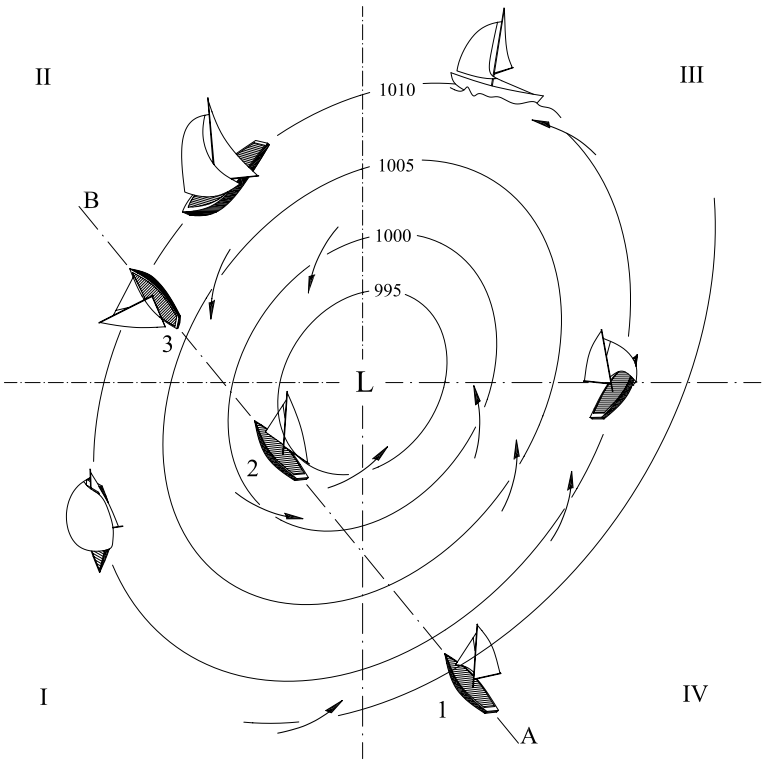

Figure 2.7: According to the so–called Buys Ballot's Law: "If you stand with your *back* to the wind in the northern hemisphere, the *low* centre is on your left."

ern route (Figure 2.8) in the region of the track followed by lows. The results of these races, as a rule, are decided by eastward moving depressions.
It was shown earlier in Section 1.1 that heavy displacement yachts, in the most favourable weather conditions, can attain a maximum relative speed $V_s^{\max} \approx 1.4\sqrt{\text{LWL}}$. Clearly, then, a yacht with a longer waterline length LWL, and so with a higher relative speed V_s, will have a better chance of keeping in contact with a low for a longer time. Thus, in the same weather conditions, a 40 feets yacht could sail $V_s^{\max} \approx 1.4\sqrt{40} = 8.8$ knots, while a 30 feets yacht could only reach $V_s^{\max} \approx 1.4\sqrt{30} = 7.7$ knots. Naturally, a more efficient crew, better navigation, sailing a yacht to her best advantage, and so on, may give the victory to a yacht of shorter waterline length. To explain what we mean, we consider the example presented in Figure 2.8. In the previous example in Figure 2.6, the depression was moving in approximately the same direction as the race; Figure 2.8,

on the contrary, shows what happens when the center of a depression moves at an angle across the course. The track of the low is shown by the broad arrow, and the course of the race is across the Baltic from Hel (point A) to Hoborg (point B). Now, if the actual wind blowing near Hel at the beginning of race were all

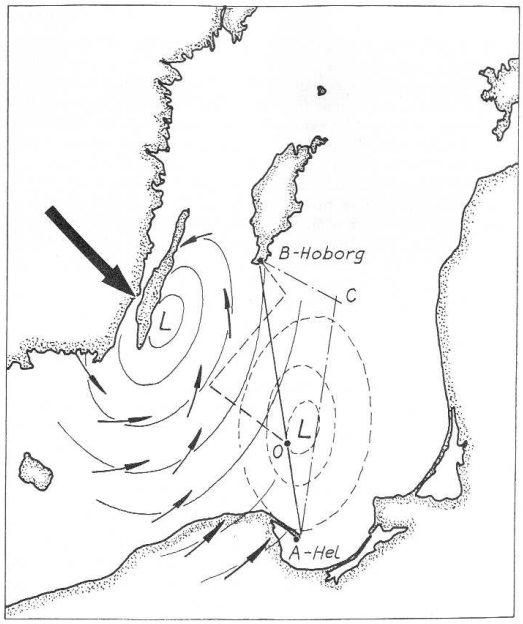

Figure 2.8: An optimum route should be based on the weather forecast. The choice of course from departure point A to the destination B depends upon the expected track of dominating depressions.

that could be known, the shortest course, AB, would be assumed to be the most advantageous. But as the depression will be moving eastwards, somewhere near point O, a boat would find herself compelled to tack close–hauled against a rising wind and rougher sea. Infact, during the race, what started as a south wind will change to a westerly, then to a northwesterly, and finally to a northerly wind. More advantageous plan, therefore, would be to anticipate these changes and follow the course ACB. This will ensure a favorable wind for the whole race, and higher speeds will be reached.
As distinct from cyclones, anticyclones (area of high pressure), generally move slowly, and winds rotate around them in a clockwise direction, the opposite way to the cyclonic winds. Because the air mobility of anticyclones is much slighter, the possibility of utilizing, in a race, the associated winds are much less than with

cyclones.
To take full advantage of variable weather, the synoptic weather chart of the area must be studied before and during a longer race.
Above all, one needs to have the plot of isobars on a map of the region involved; then during the race, by noting variations in pressure and wind direction, it is possible to deduce in which quadrant of the depression (or anticyclones) the boat is sailing. This makes it possible to determine the direction in which the weather formation is moving, its speed, and then to sail the yacht as best as possible..
The conclusions reached by observing changes in wind direction and barometric pressure can be tested by watching for such other signs of approaching changes in the weather as Mother Nature offers. The color of the sky at sunrise and sunset; the concentration, shape and movement of the clouds; different light phenomena in the atmosphere; the behaviour of birds, and so on, can greatly assist in the correct assessment of the weather situation and in forecasting changes.

2.3.2 True wind structure: local wind and sailing in sheltered waters

The surface wind, the actual wind from 0 to 100 feet, differs considerably from the wind aloft, whose direction and speed can be observed from the movements of the clouds. The factors which determine the quality of the surface wind, which acts on a sail, are:

1. the atmospheric pressure gradient introduced in Section 2.2.1 at pag.63;
2. the sun's heat input;
3. the height above water level;
4. the sea surface over which the wind is blowing;
5. the thermal differentiation of the regatta area;
6. wind barriers or obstructions.

Factors 2 to 6 modify the basic wind structure and are the main causes behind *local winds*. Because of them, the apparent wind, which actually interests the sailor is never constant in direction or strength (see Figure 2.9).
During the discussions in Section 2.2.1, it was mentioned in pag.65 (gradient wind) and in pag.69 (logarithmic law) that there is a definite wind velocity gradient produced by air friction against the water (or terrain) surface. The gradient is definable as the rate at which the wind gradually increases with height above the water level. This affects the direction of the apparent wind, and therefore the efficiency of the sail. Thus, as depicted in Figure 2.9, the apparent wind V_a *felt* by

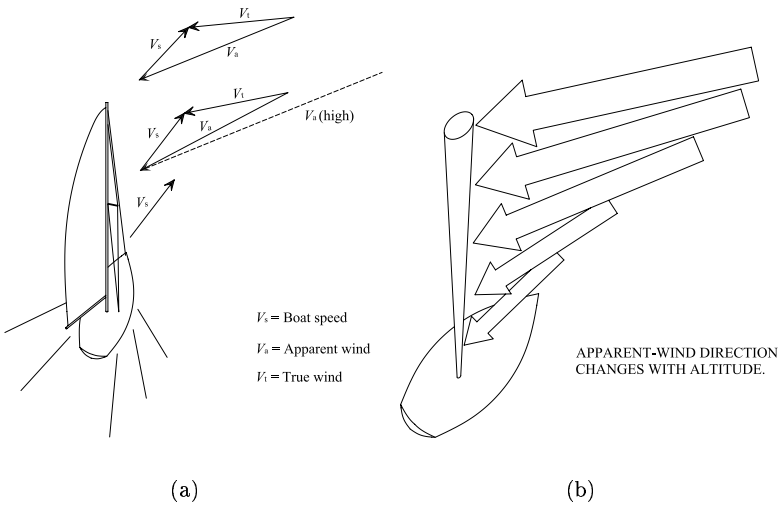

Figure 2.9: Bird's eye view of shift in apparent wind angle with height from the deck.

sails varies in strength and direction over the mast height, even if the true wind is steady.
Meteorological investigations (Marchaj 1964) have revealed that this velocity gradient varies according to the extent the sky is covered by clouds, the wind speed and turbulence. From Figure 2.10 it can be seen that in a light wind (see Beaufort scale in Appendix C), a smooth sea, and an overcast sky, the wind velocity changes are relatively great. In such conditions, therefore the permissible twist in the sail from the boom to the top of the mast can be greater because of the twist in the apparent wind (Figure 2.9(b)). Again from Figure 2.10, in gusty[5] turbulent winds, the velocity gradient is much smaller, and so it is desirable to reduce the twist in the sail as much as possible.
Futhermore, the presence of the yacht's hull between the water surface and the sail reduces the velocity gradient comparatively to that shown in Figure 2.10. The presence of the hull induces a contraction of the air flow above the deck, and this accelerates the wind speed here, reducing the effect of true wind vertical gradient on the apparent wind speed (Hypothesis 8 in pag.45).

[5] *Gust* is a period when the wind speed is increased substantially above the mean speed (Section 2.2.2).

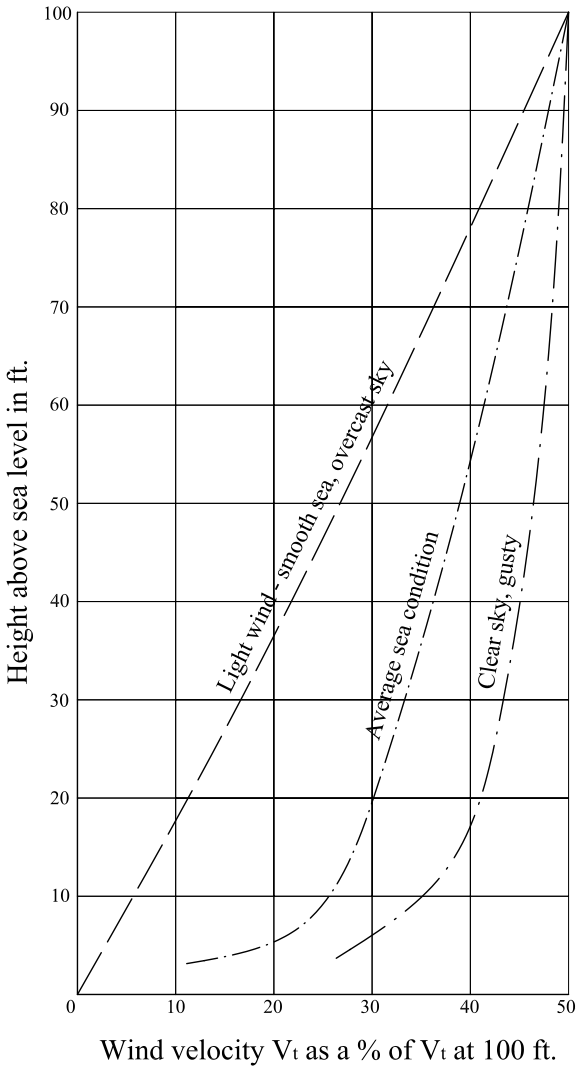

Figure 2.10: The wind gradient: the rate of change of wind speed with height above water, may vary greatly depending on the type of weather and the state of the sea.

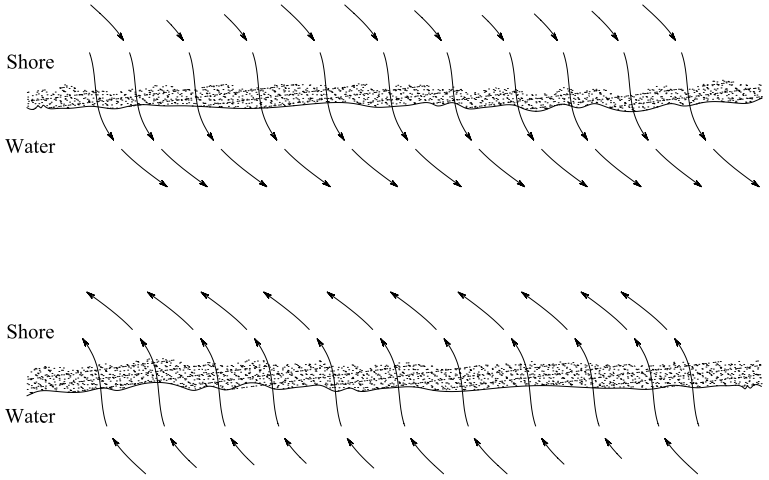

Figure 2.11: Shifts in the surface wind direction over the shoreline.

It is well known from practical experience and measurements (Marchaj 1964) that winds blowing across a coastline undergo changes in horizontal direction, due to the different thermal properties of the land and sea surface and to the different roughness characteristics of the surface over which the wind is blowing. No matter whether the wind is blowing onshore or offshore, its direction changes so that it crosses the line of the coast at an angle of approximately 90° (Figure 2.11). This shift in the wind can be used to advantage during a race if the course lies near the shore. Figure 2.12 demonstrates how one can take advantage of a directional change of wind.

Assuming that yachts A and B crossed the starting line at the same time, one may *rightly* expect that the helmsman of A, having chosen the course closer to the shore, would round buoy number I before yacht B. When yacht B reaches point X and tacks toward buoy number I, one may *wrongly* conclude, from the direction of the wind at that point that by sailing along the course X–Y the buoy will be reached on the starboard tack. However, as the boat approaches the coast, the wind may change its direction enough to force her to bear away along the course X–Z and consequently to incur a loss of time.

Furthermore, differences in temperature between land and sea, together with the change in the surface roughness, in addition to direction, also influence the wind speed over the sea. The wind over the sea is always stronger than the wind actually blowing over the land; the ratio of wind speed over the sea to that over the land is greater than one and tends to increase quite rapidly when the temperature of the sea increases.

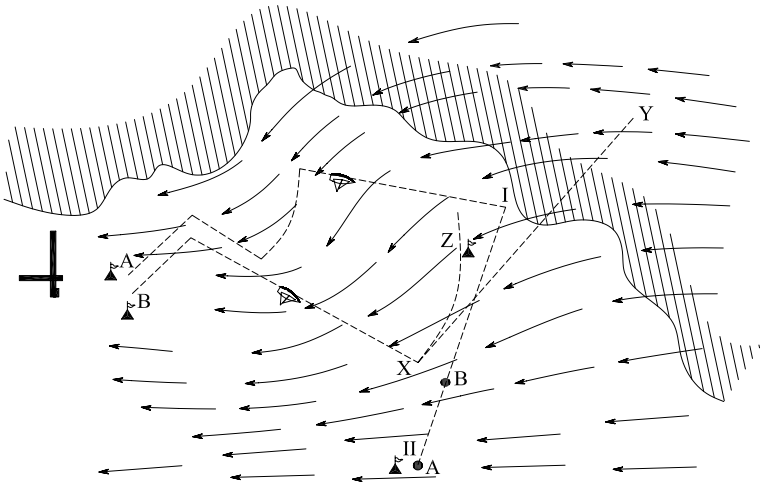

Figure 2.12: In coastal waters the surface wind is much influenced by the contours and nature of the adjacent land.

The influence of the surface over which the air is moving is also responsible for the wind's turbulent character. Air, like water, only maintains a steady laminar flow at low speeds and over a smooth surface. Unevenness in the ground, and the vertical air movements caused by thermal differences, create wind turbulence, which manifests itself in fluctuations in speed and direction.
Overall, the temperature of the surface has a marked effect on wind turbulence and gusts. If the surface is cooler than the moving air masses, it tends to stabilize the wind and slow it down. A warm surface, on the other hand, causes a rapid increase in speed in cool, fresh air masses. For example, it is the cooling of the land in the evening which is the main reason why winds tend to drop later in the day. Sailors are also aware that in the spring, while the sea's temperature is still low, the wind is usually steady and not gusty. In spite of strong winds the sea's surface will remain relatively smooth, for the character of the wave formation depends on the character of the wind. A squally wind will induce very much greater waves than a steady wind. Far offshore, a wind of 6 (Beaufort scale in Appendix C) produces waves similar to those which may develop close to land in winds of 4. As a rule, the further from shore the steadier the wind.
However, even supposedly steady winds are never really steady from the viewpoint of racing sailors, but are more or less disturbed by variation in direction and velocity. These may throw a racing crew into confusion, with particularly acute consequence on the windward leg. Indeed, as the *sailing–writer* John Masefield says:

A very queer thing is the wind
I don't know how it beginned
and nobody knows where it goes.
It is wind, it beginned and it blows.

Wind is an invisible, capricious motive power, and this fact alone makes it difficult to time one's tack correctly. There are many helmsmen who are able to do their windward work consistently well in a steady breeze; but there are few who can fully exploit the opportunities offered by unsteady winds: this can often be the deciding factor which wins a race.
Let us explaine, using two examples, in which way a skillfull helmsman can use a change in wind direction and velocity.
If a boat is sailing close–hauled (Hypothesis 9 in pag.45), as in Figure 2.13, then in position I the mainsail is trimmed to suit the apparent wind V_a (segment $\overline{\mathrm{OB}}$) at an angle α (see Figure 1.4). The vector $\overline{\mathrm{AB}}$ gives the speed of the yacht V_s, and $\overline{\mathrm{OA}}$ the speed of the true wind V_t. If at position II the speed of the true wind increases to a value $\overline{\mathrm{O_1A}}$, the yacht due to her inertia will not change her speed immediately. However, the direction and magnitude of the apparent wind will change from $\overline{\mathrm{OB}}$ to $\overline{\mathrm{O_1B}}$, thus increasing the angle of the sail α by $\Delta\alpha$. If the sail had previously been trimmed to the optimum angle α, the angle at which the most advantageous aerodynamic force was developed, then to mantain the same angle (or even to reduce it for the sake of stability) either:

1. the sheets must be eased, as in position II, or
2. the boat must luff, as in position II_a.

During this gust, the yacht will accelerate as in position III, and this will cause another shift in the direction of the apparent wind from $\overline{\mathrm{O_1B}}$ to $\overline{\mathrm{O_1B_1}}$. To prevent the sails fluttering, the sheets must now be hauled in to preserve the desirable trim angle α. Those who luffed to position II_a will not get further benefit from tightening the sheets, and will have to bear away onto their original course. A squall lasting one or two minutes, then, can help a yacht in two ways. The yacht can either continue on her original course and increase her speed or, by luffing, work up a little to windward, nearer the next marker buoy by distance l. The actual situation in a given race will determine which is the more profitable move, and the strength of the gust and the type of yacht have to be borne in mind as well.
Besides these fluctuations in speed, there are also variations in the direction of the true wind.
Skillfull exploitation of changes in the wind's direction is very important, especially when sailing to windward. Figure 2.14 shows two yachts which have turned at the marker buoy I and are now beating towards buoy II. The watchfull helmsman of yacht B, sailing on the port tack, notices the wind shift when it occurs, and quickly

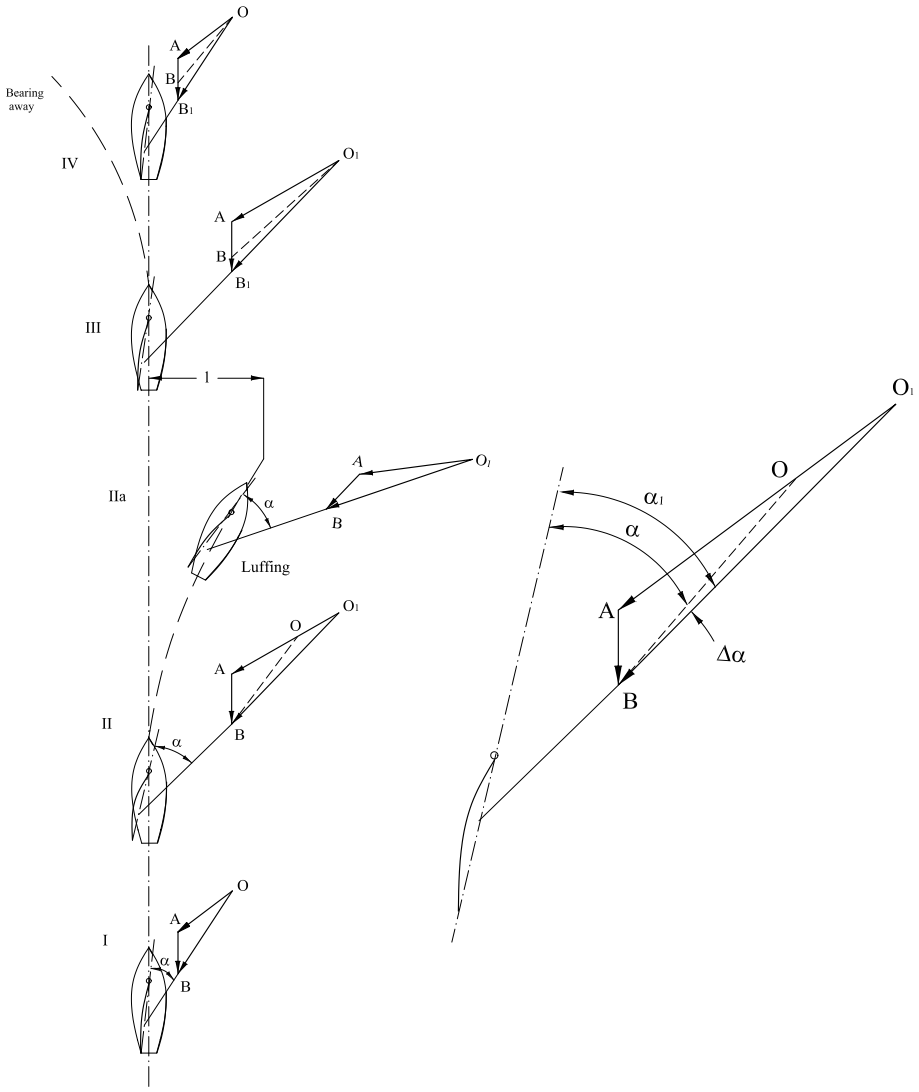

Figure 2.13: The sequence of course changes when sailing on the starboard tack in a lifting gust. Note that the true wind V_t did not change its direction but its speed only.

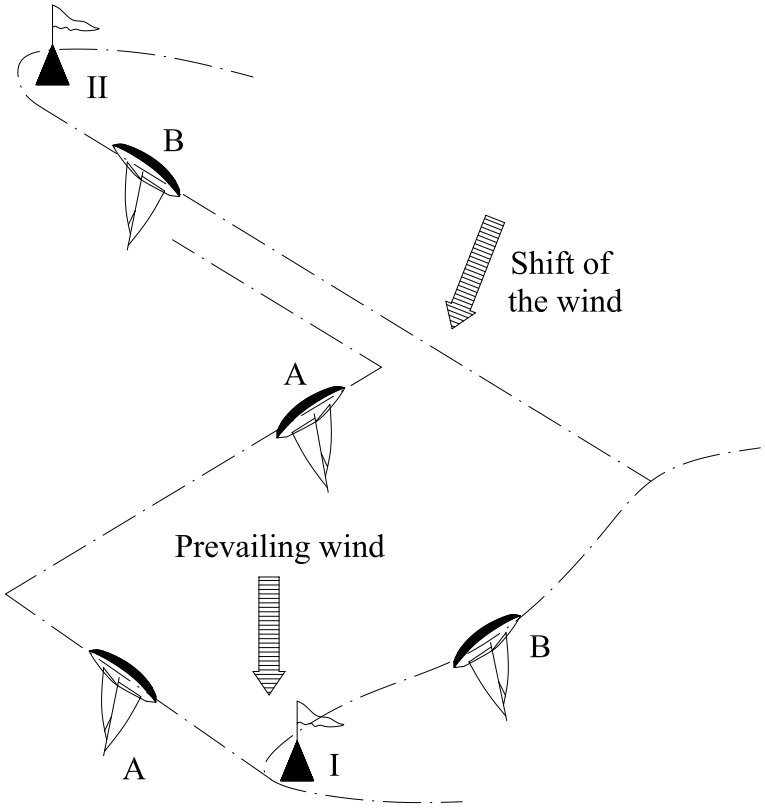

Figure 2.14: The cost of making the tack may be relatively low in terms of loss of time and distance, as compared to the cost of being on the wrong tack.

tacks onto starboard. These tactics allow him to lay buoy II without further tacking. The less observant helmsman of yacht A, choosing his tack without any proper consideration of possible wind shifts, finds himself behind his opponent.
When beating to windward, at an angle of 45° to the true wind, the distance covered will be 141 % of the distance in a straight line between buoys I and II in Figure 2.15. The geometrical constructions of this Figure show that, by making skilful use of winds shifts of no more than 5°, the distance to be covered by tacking will be reduced to 130 % of the shortest distance. If the wind shifts are as much as $10° \div 15°$, the distance gained by exploiting them will give an observant helmsman a big margin over one too careless to pay attention to variations in the wind. If the distance between the buoys I and II is one nautical mile, the helmsman who

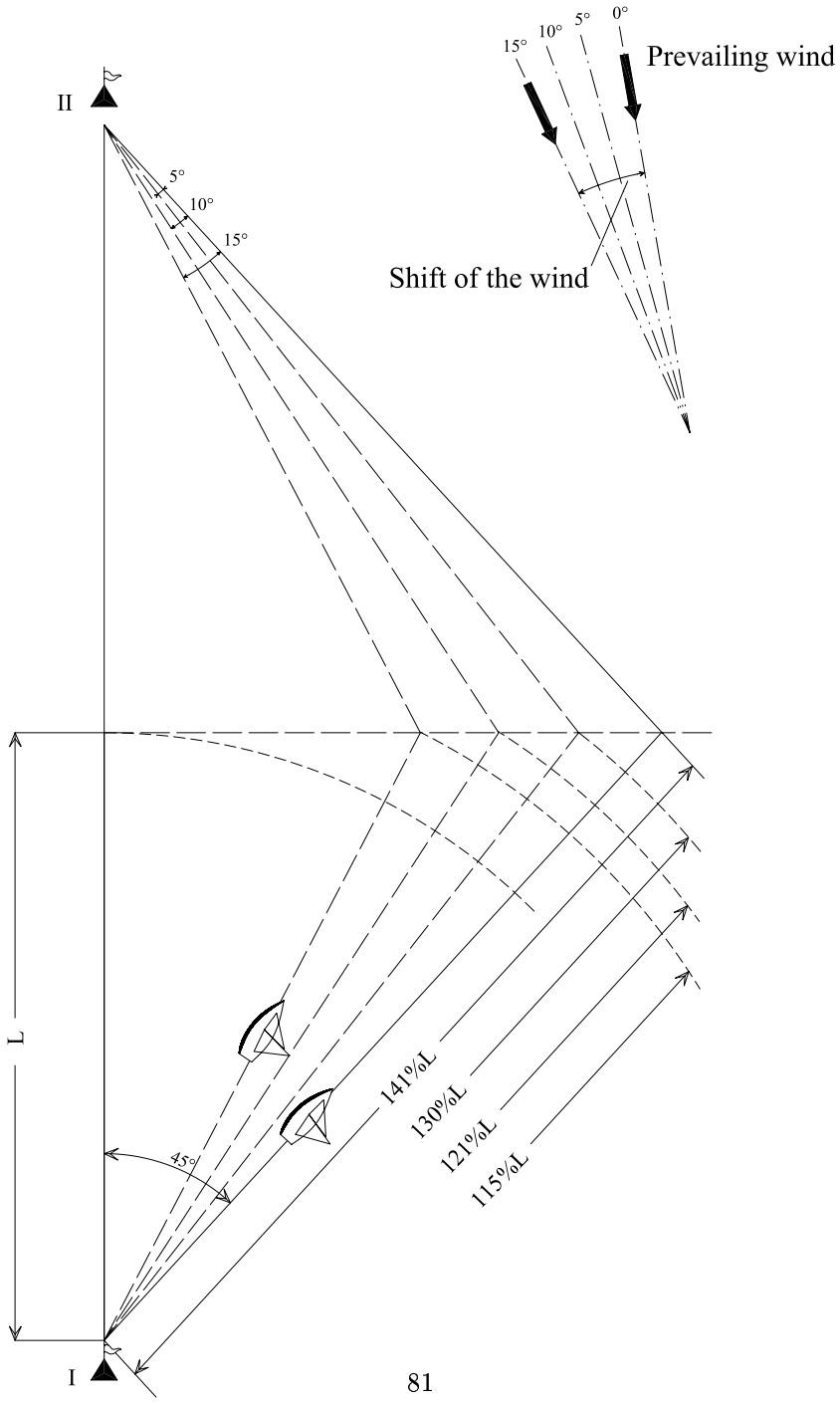

Figure 2.15: It is rather rare for the wind to be shifting by less than about 5 degrees each side of the main direction; usually the shifts are greater.

makes use of wind shifts $\pm 5°$, may theoretically gain about 120 yards made good to windward over his rival who ignore the shifts and sails an average course 45° off the wind. If the wind shifts are in the order of $\pm 10°$, the possible gain might be about 225 yards per every nautical mile sailed.

2.4 Aerodynamic wind forces and their effects on structures

Common sense, do what it will, cannot avoid being surprised occasionally. The object of science is to spare it this emotion and create mental habits which shall be in such close accord with the habits of the world as to secure that nothing shall be unexpected.
Bertrand Russell, *The Analysys of Matter*

Common sense is not so common.
Voltaire, *Dictionnaire Philosophique*

In many cases wind effects on structures are in agreement with *common sense*, easy to understand and forecast. Neverthless, there are times when our intuition may deceive us. For an example, let us look at Figure 2.16(a), illustrating a wind blowing over two types of roof, and try to determine which type is more likely to be blown off. *Common sense* would say that the steep, high roof is the more likely to be damaged, but in reality, it is usually the low pitched roof which gets lifted off by the wind.
A second example can be seen in Figure 2.16(b): here the wind blows over two sails of the same camber and curvature, but , one is set at an angle of incidence α of 20° to the wind, the other at 90°. The question is: which sail will develop the stronger force? Contrary to expectation, it will not be the latter which does so !!
A third example, which can have unpleasant consequence for an inexperienced helmsman, is shown in Figure 2.16(c). Two boats are moored in a strong current. A new question is: what would happen if the two boats were moored near one another? Many would answer that the water flowing between them would push them apart, and that, the smaller the gap between them, the greater would be the repelling force. *Infact* the opposite is true: the two boats will tend to move closer to each other, and this tendency will increase as the gap between them becomes smaller.
The reasons and explanations for the phenomena illustrated in Figures 2.16(a)–2.16(c) will be discussed in the next section.

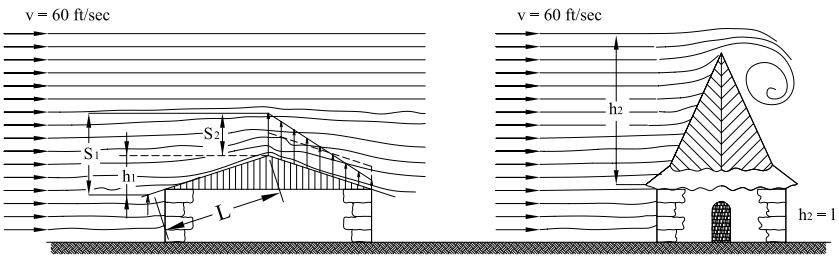

(a)

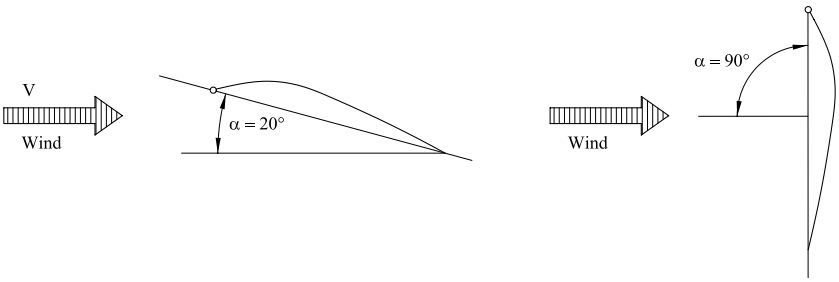

(b)

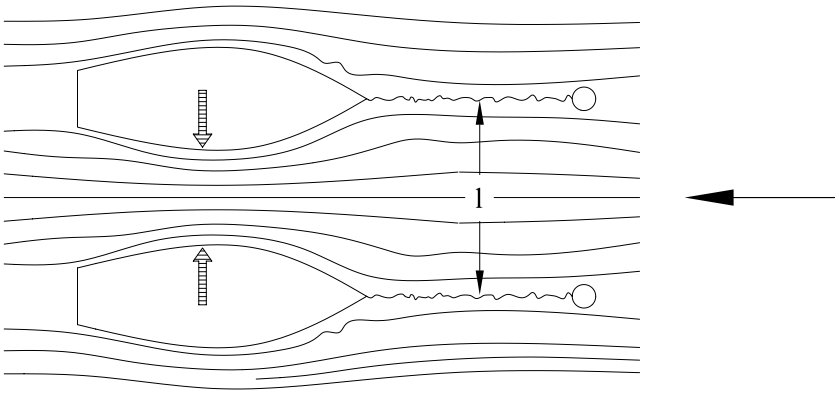

(c)

Figure 2.16: The effects of high–speed winds on buildings, roofs in particular, are not easy to predict.

2.4.1 Static and dynamic pressure: the right way to explain sail forces

A sailing yacht moves on the boundary between air and water, being partly immersed in each. The flow of air over the sail creates the driving force F_R (see Figure 1.4) necessary to overcome the hydrodynamic resistance D_h (see Figure 1.4) generated by the hull traveling through the water. For both fluids, air and water, one important characteristic is their *weight density* or *weight per unit volume* γ, which for water is about $\gamma_{\text{water}} = 9810$ N/m^3; the corresponding value for air is $\gamma_{\text{air}} = 11.76$ N/m^3.
The wind is only a special case of air in motion, and when considering its effects in terms of forces one must, according to the laws of Newton, know the *mass per unit volume* or *mass density*, ρ. The product $g\rho$, where g is the acceleration due to gravity (9.81 m/sec^2), is the weight per unit volume γ. So the air density is $\rho_{\text{air}} = 1.20\text{kg/m}^3 = 1.20\text{Nsec}^2/\text{m}^4$ and the water density is $\rho_{\text{water}} = 1000\text{kg/m}^3 = 1000\text{Nsec}^2/\text{m}^4$. The wind, having both mass and velocity possesses *kinetic energy*, the energy due to motion. This energy is usually called the *dynamic pressure* q (force per unit area) and is given by the formula:

$$q = \frac{1}{2}\rho_{\text{air}} v_{\text{wind}}^2 = 0.6 v_{\text{wind}}^2 \quad \text{in} \quad \left[\frac{\text{N}}{\text{m}^2}\right], \tag{2.16}$$

where v_{wind} is the velocity of the wind of known magnitude and direction in m/sec. The aerodynamic forces which appear on a sail depend almost entirely on the prevailing pressures on the windward and leeward sides: strictly speaking, on the prevailing *static* and dynamic pressures. There is no better way to learn about aerodynamic and hydrodynamic forces operating on a sailing boat than to know more about those pressures: how they come into existence and how they can be measured.
Let us consider, as a first example, that a glass tube of the shape shown in Figure 2.17 is filled with water to the level L–L and then placed in an air stream. Inlet 1 of the tube is placed perpendicular to the wind direction, and inlet 2 is parallel to the wind direction. We would find that the difference in water level in the two tubes will be greater for the higher wind speed v_{wind}. So long as there is no wind acting on this *primitive manometer*, the levels are the same, since through both open tubes there is the same static pressure p_{st} acting, that of atmospheric pressure p_{atm}. At sea level, which is the bottom of our atmosphere, this pressure on average is assumed to be 101325 N/m^2, and is balanced in a barometer by a column of mercury 760 mm in height and by a column of water 10.33 m in height. However, tube 1, pointing into the flow, would receive, in addition to the static pressure p_{st}, the dynamic pressure q of the wind. The sum of static pressure p_{st}, plus the dynamic pressure q, is called the *total head pressure* or the *stagnation*

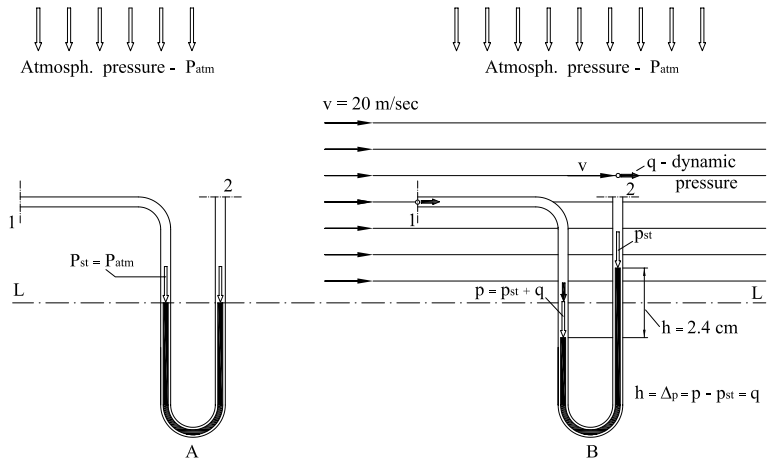

Figure 2.17: A method of measuring directly the dynamic pressure q, and indirectly the flow velocity v_{wind} by means of U–tube manometer.

pressure:

$$p_{\text{tot}} = p_{\text{st}} + q. \tag{2.17}$$

If the wind velocity $v_{\text{wind}} = 20\text{m/sec}$, then the dynamic pressure q would, according to equation 2.16, be $q = 240\text{N/m}^2$ and this value would be indicated on our manometer by a difference in water levels of $h = 2.4\text{cm}$. The height of the water column in the manometer can therefore be used to measure the dynamic pressure of the wind:

$$q = \Delta p = p_{\text{tot}} - p_{\text{st}}, \tag{2.18}$$

where Δp means the difference in pressure between the two inlets of the same manometer.
Let us carry a second example. Between and around the two plates, one straight and another convex, shown in Figure 2.18, flows an air stream passing the stations S_1, S_2, S_3 and S_4. At these four points are attached U–tube manometers filled with water to the common level L–L, and having their inlets in, and parallel to, the air stream between the plates. So long as there is no air flowing through the virtual channel, all manometers will indicate the same level. When, however, air flows through, we would see that the water levels in manometers B and C alter, thus clearly indicating reduced pressure (suction) at points 2 and 3 respectively. The greatest change in level occurs at station S_3, where the cross section is minimum. Let us try to answer the following questions: what is the reason for different levels

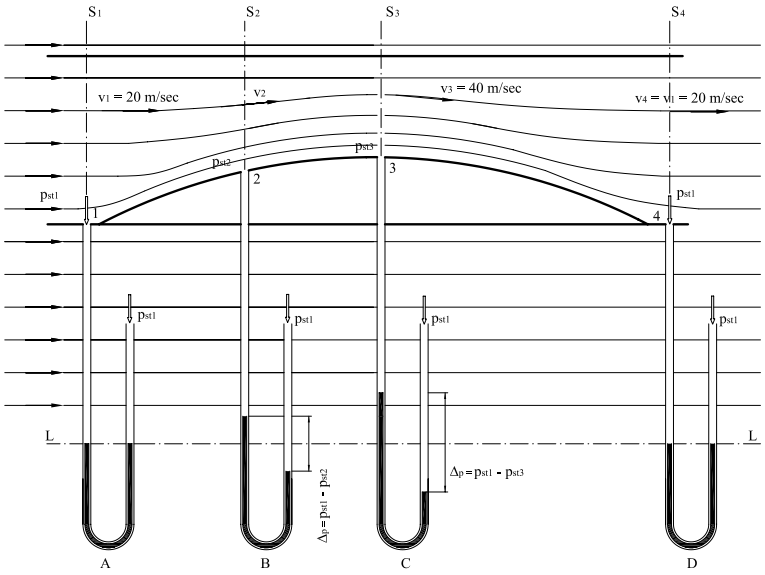

Figure 2.18: Simplified picture of the flow through a duct like *sail*.

on the manometers? Why did the pressure fall at the stations 2 and 3, relative to the surrounding static pressure $p_{\text{st}} = p_{\text{atm}}$? Evidently, these changes must be caused by the varying velocity of the air as it flows through sections S_1, S_2, S_3 and S_4. Manometers A and D will not indicate any difference in levels, because each has both ends placed tangentially to the wind direction, measuring p_{st1}. This follows because sections S_1 and S_4 does not disturb the flow of velocity v_1. The air must flow faster through the smaller sections S_2 and S_3, than through S_1 and S_4, in order that the quantity of air passing the sections in a given time interval is to be the same. This quantity of airflow is given by the product of the relevant section area and the flow velocity:

$$S_1 \cdot v_1 = S_3 \cdot v_3 \quad \text{or} \quad \frac{S_1}{S_3} = \frac{v_3}{v_1}. \tag{2.19}$$

Thus, if at section S_1, the speed of the wind is, say, $v_1 = 20$ m/sec, and the sectional area S_3 is half that of S_1, then the flow speed at S_3 will be $v_3 = 40$ m/sec. Consequently, the dynamic pressure at S_1 and S_3 will, according to Equation (2.16), be:

$$q_1 = 0.6 \cdot (20)^2 = 240 \text{ N/m}^2,$$
$$q_3 = 0.6 \cdot (40)^2 = 960 \text{ N/m}^2.$$

This means that the kinetic energy of the wind at S_3 has increased over that at S_1 by four times, which is the square of the ratio of the speeds. As shown in Figure 2.18, this increase in dynamic pressure q_3, at section S_3 was followed by a decrease in local static pressure, $p_{\rm st}$, there. Evidently, some kind of interplay between these two forms of pressure takes place. In 1738, Daniel Bernoulli published his *Hydrodynamica* where he established a simple relationship between the dynamic and static pressures in the same air stream:

$$p_{\rm st} + q = p_{\rm st} + \frac{1}{2}\rho v^2 = \text{constant along a stream line.} \qquad (2.20)$$

In other words, as the speed increases, the local static pressure decreases, and viceversa. This is essentially what occurs with a sail in a close–hauled position or with a lifting aeroplane or with a keel operating at certain leeway angle. In honour of its discoverer, the relation (2.20) is known as the *Bernoulli equation.* We are now able to calculate the static pressures at the various stations taking $p_{\rm st} = p_{\rm atm} = 101325 \text{N/m}^2$:

$$p_{\rm tot} = p_{\rm st} + q_1 = 101565 \text{ N/m}^2.$$

In order to satisfy Equation (2.20), the total pressure at station S_3 must be the same, and we already know q_3:

$$p_{\rm st3} = 101565 - 960 = 100605 \text{ N/m}^2.$$

Thus, the difference between $p_{\rm st3}$ and atmospheric pressure will be:

$$\Delta p = p_{\rm atm} - p_{\rm st3} = 720 \text{ N/m}^2,$$

and this difference will be indicated in manometer C by the column of water equal to 7.2 cm. Manometer B will indicate a value between A and C, since the section area and thus, the velocity v_2 are intermediate.

We are now in a position to explain the examples quoted earlier at pag. 82.
The low pitched roof of Figure 2.16(a) is somewhat similar to the previous example of a channel. The wind, as it passes over the ridge, will create suction forces tending to lift the roof, the pressure inside the building being equal to the atmospheric pressure. In the case of the steeply pitched roof of Figure 2.16(b), the flow over the leeside is turbulent. A consequence of this is that large suction forces are not developed over the rear half of the roof, and thus the total drag force is much less than that for the low pitched roof. Exactly the same explanation for the two sails of Figure 2.16(c).

Chapter 3

Characteristics of sailcloth

Be as clear as you can about the various theories you hold, and be aware that we all hold theories unconsciously, or take them for granted, although most of them are almost certain to be false.
Karl Popper, *Objective knowledge*

3.1 Properties of Sailcloth

Sailmakers have an interesting problem: rather than relying on rigid frames and solid materials for shape control, they must shape their foils by balancing the forces of the wind with the tension in the sail. This is a difficult and ever–changing problem. The force or pressure distribution of the wind changes constantly and is affected by the shape of the sail, while the shape of the sail, through cloth stretch and flexing, is affected by the pressure distribution of the wind. It is easy to understand that the properties of the cloth such as stretch resistance, strength, flex, and weight, play an important role in balancing these forces and shaping the sail. Below is a list of the properties that must be addressed or controlled in the design and manufacturing of most sailcloth (Whidden and Levitt 1993):

- cloth geometry: warp, fill and bias;
- stretch resistance;
- strength;
- cloth weight;
- flexibility;

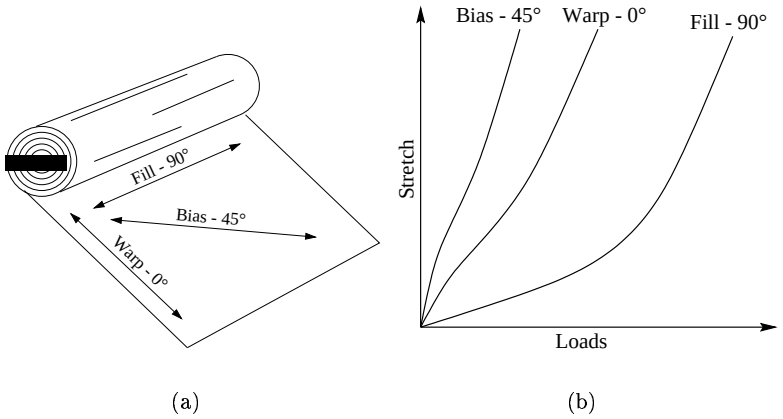

Figure 3.1: Cloth directions and comparison of stretch under load for different cloth directions.

- tear strength;
- porosity;
- water absorption;
- ultraviolet stability.

Cloth geometry: warp, fill and bias: directions in woven fabrics for sails are usually defined using traditional textile terms related to the weaving process (see Figure 3.1(a)). The warp is the longest direction in a roll of fabric; the fill direction is parallel to the filling yarns, known as weft yarns. During weaving, the fill yarns are passed back and forth through the warp yarns and are perpendicular to them. The bias direction bisects the other two at a 45 degree angle to each. In sailmaking, the textile terms of warp, fill and bias are gradually being replaced by the more modern angular conventions used in fiber–composite industry. In this system, the 0–degree direction is parallel to the warp, the 90–degree direction is parallel to the fill, and the 45–degree direction is the same as the bias.

Stretch resistance: the primary aspect to note about stretch resistance is that it can have different values in different directions. For instance, a woven fabric may have much lower stretch along one thread line than the other and, as shown qualitatively in Figure 3.1(b), will probably have much higher stretch

still when measured off the thread lines, on the bias, for example. It is easy to see that a detailed knowledge of the stretch resistance in the warp, fill and bias direction of a fabric is very important to a sailmaker when planning the panel layout and fabric orientation of a sail. This must complement a sailmaker's knowledge of the load distribution, that is *where, how much* and *in what* direction the wind pressure impacts the sails. Complicating this further is that the pressure distribution is different in each of the three groups of sails: headsails, mainsails and off–the–wind sails.

Stretch resistance can also be dependent on time. Some materials, when initially loaded, will stretch little, but if the load is maintained over a long period of time, they will gradually elongate. When the load is removed, some of these material will recover, or return to their original dimensions. In fact, this tendency in sailcloth is known as *recovery.* On the other hand, some materials when loaded will gradually elongate over time and will never recover their initial dimensions. *Creep* is the correct term that describes the nonrecoverable stretch.

Some sources of stretch are geometric, inherent in the geometry of the weave or in the construction of the sailcloth. One of the most important sources of geometric stretch is *crimp.* Crimp refers simply to the serpentine path that yarns must take in crossing over and under other yarns in a weave or a knitted construction. From the standpoint of stretch, crimp is a necessary evil in forming fabrics for sailcloth, but it can be controlled. For example, manufactures can put most of the crimp in a given weave in either the warp or the fill, leaving the other direction nearly crimp–free and therefore much less susceptible to stretch. Another type of geometric stretch is bias stretch. In woven fabrics, this is simply the deformation of the weave that cause the warp and filling to cross at other than right angles. One of the primary advantages of laminated sailcloth is the elimination or reduction of the two geometric stretch problems: crimp and bias stretch.

Stretch due to elongation of the very materials forming sailcloth is determined primarly by the choice of materials. Elongation takes place on a molecular level. This explains why *cotton* replaced *flax* as the material of choice for yacht sails. *Polyester*, which stretches less than *nylon*, is used in mainsails and jibs; *nylon*, which absorbs shock loads through high stretch, is used in spinnaker; *Mylar* film, which stretches less than most other films, is used for laminates; and *Kevlar*, the ultimate in low–stretch fibers, is important in modern racing sails. Stretch characteristics are very important in determining where a cloth can best be used. They determine how the designed shape of a sail will change with the wind, sheet, and halyard loadings, and whether it will change permanently with use.

Strength: there are two kinds of strength with which we are concerned:

Figure 3.2: The 8.8 oz[1] polyester–Dacron mainsail cloth at 30× magnification. Note low–crimp fill yarns running from lower right to upper left encased by highly crimped warp yarns. This is a fill–oriented cloth.

- breaking strength,
- yield strength.

In off–the–wind sails (i.e. spynnaker), breaking strength is the primary consideration. Just as *flax* was chosen over *cotton* for square–rigged sails because weight for weight it did not break as easily as cotton, today *nylon* rather than *Dacron* is used for downwind sails. Yield strength is the dividing line between recoverable, or elastic, elongation and nonrecoverable, or permanent, elongation. It became obvious that there is a load above which the material will no longer return to its original length after the load is removed. This load value establishes the maximum load capacity of the cloth. This is called yield strength. Combining the yield strength value with the predicted sail load value allows the sailmaker to determine the *maximum wind speed capability* of a given sail.

Cloth weight: it would be easy to make sailcloth with very high strength and very low stretch if weight were not a consideration, but weight can be a very important factor. One reason is sail–handling: it is obviously easier to set, stow and handle a lighter sail than a heavier one. Another consideration is weight aloft: minimizing weight aloft decreases the heeling moment and alleviates the pitching of the boat. By far the most important consideration

[1] 1 oz. (ounce) = 28.35 g.

of weight is, once again, shape. In light air, the shape of a sail can suffer simply because the sail is sagging under its own weight. Probably the most useful way to think about weight is to consider it as a *ratio of weight to yield strength.* From this ratio, the effective wind range of a sail can be computed. The lower limit of a sail's wind range is determined by the minimum wind required to fill a sail of a certain weight to its optimum shape; the upper limit is determined by the yield strength of the sail or the load at which the sail must be taken down to avoid permanent distortion. The remaining properties of sailcloth are usually of secondary importance because they are achieved in the course of addressing stretch resistance, strength and weight.

Flexibility: cloth flexibility is determined by a combination of factors, including the stretch of the fibers used, the thickness and weight of the material. This propertiy differs in racing and cruising sails: in racing sails, flexibility is often sacrificed to achieve lower stretch; in cruising sails, stretch resistance is often sacrificed to achieve ease of handling.

Tear strength: tear strength is, of course, important in saving a sail from an untimely death. Tear strength is sometimes a limit to the minimum weight of lightweight woven materials, such as lightweight Dacron and nylon, and is certainly a serious consideration in the lightest–weight spinnaker fabrics. Tear strength is adversely affected by resin finishes, such as melamine or urethane, which are applied to the fabric. Tear strength is often closely associated with seam strength: this is because many factors, including the size of the yarns, their placement, and the level of the finish, contribute to higher tear strength as well as higher seam strength. In practice dacron sails are the most resistant to tearing; polyester/Mylar sails also show good resistance to tearing; Kevlar/Mylar sails, however, are the most susceptible to tearing.

Porosity: porosity is only a seldom consideration in sailcloth. The processes of tight weaving, resin impregnation and lamination (used to control strength and stretch) almost always produce zero porosity as a side effect. Zero porosity makes it impossible for air to leak through the fabric. The exception to this is very lightweight nylon spinnaker cloths. Before addressing this exception, however, we should explain how sailcloth is weighed. Sailcloth weights are expressed in units of ounces per sailmaker's yard (SMY). This is the weight of a piece of cloth 28.5 inches wide by 36 inches long[2]. Nylon spinnaker cloths, weighting less than 1 SMY, are so light and thin that it is

[2]The British use ounces per square yard (oz/yd^2), and Continental Europe uses grams per square meter (g/m^2). Thus 1 SMY equals 1.26 oz/yd^2 British and 42.8 g/m^2 Europe.

difficult to achieve zero porosity. Some spinnaker cloth has a resin coating smeared over the surface to achieve this.

Water absorption: water pickup is certainly a problem for some sailcloth. An obvious example is cloth used in sailboard sails, which are repeatedly immersed in the water when the sailor falls. If the sail absorbs water, it becomes harder to uphaul, waterstart, and, indeed, hold up. Occasionally resins and fillers are applied to the cloth to fill in the voids between the filaments and the fibers in order to diminish water absorption.

Ultraviolet stability: ultraviolet radiation from the sun can break the molecular chains and weaken the materials in sailcloth. Nevertheless, the ultraviolet stability of sailcloth is only sometimes a consideration. Then, Dacron, the most common material used in sailcloth, has a self–screening property.

3.2 New materials, better sails!

Now that we know the desirable and undesirable characteristics of sailcloth, let's examine the most commonly used materials to see how they measure up and how they came to be that way.
In the beginning of the XX century the most common sailcloth's were made with cotton or flax. Flax is actually stronger than equivalent cotton, but cotton stretches less. Sailing to windward requires relatively flat well–shaped sails to form an effective airfoil, and although strength is still an important consideration, maintaining this airfoil shape without stretching is more critical. As a consequence, during the XIX century, cotton replaced flax. Cotton, being a natural fibre, has poor resistance to rot, ultraviolet light and water absorption. These qualities made it unsuitable cloth sailcloth. In spite of these undesirable properties, cotton was used almost exclusively in sailcloth design until after World War II, when synthetic fibers, with their wide array of desirable properties, including lower stretch and lighter weight, gradually became available. Nylon, named for *N*ew–*Y*ork and *Lon*don where research on the fiber was conducted, was the first man-made fibres to be used for sailcloth. The chemical formulation and general properties of nylon have changed little over the intervening years. It is a cheap, durable and relatively resistant to ultraviolet light, good flex-fatigue resistance and shows middle of the road strength properties. However Nylon is mostly restricted to use in off–the–wind sails like spinnakers and the cruising equivalents due to its poor stretch resistance. Even for spinnakers it is not the ideal material as it can absorb as much as 3in water. A group of British scientists, J. R. Whinfield, J. T. Dickson, W. K. Birtwhistle and C. G. Ritchie, in 1941 created the first

polyester[3] fiber called Terylene. In 1946 DuPont bought all legal rights and came up with another polyester fiber which they named Dacron^{TM}. Until the 1980's the only widely used sailcloth was woven polyester (or Dacron^{TM}, Dupont's trade name for their polyester yarn). Dacron is a very durable sailcloth and is resistant to mould and water absorption. Dacron is also very durable making it an excellent sailcloth. Woven sail cloths can be divided into two main categories:

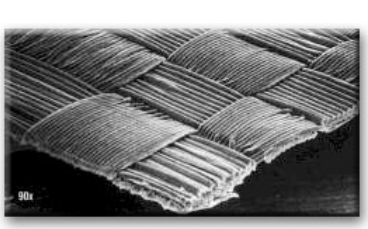

(a) Nylon

(b) Polyester Laminates

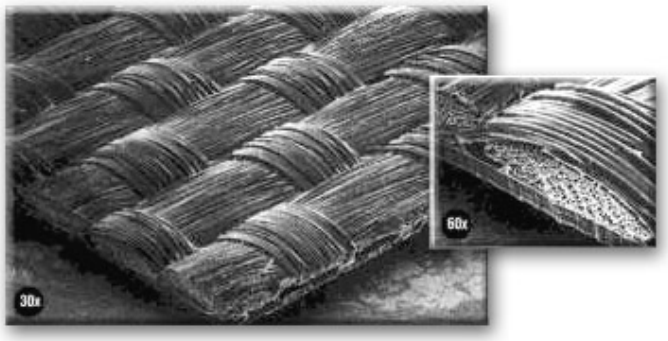

(c) Kevlar© & Spectra Laminates

Figure 3.3: Fibre to fabric: a closer look.

[3]Long-chain polymers chemically composed of at least 85 percent by weight of an ester and a di-hydric alcohol and a terephthalic acid. The name *polyester* refers to the linkage of several monomers (esters) within the fiber. Esters are formed when alcohol reacts with a carboxylic acid.

- woven polyester, more commonly known as Dacron^{TM} (see Figure 3.2). Polyester is widely used for its combination of reasonably low stretch, good strength, low cost and durability;

- woven nylon (see Figure 3.3(a)). Developed in 1938, nylon is a very strong fiber, but typically has somewhat higher stretch than polyester fiber. Like flax, nylon is strong and affordable, but somewhat stretchy, and is best used in off–the–wind sails, such as spinnaker and cruising equivalents. In these sails, light weight and strength are more important than stretch resistance.

Woven sail cloths have an inherent problem with its stretch resistance. Some yarns pass over and under one another. Over time as load is applied these yarns attempt to straighten out, this results in the fabric stretching. This is commonly referred to as crimp. This lead to the development of laminated cloths where the fibres are laid is straight as possible. Of these, the most important are:

- laminates made of polyester and Mylar film, more commonly known as polyester/Mylar (see Figure 3.3(b)). Mylar (a Dupont trademark) is a film formed by melting polyester resin, which is then extruded. When the polymer is melted and extruded, the long molecules of the polymer are oriented randomly, both in the plane of the film and perpendicular to the plane of the film. Next the material is mechanically drawn, or stretched, in both the warp and fill directions. This has the effect of stretching the molecules and changing them from a random orientation to a bidirectional orientation. The molecules line up primarly in the two directions in which they were pulled. In these two directions, the molecules are more solidly linked and have more resistance to stretch; the result is a very low–stretch polymer film. Simply applying resins to sailcloth, as occurs with impregnated Dacron, could not achieve the same low–stretch characteristics because the molecular orientation in these simple resins is random. In fact, it is impossible to apply oriented polymers to fabrics because the orientation must be done in a separate process. By marrying the unidirectional polyester fiber and the bidirectional Mylar, we realize a laminate with the most desirable properties of each. The polyester fiber shows good resistance to stretch on the thread line; the more balanced Mylar film shows good resistance to stretch off the thread line. The ratio of fiber to film, polyester to Mylar, in a laminate is an important consideration to the sailmaker in determining the stretch ratio of the material. In high aspect ratio sails, like mainsails, where through finite–element–generated stress maps, the loading is well documented, it is possible to use less film and simply orient the fibers in the load direction.

- laminates of Kevlar (a Dupont trademark) fiber and Mylar film, commonly known as Kevlar/Mylar (see Figure 3.3(c)). Kevlar fiber is about eight

times less stretchy than polyester yarn. Such miracles, however, come at a price: it is also ten times as expensive as polyester yarn. Kevlar is expensive for a very good reason: the filaments are formed in a very complicated process, wherein the polymer is liquefied in sulfuric acid (it cannot be melted) and extruded into filaments. The solvent must then be removed from the polymer, purified and recycled. All of the machinery must handle extremely corrosive low–pH sulfuric acid solutions. Running Kevlar in one direction, either the warp or the fill, and polyester in the other and then marrying the resultant fabric to Mylar opened the door to the use of Kevlar/Mylar in sailmaking. The sailmaker thus plans the panel orientation of sails to orient the Kevlar in the direction of the primary loads. In addition to being low stretch, Kevlar/Mylar is also about five times stronger than Dacron of equivalent weight and essentially has no yield point. The elongation of the yarn itself is perfectly elastic and recoverable up to the breaking point that occurs at a very low elongation (about 3%). For this reason, Kevlar/Mylar is susceptible to breaking in shock–loading condition. The primary problem with Kevlar/Mylar sailcloth is the degredation of the yarn through sharp flesing and creasing.

- laminates of Spectra fiber and Mylar film, commonly known as Spectra/Mylar (see Figure 3.3(c)). Spectra is a most highly oriented polyethylene polymer, characterized by very low stretch, similar to Kevlar, but much lighter. Kevlar is 1.41 times dense as water, whereas Spectra is 0.98 the density of water. In fact, Spectra will actually float. The stretch–to–weight ratio of Spectra is therefore much better than that of Kevlar. Spectra/Mylar also has the advantages of not degrading when flexed sharply, like Kevlar. However, Spectra/Mylar has its Achille's heel: when Spectra/Mylar is loaded to 30% or more of its breaking strength, it will creep, stretch permanently, over time.

3.3 Introduction to composite materials

Now that we know the most commonly used materials in sailmaking, let us examine the most classical theory used to model these composite materials.
A structural composite is a material system consisting of two or more phases on a macroscopic scale, whose mechanical performance and properties are designed to be superior to those of the constituent materials acting indipendently (Daniel and Ishai 1994). One of the phases is usually discontinuous, stiffer and stronger and is called *reinforcement*, whereas the less stiff and weaker phase is continuous and is called *matrix*. Sometimes, because of chemical interactions or other processing effects, an additional phase, called *interphase*, exists between the reinforcement and the matrix. The properties of a composite material depend on the properties

of the constituents, geometry and distribution of the phases.
There are three commonly accepted types of composite materials (Jones 1975):

1. *fibrous composites* are reinforced either by short discontinuous fibers or wiskers which can be oriented along one direction or randomly oriented or by long continuous fibers. These continuous fibers can be all parallel (unidirectional continuous fiber composite), can be oriented at right angles to each other (crossply or woven fabric continuous fiber composite), or can be oriented along several directions (multidirectional continuous fiber composite) (Mallick 1988);

2. *laminated composites* which consist of thin layers of different material bonded together;

3. *particulate composites* which consist of particles of various sizes and shapes randomly dispersed within the matrix. Particulate composistes may consist of nonmetallic particles in a nonmetallic matrix (concrete, glass reinforced with mica flakes, brittle polymers reinforced with rubber like particles); metallic particles in nonmetallic matrices (aluminium particles in polyurethane rubber used in rocket propellants); metallic particles in metallic matrices (lead particles in copper alloys to improve machinability); and nonmetallic particles in metallic matrices (silicon carbide particles in aluminium) (Daniel and Ishai 1994).

For the remainder of this section, emphasis will be placed on laminated composites (Point 2) and, to be more precise, taking into account the sailcloth introduced in Section 3.2, we will focus our attention on *fiber–reinforced composite laminates.*
A *lamina*, or ply, is a plane or curved layer of unidirectional fibers or woven fabric in a matrix. In the case of unidirectional fibers, it is also referred to as unidirectional lamina. The lamina, the principal reinforcing or load–carrying agent, is an orthotropic material with principle material axes in the direction of the fibers (longitudinal), normal to the fibers in the plane of the lamina (in–plane transverse) and normal to the plane of the lamina, as drawn in Figure 3.3. In the case of a woven fabric composite, the warp and the fill directions are the in–plane principal directions (see Figure 3.3). A *laminate* is made up of two or more unidirectional laminae or plies stacked together at various orientations. The laminae or plies or layers can be of various thicknesses and consist of different materials. The layers of a laminate are usually bound together by the same matrix material that is used in the laminae. Furthermore, the function of a matrix is to support and protect the fibers and to provide a means of distributing load among and trasmitting load between the fibers.
A *laminated fiber–reinforced composites* are a hybrid class of composites involving both fibrous composites and lamination techniques. Here layers of fiber–reinforced

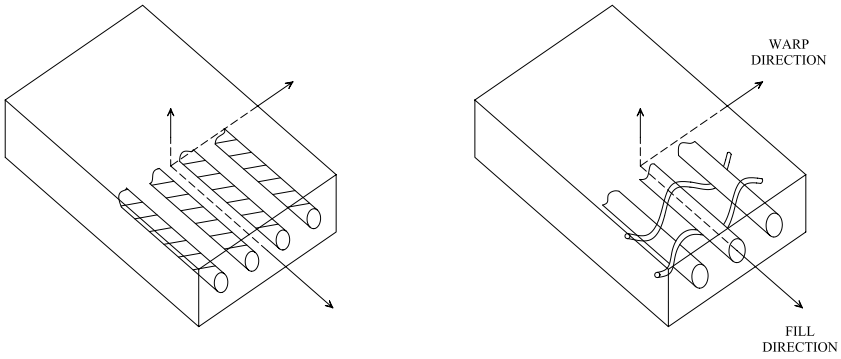

Figure 3.4: Unidirectional lamina and lamina with woven fibers.

material are built up with the fiber directions of each layer typically oriented in different directions to give different strengths and stiffnesses in the various directions. Before going inside the macromechanical behaviour of a lamina, we need to introduce some characteristics of composite materials that are different from more common engineering materials which are usually:

- *homogeneous body*: the properties are not a function of position in the body;
- *isotropic body*: the properties are not a function of orientation at a point in the body.

In contrast, composite materials are often:

- *inhomogeneous* or *heterogeneous body*: the properties are a function of position in the body;
- *orthotropic body*: the material properties are different in three mutually perpendicular directions at a point in the body. There are three mutually perpendicular planes of material symmetry;
- *anisotropic body*: the material properties are different in all directions at a point in the body. There are no planes of material property symmetry.

Usually, because of the heterogeneous nature of composite materials, they are studied from two points of view: micromechanics and macromechanics:

- *micromechanics* is the study of composite material behaviour wherein the interaction of the constituent materials is examined on a microscopic scale;

- *macromechanics* is the study of composite material behaviour wherein the material is presumed homogeneous and the effects of the constituent materials are detected only as averaged apparent properties of the composite.

In the remainder, we will focus on the macromechanical behaviour of a lamina. If we consider a general anisotropic material, the state of stress at a point in a general continuum can be represented by nine stress components σ_{ij}, $(i,j=1,2,3)$. Similarly, the state of deformation is represented by nine strain components ε_{ij}, $(i,j=1,2,3)$. The generalized Hooke's law relating stresses to strains can be written as:

$$\begin{Bmatrix} \sigma_{11} \\ \sigma_{22} \\ \sigma_{33} \\ \sigma_{23} \\ \sigma_{31} \\ \sigma_{12} \\ \sigma_{32} \\ \sigma_{13} \\ \sigma_{21} \end{Bmatrix} = \begin{bmatrix} C_{1111} & C_{1122} & C_{1133} & C_{1123} & C_{1131} & C_{1112} & C_{1132} & C_{1113} & C_{1121} \\ C_{2211} & C_{2222} & C_{2233} & C_{2223} & C_{2231} & C_{2212} & C_{2232} & C_{2213} & C_{2221} \\ C_{3311} & C_{3322} & C_{3333} & C_{3323} & C_{3331} & C_{3312} & C_{3332} & C_{3313} & C_{3321} \\ C_{2311} & C_{2322} & C_{2333} & C_{2323} & C_{2331} & C_{2312} & C_{2332} & C_{2313} & C_{2321} \\ C_{3111} & C_{3122} & C_{3133} & C_{3123} & C_{3131} & C_{3112} & C_{3132} & C_{3113} & C_{3121} \\ C_{1211} & C_{1222} & C_{1233} & C_{1223} & C_{1231} & C_{1212} & C_{1232} & C_{1213} & C_{1221} \\ C_{3211} & C_{3222} & C_{3233} & C_{3223} & C_{3231} & C_{3212} & C_{3232} & C_{3213} & C_{3221} \\ C_{1311} & C_{1322} & C_{1333} & C_{1323} & C_{1331} & C_{1312} & C_{1332} & C_{1313} & C_{1321} \\ C_{2111} & C_{2122} & C_{2133} & C_{2123} & C_{2131} & C_{2112} & C_{2132} & C_{2113} & C_{2121} \end{bmatrix} \begin{Bmatrix} \varepsilon_{11} \\ \varepsilon_{22} \\ \varepsilon_{33} \\ \varepsilon_{23} \\ \varepsilon_{31} \\ \varepsilon_{12} \\ \varepsilon_{32} \\ \varepsilon_{13} \\ \varepsilon_{21} \end{Bmatrix} \tag{3.1}$$

or in indicial[4] and tensorial notation:

$$\sigma_{ij} = C_{ijkl}\varepsilon_{kl} \qquad i,j,k,l = 1,2,3 \tag{3.2}$$

$$\boldsymbol{\sigma} = \mathbf{C} : \boldsymbol{\varepsilon}, \tag{3.3}$$

where $\mathbf{C}$ is the material stiffness matrix of components C_{ijkl} and ": " is the double product or double contraction of two tensors. It is customary in mechanics of composites to use a contracted notation for the stress, strain and material stiffness tensors as shown in Table 3.1 (Jones 1975; Hull 1981). In general, moving from Equation (3.1), it requires 81 elastic constants to characterize a material fully. However, the symmetry of the stress and strain tensors ($\sigma_{ij} = \sigma_{ji}$ and $\varepsilon_{ij} = \varepsilon_{ji}$) reduces the number of indipendent elastic constant to 36. So, we can rewrite Equation (3.1) as follows:

$$\begin{Bmatrix} \sigma_1 \\ \sigma_2 \\ \sigma_3 \\ \tau_{23} \\ \tau_{31} \\ \tau_{12} \end{Bmatrix} = \begin{bmatrix} C_{11} & C_{12} & C_{13} & C_{14} & C_{15} & C_{16} \\ C_{21} & C_{22} & C_{23} & C_{24} & C_{25} & C_{26} \\ C_{31} & C_{32} & C_{33} & C_{34} & C_{35} & C_{36} \\ C_{41} & C_{42} & C_{43} & C_{44} & C_{45} & C_{46} \\ C_{51} & C_{52} & C_{53} & C_{54} & C_{55} & C_{56} \\ C_{61} & C_{62} & C_{63} & C_{64} & C_{65} & C_{66} \end{bmatrix} \begin{Bmatrix} \varepsilon_1 \\ \varepsilon_2 \\ \varepsilon_3 \\ \gamma_{23} \\ \gamma_{31} \\ \gamma_{12} \end{Bmatrix} \tag{3.4}$$

[4] Obviously, repeated index or dummy index implies summation for all values of that subscript.

[5] Note that γ_{ij} $(i \neq j)$ represents engineering shear strain whereas ε_{ij} $(i \neq j)$ represents tensor shear strain (infinitesimal strains).

Stresses		**Strains**	
Tensor notation	Contracted notation	Tensor notation	Contracted notation
σ_{11}	σ_1	ε_{11}	ε_1
σ_{22}	σ_2	ε_{22}	ε_2
σ_{33}	σ_3	ε_{33}	ε_3
$\tau_{23} = \sigma_{23}$	σ_4	$\gamma_{23} = 2\varepsilon_{23}$[5]	ε_4
$\tau_{31} = \sigma_{31}$	σ_5	$\gamma_{31} = 2\varepsilon_{31}$	ε_5
$\tau_{12} = \sigma_{12}$	σ_6	$\gamma_{12} = 2\varepsilon_{12}$	ε_6

Table 3.1: Tensor and contracted notation for stresses and strains.

or in indicial form:

$$\sigma_i = C_{ij}\varepsilon_j \qquad i,j = 1,\ldots,6. \tag{3.5}$$

The stiffness matrix $\mathbf{C}$ in Equation (3.4), has 36 constants. However, less than 36 of the constants are needed for elastic materials because strain energy considerations require additional symmetries. Elastic materials, for which an elastic potential of strain energy density function exists, have incremental work per unit volume of:

$$dW = \sigma_i\, d\varepsilon_i = \boldsymbol{\sigma} : d\boldsymbol{\varepsilon}, \tag{3.6}$$

where $\boldsymbol{\sigma}$ and $\boldsymbol{\varepsilon}$ are work conjugate (Bonet and Wood 1997). Because of the relation (3.5), the incremental work (3.6) becomes:

$$dW = C_{ij}\varepsilon_j\, d\varepsilon_i = \boldsymbol{\varepsilon} : \mathbf{C} : \mathbf{d}\boldsymbol{\varepsilon}, \tag{3.7}$$

and upon integration, the work per unit volume is expressed as:

$$W = \frac{1}{2}C_{ij}\varepsilon_i\varepsilon_j = \frac{1}{2}\boldsymbol{\varepsilon} : \mathbf{C} : \boldsymbol{\varepsilon}. \tag{3.8}$$

Hooke's law, Equation (3.5), can be derived from Equation (3.8):

$$\frac{\partial W}{\partial \varepsilon_i} = C_{ij}\varepsilon_j, \tag{3.9}$$

whereupon:

$$\frac{\partial^2 W}{\partial \varepsilon_i \partial \varepsilon_j} = C_{ij} \quad \text{and} \quad \frac{\partial^2 W}{\partial \varepsilon_j \partial \varepsilon_i} = C_{ji}. \tag{3.10}$$

Because the order of differentiation of W is immaterial, Equations $(3.10)_1$ and $(3.10)_2$, read:

$$C_{ij} = C_{ji} \quad \text{and} \quad \mathbf{C}^{\mathrm{T}} = \mathbf{C}. \tag{3.11}$$

Thus the material stiffness matrix $\mathbf{C}$ is symmetric and just 21 of the constants are indipendent. So, the stress–strain relation (3.4), can be written as:

Triclinic

$$\begin{Bmatrix} \sigma_1 \\ \sigma_2 \\ \sigma_3 \\ \tau_{23} \\ \tau_{31} \\ \tau_{12} \end{Bmatrix} = \begin{bmatrix} C_{11} & C_{12} & C_{13} & C_{14} & C_{15} & C_{16} \\ C_{12} & C_{22} & C_{23} & C_{24} & C_{25} & C_{26} \\ C_{13} & C_{23} & C_{33} & C_{34} & C_{35} & C_{36} \\ C_{14} & C_{24} & C_{34} & C_{44} & C_{45} & C_{46} \\ C_{15} & C_{25} & C_{35} & C_{45} & C_{55} & C_{56} \\ C_{16} & C_{26} & C_{36} & C_{46} & C_{56} & C_{66} \end{bmatrix} \begin{Bmatrix} \varepsilon_1 \\ \varepsilon_2 \\ \varepsilon_3 \\ \gamma_{23} \\ \gamma_{31} \\ \gamma_{12} \end{Bmatrix} \tag{3.12}$$

Equation (3.12) is the most general expression within the framework of linear elasticity and is usually referred to characterize anisotropic or triclinic material. If there is one plane of material property symmetry (i.e. $x_3 = 0$), the Equation (3.12) reduces to:

Monoclinic

$$\begin{Bmatrix} \sigma_1 \\ \sigma_2 \\ \sigma_3 \\ \tau_{23} \\ \tau_{31} \\ \tau_{12} \end{Bmatrix} = \begin{bmatrix} C_{11} & C_{12} & C_{13} & 0 & 0 & C_{16} \\ C_{12} & C_{22} & C_{23} & 0 & 0 & C_{26} \\ C_{13} & C_{23} & C_{33} & 0 & 0 & C_{36} \\ 0 & 0 & 0 & C_{44} & C_{45} & 0 \\ 0 & 0 & 0 & C_{45} & C_{55} & 0 \\ C_{16} & C_{26} & C_{36} & 0 & 0 & C_{66} \end{bmatrix} \begin{Bmatrix} \varepsilon_1 \\ \varepsilon_2 \\ \varepsilon_3 \\ \gamma_{23} \\ \gamma_{31} \\ \gamma_{12} \end{Bmatrix} \tag{3.13}$$

that corresponds to a monoclinic material. In Equation (3.13) there are 13 indipendent elastic constants. In the case of an orthotropic material which has three mutually perpendicular planes of material symmetry, the stress–strain relation in general has the form:

Orthotropic

$$\begin{Bmatrix} \sigma_1 \\ \sigma_2 \\ \sigma_3 \\ \tau_{23} \\ \tau_{31} \\ \tau_{12} \end{Bmatrix} = \begin{bmatrix} C_{11} & C_{12} & C_{13} & 0 & 0 & 0 \\ C_{12} & C_{22} & C_{23} & 0 & 0 & 0 \\ C_{13} & C_{23} & C_{33} & 0 & 0 & 0 \\ 0 & 0 & 0 & C_{44} & 0 & 0 \\ 0 & 0 & 0 & 0 & C_{55} & 0 \\ 0 & 0 & 0 & 0 & 0 & C_{66} \end{bmatrix} \begin{Bmatrix} \varepsilon_1 \\ \varepsilon_2 \\ \varepsilon_3 \\ \gamma_{23} \\ \gamma_{31} \\ \gamma_{12} \end{Bmatrix} \tag{3.14}$$

The number of indipendent elastic constants is reduced to 9. Note that there is no interaction between normal stress σ_1, σ_2, σ_3 and shearing strains γ_{23}, γ_{31} and γ_{12}; similarly there is no interaction between shearing stresses and normal strains. If at every point of a material there is one plane in which the mechanical properties are equal in all directions, then the material is termed transversely isotropic with

5 indipendent constants. If, for example, the $x_1 - x_2$ plane is the special plane of isotropy, then we have:

$$\text{Transversely Isotropic} \quad \begin{Bmatrix} \sigma_1 \\ \sigma_2 \\ \sigma_3 \\ \tau_{23} \\ \tau_{31} \\ \tau_{12} \end{Bmatrix} = \begin{bmatrix} C_{11} & C_{12} & C_{13} & 0 & 0 & 0 \\ C_{12} & C_{11} & C_{13} & 0 & 0 & 0 \\ C_{13} & C_{13} & C_{33} & 0 & 0 & 0 \\ 0 & 0 & 0 & C_{44} & 0 & 0 \\ 0 & 0 & 0 & 0 & C_{44} & 0 \\ 0 & 0 & 0 & 0 & 0 & \frac{(C_{11}-C_{12})}{2} \end{bmatrix} \begin{Bmatrix} \varepsilon_1 \\ \varepsilon_2 \\ \varepsilon_3 \\ \gamma_{23} \\ \gamma_{31} \\ \gamma_{12} \end{Bmatrix} \tag{3.15}$$

If there are an infinite number of planes of material property symmetry, then Equation (3.15) simplifies to the isotropic material case with only 2 indipendent constants:

$$\text{Isotropy} \quad \begin{Bmatrix} \sigma_1 \\ \sigma_2 \\ \sigma_3 \\ \tau_{23} \\ \tau_{31} \\ \tau_{12} \end{Bmatrix} = \begin{bmatrix} C_{11} & C_{12} & C_{12} & 0 & 0 & 0 \\ C_{12} & C_{11} & C_{12} & 0 & 0 & 0 \\ C_{12} & C_{12} & C_{11} & 0 & 0 & 0 \\ 0 & 0 & 0 & \frac{(C_{11}-C_{12})}{2} & 0 & 0 \\ 0 & 0 & 0 & 0 & \frac{(C_{11}-C_{12})}{2} & 0 \\ 0 & 0 & 0 & 0 & 0 & \frac{(C_{11}-C_{12})}{2} \end{bmatrix} \begin{Bmatrix} \varepsilon_1 \\ \varepsilon_2 \\ \varepsilon_3 \\ \gamma_{23} \\ \gamma_{31} \\ \gamma_{12} \end{Bmatrix} \tag{3.16}$$

3.3.1 Classification of structural theories

Whereas in the past, the use of composite materials has been mainly restricted to secondary, noncritical structural components, nowadays, the dramatic increase in the use of composite materials in all types of engineering structures (i.e. aerospace, automotive, underwater structures, medical devices, electronic circuit boards and sports equipment) attests to the fact that there has been a major effort to develop composite material systems, and analyze and design structural components made from composite materials.
The method used so far for the structural analysis of fabrics may be considered as belonging to five groups:

- analytical methods;
- *smeared* approach;
- numerical methods;
- probabilistic approaches;
- homogeneization methods.

Analytical methods: the correct laminar theory (Norman et al. 1996; Whitcomb et al. 1999) consider that the textiles consist of the union of unidirectional layers whose directions respect the typical axes of real material (Naik and Kuchibhotla 2002). Under these conditions, it is possible to apply the *classical lamination theory* (CLT) (Jones 1975, pag.147) and (Mallick 1988, pag.133), which, however, has been corrected with average value of the in/out–of–plane angle of the braid tows (Whitcomb et al. 1999) experimentally determined by using micro–photographs taken on various fabric sections (Norman et al. 1993; Norman et al. 1996).
The *fabric geometry model* (FGM) (Pastore and Gowayed 1994) is widely used to predict composite fabric characteristics. The basic idea behind the FGM is to treat the fibers and matrix as a set of composite rods (yarns) having various spatial orientations. The local stiffness tensor for each of these bars is calculated and rotated in space to fit the global composite axes. Once the whole group of rods has been locally characterized, the composite global stiffness matrix is obtained by superimposing the contributions of single bars that should demonstrate transverse isotropy (see pag. 103) in the plane normal to the fiber axis. Gowayed and Hwang in 1995 adapted this approach to predict the thermal conductivity of textile composites.
The *weighted average model* (WAM) (Kalidindi and Abusafieh 1996) uses a weighted average of the results obtained with the FGM method (Bogdanovich and Deepak 1997). After the groups of bars has been characterized accordingly to the FGM method, the composite stiffness tensor is obtained as a weighted average of the single rod contributions to global stiffness, where the weights used are the volume fractions[6] of every beam (Kalidindi and Franco 1997).

***Smeared* approach:** in such methods, the main emphasis of an analysis is to determine the overall global response of the laminated component, for example, gross deflections, critical buckling loads, fundamental frequencies and associated mode shapes (Hashin 1983). Such global behaviour can often be accurately determined using one of the following approaches (Reddy 1997):

1. *Equivalent single–layer theories* (ESL).
   The simplest ESL laminate theory is the *classical laminated plate theory* (CLPT) which is an extension of the Kirchhoff plate theory to laminated composite plates (Reddy and Robbins 1994).
   The next theory in the hierarchy of ESL laminate theories is the *first order shear deformation theory* (FSDT) which extends the kinematic of the CLPT by including a gross transverse shear deformation in its kinematic assumptions (Reddy 1984a).

[6] Ratio between the volume of fibers and the total volume of composite.

The *third order laminate theory* of Reddy (1984b), (1990) (TSDT or generally HSDT[7]) provides a slight increase in accuracy relative to the FSDT solution, at the expense of a significant increase in computational effort.

2. *Three–dimensional elasticity theory.*
As laminated composite materials undergo the transition from secondary structural components to primary critical structural components, the goals of analysis must be broadened to include a highly accurate assessment of localized regions where damage initiation is likely. The simple ESL laminate theories that often prove adequate for modeling secondary structures, are of limite value in modeling primary structures. Thus the analysis of primary composite structural components may require the use of 3D elasticity theory (Sun et al. 1968; Chao and Reddy 1984; Brank and Carrera 2000) or *layerwise laminate model* (LWM) (Reddy 1989) that contains full 3D kinematics and constitutive relations.

Numerical methods: the numerical methods are mainly of the finite element family (Haan, Charalambides, and Suri 2001). The analysis of braids is usually based on the use of either a simple diagonal brick model or a more complex inhomogeneous finite element model (Hu and Teng 1996). The first most common approach to modeling the macroscopic properties of textile composites has been to create a *representative volume element* (RVE) or a *unit cell* that captured the major features of the underlying microstructure and composition in the material (Masters et al. 1993). Through this method, volumes having different properties (fiber and matrix) are transformed into an element with homogeneous properties by using an analytical method, such as FGM. The solution of the global structure can be obtained through a finite element analysis of the mechanical model based on the previous concept of a simplified unit cell representation of the composite–reinforcing microstructure (Gowayed et al. 1996; Gowayed 1997). Gowayed, Hwang, and Chapman in 1995 constructed an extended model of the previous method able to predict the thermal conductivity of textile composite materials under steady state heat transfer conditions. One concern about unit cell modelling is that the unit cell does not correctly characterize the general textile reinforced material, which may not have true repeating volume.
The second approach (Bogdanovich 1993) divides the structure into *meso–volumes* (Masters, Foye, Pastore, and Gowayed 1993; Bogdanovich and Pastore 1996), and each one of these volumes (unit cell) contains several single

[7]High Order Shear Deformation Theory

cells (subcell[8]), the material properties of which are calculated through the FGM method (Pastore et al. 1993). This *hierarchical* method gives a more general tool for the analysis of structures than the previous approach with single unit cells. Here, *hierarchical* means that:

1. for the case when only displacements are of interest, the analysis of a fully homogenized textile structure may be adopted. Thus, the whole structure can be identified as a single meso–volume (Masters, Foye, Pastore, and Gowayed 1993);
2. if information on all six stress components in the structural part is needed, the internal interfaces gain importance and, correspondingly, the next hierarchical level has to be considered. At this level, the whole structure can be treated as an assemblage of several distinct, anisotropic structurally homogeneous small meso–volumes (Bogdanovich 1993);
3. in the case when local failure effects are of interest, one has to start at the next hierarchical level, namely, the level of a single yarn surrounded by matrix material. The same concept of a meso–volume can be applied to this analysis supposing that a structurally homogeneous yarn element and matrix element represent two distinct types of meso–volumes (Bogdanovich and Pastore 1996).

A new approach, in contrast with the usual choices, previously defined, of either adding more elements to account for microstructure or using averaged material properties within each element, has been introduced in 1994 by Whitcomb et al. These new elements, called *macro–elements* (Whitcomb and Woo 1994), are based on the use of finite element, the formulation of which implicitly takes the composite micro–geometry and, therefore, fiber and matrix mechanical properties, into account (Woo and Whitcomb 1994). This method gives good results in the prediction of fabric global movements and deformation, whereas it is not effective in calculating deformations and tensions inside the elements.
Global/local methodology or *multiple model methods* (Reddy 1997), combined with special macro–elements is proposed in (Woo and Whitcomb 1994; Whitcomb et al. 1995) as a practical alternative to conventional finite element analysis of textile composite structures. Global/local finite element analysis is often used to study the stress distribution in a small portion of structures in great detail (Jara-Almonte and Knight 1988; Whitcomb 1991; Fish and Markolefas 1992). It makes a distinction between three microstructural scales (Chapman and Whitcomb 1995):

[8] One unit cell divided into nine subcells, three elements per side (Bogdanovich 1993)

1. the basic repeating microstructural element labeled *coarse microstructure*. At this level, the very distinctive phases of textile composites are observed;
2. a second level where a very large number of unit cells are considered and the characteristic dimensions are of the order of the structural elements, is called *fine microstructure*;
3. between these two levels lies another level of microstructure, called, the *transitional level*.

In analyzing a textile composite structure by the global/local method, a relatively crude global mesh with homogenized material properties can be used at the fine microstructural level (Whitcomb et al. 1995). In the local meshes, the details of the coarse microstructure of textile composites (i.e. individual tows and matrix pockets) are modelled discretely (Woo and Whitcomb 1996). However, in the transitional range of microstructure, discrete modelling is not practical (i.e. cpu requirements) and special finite element are needed which account for microstructure within a single element (Whitcomb and Srirengan 1996; Whitcomb et al. 1999; D'Amato 2001).
The last FEM approach is called *semi–microscopic approach* (Fujita et al. 1992). It adopts discretization of fibers with beam (Fujita et al. 1993) or truss (Sidhu et al. 2001) elements, which correspond to the real geometry of tows, and simulation of the typical cohesive effect of matrix with other beam elements are adequately arranged (Fujita et al. 1993) or, more precisely, using shell elements (Sidhu et al. 2001). This kind of approach is used to analyze the evolution of cracks inside the material and calculate the ultimate strength.

Probabilistic approaches: in the implementation of all the above finite element methods, it is difficult to throughly describe the mechanical and geometrical characteristic. In fabrics manufacturing, there are several factors that impose a probabilistic approach (Yushanov and Bogdanovich 1998a) in the definition of the typical parameters of the model (Yushanov and Bogdanovich 1998b).

Homogeneization methods: we can consider a composite as a structure assembled from a very large number of fragments of given materials mixed in a prescribed way (Carvelli and Poggi 2001). Each fragment is assumed to be much smaller than the rate of varying of acting fields and than the size of a considered domain. At the same time, these domains are large enough to assume that the governing equations are valid in each fragment of material, which means that fragments are much larger than molecular size. It is hopelessly difficult and often useless to describe fields at each point of the composite. For most purpose we do not need to know all the details.

Instead, we simplify the problem by introducing an averaged description of a composite. The procedure that replaces the original problem by a simpler averaged problem is called *homogenization.*
The physical ideas of homogenization, averaging heterogeneous media in order to derive effective properties, have a very long history going back at least to Poisson (1822), Maxwell (1881) and Rayleigh (1892). There is a huge literature in physics and mechanics concerning averaging and effective properties (Jones 1975; Hull 1981; Mallick 1988; Daniel and Ishai 1994; Gürdal, Haftka, and Hajela 1999). However, the mathematical theory of homogenization is much younger and it is interesting to note that it started in at least three main direction.
The first direction, the oldest one, is concerned with a general theory for the convergence of operators (namely H–convergence or G–convergence). The first contributions are probabily those of Spagnolo (1968), DeGiorgi and Spagnolo (1973), Murat and Tartar (1985) and Tartar (1986).
The second direction is the asymptotic study of perforated domains containing many small holes (Rauch and Taylor 1975).
The third direction is a systematic study of periodic structures by means of an asymptotic analysis: we call such problems *periodic homogenization problems.* Pioneering works in this direction have been done by Babuska (1974), Bakhvalov and Panasenko (1990) and Bensoussan, Lions, and Papanicolaou (1978).
Eventually, let us mention that there is also a stochastic theory of homogenization (Kozlov 1980; DalMaso and Modica 1986) and a variational theory of homogenization: the Γ–convergence of DeGiorgi (DeGiorgi 1975; DeGiorgi 1983).

After having introduced all the possible analytical and numerical methods classically used for the structural analysis of fabrics, it is important to say that our model (presented in Section 3.6.3 using the finite elements introduced in Sections 5.2 and 5.3), is completely different from the previous ones.
To resume: we are going to consider the macromechanical behaviour of a fiber–reinforced composite laminates (the sails!) using a new membrane element (Section 5.2 and (Gobetti and Nascimbene 2002)) to model the material matrix, in conjunction with a new fiber–element (Section 5.3 and (Gobetti and Nascimbene 2001)) to model the yarns distribution. Using this approach we are able to work at the level of a single yarn surrounded by matrix material with a very moderate CPU requirements. This last condition is absolutely important from an optimization point of view, that is the scope of the next sections: to introduce an algorithm able to obtain the best possible yarn distribution in order to minimize the total volume of the fibers with some displacement constraints (mast and boom).

3.4 Topology optimization and something more ... a review!

Two scientists established not only the classical theory of elasticity, but they also laid the foundation for the increasingly important field of structural optimization. The first concepts of seeking the optimal shapes of structural elements are contained in the book of Galileo Galilei (1564–1642), *Discorsi*. He was the first to perform systematic investigations into the fracture process of brittle bodies. In this context, he described the influence of the shape of a body (hollow bodies, bones, blades of glass) on its strength.
On the other hand, Robert Hooke (1653–1703) formulated the fundamental law of linear theory of elasticity: strain (change of length) and stress (load) are proportional to each other. Based on these considerations one could assume the theory of elasticity and to a wider extent, continuum mechanics, to be a field of sciences whose problems might be considered as being solved to a large extent. This, however, would be a fundamental error!!
The previous years have witnessed increasing challenges in terms of the design of ever more complex mechanical systems and components as well as of extremely lightweigth (sails!) constructions, a fact that has led, among others, to the development of advanced materials and hence to the demand for increasingly precise calculation methods. The substantial and still undiminished importance of structural mechanics is due to the fact that questions toward finding an optimal design in terms of load bearing capacity, reliability, accuracy and costs, have to be answered already in an early stage of the design process. In this respect, a new area in the scope of computer aided engineering has emerged, namely the optimization of structures, commonly called *Structural Optimization*. It offers to the engineers a tool which, by means of mathematical algorithms, allows to determine better, possibly optimal, designs in terms of admissible structural responses (deformations, stresses, eigenfrequencies), manufacturing and the interaction of all structural components.
The foundations of structural optimization, date back to one of the last universal scholars of modern times, Gottfried Wilhelm Leibniz (1646–1716), whose works in the fields of mathematics and natural sciences can be seen as the basis of any analytical procedure and highlight the tremendous importance of coherent scientific thinking. He laid the foundation of differential calculus; without these achievements, modern optimization calculations would not be possible to a larger extent. In this respect, it is of utmost importance to mention Leonard Euler (1707–1783) who achieved a lot of results in the theory of extremals which provide the basis for the development of the calculus of variations. With this method, Jakob Bernoulli (1655–1705) determined the curve of the shortest falling time (*brachistochrone*) and Sir Isaac Newton (1643–1727) the body of revolution with the smallest resis-

tance. By formulation the *Principle of the smallest effect*, and by developing an integral principle, Lagrange (1736–1813) and Hamilton (1805–1865) contributed toward the completion of variational calculus as one of the fundamentals for several types of optimization problems.
On the bases of the previous works, in recent years, substantial efforts have been made in the development of *topology optimization* procedures, and there are several different strategies whose use is in most cases highly problem dependent (Eschenauer and Olhoff 2001). Topology optimization is often referred to as *layout optimization* or *generalized shape optimization* in the literature (Kirsch 1990; Bendsøe, Diaz, and Kikuchi 1993; Rozvany, Bendsøe, and Kirsch 1995). The importance of this type of optimization lies in the fact that the choice of the appropriate topology of a structure in the conceptual phase is generally the most decisive factor for the efficiency of a novel product.
Two types of topology optimization exist, discrete or continuous, depending on the type of a structure. For inherently *discrete* structures, the optimum topology or layout design problem consists in determining the optimum number, positions, and mutual connectivity of the structural members (Topping and Papadrakis 1994). The following sections are dedicated to introduce our method in the field of topology optimization of *continuum* structures, due to the fact that *a sail* is a continuous membrane. Furthermore, after having defined in Section 1.3.2.3 and Figure 1.22 the *based–aero/hydrodynamic* optimal shape, in the next sections we are going to achieve the optimum in terms of thickness and yarn distributions. Very roughly, one can distinguish two classes of topology continuum design processes:

the material or microstructure technique: the goal is to find that structural topology which renders a given design objective an optimum value subject to a prescribed amount of structural material (Olhoff, Lurie, Cherkaev, and Fedorov 1981; Kohn and Strang 1986). The optimization consists in determining whether each element in the continuum should contain material or not;

the geometrical or macrostructure technique: in this class, continuous materials are considered as opposed to porous, microstructured ones, and as the topology optimization is performed in conjunction with a shape optimization, the finite element mesh cannot be a fixed one, but must change with the changes of the boundaries of the design. In each iteration, the thickness, the yarn layouts and the sail shape's of the continuous body are simultaneously subjected to a optimization procedure.

It is object of this chapter to present our *continuum macrostructure topology* optimization applied to the design of a mainsail that will be computationally analysed in Sections 3.6.3 (from an optimization point of view) and in Section 6.1 (from a structural point of view).

3.5 Optimization of sail properties: thickness and yarn layout

In spite of the growing importance of textile composite materials (Tan, Tong, and Steven 1997; Lomov, Huysmans, Luo, Parnas, Prodromou, Verpoest, and Phelan 2001), there is no systematic tool that can help to optimize its design while satisfying a set of target properties. The designer of a textile composite material seeks to identify the best fiber and matrix thickness, the most appropriate fiber preform structure and different yarn volume fractions (McIlhagger, Hill, Brown, and Limmer 1995). Optimum design of textile composites, or even its estimation thereof, is important for the following reasons:

1. to reduce expenses envolved in trial and error procedures;
2. to open grounds for possible new fabric designs able to deliver a set of unique target properties;
3. to obtain the best performance of a material in an application;
4. to identify a cost–effective design.

Previous efforts to optimize the properties fiber–textile composite materials have been restricted to laminated composites (Gürdal, Haftka, and Hajela 1999), using different algorithmic treatments:

- after the pioneering works of Schmit and Farshi (1977), Banichuk (1981) and Kartevelishvili and Kobelev (1984), mention should also be made of the more recent results obtained by Ding (1987), Vanderplaats and Weisshaar (1989), Fukunaga and Vanderplaats (1991), Rovati, Taliercio, and Cinquini (1991) and Vaidyanathan and Gowayed (1996). These results have been also extended to the three–dimensional elastic case by Rovati and Taliercio (1990) and to the plastic case by SacchiLandriani and Rovati (1989).

- Watkins and Morris (1987), Borri and Speranzini (1993) and Kere and Koski (2001) proposed a *multilevel* structural optimization scheme to identify the optimum layer/yarn thickness and ply angles to minimize the overall weight of the laminate.

- some authors, Nagendra, Haftka, and Gürdal (1993) and Muc and Gurba (2001), demonstrated the application of genetic algorithm to the design of composite structures.

- some papers presented the simulated annealing method (Correia, Gomes, Suleman, Soares, and Soares 2000; Correia, Soares, and Soares 2001) and the

evolutionary technique (Steven, Li, and Xie 2000) for structural topology as an alternative to the classical gradient–based procedure.

Aim of our formulation is to integrate the FEM computational code (Chapter 5) with Mathematical Programming methods (MP) (Sections 3.5.1–3.5.4). In this approach FEM is used as an analysis tool to evaluate structural responses (i.e., displacements and stresses) and their sensitivities with respect to design variables under the given loading conditions; MP is an iterative optimization algorithm aimed to find improved feasible designs with the knowledge of structural responses and sensitivity information. Due to the implicit relationship between structural responses and design variables, the strategy herein called Sequential Convex Programming (SCP) is used to replace approximately the original problem by solving a sequence of explicit and convex *sub–problems*.

3.5.1 Mathematical background: the mixed variables method

Two notions are used to characterize the following formulation in the step of constructing explicit sub–problems: *convexity* and *conservativeness*.
Let us consider a continous and differentiable function $g(\mathbf{X})$, with $g\colon \mathbb{R}^n \to \mathbb{R}$, and a design point $\mathbf{X}^k \in \mathbb{R}^n$. The approximation process of *direct linearization* of $g(\mathbf{X})$ at $\mathbf{X}^k$, denoted by $\tilde{g}_D\left(\mathbf{X};\mathbf{X}^k\right)$, consists of replacing it with the first–order Taylor series expansion (Fleury and Braibant 1986; Nguyen, Strodiot, and Fleury 1987):

$$\tilde{g}_D\left(\mathbf{X};\mathbf{X}^k\right) = g\left(\mathbf{X}^k\right) + \sum_{i=1}^{n} \left.\frac{\partial g}{\partial x_i}\right|_{\mathbf{X}^k} \left(x_i - x_i^k\right), \tag{3.17}$$

where x_i are the design variables (direct variables), and $\mathbf{X}^k$ is, as said before, the current design point in a step k of an optimization problem. By this technique the function $g(\mathbf{X})$ is approximated as a linear function of the direct design variables x_i. In structural optimization another form of approximation that is often used is a linear function of the reciprocals of the design variables $1/x_i$, which can be named *reciprocal linearization*:

$$\tilde{g}_R\left(\mathbf{X};\mathbf{X}^k\right) = g\left(\mathbf{X}^k\right) + \sum_{i=1}^{n} \left.\frac{\partial g}{\partial x_i}\right|_{\mathbf{X}^k} \frac{x_i^k}{x_i}\left(x_i - x_i^k\right). \tag{3.18}$$

Let us now assume that, for the linearization purpose, the variables are arbitrarily split into two groups:

- Group (A), which contains the original direct design variables x_i;
- Group (B), which is concerned with intermediate reciprocal variables $1/x_i$.

Performing then a first–order Taylor series expansion of the function $g(\mathbf{X})$, the following *mixed linearization* is obtained:

$$\tilde{g}_M\left(\mathbf{X};\mathbf{X}^k\right) = g\left(\mathbf{X}^k\right) + \sum_{(A)} \left.\frac{\partial g}{\partial x_i}\right|_{\mathbf{X}^k} \left(x_i - x_i^k\right) + \sum_{(B)} \left.\frac{\partial g}{\partial x_i}\right|_{\mathbf{X}^k} \frac{x_i^k}{x_i}\left(x_i - x_i^k\right), \quad (3.19)$$

where $\sum_{(A)}$ and $\sum_{(B)}$ mean "summation over the variables belonging to group (A) and (B) respectively". It is important to recognize that reciprocal linearization represented in Equation (3.18) yields a convex approximation only if all the first derivatives $\left(\partial g/\partial x_i\right)\big|_{\mathbf{X}^k}$ are non–negative. This feature cannot be controlled: it is an entry in the linearization process. On the other hand, mixed linearization is always capable of generating a convex approximation provided that group (A) and (B) are appropriately chosen. Hence the idea of *convex linearization*, which is achieved when group (A) is selected as containing the variables for which $\left(\partial g/\partial x_i\right)\big|_{\mathbf{X}^k}$ is positive, and group (B) contains the remaining variables:

$$\tilde{g}_C\left(\mathbf{X};\mathbf{X}^k\right) = g\left(\mathbf{X}^k\right) + \sum_{i\in I_k^+(g)} \left.\frac{\partial g}{\partial x_i}\right|_{\mathbf{X}^k} \left(x_i - x_i^k\right) + \sum_{i\in I_k^-(g)} \left.\frac{\partial g}{\partial x_i}\right|_{\mathbf{X}^k} \frac{x_i^k}{x_i}\left(x_i - x_i^k\right), \quad (3.20)$$

where:

$$\begin{aligned} I_k^+ &= \left\{ i \in \{1,\ldots,n\} \text{ s.t. } \left.\frac{\partial g}{\partial x_i}\right|_{\mathbf{X}^k} > 0 \right\}, \\ I_k^- &= \left\{ i \in \{1,\ldots,n\} \text{ s.t. } \left.\frac{\partial g}{\partial x_i}\right|_{\mathbf{X}^k} < 0 \right\}. \end{aligned} \quad (3.21)$$

Note that this apparently *tricky* linearization scheme takes advantage of the trivial fact that:

$$\frac{\partial g}{\partial\left(\dfrac{1}{x_i}\right)} = -x_i^2 \frac{\partial g}{\partial x_i}. \quad (3.22)$$

Remember that a function is said to be convex when its *Hessian matrix* $\mathbf{H}$ defined by second order derivatives is positive definite. Generally, the convexity can be regarded as a curvature measure. Zhang and Fleury suggested to quantify the convexity of a function by averaging arithmetically the diagonal terms of second order derivatives. For optimization problems without equality constraints, the convexity means that the Hessian matrices of the objective function and constraints are all positive definite. Theoretically, this pleasant property ensures the uniqueness of the optimum solution of the considered problem.

An attractive property of convex linearization is that it also yields the most conservative approximation among all the possible combinations of direct/reciprocal variables (i.e. selection of group (A) and group (B)). Conservativeness is a relative measure concerned with inequality constraints. Given two approximate constraint functions $g_1(\mathbf{X}) \leqslant 0$ and $g_2(\mathbf{X}) \leqslant 0$ which might be differently constructed from the original $g(\mathbf{X}) \leqslant 0$. The latter is said to be more conservative that the former if the relation $g_1(\mathbf{X}) \leqslant g_2(\mathbf{X})$ is held. As illustrated in Figure 3.5, the design space formed by $g_1(\mathbf{X}) \leqslant 0$ is a reduced one of that by $g(\mathbf{X}) \leqslant 0$ and any feasible design with respect to $g_1(\mathbf{X}) \leqslant 0$ is absolutely feasible with respect to $g(\mathbf{X}) \leqslant 0$. This remarkable property is easy to prove by substracting Equation (3.19) from

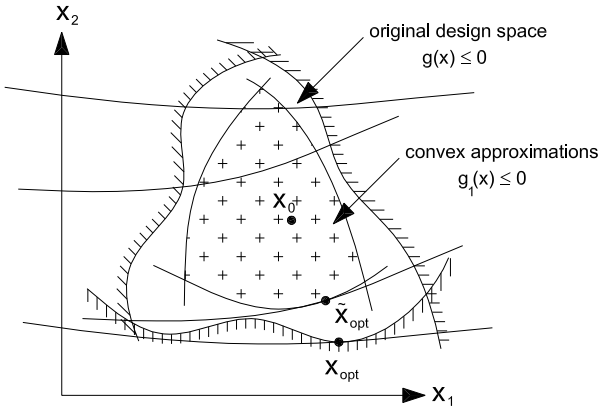

Figure 3.5: Approximation concepts.

Equation (3.20) to get:

$$\tilde{g}_C\left(\mathbf{X};\mathbf{X}^k\right) - \tilde{g}_M\left(\mathbf{X};\mathbf{X}^k\right) = \sum_{(B)i\in I_k^+(g)} \left.\frac{\partial g}{\partial x_i}\right|_{\mathbf{X}^k} \frac{1}{x_i}\left(x_i - x_i^k\right)^2 - \sum_{(A)i\in I_k^-(g)} \left.\frac{\partial g}{\partial x_i}\right|_{\mathbf{X}^k} \frac{1}{x_i}\left(x_i - x_i^k\right)^2. \quad (3.23)$$

By requiring that the x_i's are non–negative variables, a simple translation can do it, the first summation in Equation (3.23) will contain only positive terms from group (B), and the second, negative terms from group (A). Therefore it can be concluded that $\tilde{g}_C(\mathbf{X};\mathbf{X}^k)$ is always greater than $\tilde{g}_M(\mathbf{X};\mathbf{X}^k)$. In other words, *convex linearization is the most conservative approximation of any mixed linearization*, including the two extreme cases: direct linearization (Equation (3.17)) and reciprocal linearization (Equation (3.18)).
Finally, it should be pointed out that when the comparison is made between convex approximations, the convexity and the conservativeness will have equivalent

effects. The more convex the constraint function, the more conservative it is.
In summary then, when one wants a function $g(\mathbf{X})$ to be approximated in a conservative way by using mixed direct/reciprocal variables, the *only* possible scheme is to employ convex linearization. The word "only" is important, because it is the basis for the generality of the method proposed in the sequel. Indeed, this method intrinsecally contains a rational scheme to select by itself the mixed variables.

3.5.2 Solution procedure: the convex linearization method

Considering a general mathematical programming problem, (Fleury and Braibant 1986; Nguyen, Strodiot, and Fleury 1987; Kuritz and Fleury 1989):

$$\begin{array}{lll} \text{minimize} & f(\mathbf{X}) & \mathbf{X} = \{x_1, x_2, \ldots, x_n\} \\ \text{subject to} & h_j(\mathbf{X}) \geqslant 0 & j = 1, \ldots, m \\ & \overline{x}_i \geqslant x_i \geqslant \underline{x}_i & i = 1, \ldots, n \end{array} \tag{3.24}$$

the approach herein presented, proceeds by transforming the previously defined problem into a sequence of *linearized sub–problems* having a simple explicit algebraic structure. Because the method employs the convex linearization scheme described in Section 3.5.1, it is very general and easy to use: the algorithm inherently chooses itself the intermediate linearization variables. Therefore, the only input data are the initial values of the objective and constraint functions:

$$f^k = f\left(\mathbf{X}^k\right) \quad \text{and} \quad h_j^k = h_j\left(\mathbf{X}^k\right), \tag{3.25}$$

as well as their first derivatives with respect to the design variables x_i[9]:

$$f_i = \left.\frac{\partial f}{\partial x_i}\right|_{\mathbf{X}^k} \quad \text{and} \quad h_{ij} = \left.\frac{\partial h_j}{\partial x_i}\right|_{\mathbf{X}^k}, \tag{3.26}$$

where $\mathbf{X}^k$ denotes the current point, i.e. the design point where the problem is linearized. Conventional linearization methods also benefit from this attractive properties of generality and simplicity, and it is probably the reason why they have met with considerable success in engineering design. However, because such a technique replaces the primary problem with a sequence of linear programming problems, it suffers from severe limitations. It does not converge to a local minimum unless the latter occurs at a vertex of the feasible domain. Otherwise, the optimization process either converges to a non–optimal vertex or it oscillates indefinitely between two or more vertices. One way of avoiding this undesirable behaviour is to add artificial side constraints (called *move limits* (Svanberg 1987)) to the linear subproblem statement. This move limits must then be gradually

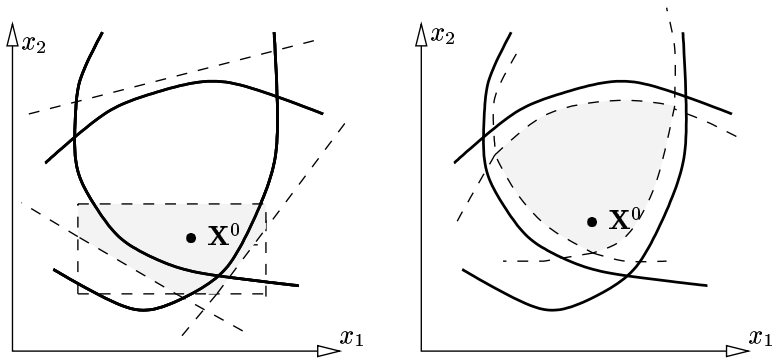

Figure 3.6: Conventional vs. convex linearization method.

tightened at each stage of the process by using some properly chosen update formula (see Figure 3.6). Because it introduces some convex curvature in the approximate functions, the approach proposed herein does not require any control parameters such as move limits. The key idea of the method is to perform the linearization process with respect to mixed variables, either direct (x_i) or reciprocal ($1/x_i$), independently for each function involved in the problem, so that a convex and separable subproblem is generated. Separability is automatically obtained because first–order Taylor series expansions are employed, while convexity is achieved by using *ad hoc* criteria to select the mixed linearization variables (see Equation (3.20)):

- objective function $f(\mathbf{X})$:

$$\begin{aligned} \text{direct variables} \quad & x_i \text{ if } \quad f_i > 0, \\ \text{reciprocal variables} \quad & \frac{1}{x_i} \text{ if } \quad f_i < 0, \end{aligned} \tag{3.27}$$

- constraint functions $h_j(\mathbf{X})$:

$$\begin{aligned} \text{direct variables} \quad & x_i \text{ if } \quad h_{ij} < 0, \\ \text{reciprocal variables} \quad & \frac{1}{x_i} \text{ if } \quad h_{ij} > 0. \end{aligned} \tag{3.28}$$

In this way, considering for example the objective function $f(\mathbf{X})$, employing the graphic notation introduced by the Equations (3.25) and (3.26), and considering

[9] The so called *sensitivity derivatives*.

relation (3.27), its own approximation given by the convex linearization scheme defined by Equation (3.20) comes out from the expressions:

$$f\left(\mathbf{X};\mathbf{X}^k\right) = f\left(\mathbf{X}^k\right) + \sum_{i\in I_k^+(f)} f_i\left(x_i - x_i^k\right) + \sum_{i\in I_k^-(f)} f_i\frac{x_i^k}{x_i}\left(x_i - x_i^k\right). \qquad (3.29)$$

It is convenient to normalize the design variables x_i so that they become equal to unity at the current point $\mathbf{X}^k$ where the problem is linearized in the form:

$$x_i^{\text{norm}} = \frac{x_i}{x_i^k} \quad \Longrightarrow \quad f_i^{\text{norm}} = f_i x_i^k, \qquad (3.30)$$

consequently, the Equation (3.29) becomes easier, (Fleury 1989):

$$f\left(\mathbf{X}^{\text{norm}};\mathbf{X}^k\right) = f\left(\mathbf{X}^k\right) + \sum_{i\in I_k^+(f)} f_i^{\text{norm}}\left(x_i^{\text{norm}} - 1\right) + \\ + \sum_{i\in I_k^-(f)} f_i^{\text{norm}}\left(1 - \frac{1}{x_i^{\text{norm}}}\right). \qquad (3.31)$$

Adopting these simple rules, applying the same linearization techniques also to each constraint function $h_j(\mathbf{X})$ as done before for the objective function $f(\mathbf{X})$, and dropping the superscript $^{\text{norm}}$ for the normalized variables, the following *convex* and *separable* subproblem is generated (Fleury and Braibant 1986; Nguyen, Strodiot, and Fleury 1987; Fleury 1989):

$$\begin{aligned} \min \quad & \sum_{i\in I_k^+(f)} f_i x_i - \sum_{i\in I_k^-(f)} \frac{f_i}{x_i} \\ \text{subject to} \quad & \sum_{i\in I_k^+(h_j)} \frac{h_{ij}}{x_i} - \sum_{i\in I_k^-(h_j)} h_{ij}x_i \leqslant \overline{h}_j \qquad j = 1,\ldots,m \\ & \underline{x}_i \leqslant x_i \leqslant \overline{x}_i \qquad\qquad\qquad\qquad i = 1,\ldots,n \end{aligned} \qquad (3.32)$$

where the constraints $\overline{h}_j$ contain the zero order contributions in the Taylor series expansion in the form:

$$\overline{h}_j = h_j^k + \sum_{i\in I_k^+(h_j)} h_{ij} - \sum_{i\in I_k^-(h_j)} h_{ij}. \qquad (3.33)$$

It is important to notice that, even if the main variables in the primary problem statement had been chosen as the reciprocal variables, nothing would be changed in the explicit subproblem statement.

It should be now pointed out that iteratively solving subproblem of Equation (3.32) is easier than solving problem of Equation (3.24). Therefore, it is natural to consider solving this last problem by a sequence of convex separable subproblems since the technology for solving subproblems is so advanced. One efficient way to solve the explicit subproblem is by *Lagrangian dual techniques* of mathematical programming (Fletcher 1987, pag.236) because of its properties of convexity and separability (see Section 3.5.3). After these preliminaries the final version of the convex linearization method can be stated as follows:

Complete algorithm:

STEP 1 : choose a starting point $\mathbf{X}^0$ for the original subproblem defined by Equation (3.24). Let $k = 0$;

STEP 2 : solve the explicit convex separable subproblem of Equation (3.32) for the approximated solution $\tilde{\mathbf{X}}$;

STEP 3 : let $k = k + 1$, and let $\mathbf{X}^k = \tilde{\mathbf{X}}$;

STEP 4 : if the stopping criterion is satisfied, then stop with $\mathbf{X}^k$. Otherwise, go to STEP 2.

In the next Sections the techniques for solving **STEP 2** will be presented following the work done Fleury and Braibant in (1986).
As shown in Section 3.5.1, the first–order explicit approximations of the objective functions (Equation (3.32)) and of the constraint functions (Equation (3.33)), because they result from convex linearization, are locally conservative. This means that they tend to overestimate the values of the true functions. In other words, the *linearized* feasible domain corresponding to the explicit subproblem of Equation (3.32) is generally inside the true feasible domain corresponding to the primary problem of Equation (3.24). This property is illustrated in Figure 3.6. As a result, the convex linearization method has a tendency to generate a sequence of design points that *funnel down the middle* of the feasible region. The primal philosophy, consisting in using a sequence of steadily improved feasible designs, is maintained. This represents an attractive feature from an engineering point of view, since the designer may stop the optimization process at any stage, and still get an acceptable non–critical design, better than its initial estimate.
In summary then, the explicit subproblem defined by Equation (3.32) exhibits the following remarkable properties:

- high–quality first–order approximations;
- conservative feasible subdomain;
- convexity;
- separability.

3.5.3 The dual solution scheme

Since the convex linearization method benefits from the properties of convexity and separability, the explicit problem presented in Equation (3.32), which is reported in the following for the sake of simplicity, can be solved efficiently by dual mathematical programming methods:

$$\begin{aligned} \min \quad & \sum_{i \in I_k^+(f)} f_i x_i - \sum_{i \in I_k^-(f)} \frac{f_i}{x_i} \\ \text{subject to} \quad & \sum_{i \in I_k^+(h_j)} \frac{h_{ij}}{x_i} - \sum_{i \in I_k^-(h_j)} h_{ij} x_i \leqslant \overline{h}_j \quad j = 1, \ldots, m \text{ inequality constraints} \\ & \underline{x}_i \leqslant x_i \leqslant \overline{x}_i \qquad\qquad i = 1, \ldots, n \text{ side constraints} \end{aligned} \tag{3.34}$$

It is worth to note that the side constraints represent a particular case of the inequality constraints, also called *behaviour constraints*. However, they are written separately in our explicit problem statement, because the dual method approach described in the sequel can handle them more efficiently when considered apart from the general constraints.
Given a general constrained optimization problem such as the standard one defined by Equation (3.24), its *dual* problem consists in maximizing a quasi-unconstrained auxiliary dual function that depends only on the Lagrangian multipliers associated with the main primal constraints, linearized by an appropriate approximation scheme. In this case, these Lagrangian multipliers, also called *dual variables*, have to remain non–negative. The effectiveness of the dual formulation mainly lies in the fact that the maximization of the objective function is performed in the dual space with respect to the space of the original problem: the dimension of the dual space is relatively short and it depends only on the number of the active constraints involved in the considered optimization step (Fleury and Braibant 1986; Fleury 1989). Since the side constraints can be treated separately from the behaviour constraints, the dual variables to be used are limited to the Lagrange multipliers

associated with the approximated behaviour constraints. Thus, denoted by $\mathbf{X}$ the vector of the design variables x_i and by $\mathbf{\Lambda}$ the vector of the Lagrangian multipliers λ_i, the Lagrangian function can be written in the following way:

$$L(\mathbf{X}, \mathbf{\Lambda}) = \sum_{+} f_i x_i - \sum_{-} \frac{f_i}{x_i} + \sum_{j=1}^{m} \lambda_j \left(\sum_{+} \frac{h_{ij}}{x_i} - \sum_{-} h_{ij} x_i - \overline{h}_j \right), \tag{3.35}$$

where the following notation has been introduced:

- objective function f:

$$\sum_{+} = \sum_{i \in I_k^+(f)} \qquad \text{and} \qquad \sum_{-} = \sum_{i \in I_k^-(f)} \tag{3.36}$$

- constraint functions h_j:

$$\sum_{+} = \sum_{i \in I_k^+(h_j)} \qquad \text{and} \qquad \sum_{-} = \sum_{i \in I_k^-(h_j)} \tag{3.37}$$

The dual maximization problem corresponding to the original minimization problem described by Equation (3.32) assumes the form:

$$\begin{aligned} \max \quad & l(\mathbf{\Lambda}) = \sum_{+} f_i x_i(\mathbf{\Lambda}) - \sum_{-} \frac{f_i}{x_i(\mathbf{\Lambda})} + \\ & + \sum_{j=1}^{m} \lambda_j \left[\sum_{+} \frac{h_{ij}}{x_i(\mathbf{\Lambda})} - \sum_{-} h_{ij} x_i(\mathbf{\Lambda}) - \overline{h}_j \right] \\ \text{subject to} \quad & \lambda_j \geqslant 0 \end{aligned} \tag{3.38}$$

where $\mathbf{X}(\mathbf{\Lambda})$ denotes the original solution design point of the auxiliary minimization problem (given a vector $\mathbf{\Lambda}$):

$$\begin{aligned} \min \quad & L(\mathbf{X}, \mathbf{\Lambda}) \\ \text{subject to} \quad & \underline{x}_i \leqslant x_i \leqslant \overline{x}_i. \end{aligned} \tag{3.39}$$

Because the Lagrangian is separable, this n–variable problem can be decomposed in n single variable problems:

$$\min_{\underline{x}_i \leqslant x_i \leqslant \overline{x}_i} L_i(x_i, \mathbf{\Lambda}). \tag{3.40}$$

The explicit statement of this minimization problem depends upon the sign of f_i (Equation (3.26)):

$$\begin{aligned} f_i > 0 \quad &\Longrightarrow \quad L_i\left(x_i, \mathbf{\Lambda}\right) = f_i x_i + \frac{p_i}{x_i} + q_i x_i, \\ f_i < 0 \quad &\Longrightarrow \quad L_i\left(x_i, \mathbf{\Lambda}\right) = -\frac{f_i}{x_i} + \frac{p_i}{x_i} + q_i x_i, \end{aligned} \tag{3.41}$$

where p_i and q_i are constants depending only by the dual variables λ_j (Lagrange multipliers):

$$\begin{aligned} p_i &= \sum_{+} h_{ij} \lambda_j \geqslant 0, \\ q_i &= -\sum_{-} h_{ij} \lambda_j \geqslant 0. \end{aligned} \tag{3.42}$$

This coefficients have to always remain non–negative in the feasible domain of the dual space, because, as earlier imposed, the inequality $\lambda_j \geqslant 0$ must be satisfied. Moreover, the Lagrangian problem of Equation (3.40) necessarily has a unique solution, obtained imposing that the first order derivative of the function $L_i\left(x_i, \mathbf{\Lambda}\right)$ with respect to the design variable x_i vanishes. It turns out that, because the side constraints must to be satisfied, each one–dimensional minimization problem defined by Equation (3.40) can be solved in closed form, yielding explicity the primal design variables x_i in terms of the dual variables λ_j respecting the following expressions:

- Case one:

$$\begin{aligned} f_i > 0 \quad \Longrightarrow \quad x_i &= \sqrt{\frac{p_i}{f_i + q_i}} \quad \text{if} \quad \underline{x}_i^2 < \frac{p_i}{f_i + q_i} < \overline{x}_i^2 \\ x_i &= \underline{x}_i \qquad\qquad \text{if} \quad p_i \leqslant \left(f_i + q_i\right) \underline{x}_i^2 \\ x_i &= \overline{x}_i \qquad\qquad \text{if} \quad p_i \geqslant \left(f_i + q_i\right) \overline{x}_i^2 \end{aligned} \tag{3.43}$$

- Case two:

$$\begin{aligned} f_i < 0 \quad \Longrightarrow \quad x_i &= \sqrt{\frac{p_i - f_i}{q_i}} \quad \text{if} \quad \underline{x}_i^2 < \frac{p_i - f_i}{q_i} < \overline{x}_i^2 \\ x_i &= \underline{x}_i \qquad\qquad \text{if} \quad p_i \leqslant f_i + q_i \underline{x}_i^2 \\ x_i &= \overline{x}_i \qquad\qquad \text{if} \quad p_i \geqslant f_i + q_i \overline{x}_i^2 \end{aligned} \tag{3.44}$$

Remembering that the coefficients p_i and q_i depend only upon the dual variables λ_j (as earlier shown in Equations (3.42)), we have obtained completely explicit relations between the primal variables and the dual ones. We can now note that, for each point belonging to the dual space, the primal variables are subdivided in two categories: the *fixed variables* and the *free variables*. It is then convenient to introduce the following *set of free variables* I for the indices i of the design variables:

$$I = \{i\text{: such that} \quad \underline{x}_i < x_i < \overline{x}_i\}\,. \tag{3.45}$$

The free variables ($i \in I$) are given, dependently from the sign of the first derivative f_i of the objective function with respect to the design variables, by the first expression of Equation (3.43) or by the first expression of Equation (3.44). The second and the third terms of Equations (3.43) and (3.44) give the expressions of the remaining fixed variables.
For the sake of completeness, it is worth noticing that in the special case where $f_i = 0$, both formulae of Equation (3.43) or of Equation (3.44) can be used. The two following particular cases should also be mentioned:

$$\begin{aligned} x_i &= \underline{x}_i \quad \text{if} \quad p_i = 0 \quad \text{and} \quad f_i \geqslant 0, \\ x_i &= \overline{x}_i \quad \text{if} \quad q_i = 0 \quad \text{and} \quad f_i \leqslant 0. \end{aligned} \tag{3.46}$$

Knowing $\mathbf{X}(\mathbf{\Lambda})$, the dual problem formuled by Equation (3.38) is explicitly defined. It is a quasi-unconstrained problem and it can therefore be readily solved using a *steepest ascent* algorithm[10] slightly modified to handle the non–negativity constraints on the dual variables λ_j. Such a gradient method requires the first derivatives of the dual function to be available. Fortunately, an interesting feature of the dual formulation is that these derivatives are extremely simple to compute, because they are given by the primal constraints:

$$g_j \equiv \frac{\partial l}{\partial \lambda_j} = \sum_{+} \frac{h_{ij}}{x_i(\mathbf{\Lambda})} - \sum_{-} h_{ij} x_i(\mathbf{\Lambda}) - \overline{h}_j. \tag{3.47}$$

At this point it is worth pointing out that the convex linearization method can be used when some or all of the design variables, instead of varying continuously, can only take on discrete values. In such a case the dual method formulation becomes still more attractive. The dual function remains continuous, while its first–order derivatives are discontinuous.
For the purposes of a deeper discussion of the solution process of the dual problem that will be presented in the following part of section, it is convenient to

[10]The steepest ascent is the dual algorithm of the more popular and used *steepest descent* algorithm which, in opposition to the first, searches the optimal condition by minimizing the objective function while the first does the same thing by maximizing the objective function.

re–formulate the starting main problem of Equation (3.34) by using a different mathematical notation: until now, in fact, with $f(\mathbf{X})$ we have denoted the objective function of a general optimization problem, while with $h_j(\mathbf{X}), j = 1, \ldots, m$ we have denoted the constraint functions. For the rest of the sections, indeed, it becomes more easy to assume the following more compact and synthetic notation:

- $h_0(\mathbf{X})$ = objective function;
- $h_j(\mathbf{X}), \quad j = 1, \ldots, m$ = constraint functions.

Trivially, in this way, with the notation:

$$h_j(\mathbf{X}), \qquad j = 0, \ldots, m, \tag{3.48}$$

letting start the index j from 0 and no more from 1, we can indicate all the categories of the functions involved in the problem, as the objective function and the constraint ones. The objective function is simply obtained putting $j = 0$. In this way, the Equations (3.26) can be written as it follows:

$$h_{i0} = \left.\frac{\partial h_0}{\partial x_i}\right|_{\mathbf{X}^k} \qquad \text{and} \qquad h_{ij} = \left.\frac{\partial h_j}{\partial x_i}\right|_{\mathbf{X}^k}. \tag{3.49}$$

With this new notation the primal optimization problem of Equation (3.34) becomes:

$$\begin{aligned} \min \quad & \sum_{+} h_{i0} x_i - \sum_{-} \frac{h_{i0}}{x_i} - \overline{h}_0 \\ \text{subject to} \quad & \sum_{+} \frac{h_{ij}}{x_i} - \sum_{-} h_{ij} x_i \leqslant \overline{h}_j \quad j = 1, \ldots, m \\ & \underline{x}_i \leqslant x_i \leqslant \overline{x}_i \qquad\qquad i = 1, \ldots, n \end{aligned} \tag{3.50}$$

It is worth noticing that in this case, adapting the expressions to the new formulation, provided that the generic design point where the objective and constraint functions are evaluated continues to be written with the notation $\mathbf{X}^k$, the coefficients $\overline{h}_j$ contain the contributions of zero–order in the Taylor series expansion in the form:

$$\overline{h}_j = \sum_i |h_{ij}| x_i^k - h_j\left(\mathbf{X}^k\right) \qquad j = 0, \ldots, m. \tag{3.51}$$

At this point, remembering again that following this new compact notation, j starts from 0, we can briefly re–write the new version of the Equations (3.35)–(3.41) that define the dual problem presented before. Obviously, such equations can be obtained by applying the same logical processes followed for the first formulation (3.50):

- the Lagrangian function of Equation (3.35) becomes:

$$L(\mathbf{X}, \mathbf{\Lambda}) = \sum_{j=0}^{m} \lambda_j \left(\sum_{+} \frac{h_{ij}}{x_i} - \sum_{-} h_{ij} x_i - \overline{h}_j \right); \tag{3.52}$$

- the dual problem statement of Equation (3.38) assumes the following expression:

$$\begin{aligned} \max \quad & l(\mathbf{\Lambda}) = \sum_{j=0}^{m} \lambda_j \left[\sum_{+} \frac{h_{ij}}{x_i(\mathbf{\Lambda})} - \sum_{-} h_{ij} x_i(\mathbf{\Lambda}) - \overline{h}_j \right] \\ \text{subject to} \quad & \lambda_j \geqslant 0 \qquad j = 0, \ldots, m \end{aligned} \tag{3.53}$$

  where, following the common practice, it is assumed that the Lagrange multiplier λ_0 associated to the objective function is fixed to the unit value;

- the Equations (3.39) and (3.40) do not change, consequently remaining:

$$\begin{aligned} \min \quad & l(\mathbf{\Lambda}) = L(\mathbf{X}, \mathbf{\Lambda}) \\ \text{subject to} \quad & \underline{x}_i \leqslant x_i \leqslant \overline{x}_i \end{aligned} \tag{3.54}$$

$$\min_{\underline{x}_i \leqslant x_i \leqslant \overline{x}_i} L_i(x_i, \mathbf{\Lambda}); \tag{3.55}$$

- in this case, the value of $L_i(x_i, \Lambda)$ is given by the following expression and no more by the Equations (3.41):

$$L_i(x_i, \Lambda) = \frac{p_i}{x_i} + q_i x_i, \tag{3.56}$$

  where the constants p_i and q_i are given again by the Equations (3.42);

- the Equations (3.43) and (3.44), following the new notations become the same expression:

$$\begin{aligned} x_i &= \sqrt{\frac{p_i}{q_i}} \qquad \text{if} \qquad \underline{x}_i^2 < \frac{p_i}{q_i} < \overline{x}_i^2, \\ x_i &= \underline{x}_i \qquad \text{if} \qquad p_i \leqslant q_i \underline{x}_i^2, \\ x_i &= \overline{x}_i \qquad \text{if} \qquad p_i \geqslant q_i \overline{x}_i^2. \end{aligned} \tag{3.57}$$

Now, completed the udpating phase of the equations governing the dual problem statement, we can proceed in the explanation of the formulation of the dual solution scheme.

Because the dual problem is completely explicit, and because the corresponding primal problem has an easy algebraic structure, the second–order derivatives of the dual function:

$$\mathbf{H}_{jk} \equiv \frac{\partial^2 l}{\partial \lambda_j \partial \lambda_k}, \tag{3.58}$$

can be written in closed form. From Equation (3.47) we have:

$$\mathbf{H}_{jk} \equiv \frac{\partial g_j}{\partial \lambda_k} = \sum_{+} \frac{h_{ij}}{x_i^2} \frac{\partial x_i}{\partial \lambda_k} - \sum_{-} h_{ij} \frac{\partial x_i}{\partial \lambda_k}, \tag{3.59}$$

where $\mathbf{H}_{jk}$ is the *Hessian matrix* defined by the second–order derivatives of the dual function. Differentiating the first expression of the Equations (3.57), which represent the relations between primal and dual variables, it follows that:

$$\frac{\partial x_i}{\partial \lambda_k} = \frac{q_i \dfrac{\partial p_i}{\partial \lambda_k} - p_i \dfrac{\partial q_i}{\partial \lambda_k}}{2 x_i q_i^3}, \qquad (i \in I), \tag{3.60}$$

for the primal free variables. Of course, this derivatives are equal to zero for the remaining fixed variables. By using the definitions of the coefficients p_i and q_i reported in Equation (3.42), it can be seen that:

$$\begin{aligned} \frac{\partial p_i}{\partial \lambda_k} &= +h_{ik} \quad \text{if} \quad h_{ik} > 0 \quad \text{and} \quad \frac{\partial p_i}{\partial \lambda_k} = 0 \quad \text{if} \quad h_{ik} \leqslant 0, \\ \frac{\partial q_i}{\partial \lambda_k} &= -h_{ik} \quad \text{if} \quad h_{ik} < 0 \quad \text{and} \quad \frac{\partial q_i}{\partial \lambda_k} = 0 \quad \text{if} \quad h_{ik} \geqslant 0, \end{aligned} \tag{3.61}$$

so that:

$$\begin{aligned} \frac{\partial x_i}{\partial \lambda_k} &= \frac{h_{ik}}{2 x_i q_i^2} \quad \text{if} \quad h_{ik} > 0, \\ \frac{\partial x_i}{\partial \lambda_k} &= \frac{h_{ik} x_i}{2 q_i^2} \quad \text{if} \quad h_{ik} < 0. \end{aligned} \tag{3.62}$$

Finally, combining the previous results, we can obtain the following explicit form for the elements of the dual Hessian matrix:

$$\mathbf{H}_{jk} = \frac{1}{2} \sum_{i \in I} n_{ij} n_{ik} \frac{x_i}{q_i}, \tag{3.63}$$

where:

$$\begin{aligned} n_{ij} &= h_{ij} \quad \text{if} \quad h_{ij} > 0, \\ n_{ij} &= \frac{h_{ij}}{x_i^2} \quad \text{if} \quad h_{ij} < 0, \end{aligned} \tag{3.64}$$

and the coefficients n_{ik} obey the same rules. It is important to underline the fact that in the summation of Equation (3.63) the index i only refers to the primal free variables, i.e. to the variables x_i that do not reach their own lower bound $\underline{x}_i$ or upper bound $\overline{x}_i$ (Equation (3.57)). This means that the second–order derivatives of the dual functions are discontinuous whenever a free primal variable becomes fixed, or conversely.
The fundamental difficulty in using Newton type methods for solving the dual problem resides in these inherent discontinuities of the Hessian matrix. Fortunately, the topology of the dual space can be described in an exact mathematical way via the concept of *second order discontinuity planes*. Based on this concept, Fleury in 1989 proposed a very reliable *sequential quadratic programming* (SQP) method to solve the dual problem.

3.5.4 The constraint relaxation

In practical applications a difficulty that frequently occurs is that the initial design violates some of the constraints. Very often it is difficult to get a feasible design point because two or more constraints are incompatible. In the convex linearization method, this difficult might be acute because of the conservative character of the approximate constraints. It can even lead to a breakdown of the optimization process. In fact, although conservativeness is most of the time a desirable property, it is not so when the initial starting point is seriously infeasible. In such a case it can happen that the linearized feasible subdomain be empty, so that the method can no longer be applied. To cope with this difficulty an additional variable δ, called *relaxation variable*, is introduced into the explicit subproblem statement of Equation (3.50), which becomes the following *relaxed* subproblem:

$$\begin{aligned}
\min \quad & \sum_{+} h_{i0} x_i - \sum_{-} \frac{h_{i0}}{x_i} + z_0 w \delta \\
\text{subject to} \quad & \sum_{+} \frac{h_{ij}}{x_i} - \sum_{-} h_{ij} x_i \leqslant \overline{h}_j + z_j \left(1 - \frac{1}{2}\right) \qquad j = 1, \ldots, m \\
& \underline{x}_i \leqslant x_i \leqslant \overline{x}_i \qquad\qquad\qquad\qquad\qquad\quad i = 1, \ldots, n \\
& \delta \geqslant 1
\end{aligned} \tag{3.65}$$

where w is a user–supplied *weighting factor*, and:

$$z_j = \sum_{i=1}^{n} |h_{ij}| x_i^k \qquad j = 0, \ldots, m \tag{3.66}$$

represent increments to the functions $h_j(\mathbf{X})$, $j = 0, \ldots, m$, opening up the feasible domain in the design space if necessary.

Clearly, if the relaxation variable δ hits lower bound ($\delta = 1$), nothing is changed in the problem statement, which will usually happen when the starting design point $\mathbf{X}^k$, with $k = 0$, is feasible or nearly feasible. On the other hand, if the starting point $\mathbf{X}^k$ is seriously infeasible, the algorithm will find a value of δ greater than unity, which means that the linearized feasible domain will be artificially enlarged. Taking the solution of the current explicit subproblem of Equation (3.65) as a new linearization point, the next feasible subdomain will generally be non empty. The method can then be applied as initially stated in Section 3.5.2, yielding unit values of the relaxation variable δ at each subsequent iterations.
From the modified primal problem of Equation (3.65), it is easily seen that the Lagrangian problem related to the relaxation variable δ has the form:

$$\min_{\delta \geqslant 1} \quad z_0 w \delta - \left(1 - \frac{1}{\delta}\right) \sum_{j=0}^{m} \lambda_j z_j. \tag{3.67}$$

From this minimum condition, δ is given in terms of the dual variables λ_j by the relations:

$$\begin{aligned} &\delta = \sqrt{\frac{\sum_{j=0}^{m} \lambda_j z_j}{w z_0}} \qquad \text{if} \qquad \sum_{j=0}^{m} \lambda_j z_j > w z_0, \\ &\delta = 1 \qquad\qquad\quad \text{if} \qquad \sum_{j=0}^{m} \lambda_j z_j \leqslant w z_0. \end{aligned} \tag{3.68}$$

The dual solution scheme of Section 3.5.3 needs only little modification to take care of the addition of a relaxation variable δ. Whenever a new dual point has been obtained in the iterative process, the relaxation variable δ is computed from Equation (3.68). As long as δ remains fixed to 1, nothing is changed in the optimization process. If the relaxation has to be activated, i.e. $\delta > 1$, then it is necessary to modify the definitions of the dual gradient vector g_j of the dual function $l(\mathbf{\Lambda})$ of the Equation (3.47) and the definition of the Hessian matrix of Equation (3.63) as it follows:

$$g_j \equiv \frac{\partial l}{\partial \lambda_j} = \sum_{+} \frac{h_{ij}}{x_i(\mathbf{\Lambda})} - \sum_{-} h_{ij} x_i(\mathbf{\Lambda}) - \overline{h}_j - z_j \left(1 - \frac{1}{\delta}\right), \tag{3.69}$$

$$\mathbf{H}_{jk} = \frac{1}{2} \sum_{i \in I} n_{ij} n_{ik} \frac{x_i}{q_i} - \frac{1}{2} \frac{z_j z_k}{w \delta^3}. \tag{3.70}$$

As implemented herein, relaxation is uniformly applied to all the constraints and its purpose is simply to balance the effect of conservativeness in the convex linearization method. For this uniform relaxation being effective, it is implicitly assumed

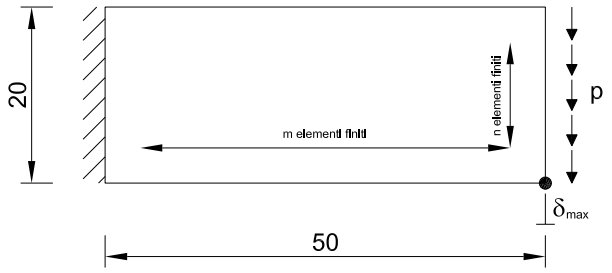

Figure 3.7: Cantilevered structure with tip load.

that the feasible domain corresponding to the primary problem (Equation (3.24)) is non–empty. If is not the case, for example because two or more constraints are really in conflict, then uniform relaxation is not a satisfactory technique. Current researches are directed toward other relaxation methods that would be capable of finding a minimal relaxation for an infeasible problem. These methods imply introducing several additional relaxation variables δ_j, one for each constraint that the user accepts to relax.
More deeper formulations and demonstrations about the constraints relaxation technique are given in the contribute of Nguyen, Strodiot, and Fleury (1987), in which it is also perfomed a complete convergence analysis of the convex linearization method, introducing also two sofisticated modifications of the algorithm itself.

3.6 Numerical examples

The computational solution procedure that was employed for the examples shown below is based on a FEM approximation of the considered structure, combine with the use of the MP routine for solving the associated discrete, convex optimization problem. The FEM discretization is based on the elements introduced in Sections 5.2 (shell) and 5.3 (arch) modelled using the surface geometry of Chapter 4. About optimization, the method proposed in Section 3.5.2 is used and the global design problem is solved as a combined FEM–MP problem involving stresses as well as displacements as variables in the optimization routines.

3.6.1 Thickness optimization

The various concepts discussed in the previous sections have been applied to a wide variety of classical problem (Bendsøe 1996), in order to test the effectiveness and capability of the proposed approach. In this section we consider the membrane–thickness optimization, using the element proposed in Section 5.2.

The first four examples refer to *planar* design domain (Krog and Olhoff 1997) with different loading, geometry and support conditions as depicted in Figures 3.7, 3.9, 3.11 and 3.13(a). The results, obtained asking for the optimum thickness distribution under displacement constraints and a minimum of the total volume of the elements, are shown in Figure 3.8 (with different mesh refinement) and in Figures 3.10, 3.12, 3.13(b) and 3.13(c).
The task in examples of Figures 3.14(a) and 3.15(a) is to find a best–possible thickness distribution for a prescribed domain an loading, a maximum displacement imposed and two different constraints: a beam simply supported in the first case (Figure 3.14(a)) and clamped in the second (Figure 3.15(a)). Figures 3.14(b) and 3.14(c) display the optimum solution to the simply–supported beam problem and Figures 3.15(b) and 3.15(c) illustrate the optima to the clamped problem.

3.6.2 Fiber–truss optimization

After having tested the capability of the membrane–thickness optimization, in the following we show six numerical examples dealing with the arch finite element proposed in Section 5.3. All the examples herein shown, ask for the optimal design of the fiber sectional area under displacement constraints and a minimum of the total volume of the elements.
The first two examples deal with the optimization of the side part of two different bridges. As an illustration, Figures 3.16 and 3.18 show geometry, load, boundary conditions and the maximum displacement constraint. The resulting optimum structures are shown in Figures 3.17, 3.19 and 3.20. Note that the shape of the bridge is predetermined, but is a pure outcome of the optimization process the thickness distribution.
The third example (Figure 3.21) considers a well–known 2D structure which is fixed at one side, and loaded by a vertical force at the right–down corner of the opposite side. Figure 3.22 shows the result for a 19–bar structure.
The last cases consider three full 3D optimization examples. The first one is presented in Figures 3.23 and 3.24 where a one–floor and two–floor building, respectively, are subjected to torsion loads at the upper surface and equipped with simple supports at the lower surface corners. Figures 3.23 and 3.24 display the optimum thickness distribution. The second example, in Figures 3.25 and 3.26, deal with a 3D cantilever which has a triangular cross–sectional area. Three nodes at one end of the cantilever are fixed while at the opposite, three end nodes are free; one vertical force applies at the free end–down node. The optimal design for this load case looks like that shown in Figures 3.25 and 3.26. In the last example we consider a 3D truss–dome that consists of three *floors*, containing 12 nodes each and an additional top node. Application of a single vertical load at the top node results in the design of Figures 3.27.

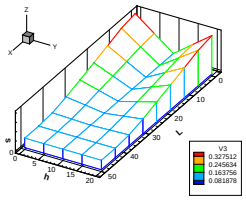

(a) 4×8

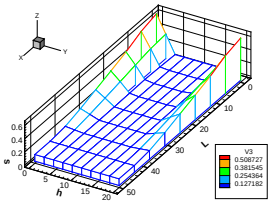

(b) 8×8

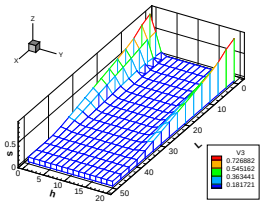

(c) 15×15

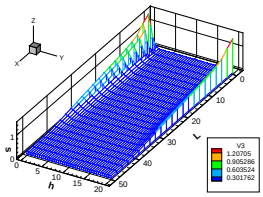

(d) 22×40

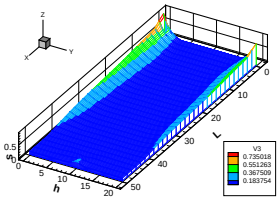

(e) 30×90

Figure 3.8: Optimum thickness distribution with different mesh discretizations referred to the cantilever beam of Figure 3.7.

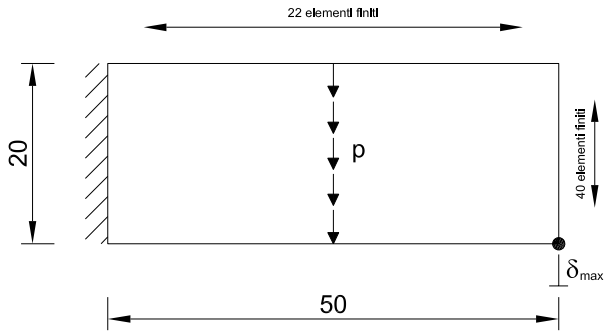

Figure 3.9: Cantilever beam with a through–thickness distributed load at the center of the plate.

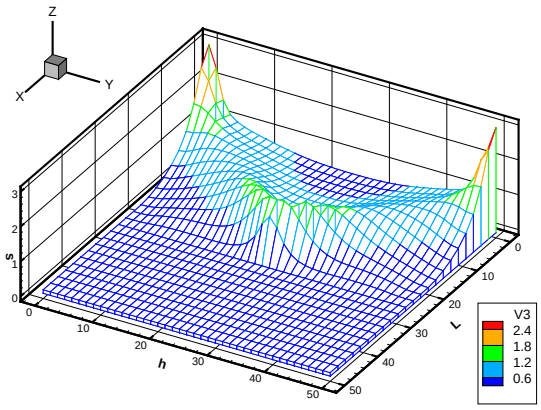

Figure 3.10: Optimum thickness distribution with a 22×40 elements discretization for the cantilever beam of Figure 3.9.

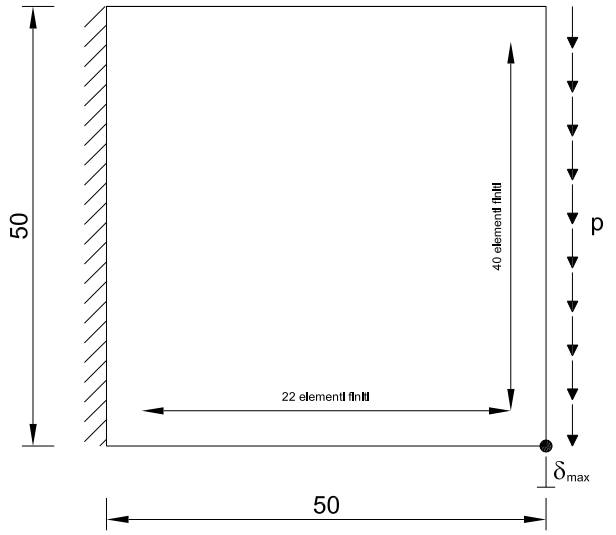

Figure 3.11: Square plane–stress plate with a tip load.

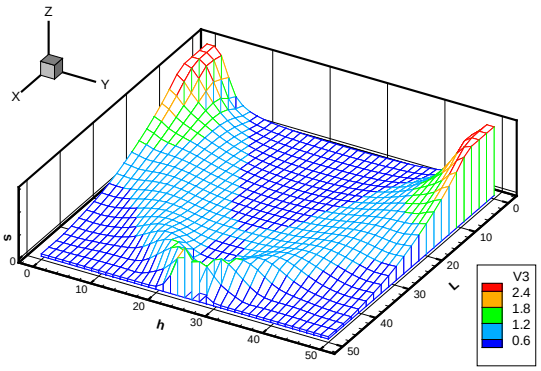

Figure 3.12: Optimum thickness distribution with a 22×40 elements discretization for the square plate of Figure 3.11.

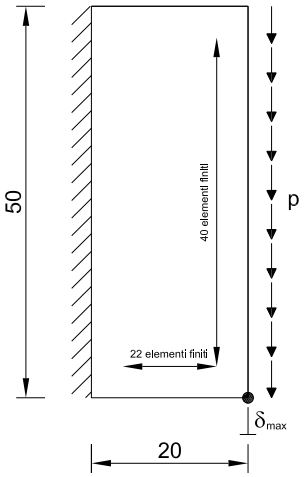

(a)

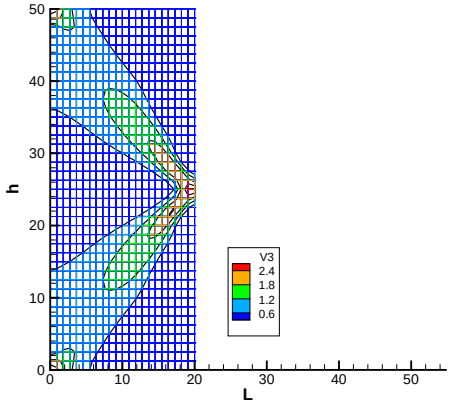

(b)

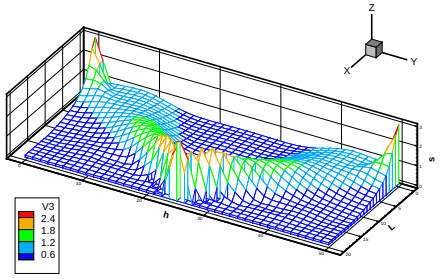

(c) 22×40

Figure 3.13: (a) Thick cantilever beam subjected to a end–free distributed load and its optimum thickness distribution. (b) Two–dimensional view and (c) three–dimensional view.

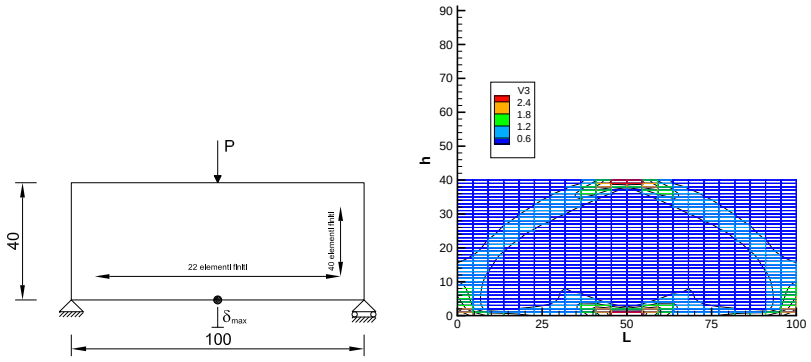

(a) (b)

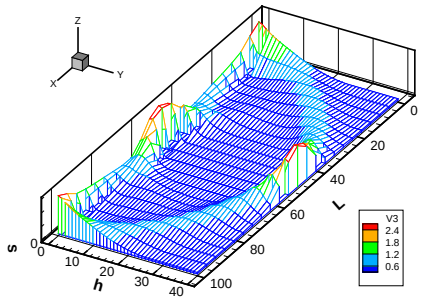

(c) 22×40

Figure 3.14: (a) Optimum thickness distribution for a simply supported beam under a mid–point transverse load. (b) Two–dimensional view and (c) three–dimensional view.

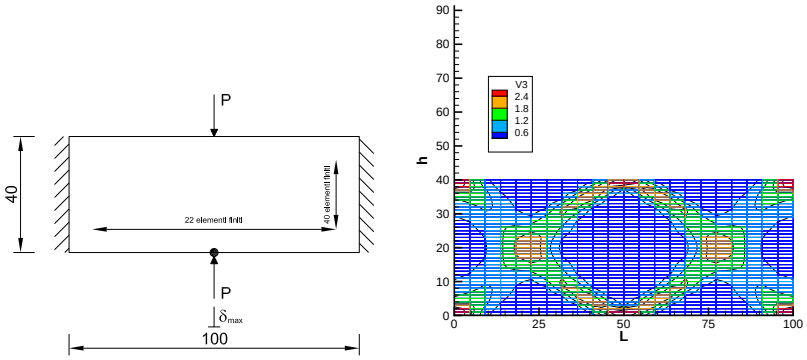

(a) (b)

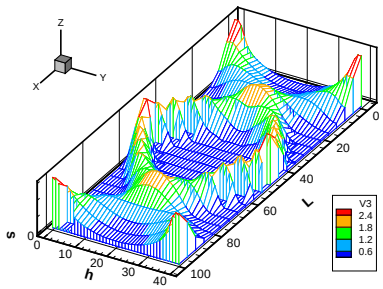

(c) 22×40

Figure 3.15: (a) Rectangular box domain with clamped ends and a pinched load at the center. (b) Two–dimensional view and (c) three–dimensional view.

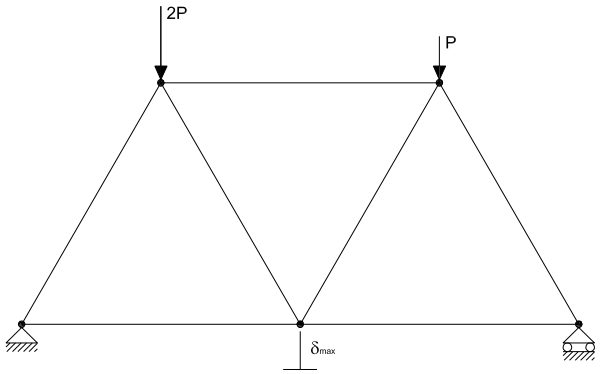

Figure 3.16: Seventh bar truss initial design.

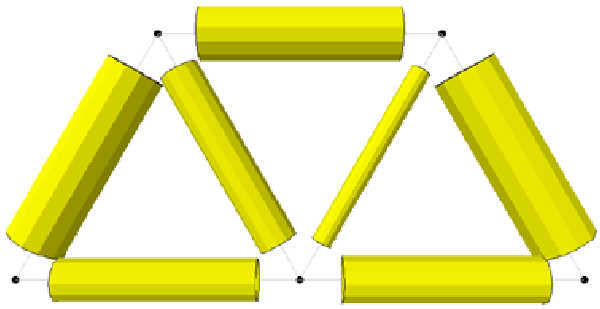

Figure 3.17: Optimum transverse sectional area distribution.

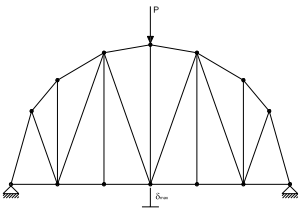

Figure 3.18: Twenty–five bar truss initial design.

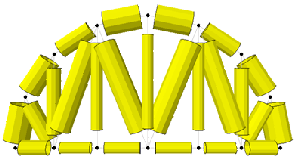

Figure 3.19: Twenty–five bar truss final design.

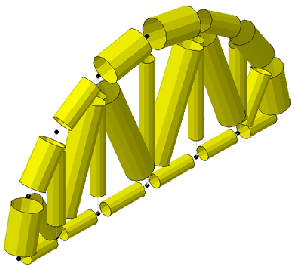

Figure 3.20: Optimum area distribution.

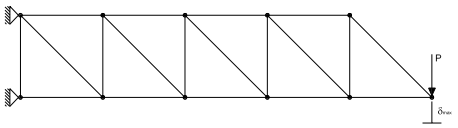

Figure 3.21: Nineteen bar truss under a tip load.

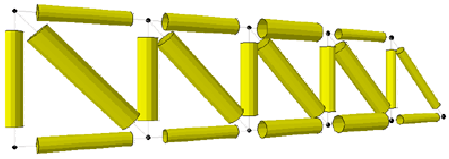

Figure 3.22: Optimum sectional area distribution.

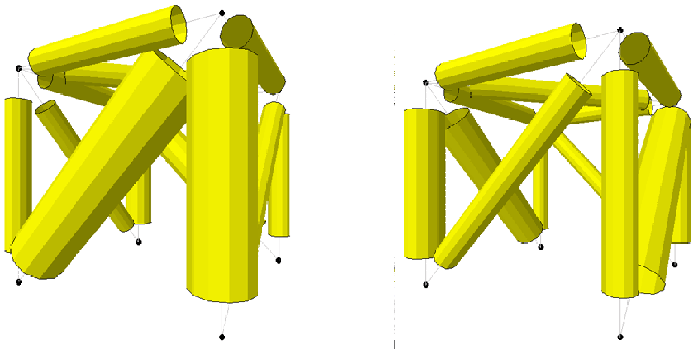

(a) (b)

Figure 3.23: Cubic one–floor design domain subjected to a pure torsion.

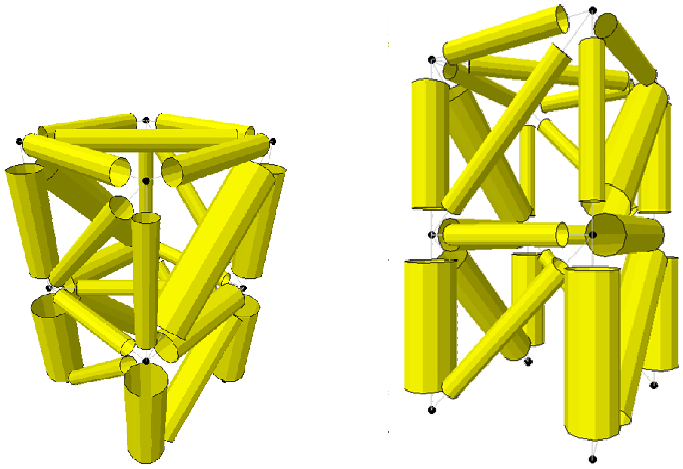

(a) (b)

Figure 3.24: Cubic two–floor design domain subjected to a pure torsion.

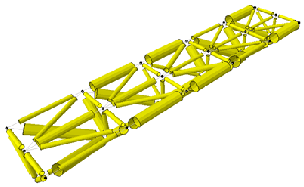

Figure 3.25: Three dimensional cantilever truss under a tip load: optimum distribution of the sectional area (View 1).

Figure 3.26: Three dimensional cantilever truss under a tip load: optimum distribution of the sectional area (View 2).

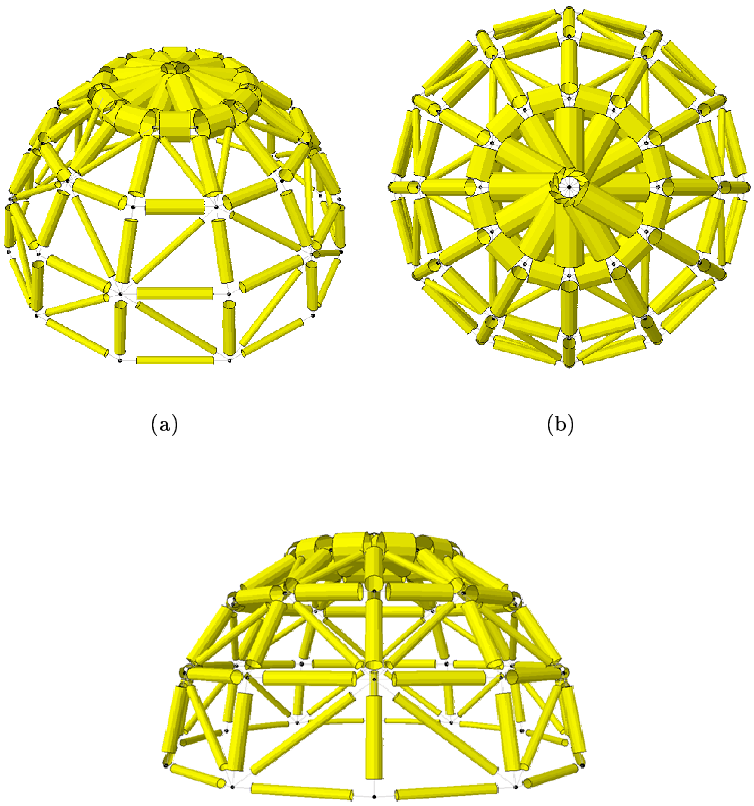

(a) (b)

(c)

Figure 3.27: Optimization of the sectional area of a three dimensional truss-dome structure.

3.6.3 Fiber–membrane optimization

While in Section 3.6.1 we have tested the membrane thickness optimization, in Section 3.6.2 we have verified the fiber sectional area optimum design. At this point it is natural to link both together, in order to model the sail as a fiber–membrane element. This approach results completely different from any other sail theory involving a fiber–reinforced composite laminates (for references see Section 3.3.1). Before coming to the real sail optimization, we need to test the fiber–membrane linking on an easier structure than the sail.
The first two examples show the unit cell with and without reinforcement in Figures 3.28(a) and 3.29(a), respectively. All these examples ask for a minimum fiber volume with membrane geometry predetermined and maximum displacement imposed. The results of the optimization routine are shown in Figures 3.28(b) and 3.29(b) for the unit cell examples.
A combination of 4 basic upwind cells are considered and optimized in Figure 3.30. In order to confirm the effective collaboration between fibers and membranes, it has been analysed the two structures presented in Figures 3.31(a) and 3.32(a) composed of quadratic domain with a few holes, where we have only fiber and not membrane elements. Obviously, as shown in Figures 3.31(b), 3.31(c), 3.32(b) and 3.32(c), the optimal distribution needs more area in the trusses within the holes than elsewhere in the structure. This transverse area concentration is due to the lost in collaboration together with the membrane in order to capture the stress distribution.
The last example, in Figure 3.33(a), is absolutely similar to the one presented in Figure 3.15(a). We have obtained exactly the same optimum distribution in thickness as shown in Figures 3.33(b) and 3.33(c) compared with Figures 3.15(b) and 3.15(c).
After having succesfully tested our approach in the previous sections, we are ready to model and optimize the sail. We start from the aerodynamically optimized plain–sail of Section 1.3.2.3 shown in Figure 1.22, using Kevlar–fiber and Mylar–matrix film material introduced in Section 3.2. Geometrical boundary conditions, coming from the mast and boom, and force boundary conditions due to the gradient wind load are shown in Figure 3.34 and completely explained in Chapter 2. After having determined, from a structural analysis, the *isostress* lines over the sail (see Figures 3.35 and 3.36), we re–orient the mesh in order to better follow the same lines. Figure 3.37 shows the re–oriented mesh. Now, the fiber network, in Figure 3.38, must follow the re–oriented mesh of Figure 3.37 to determine a uniform stress distribution over the entire sail. Then we can apply our optimization algorithm to obtain the best possible thickness distribution in the chord network. In Figures 3.39, we show some results from an intermediate configuration in the iterative optimization routine, and in Figures 3.40 the final optimum design.

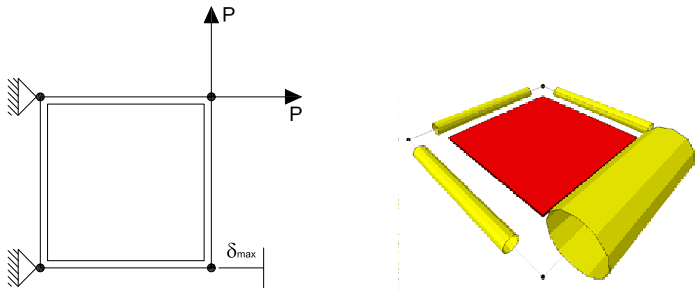

(a) (b)

Figure 3.28: (a) Design domain, load, support conditions: the unit cell truss–membrane model. (b) Optimum solution of the unit cell.

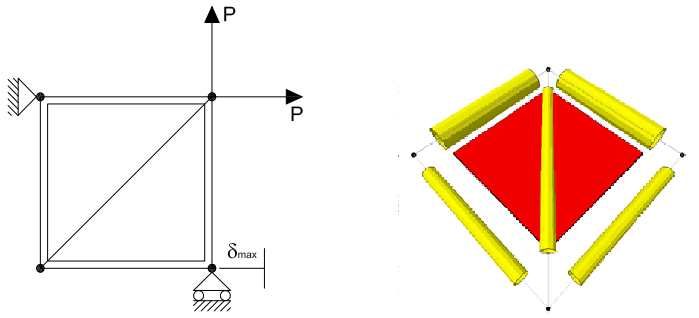

(a) (b)

Figure 3.29: (a) Design domain, load, support conditions: the *upwind* unit cell truss–membrane model. (b) The optimum solution.

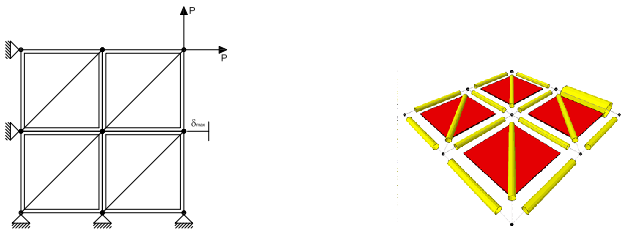

(a) (b)

Figure 3.30: Optimum design of the portion of a sail between the mast and the boom using the cells defined in Figure 3.28(a) and 3.29(a).

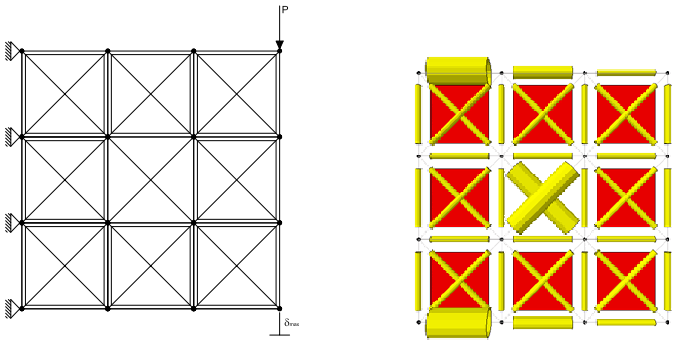

(a) (b)

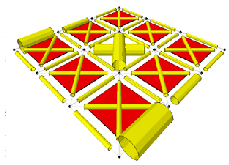

(c)

Figure 3.31: Optimum design of a coupled truss–membrane cantilever beam with a hole in the center.

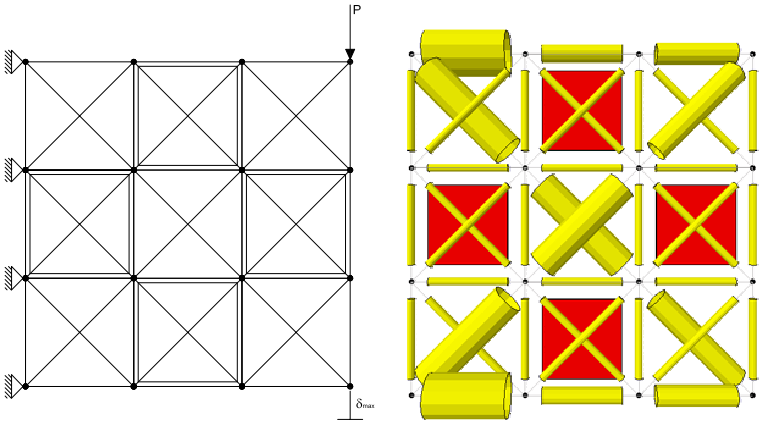

(a) (b)

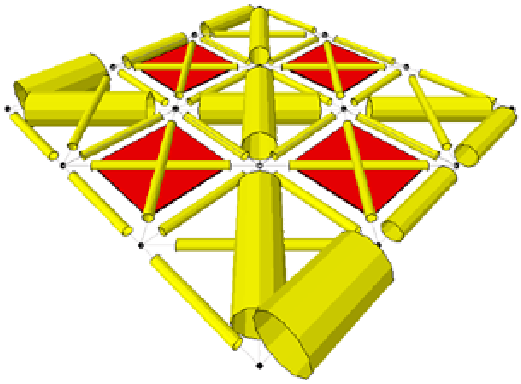

(c)

Figure 3.32: *Chess–board* optimization.

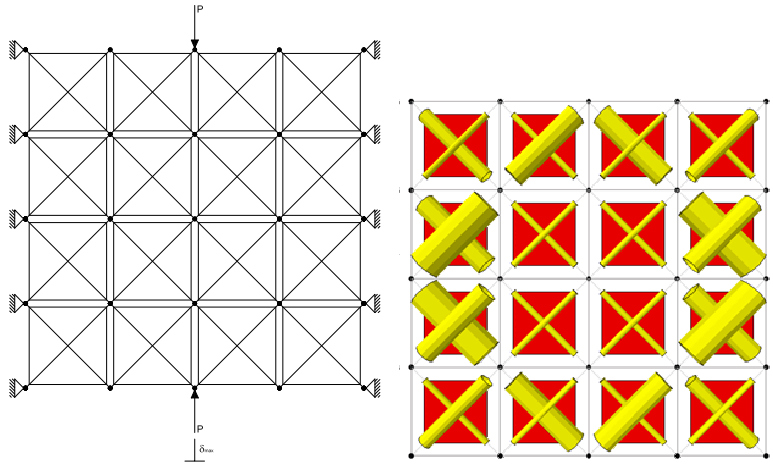

(a) (b)

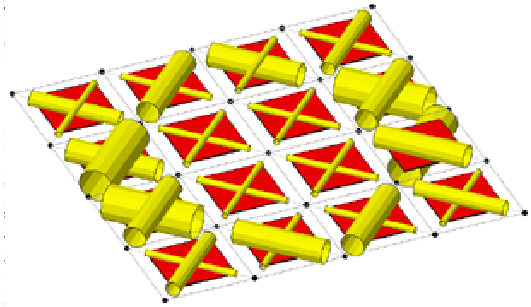

(c)

Figure 3.33: Optimum design of a pinched beam composed of a system of membranes and trusses.

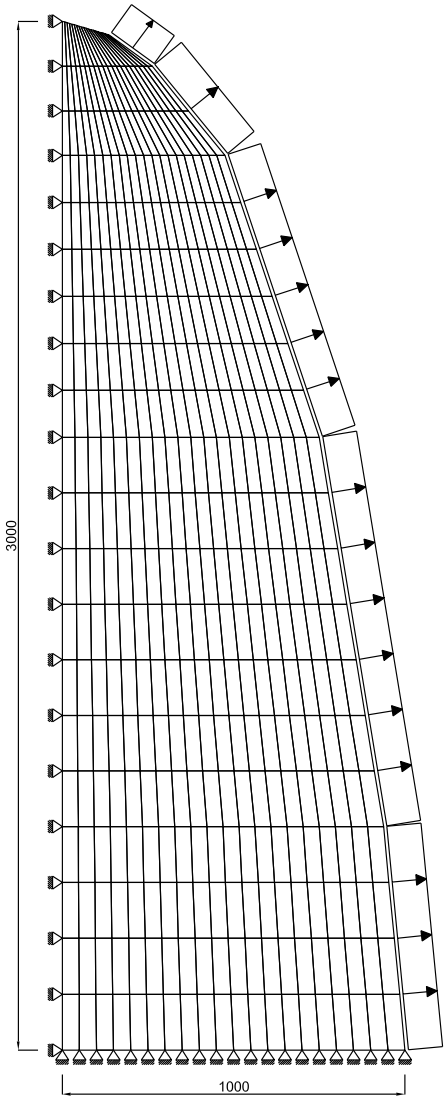

Figure 3.34: Geometrical and statical boundary condition.

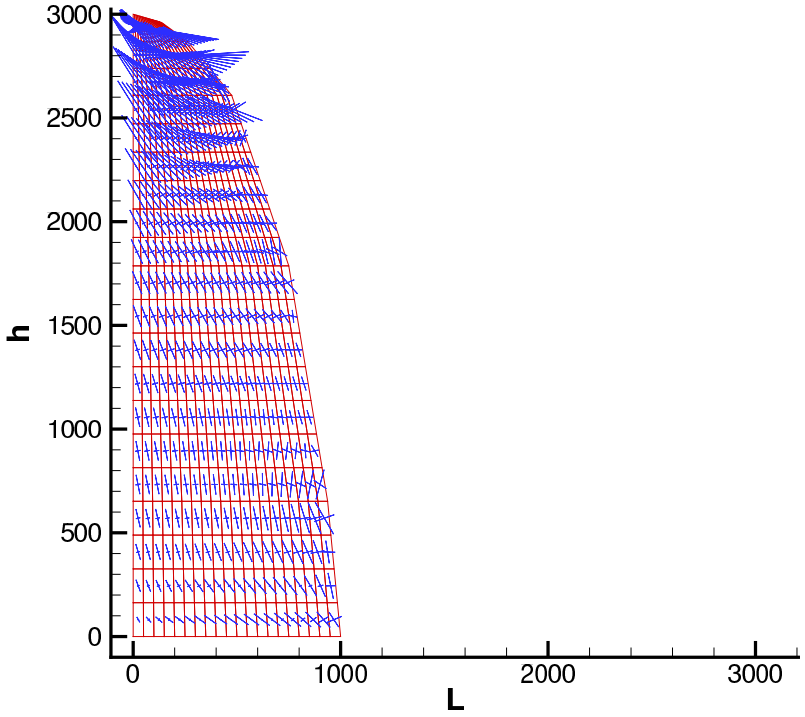

Figure 3.35: Isostress line path over the sail after the pure structural analysis applied to the aerodynamically optimized sail.

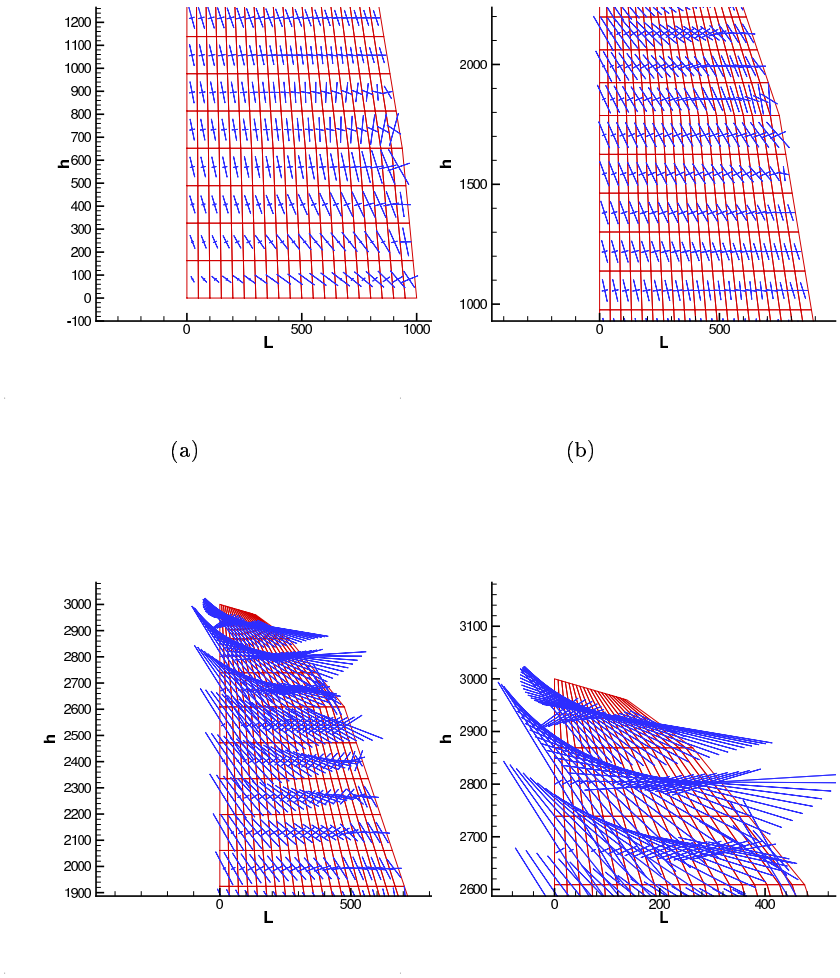

Figure 3.36: Four different *zoom* of the sail: (a) Boom. (b) Middle mainsail. (c) Upper part of the sail. (d) Top of the sail.

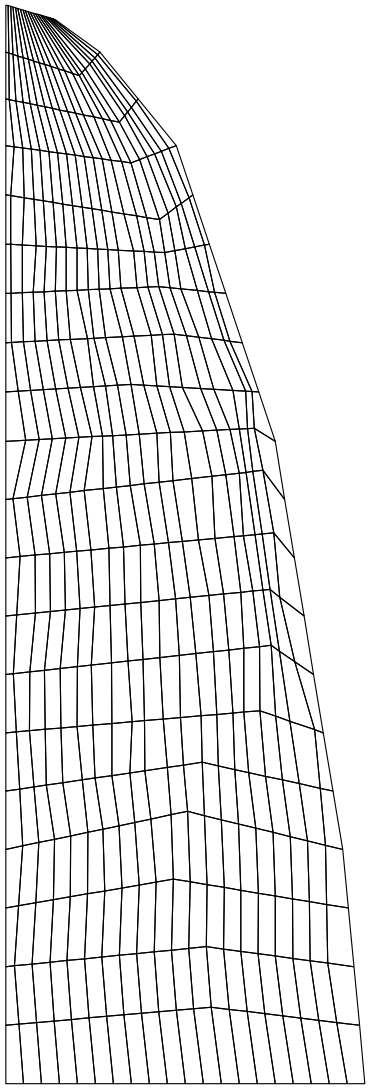

Figure 3.37: Re–oriented mesh following the isostress lines.

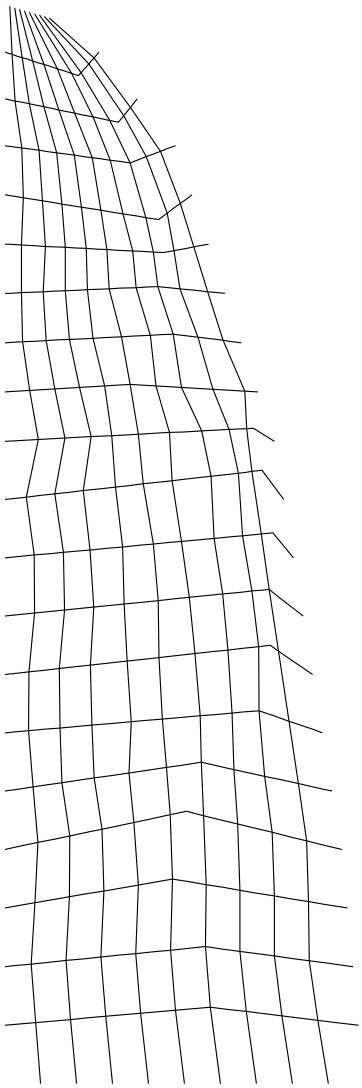

Figure 3.38: Kevlar fiber network in the sail.

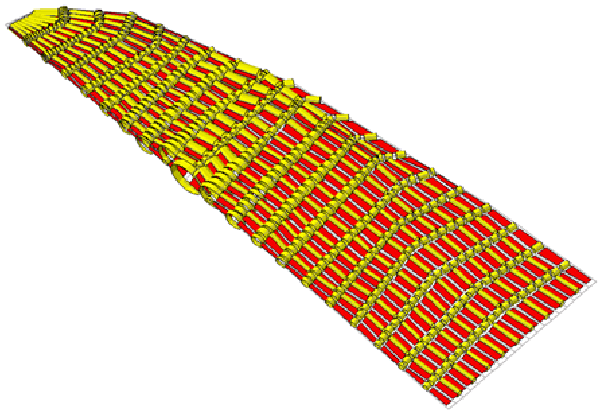

(a)

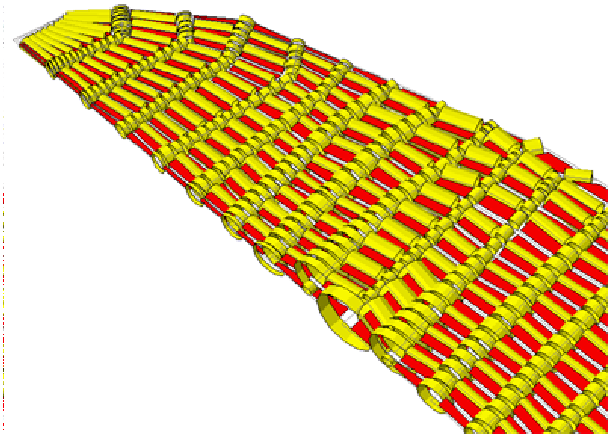

(b)

Figure 3.39: (a) Fiber–membrane distribution during an intermediate configuration of the optimization process. (b) Top of the sail (zoom).

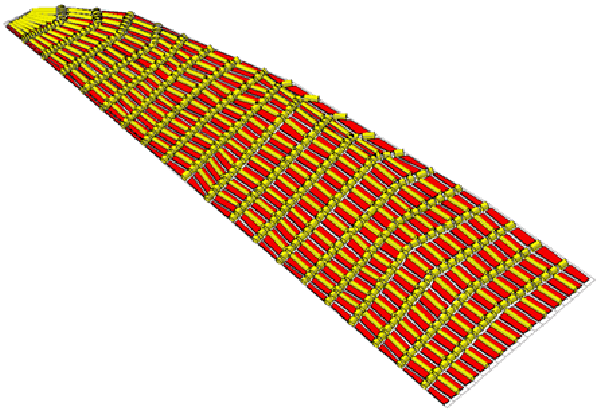

(a)

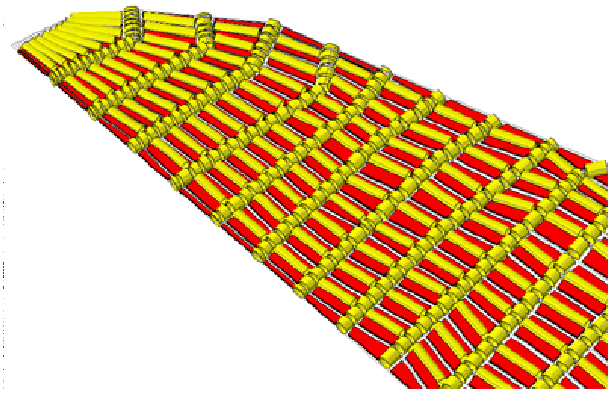

(b)

Figure 3.40: (a) Fiber–membrane optimum design at the end of the optimization process. (b) Top of the sail (zoom).

Chapter 4

General fundamentals of shells

Ach Gott! die Kunst ist lang;
Und kurz ist unser Leben.
Mir wird, bei meinem kritischen Bestreben,
Doch oft um Kopf und Busen bang.
Wie schwer sind nicht die Mittel zu erwerben, Durch die man zu den Quellen steight!
Und eh man nur den halben Weg erreicht,
Muss wohl ein armer Teufel sterben.
Goethe–Faust Erster Teil

This chapter deals with the mathematical formulation of the theory of general *thin shell–like–membranes*, and in Chapter 5 we will discretize the previously defined equations.
A shell may be defined as a three–dimensional body that is bounded by two closely spaced surfaces. The sail, that is the *shell structure* we are trying to model, is extremely thin and therefore heavily rely on an almost pure membrane stress state. In order to guarantee this stress state, the shape of the shell plays a dominant role in the initial design of the structure. Then, the basic components of the theory of shells are designated herein as: shape, equilibrium, compatibility and a constitutive law.
Sections 4.1 and 4.2 begin by defining the vector and tensor notation and a number of fundamental relationships which are essential in the representation of the surface geometry (see Section 4.3).
Sections 4.4 and 4.5 deal with the strain–displacement equations and the definition of stress within a continuous three–dimensional body.
For materials which are isotropic in nature, Section 4.6 contains the development of the stress–strain relationship in tensor form.

Finally, the strain–displacement equations of general thin shell–like–membrane are derived in Section 4.7.

4.1 Vector and tensor algebra: definitions, formulas and concepts

If P and Q are any two points in $\mathbb{R}^3$ space, the directed line segment from P to Q locates the position of Q with respect to P. Such a directed line segment is called *position vector*, and is characterized by its lenght, which gives the magnitude of the distance from P and Q, and its direction (Figure 4.1(a)). We will use the notation by which vectors are written in **bold**, i.e. $\mathbf{v}$. It's important to note that whenever two or more vectors are parallel to the same line, they are said to be *collinear*; parallel to the same plane, they are *coplanar*; otherwise it is a free vector. Let's now explain in brief the more important properties and operations of vector algebra:

- addition and subtraction: according to the parallelogram law, we can write:

$$\mathbf{C} = \mathbf{A} + \mathbf{B} = \mathbf{B} + \mathbf{A}, \quad \text{commutative law} \tag{4.1}$$

$$\mathbf{A} - \mathbf{B} = \mathbf{A} + (-\mathbf{B}), \tag{4.2}$$

- multiplication by a scalar: if a vector $\mathbf{A}$ is multiplied by a scalar m, one obtains another vector which has m times the magnitude of $\mathbf{A}$:

$$m\mathbf{A} = \mathbf{A}m, \tag{4.3}$$

- scalar product: also known as the *dot product* and *inner product*:

$$\mathbf{A} \cdot \mathbf{B} = \mathbf{B} \cdot \mathbf{A}, \quad \text{commutative law} \tag{4.4}$$

$$\mathbf{A} \cdot \mathbf{A} = AA = A^2, \tag{4.5}$$

$$\mathbf{A} \cdot (\mathbf{B} + \mathbf{C}) = (\mathbf{A} \cdot \mathbf{B}) + (\mathbf{A} \cdot \mathbf{C}), \quad \text{distributive law} \tag{4.6}$$

- vector product: also called the *cross product*, *skew product* and *outer product*:

$$\mathbf{A} \times \mathbf{B} = -\mathbf{B} \times \mathbf{A}, \tag{4.7}$$

$$(\mathbf{A} + \mathbf{B}) \times \mathbf{C} = (\mathbf{A} \times \mathbf{C}) + (\mathbf{B} \times \mathbf{C}), \quad \text{distributive law} \tag{4.8}$$

- a vector of unit lenght, called unit vector, may be defined as:

$$\hat{\mathbf{e}}_A = \frac{\mathbf{A}}{A}, \tag{4.9}$$

- linear dependence and components of a vector: a set of n vectors $\mathbf{A}_1 \ldots \mathbf{A}_n$ is said to be linearly dependent, if a set of n numbers $\beta_1, \beta_2, \ldots, \beta_n$ can be found such that:

$$\beta_1 \mathbf{A}_1 + \beta_2 \mathbf{A}_2 + \cdots + \beta_n \mathbf{A}_n = \mathbf{0}, \tag{4.10}$$

where $\beta_1, \beta_2, \ldots, \beta_n$ cannot be all zero. If the expression (4.10) cannot be satisfied, the vectors are said to be linearly independent. If there exists in a properly space (i.e. manifold (Berger and Gostiaux 1988)) a set of n linearly independent vectors, and a set of $n+1$ linearly independent vectors cannot be found, then we are in a n–dimensional space. In a $\mathbb{R}^3$ space a set of four linearly independent vectors cannot be found. On the other hand, a set of three linearly indipendent vectors, like:

$$\mathbf{e}_1 \quad \mathbf{e}_2 \quad \mathbf{e}_3, \tag{4.11}$$

is called a *basis* for this space. It is clear from the concept of linear dependence that we can represent any vector in a three–dimensional space as a linear combination of the basis vector (4.11) (see Figure 4.1(b)):

$$\mathbf{A} = A^1 \mathbf{e}_1 + A^2 \mathbf{e}_2 + A^3 \mathbf{e}_3. \tag{4.12}$$

The vectors $A^1\mathbf{e}_1, A^2\mathbf{e}_2$ and $A^3\mathbf{e}_3$ are called the vector components of $\mathbf{A}$, and A^1, A^2 and A^3 are called the scalar components or measure numbers of $\mathbf{A}$ associated with the basis $\mathbf{e}_1, \mathbf{e}_2$ and $\mathbf{e}_3$.

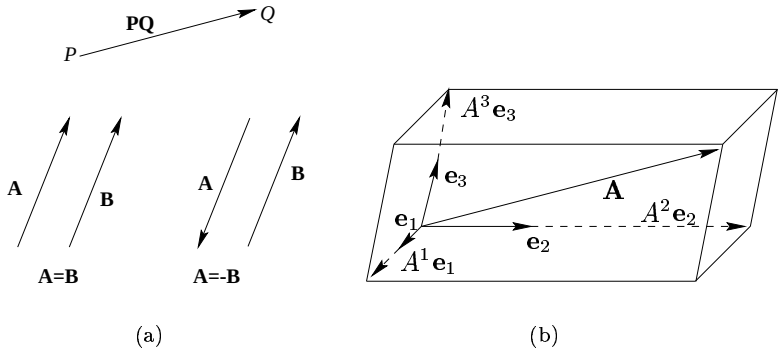

Figure 4.1: Vector representation.

Associated with any arbitraty basis is another basis that can be derived from it. We can construct this basis by taking the scalar product of the vector $\mathbf{A}$ with the

cross product $\mathbf{e}_1 \times \mathbf{e}_2$:

$$\mathbf{A} \cdot (\mathbf{e}_1 \times \mathbf{e}_2) = A^3 \mathbf{e}_3 \cdot (\mathbf{e}_1 \times \mathbf{e}_2), \tag{4.13}$$

since $\mathbf{e}_1 \times \mathbf{e}_2$ is perpendicular to both $\mathbf{e}_1$ and $\mathbf{e}_2$; then solving this expression for A^3 we obtain:

$$A^3 = \mathbf{A} \cdot \frac{\mathbf{e}_1 \times \mathbf{e}_2}{\mathbf{e}_3 \cdot (\mathbf{e}_1 \times \mathbf{e}_2)} = \mathbf{A} \cdot \frac{\mathbf{e}_1 \times \mathbf{e}_2}{[\mathbf{e}_1 \mathbf{e}_2 \mathbf{e}_3]}, \tag{4.14}$$

where [ ] is the scalar triple product. In a similar fashion, we can obtain the following expression for A^1 and A^2:

$$A^1 = \mathbf{A} \cdot \frac{\mathbf{e}_2 \times \mathbf{e}_3}{[\mathbf{e}_1 \mathbf{e}_2 \mathbf{e}_3]}, \tag{4.15}$$

$$A^2 = \mathbf{A} \cdot \frac{\mathbf{e}_3 \times \mathbf{e}_1}{[\mathbf{e}_1 \mathbf{e}_2 \mathbf{e}_3]}. \tag{4.16}$$

We thus observe that we can obtain the components A^1, A^2 and A^3 by taking the scalar product of the vector $\mathbf{A}$ with special vectors, which we denote as follows:

$$\mathbf{e}^1 = \frac{\mathbf{e}_2 \times \mathbf{e}_3}{[\mathbf{e}_1 \mathbf{e}_2 \mathbf{e}_3]}, \tag{4.17a}$$

$$\mathbf{e}^2 = \frac{\mathbf{e}_3 \times \mathbf{e}_1}{[\mathbf{e}_1 \mathbf{e}_2 \mathbf{e}_3]}, \tag{4.17b}$$

$$\mathbf{e}^3 = \frac{\mathbf{e}_1 \times \mathbf{e}_2}{[\mathbf{e}_1 \mathbf{e}_2 \mathbf{e}_3]}. \tag{4.17c}$$

The set of vectors, in Equations (4.17), constitutes the *dual* or *reciprocal basis.* Notice from the basic definitions that we have the following relations:

$$\mathbf{e}^1 \cdot \mathbf{e}_1 = \mathbf{e}^2 \cdot \mathbf{e}_2 = \mathbf{e}^3 \cdot \mathbf{e}_3 = 1, \tag{4.18}$$

and in general

$$\mathbf{e}^i \cdot \mathbf{e}_j = \delta^i_j \begin{cases} 1 & \text{if } i = j, \\ 0 & \text{if } i \neq j, \end{cases} \tag{4.19}$$

where the symbol δ^i_j is called the Kronecker delta.
It is possible, since the dual basis is linearly independent, to express a vector in terms of the dual basis (as we did for the expression (4.12)):

$$\mathbf{A} = A_1 \mathbf{e}^1 + A_2 \mathbf{e}^2 + A_3 \mathbf{e}^3, \tag{4.20}$$

and we can express the original basis (4.11) in terms of the dual basis (4.17) in the following way:

$$\mathbf{e}_1 = \frac{\mathbf{e}^2 \times \mathbf{e}^3}{[\mathbf{e}^1\mathbf{e}^2\mathbf{e}^3]}, \tag{4.21a}$$

$$\mathbf{e}_2 = \frac{\mathbf{e}^3 \times \mathbf{e}^1}{[\mathbf{e}^1\mathbf{e}^2\mathbf{e}^3]}, \tag{4.21b}$$

$$\mathbf{e}_3 = \frac{\mathbf{e}^1 \times \mathbf{e}^2}{[\mathbf{e}^1\mathbf{e}^2\mathbf{e}^3]}, \tag{4.21c}$$

It follows from the above expressions that:

$$A^1 = \mathbf{A}\cdot\mathbf{e}^1, \quad A^2 = \mathbf{A}\cdot\mathbf{e}^2, \quad A^3 = \mathbf{A}\cdot\mathbf{e}^3, \quad \text{or} \quad A^i = \mathbf{A}\cdot\mathbf{e}^i, \tag{4.22}$$

$$A_1 = \mathbf{A}\cdot\mathbf{e}_1, \quad A_2 = \mathbf{A}\cdot\mathbf{e}_2, \quad A_3 = \mathbf{A}\cdot\mathbf{e}_3, \quad \text{or} \quad A_i = \mathbf{A}\cdot\mathbf{e}_i. \tag{4.23}$$

It is now clear, from Equations (4.22) and (4.23), that there are two ways of expressing the same vector for a given basis: the *cogredient* (A_1, A_2, A_3) and *contragradient* (A^1, A^2, A^3) descriptions. It is important to note that we introduced a basis system, but *not* an unitary one. For a unitary basis, in a related coordinate system, the term cogredient is called *covariant* and contragredient is called *contravariant*.

4.2 Coordinate systems

Before entering the coordinate systems world, in order to understand why we are looking for the derivative of a vector $\mathbf{A}$ in a kind of coordinate system, we have to underline the physical meaning of the differentiation of $\mathbf{A}$ with respect to a scalar. Suppose that a vector is written as a function of a general scalar $t \Rightarrow \mathbf{A} = \mathbf{A}(t)$. This vector will usually have different magnitudes and direction for different values of the parameter t, as shown in Figure 4.2. Consider now two values of t differing by an infinitesimal amount, say t and $t + \Delta t$; then the definition of the derivative of a vector with respect to t, having in mind Figure 4.2, reads:

$$\frac{d\mathbf{A}}{dt} = \lim_{\Delta t \to 0} \frac{\mathbf{A}(t+\Delta t) - \mathbf{A}(t)}{\Delta t}. \tag{4.24}$$

By imposing now $\Delta s = |\Delta \mathbf{A}|$ so that s can be considered as the distance measured along the trajectory, we can write Equation (4.24) as follows:

$$\frac{d\mathbf{A}}{dt} = \lim_{\Delta t \to 0} \frac{\Delta \mathbf{A}}{\Delta s}\frac{\Delta s}{dt}. \tag{4.25}$$

In the limit, $\Delta\mathbf{A}/\Delta s$ is a unit vector that is tangent to the trajectory:

$$\frac{d\mathbf{A}}{dt} = \frac{ds}{dt}\hat{\mathbf{e}}_s. \tag{4.26}$$

It is clear that whenever the $\mathbf{A}$ direction changes, but its lenght is fixed, then the derivative $\Delta\mathbf{A}/dt$ is perpendicular to the same $\mathbf{A}$ vector.

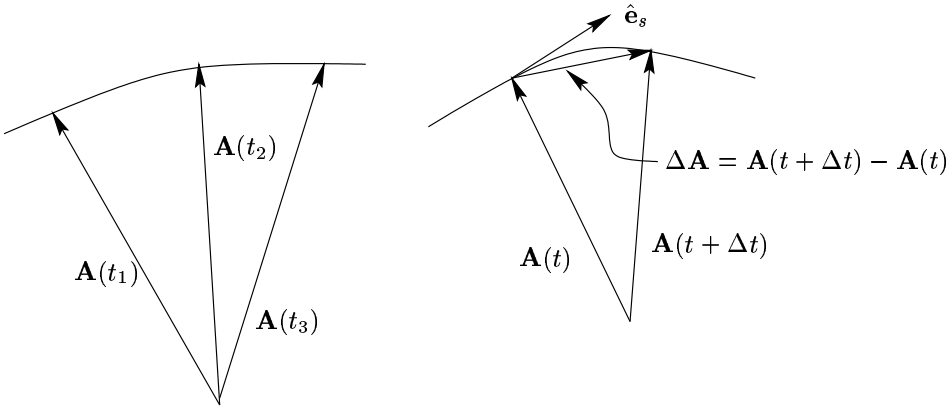

Figure 4.2: Variation of a vector as a function of a scalar t and its differential change.

4.2.1 Cartesian Coordinate System

When the basis vectors are constant, that is, with fixed lenghts and directions, the basis is called *Cartesian*. The general Cartesian system is oblique. When the basis vectors are unit and orthogonal (orthonormal), the basis system is called *rectangular Cartesian*, or simply *Cartesian*. For an orthonormal system, there is no distinction between cogredient and contragredient components;

$$[\mathbf{e}_1\mathbf{e}_2\mathbf{e}_3] = 1, \tag{4.27}$$

$$\mathbf{e}^1 = \mathbf{e}_1, \qquad \mathbf{e}^2 = \mathbf{e}_2, \qquad \mathbf{e}^3 = \mathbf{e}_3, \tag{4.28}$$

hence, let us introduce an orthonormal cartesian basis system:

$$\{\hat{\mathbf{e}}_x, \hat{\mathbf{e}}_y, \hat{\mathbf{e}}_z\} \qquad \text{or} \qquad \{\hat{\imath}_1, \hat{\imath}_2, \hat{\imath}_3\}, \tag{4.29}$$

where $\mathbf{e}^i = \mathbf{e}_i \equiv \hat{\mathbf{e}}_i, (i = x, y, z)$. A position vector to an arbitrary point (x, y, z) or (x^1, x^2, x^3), measured from the origin, is given in Figure 4.3(a) by:

$$\begin{aligned} \mathbf{r} &= x\hat{\mathbf{e}}_x + y\hat{\mathbf{e}}_y + z\hat{\mathbf{e}}_z \\ &= x^1\hat{\imath}_1 + x^2\hat{\imath}_2 + x^3\hat{\imath}_3 = x^j\hat{\imath}_j. \end{aligned} \tag{4.30}$$

The distance between two infinitesimally removed points is given by:

$$\mathrm{d}\mathbf{r} \cdot \mathrm{d}\mathbf{r} = (ds)^2 = (dx)^2 + (dy)^2 + (dz)^2. \tag{4.31}$$

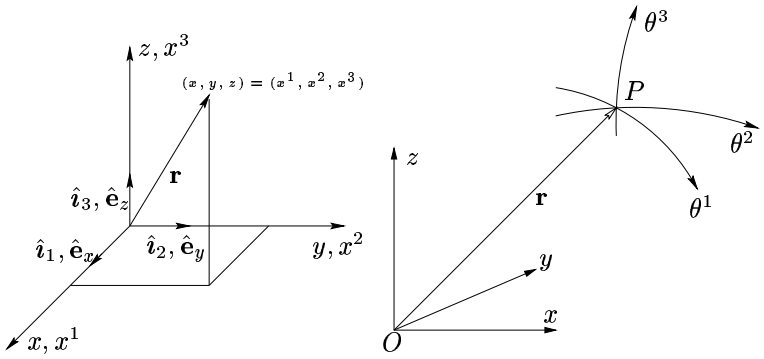

(a) Rectangular Cartesian (b) Curvilinear

Figure 4.3: Coordinate systems

4.2.2 Curvilinear Coordinates

Consider now a transformation to a new set of coordinates denoted by $(\theta^1, \theta^2, \theta^3)$:

$$\theta^1 = \theta^1(x^1, x^2, x^3) = \theta^1(x, y, z) \tag{4.32a}$$
$$\theta^2 = \theta^2(x^1, x^2, x^3) = \theta^2(x, y, z) \tag{4.32b}$$
$$\theta^3 = \theta^3(x^1, x^2, x^3) = \theta^3(x, y, z), \tag{4.32c}$$

the inverse transformation of which is ($|\partial x^j / \partial \theta^i| \neq 0$):

$$x^1 = x = x(\theta^1, \theta^2, \theta^3) \tag{4.33a}$$
$$x^2 = y = y(\theta^1, \theta^2, \theta^3) \tag{4.33b}$$
$$x^3 = z = z(\theta^1, \theta^2, \theta^3). \tag{4.33c}$$

When the above transformation (4.33) is nonlinear, the coordinate curves denoted by θ^1, θ^2 and θ^3 are curved lines and the system $(\theta^1, \theta^2, \theta^3)$ is called *curvilinear*.

When the transformation is linear, the coordinate curves will be straight lines, but not necessarly parallel to the original (x, y, z) system, and a new Cartesian system will be defined.
Consider a point P and its associated curvilinear coordinate system as illustrated in Figure 4.3(b). The position vector $\mathbf{r}$ leading from a fixed point O to the point P, can be expressed as a function of the general coordinates θ^i:

$$\mathbf{r} = \mathbf{r}(\theta^1, \theta^2, \theta^3). \tag{4.34}$$

The covariant base vector $\mathbf{g}_i$ (see pag. 157) characterize the change in the position vector along one of the coordinate curves from the given point P. Mathematically, they can be defined by the relationship:

$$\mathbf{g}_i = \frac{\partial \mathbf{r}}{\partial \theta^i}. \tag{4.35}$$

These vectors

$$\mathbf{g}_1 = \frac{\partial \mathbf{r}}{\partial \theta^1}, \quad \mathbf{g}_2 = \frac{\partial \mathbf{r}}{\partial \theta^2}, \quad \mathbf{g}_3 = \frac{\partial \mathbf{r}}{\partial \theta^3}, \tag{4.36}$$

are directed tangentially along the coordinate curves and may be applied to all vectors associated with the point P; furthermore this basis is referred to as the *unitary basis*, noting that these vectors (Equation (4.36)) are *not* unit *nor* orthogonal. Equation (4.35) assumes the position vector (4.34) to be differentiable and uniquely defined at each point. As we will see in Chapter 5, this condition is of particular importance in the numerical analysis of shells (Naomis and Lau 1990) where the continuum is discretized into a finite number of elements and the displacements behaviour of each element is specified in terms of a local coordinate system, (see Figure 4.4 for an example).
A set of vectors, referred to as contravariant base vectors, $\mathbf{g}^i$, (see pag. 157 and Figure 4.4) can be defined such that they are normal to all the covariant base vectors:

$$\mathbf{g}_i \cdot \mathbf{g}^j = \delta_i^j. \tag{4.37}$$

4.2.3 The fundamental metric

The metric tensor can be defined by considering the elementary distance between two adjacent points. Let P be a point whose coordinates are θ^a and Q a neighbouring point with coordinates $\theta^a + d\theta^a$, if $d\mathbf{r}$ defines the infinitesimal vector $\mathbf{PQ}$, then:

$$\mathrm{d}\mathbf{r} = \mathbf{g}_i d\theta^i. \tag{4.38}$$

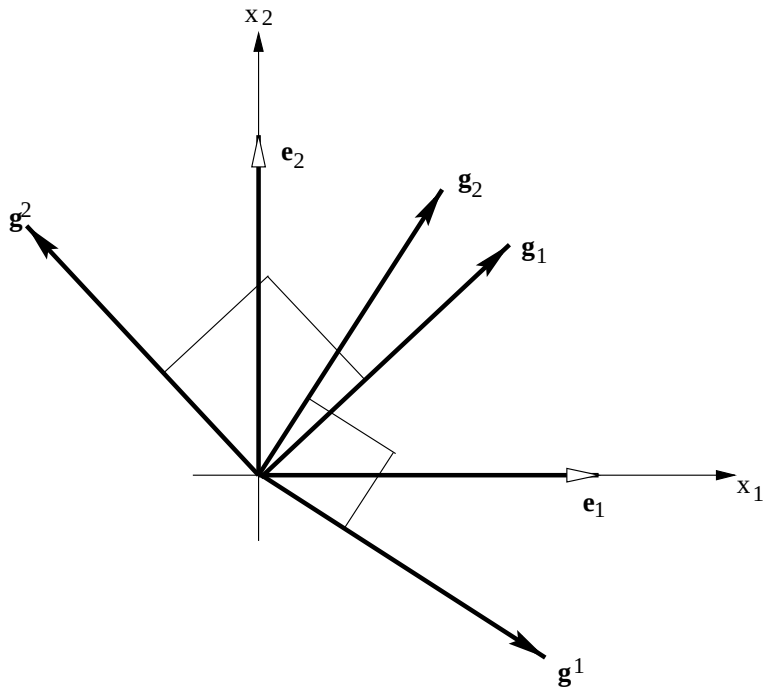

Figure 4.4: Example of a covariant and contravariant base vectors in two dimensions in a Cartesian orthogonal coordinate system.

The magnitude of the vector d$\mathbf{r}$, conventionally referred as the line element ds, can be computed by dot multiplying Equation (4.38) by itself, so as to write the square of the infinitesimal distance between two points in the unitary basis in the following way:

$$ds^2 = \mathrm{d}\mathbf{r} \cdot \mathrm{d}\mathbf{r} = \mathbf{g}_i d\theta^i \cdot \mathbf{g}_j d\theta^j, \tag{4.39}$$

and defining

$$g_{ij} = \mathbf{g}_i \cdot \mathbf{g}_j, \tag{4.40}$$

then Equation (4.39) becomes:

$$ds^2 = g_{ij} d\theta^i d\theta^j. \tag{4.41}$$

The quantities g_{ij} are the components of a symmetric tensor ($g_{ij} = g_{ji}$) referred to as the *metric* or *fundamental tensor*. The metric tensor plays a key role in

the fundamental absolute tensor calculus (Reddy and Rasmussen 1982a): if it is possible to find a transformation to a coordinate system such that all g_{ij}'s are constant, the space is *Euclidean*, otherwise it is said to be *non–Euclidean* or *Riemannian*.
By dot multiplying both sides of Equation (4.40) with the base vector $\mathbf{g}^j$, the metric tensor can be used to relate the covariant and contravariant base vectors:

$$\mathbf{g}_i = g_{ij}\mathbf{g}^j. \tag{4.42}$$

Similarly, the contravariant components of the metric tensor can be defined by the dot product of two contravariant base vectors and expressions analogous to Equation (4.40) and (4.42) can be constructed:

$$g^{ij} = \mathbf{g}^i \cdot \mathbf{g}^j, \tag{4.43}$$

$$\mathbf{g}^i = g^{ij}\mathbf{g}_j. \tag{4.44}$$

An important relationship which is often used in the numerical computation of the contravariant components of the metric tensor can be derived by dot multiplying both sides of Equation (4.44) by $\mathbf{g}_k$:

$$\mathbf{g}^i \cdot \mathbf{g}_k = g^{ij}\mathbf{g}_j \cdot \mathbf{g}_k. \tag{4.45}$$

Subsituting Equations (4.37) and (4.40) into the above relationship yelds:

$$g^{ik}g_{kj} = \delta^i_j, \tag{4.46}$$

which can be written in matrix form to represent a system of nine equations:

$$\begin{bmatrix} g_{11} & g_{12} & g_{13} \\ g_{21} & g_{22} & g_{23} \\ g_{31} & g_{32} & g_{33} \end{bmatrix} \begin{bmatrix} g^{11} & g^{12} & g^{13} \\ g^{21} & g^{22} & g^{23} \\ g^{31} & g^{32} & g^{33} \end{bmatrix} = \begin{bmatrix} 1 & 0 & 0 \\ 0 & 1 & 0 \\ 0 & 0 & 1 \end{bmatrix}. \tag{4.47}$$

Having computed the covariant components of the metric tensor and assembled them in the form required by Equation (4.47) it becomes possible to compute the contravariant components by simply inverting the covariant component matrix. Provided two independent base vectors are selected, an inverse will always exists.

4.2.4 Relation between two curvilinear coordinate sustems

The ability to establish a set of transformation equations between two coordinate systems provides a valuable tool in the numerical analysis of shell structures (Bernadou 1996). Consider a set of two different curvilinear coordinate systems $\theta^i, \tilde{\theta}^{i'}$ and assume a relationship between them exists in the form:

$$\theta^i = \theta^i(\tilde{\theta}^{1'}, \tilde{\theta}^{2'}, \tilde{\theta}^{3'}), \tag{4.48}$$

if the above transformation is reversible and possesses as many derivatives as required, the inverse can be written in the form:

$$\tilde{\theta}^{i'} = \tilde{\theta}^{i'}(\theta^1, \theta^2, \theta^3). \tag{4.49}$$

From Equations (4.48) and (4.49), the transformation derivatives $d\theta^i$ and $d\tilde{\theta}^{i'}$ are:

$$d\theta^i = \frac{\partial \theta^i}{\partial \tilde{\theta}^{j'}} d\tilde{\theta}^{j'} = \beta^i_{j'} d\tilde{\theta}^{j'}, \tag{4.50}$$

$$d\tilde{\theta}^{j'} = \frac{\partial \tilde{\theta}^{j'}}{\partial \theta^i} d\theta^i = \beta^{j'}_i d\theta^i, \tag{4.51}$$

which can be combined to form the relationship:

$$\delta^i_j = \frac{\partial \theta^i}{\partial \tilde{\theta}^{k'}} \frac{\partial \tilde{\theta}^{k'}}{\partial \theta^j} = \beta^i_{k'} \beta^{k'}_j. \tag{4.52}$$

Consider an arbitrary vector $\mathbf{v}$ at a point P and define $\mathbf{v}^i = (\mathbf{v}^1, \mathbf{v}^2, \mathbf{v}^3)$ and $\mathbf{v}^{i'} = (\mathbf{v}^{1'}, \mathbf{v}^{2'}, \mathbf{v}^{3'})$ as the contravariant components of $\mathbf{v}$ with coordinates θ^i and $\theta^{i'}$ respectively. Using the definitions introduced by Equations (4.50) and (4.51), the following contravariant transformations can be written:

$$\mathbf{v}^i = \beta^i_{j'} \mathbf{v}^{j'}, \tag{4.53}$$

$$\mathbf{v}^{j'} = \beta^{j'}_i \mathbf{v}^i, \tag{4.54}$$

and similarly, the relationship between the covariant components are:

$$\mathbf{v}_i = \beta^{j'}_i \mathbf{v}_{j'}, \tag{4.55}$$

$$\mathbf{v}_{j'} = \beta^i_{j'} \mathbf{v}_i. \tag{4.56}$$

Now, the displacement vector $\mathbf{v}$, can be defined with respect to either of the coordinate systems:

$$\mathbf{v} = v^i \mathbf{g}_i = v^{i'} \mathbf{g}_{i'} \quad \text{or} \quad \mathbf{v} = v_j \mathbf{g}^j = v_{j'} \mathbf{g}^{j'}, \tag{4.57}$$

and dot multiplying both sides of Equations (4.57) by $\mathbf{g}^k$ and $\mathbf{g}_k$:

$$\mathbf{v}^k = v^{i'} \mathbf{g}_{i'} \cdot \mathbf{g}^k \quad \text{and} \quad \mathbf{v}_k = v_{j'} \mathbf{g}^{j'} \cdot \mathbf{g}_k. \tag{4.58}$$

Comparing Equations (4.53) and (4.55) with Equation (4.58), enables the *transformation tensors* $\beta^i_{j'}$ and $\beta^{j'}_i$, to be defined alternatively as:

$$\beta^i_{j'} = \mathbf{g}_{j'} \cdot \mathbf{g}^i \quad \text{and} \quad \beta^{j'}_i = \mathbf{g}^{j'} \cdot \mathbf{g}_i. \tag{4.59}$$

Furthermore, the general tensor $\mathbf{T}$ can be given either in the old base $\mathbf{g}_i$ or in the new base $\mathbf{g}_{i'}$ (Eschenauer, Olhoff, and Schnell 1997):

$$\mathbf{T} = t^{k'l'}\mathbf{g}_{k'}\mathbf{g}_{l'} = t^{ij}\mathbf{g}_i\mathbf{g}_j. \tag{4.60}$$

The transformation formulas read as follows:

$$t^{ij} = \beta^i_{k'}\beta^j_{l'}t^{k'l'} \quad \text{or} \quad t^{i'j'} = \beta^{i'}_k\beta^{j'}_l t^{kl}, \tag{4.61}$$

then from:

$$\mathbf{T} = t_{ij}\mathbf{g}^i\mathbf{g}^j = t_{k'l'}\mathbf{g}^{k'}\mathbf{g}^{l'}, \tag{4.62}$$

follows:

$$t_{ij} = \beta^{k'}_i\beta^{l'}_j t_{k'l'} \quad \text{or} \quad t_{i'j'} = \beta^k_{i'}\beta^l_{j'}t_{kl}. \tag{4.63}$$

4.2.5 Christoffel symbols

In a general curvilinear coordinate system we are interested in derivatives of the basis vectors with respect to the coordinates. Consider the partial derivative of the i–th unitary vector with respect to the j–th coordinate. We can express this vector as follows:

$$\mathbf{g}_{i,j} = \Gamma^k_{ij}\mathbf{g}_k = \Gamma_{ijk}\mathbf{g}^k. \tag{4.64}$$

By dot multiplying Equation (4.64) with $\mathbf{g}^l$ or $\mathbf{g}_l$, the symbols Γ^k_{ij} and Γ_{ijk} can be isolated:

$$\Gamma_{ijk} = \mathbf{g}_{i,j} \cdot \mathbf{g}_k, \tag{4.65}$$

$$\Gamma^k_{ij} = \mathbf{g}_{i,j} \cdot \mathbf{g}^k. \tag{4.66}$$

Equations (4.65) and (4.66) define the *Christoffel symbols of the first and second kind* respectively (DoCarmo 1976, pag.231). The third index of Christoffel symbol can be raised and lowered by using the metric tensor (4.40) and (4.43):

$$\Gamma_{ijk} = \Gamma^l_{ij}\mathbf{g}_{lk}, \tag{4.67}$$

$$\Gamma^k_{ij} = \Gamma_{ijl}\mathbf{g}^{lk}. \tag{4.68}$$

In addition, differentiating Equation (4.34), yields:

$$\mathbf{r}_{,ij} = \mathbf{g}_{i,j} = \mathbf{r}_{,ji} = \mathbf{g}_{j,i}, \tag{4.69}$$

which, combined with Equation (4.64) shows that the Christoffel symbols are symmetric with respect to the first two subscripts:

$$\Gamma_{ijk} = \Gamma_{jik}, \tag{4.70}$$

$$\Gamma^k_{ij} = \Gamma^k_{ji}. \tag{4.71}$$

In determining the tensorial quantities associated with a coordinate system, it is usually possible to obtain explicit expressions for the covariant components of the metric tensor (4.40). These expressions can be differentiated and combined with Equation (4.64) to yield an alternative form for the definition of the Christoffel symbols (Reddy and Rasmussen 1982a, pag.75-77):

$$\Gamma_{ijk} = \frac{1}{2}(g_{jk,i} + g_{ki,j} - g_{ij,k}) \quad \Gamma^k_{ij} = \frac{1}{2}g^{kl}(g_{li,j} + g_{lj,i} - g_{ij,l}). \tag{4.72}$$

4.2.6 Covariant derivatives

Let $\mathbf{v}$ be an arbitrary vector defined in terms of its contravariant components:

$$\mathbf{v} = v^i\mathbf{g}_i. \tag{4.73}$$

Differentiating Equation (4.73) yields:

$$\mathbf{v}_{,j} = v^i_{,j}\mathbf{g}_i + v^i\mathbf{g}_{i,j},$$

which can be combined with Equation (4.64) to form:

$$\mathbf{v}_{,j} = (v^i_{,j} + v^k\Gamma^i_{kj})\mathbf{g}_i. \tag{4.74}$$

Defining (Naomis and Lau 1990, pag.20):

$$v^i|_j = (v^i_{,j} + v^k\Gamma^i_{kj}), \tag{4.75}$$

enables Equation (4.74) to be semplified to:

$$\mathbf{v}_{,j} = v^i|_j\mathbf{g}_i. \tag{4.76}$$

The quantity $v^i|_j$ is called the *covariant derivative* of the contravariant component v^i and is a second order tensor (Ciarlet 2000, pag.30). By adopting a similar approach, the covariant derivative of the covariant component v_i can be expressed in the form:

$$v_i|_j = (v_{i,j} - v^k \Gamma^k_{ij}). \tag{4.77}$$

Since $v^i|_j$ and $v_i|_j$ are the components of a tensor, the index i can be raised and lowered in the conventional manner:

$$v_i|_j = v^k|_j g_{ki}, \tag{4.78}$$

$$v^i|_j = v_k|_j g^{ki}. \tag{4.79}$$

The above concepts can be extended to obtain expressions for the covariant derivatives of higher order tensors. Of particular interest are the equations describing the covariant derivatives of second order tensors. These are used in the formulation of a number of geometric properties related to a surface's curvature (Gould 1988, pag.17-45).
Let ϕ be a scalar expressed as the product of a second order tensor A_{ij} with two arbitrary vectors u^i and v^j:

$$\phi = A_{ij} u^i v^j. \tag{4.80}$$

Differentiating ϕ with respect to x^k yields:

$$\phi_{,k} = A_{ij,k} u^i v^j + A_{ij} u^i_{,k} v^j + A_{ij} u^i v^j_{,k}. \tag{4.81}$$

Similarly the covariant derivative of Equation (4.80) may be written in the form:

$$\phi|_k = A_{ij}|_k u^i v^j + A_{ij} u^i|_k v^j + A_{ij} u^i v^j|_k. \tag{4.82}$$

Using Equation (4.75),

$$\phi|_k = A_{ij,k} u^i v^j + A_{ij} u^i|_k v^j + A_{ij} u^i v^j|_k - A_{ij} u^l \Gamma^i_{kl} v^j - A_{ij} u^i v^l \Gamma^j_{kl}, \tag{4.83}$$

and since ϕ is a scalar, $\phi_{,k} = \phi|_k$, enabling Equations (4.82) and (4.83) to be used to define the covariant derivative of A_{ij} as:

$$A_{ij}|_k = A_{ij,k} - A_{lj} \Gamma^l_{ik} - A_{il} \Gamma^l_{kj}. \tag{4.84}$$

In a similar way, relationships can be derived for the contravariant and mixed components of the tensor A (Naomis and Lau 1990, pag.21):

$$A^i_j|_k = A^i_{j,k} + A^l_j \Gamma^i_{kl} - A^i_l \Gamma^l_{jk}, \tag{4.85}$$

$$A^j_i|_k = A^j_{i,k} - A^j_l \Gamma^l_{ik} + A^l_i \Gamma^j_{kl}, \tag{4.86}$$

$$A^{ij}|_k = A^{ij}_{,k} + A^{lj} \Gamma^i_{kl} + A^{il} \Gamma^j_{kl}. \tag{4.87}$$

4.3 Surface geometry

4.3.1 Curvilinear coordinates on a surface

We[1] give here the main results in the geometrical description of a shell; for further details, we refer the reader to (Koiter 1959), (Green and Zerna 1968, pag.373-451), (Krätzig 1980) and more recently to (Bernadou 1996) and (Ciarlet 2000). First we will define the middle surface of the shell and then we introduce its thickness. Let $\mathcal{E}^3$ be the usual euclidean space referred to a fixed orthonormal reference system $(O, \hat{\imath}_1, \hat{\imath}_2, \hat{\imath}_3)$ (pag. 158), and Ω a bounded open subset of the plane $\mathcal{E}^2$ whose boundary is denoted Γ. Then the *middle surface* $\overline{S}$ of the shell is the image in $\mathcal{E}^3$ of the set $\overline{\Omega} = \Omega \cup \Gamma$ (Ω is called the *reference domain*) by the mapping $\mathbf{s}$:

$$\mathbf{s}\colon (x^\alpha, x^\beta) \in \overline{\Omega} \subset \mathcal{E}^2 \longrightarrow \mathbf{s}(x^\alpha, x^\beta) \in \overline{S} \subset \mathcal{E}^3.$$

We write $\partial S = \mathbf{s}(\Gamma)$, such that $\overline{S} = S \cup \partial S$, and we assume $\mathbf{s}$ and Γ to be sufficiently regular. In particular, we assume that all points on the middle surface $\overline{S} = \mathbf{s}(\overline{\Omega})$ are regular so that, using Equation (4.35), the vectors

$$\mathbf{a}_i = \mathbf{s}_{,i} = \frac{\partial \mathbf{s}}{\partial x^i}, \quad i = \alpha, \beta, \tag{4.88}$$

are linearly independent for all points $(x^\alpha, x^\beta) \in \overline{\Omega}$. These two vectors define the *tangent plane* at the surface $\overline{S}$ in all points $\mathbf{s}(x^\alpha, x^\beta)$ and are usually referred as the *first fundamental forms* of the middle surface (Bernadou 1996). The *normal vector* to the tangent plane is given by:

$$\mathbf{a}^3 = \mathbf{a}_3 = \frac{\mathbf{a}_\alpha \times \mathbf{a}_\beta}{|\mathbf{a}_\alpha \times \mathbf{a}_\beta|}, \tag{4.89}$$

$|\cdot|$ denoting the euclidean norm in the space $\mathcal{E}^3$ equipped with the usual scalar product $(\mathbf{a}, \mathbf{b}) \longrightarrow \mathbf{a} \cdot \mathbf{b}$. Then the point $\mathbf{s}(x^\alpha, x^\beta)$ and the three vectors $\mathbf{a}_i$ define a *local curvilinear coordinate frame* for the middle surface with the *covariant basis* attached to the point $\mathbf{s}(x^\alpha, x^\beta)$ (see Figure 4.5).
We add to the two curvilinear coordinates x^α and x^β, which enable the middle surface to be defined, a third coordinate z, which is measured along the normal $\mathbf{a}_3$ to the surface $\overline{S}$ at the point $\mathbf{s}(x^\alpha, x^\beta)$. This system (x^α, x^β, z) is, at least locally, a system of curvilinear coordinates of $\mathcal{E}^3$. The *thickness* t of the shell is defined through the mapping:

$$t\colon (x^\alpha, x^\beta) \in \overline{\Omega} \longrightarrow \{x \in \mathbb{R}; x > 0\}.$$

[1] It should be remembered that all Greek indices take the values 1, 2 and all Latin indices the values 1, 2, 3.

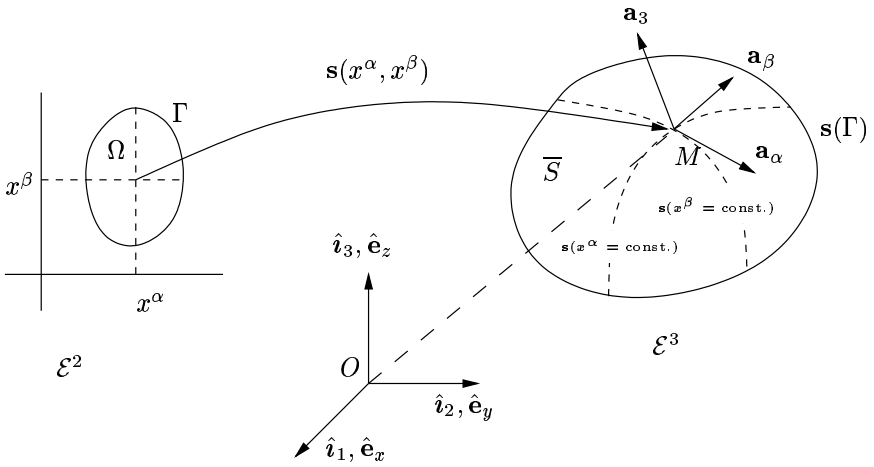

Figure 4.5: Definition of the middle surface $\overline{S}$.

The *shell* $\mathcal{C}$ is then the closed subset of $\mathcal{E}^3$ defined by:

$$\mathcal{C} = \Big\{ M \in \mathcal{E}^3; \mathbf{OM} = \mathbf{r} = \mathbf{s}(x^\alpha, x^\beta) + z\mathbf{a}_3, \quad (x^\alpha, x^\beta) \in \overline{\Omega}, \\ -\frac{1}{2}t(x^\alpha, x^\beta) \leq z \leq \frac{1}{2}t(x^\alpha, x^\beta) \Big\}. \tag{4.90}$$

The derivatives of the vector $\mathbf{OM} = \mathbf{r} = \mathbf{s}(x^\alpha, x^\beta) + z\mathbf{a}_3$ are given by the vector $\mathbf{g}_i$:

Equation (4.88)

$$\mathbf{g}_i = \mathbf{OM}_{,i} = \mathbf{r}_{,i} = \mathbf{s}_{,i} + z\mathbf{a}_{3,i} \overset{\downarrow}{=} \mathbf{a}_i + z\mathbf{a}_{3,i}, \quad i = \alpha, \beta. \tag{4.91}$$

It also becomes advantageous to adopt separate notations for tensorial quantities related to points lying on the middle surface and those which are within its immediate vicinity: the notations are summarized in Table 4.1.
Since $\mathbf{g}_3$ is assumed to be normal to the vectors $\mathbf{g}_\alpha$ and $\mathbf{g}_\beta$, it follows that:

$$\mathbf{g}_3 = \frac{\mathbf{g}_\alpha \times \mathbf{g}_\beta}{\|\mathbf{g}_\alpha \times \mathbf{g}_\beta\|}, \tag{4.92}$$

Geometry	Middle Surface	General Surface
Position vector	$\mathbf{s}$	$\mathbf{r}$
Line element	$\mathrm{d}\mathbf{s}$	$\mathrm{d}\mathbf{r}$
Base vectors	$\mathbf{a}_i \quad \mathbf{a}^i \quad \mathbf{a}_3 = \mathbf{a}^3$	$\mathbf{g}_i \quad \mathbf{g}^i \quad \mathbf{g}_3 = \mathbf{g}^3$
Metric tensors	$a_{\alpha\beta} \quad a^{\alpha\beta}$	$g_{\alpha\beta} \quad g^{\alpha\beta}$
Christoffel symbols	$\Gamma^{\gamma}_{\beta\alpha}$	$\overline{\Gamma}^{\gamma}_{\beta\alpha}$

Table 4.1: Middle and general surface notation.

and

$$\mathbf{g}_3 \cdot \mathbf{g}_3 = 1 \tag{4.93a}$$

$$\mathbf{g}_\alpha \cdot \mathbf{g}_3 = g_{\alpha 3} = 0 \tag{4.93b}$$

$$\mathbf{g}_{3,\alpha} \cdot \mathbf{g}_3 = 0 \tag{4.93c}$$

$$\mathbf{g}_{3,3} \cdot \mathbf{g}_3 = 0 \tag{4.93d}$$

As a result, the metric tensor components (Equation (4.40)) expressed in matrix form are:

$$g_{ij} = \begin{bmatrix} g_{11} & g_{12} & 0 \\ g_{21} & g_{22} & 0 \\ 0 & 0 & 1 \end{bmatrix}. \tag{4.94}$$

The Christoffel symbol Γ_{ijk} has been defined previously by Equation (4.65); it follows from Equations (4.93c) and (4.93d) that

$$\overline{\Gamma}_{3\alpha 3} = \overline{\Gamma}_{\alpha 33} = \overline{\Gamma}_{33\alpha} = \overline{\Gamma}_{333} = 0. \tag{4.95}$$

In addition, by differentiating Equation (4.93b):

$$\mathbf{g}_{\alpha,\beta} \cdot \mathbf{g}_3 + \mathbf{g}_{3,\beta} \cdot \mathbf{g}_\alpha = 0, \tag{4.96}$$

which after combining with Equation (4.65) yields:

$$\overline{\Gamma}_{\alpha\beta 3} = -\overline{\Gamma}_{3\beta\alpha} = -\overline{\Gamma}_{\beta 3\alpha} = \overline{\Gamma}_{\beta\alpha 3} = -\overline{\Gamma}_{3\alpha\beta} = -\overline{\Gamma}_{\alpha 3\beta}. \tag{4.97}$$

In addition, Equation (4.68) may be combined with Equations (4.94) and (4.95) to simplify a number of the Christoffel symbols of the second kind:

$$\overline{\Gamma}^3_{3\alpha} = \overline{\Gamma}^{\alpha}_{33} = \overline{\Gamma}^3_{33} = 0. \tag{4.98}$$

These results can be substituted into Equations (4.75) and (4.77) to arrive at the following relationship for the covariant derivatives of a vector component v_α in the general surface:

$$\begin{aligned} v_\alpha|_\beta &= v_{\alpha,\beta} - v_\gamma \overline{\Gamma}^\gamma_{\alpha\beta} - v_3 \overline{\Gamma}^3_{\alpha\beta} \\ v_\alpha|_3 &= v_{\alpha,3} - v_\gamma \overline{\Gamma}^\gamma_{\alpha 3} \\ v_3|_\alpha &= v_{3,\alpha} - v_\gamma \overline{\Gamma}^\gamma_{3\alpha} \\ v^\alpha|_\beta &= v^\alpha_{,\beta} + v^\gamma \overline{\Gamma}^\alpha_{\beta\gamma} + v^3 \overline{\Gamma}^\alpha_{\beta 3} \\ v^\alpha|_3 &= v^\alpha_{,3} + v^\gamma \overline{\Gamma}^\alpha_{\gamma 3} \\ v^3|_\alpha &= v^3_{,\alpha} + v^\gamma \overline{\Gamma}^3_{\alpha\gamma}. \end{aligned} \tag{4.99}$$

In Section 4.2.5, the Christoffel symbol has been introduced to represent the components of the derivative of a base vector. For the middle surface $z = 0$, the third component of Equation (4.64) may be expanded and written in the form:

$$\mathbf{a}_{3,\alpha} = \Gamma_{3\alpha\beta}\mathbf{a}^\beta + \Gamma_{3\alpha 3}\mathbf{a}^3. \tag{4.100}$$

Using Equations (4.95) and (4.97), the above expression can be simplified to:

$$\mathbf{a}_{3,\alpha} = -\Gamma_{\alpha\beta 3}\mathbf{a}^\beta. \tag{4.101}$$

The term $\Gamma_{\alpha\beta 3}$ is a measure of the rate of change of the base vector $\mathbf{a}_3$ along a parametric curve. $\Gamma_{\alpha\beta 3}$ is a plane symmetric tensor and is expressed by the symbol $b_{\alpha\beta}$ which is referred to as the *curvature tensor* or the *second fundamental form* of the middle surface (Bernadou 1996). Thus, Equation (4.101) can be rewritten as:

$$b_{\alpha\beta} = \Gamma_{\alpha\beta 3} = -\mathbf{a}_{3,\alpha} \cdot \mathbf{a}_\beta. \tag{4.102}$$

Alternatively, if Equation (4.96) is restricted to the middle surface $z = 0$, the curvature tensor may be defined by the expression:

$$\mathbf{a}_{\alpha,\beta} \cdot \mathbf{a}_3 = -\mathbf{a}_{3,\beta} \cdot \mathbf{a}_\alpha = b_{\alpha\beta}. \tag{4.103}$$

The above formula is simple and particularly useful in the numerical computation of the curvature tensor where it is often possible to express the base vectors $\mathbf{a}_\alpha$ as functions of the curvilinear coordinates x^α.
The mixed and contravariant components of the curvature tensor can be derived using the metric tensor of the middle surface:

$$\begin{aligned} b^\beta_\alpha &= b_{\alpha\gamma} a^{\gamma\beta} \\ b^{\alpha\beta} &= b^{\alpha\gamma} a^{\gamma\beta}. \end{aligned} \tag{4.104}$$

Consider a vector $\mathbf{v}$ which is defined in the form:

$$\mathbf{v} = v_\alpha \mathbf{a}^\alpha + v_3 \mathbf{a}^3. \tag{4.105}$$

Taking the derivative of $\mathbf{v}$ with respect to x^β and making use of Equations (4.76) and (4.99) we obtain:

$$\mathbf{v}_{,\beta} = v_\alpha|_\beta \mathbf{a}^\alpha + v_3|_\beta \mathbf{a}^3 = (v_{\alpha,\beta} - v_\gamma \Gamma^\gamma_{\alpha\beta} - v_3 b_{\alpha\beta})\mathbf{a}^\alpha + (v_{3,\beta} + v_\gamma b^\gamma_\beta)\mathbf{a}^3. \tag{4.106}$$

Moving from the definition of the *covariant derivative in a three–dimensional manifold* $\mathcal{E}^3$, given by Equation (4.77), we can introduce the covariant derivative on a surface (middle) in $\mathcal{E}^2$ (Ciarlet 2000, pag.88-89), that is the two dimensional counterpart of Equation (4.77):

$$v_\alpha \|_\beta = v_{\alpha,\beta} - v_\gamma \Gamma^\gamma_{\alpha\beta}. \tag{4.107}$$

This enables Equation (4.106) to be semplified yielding:

$$\mathbf{v}_{,\beta} = (v_\alpha \|_\beta - v_3 b_{\alpha\beta})\mathbf{a}^\alpha + (v_{3,\beta} + v_\gamma b^\gamma_\beta)\mathbf{a}^3. \tag{4.108}$$

The covariant derivative of v_α can therefore be written in the form:

$$v_\alpha|_\beta = v_\alpha \|_\beta - v_3 b_{\alpha\beta}. \tag{4.109}$$

Similarly, if the vector $\mathbf{v}$ is defined in terms of its contravariant components the following relationship can be derived:

$$v^\alpha \|_\beta = v^\alpha_{,\beta} + v^\gamma \Gamma^\alpha_{\beta\gamma} \tag{4.110}$$

$$v^\alpha|_\beta = v^\alpha \|_\beta - v^3 b^\alpha_\beta \tag{4.111}$$

$$\mathbf{v}_{,\beta} = \left(v^\alpha \|_\beta + v^3 b^\alpha_\beta\right) \mathbf{a}_\alpha + \left(v^3_{,\beta} + v^\gamma b_{\gamma\beta}\right) \mathbf{a}_3. \tag{4.112}$$

Generally, $\mathbf{v}$ is also defined for points adjacent to the surface. Hence the partial derivative of $\mathbf{v}$ with respect to x^3 exists and can be expresed as a function of the contravariant or covariant base vectors as detailed below:

$$\mathbf{v}_{,3} = v_\alpha|_3 \mathbf{a}^\alpha + v_3|_3 \mathbf{a}^3 = (v_{\alpha,3} + v_\gamma b^\gamma_\alpha)\, \mathbf{a}^\alpha + v_{3,3}\mathbf{a}^3, \tag{4.113}$$

$$\mathbf{v}_{,3} = v^\alpha|_3 \mathbf{a}_\alpha + v^3|_3 \mathbf{a}_3 = \left(v^\alpha_{,3} + v^\gamma b^\alpha_\gamma\right) \mathbf{a}_\alpha + v^3_{,3}\mathbf{a}_3. \tag{4.114}$$

The idea of a two dimensional counterpart for the covariant derivative of surface vectors can be extended to surface tensors of any order. Of particular interest is

its application to plane tensors such as the curvature tensor. Since $b_{3\alpha} = b_{\alpha 3} = b_{33} = 0$, Equation (4.84) can be expanded to yield:

$$b_{\alpha\beta}|_\gamma = b_{\alpha\beta}\|_\gamma = b_{\alpha\beta,\gamma} - b_{\delta\beta}\Gamma^\delta_{\alpha\gamma} - b_{\alpha\delta}\Gamma^\delta_{\beta\gamma}. \tag{4.115}$$

An important group of relationships required in developing a general shell theory in tensor form are the Gauss-Codazzi equations of differential geometry. Briefly, these equations allow the terms β and γ within Equation (4.115) to be interchanged and can be derived by comparing the components of the partial derivatives $\mathbf{a}_{\alpha,\beta\gamma}$ and $\mathbf{a}_{\alpha,\gamma\beta}$. Restating Equation (4.64) in planar form:

$$\mathbf{a}_{\alpha,\beta} = \Gamma^\delta_{\alpha\beta}\mathbf{a}_\delta + b_{\alpha\beta}\mathbf{a}_3. \tag{4.116}$$

Differentiating Equation (4.116) with respect to x^γ and collecting terms, we write:

$$\mathbf{a}_{\alpha,\beta\gamma} = \left(\Gamma^\delta_{\alpha\beta,\gamma} + \Gamma^\xi_{\alpha\beta}\Gamma^\delta_{\xi\gamma} - b_{\alpha\beta}b^\delta_\gamma\right)\mathbf{a}_\delta + \left(\Gamma^\xi_{\alpha\beta}b_{\xi\gamma} + b_{\alpha\beta,\gamma}\right)\mathbf{a}_3. \tag{4.117}$$

Now $\mathbf{a}_{\alpha,\gamma\beta}$ can be obtained by interchanging the indices β and γ. Since $\mathbf{a}_{\alpha,\beta\gamma}$ and $\mathbf{a}_{\alpha,\gamma\beta}$ are equivalent, the $\mathbf{a}_3$ components may be compared to yield the relationship:

$$b_{\alpha\beta,\gamma} - \Gamma^\xi_{\alpha\gamma}b_{\xi\beta} = b_{\alpha\gamma,\beta} - \Gamma^\xi_{\alpha\beta}b_{\xi\gamma}. \tag{4.118}$$

Substituting Equation (4.118) into Equation (4.115) enables the standard form of the Gauss-Codazzi equations to be written:

$$\boxed{b_{\alpha\beta}\|_\gamma = b_{\alpha\gamma}\|_\beta.} \tag{4.119}$$

Adopting a similar line of reasoning it may also be concluded that:

$$\boxed{b^\alpha_\beta\|_\gamma = b^\alpha_\gamma\|_\beta.} \tag{4.120}$$

4.4 The strain tensor

Consider two adjacent points A and B which are within a continuous three dimensional body as illustrated in Figure 4.6. While the body is in an undeformed state, a curvilinear coordinate system x^i is established and the points A and B are assumed to denote the end points of an element vector $\mathrm{d}\mathbf{s}$. Using Equations (4.38) and (4.39), the vector $\mathrm{d}\mathbf{s}$ may be written in the form:

$$\mathrm{d}\mathbf{s} = \mathbf{g}_i \mathrm{d}x^i, \tag{4.121}$$

and the square of the line element, ds, may be computed from the relationship:

$$ds^2 = \mathrm{d}\mathbf{s}\cdot\mathrm{d}\mathbf{s} = g_{ij}dx^i dx^j. \tag{4.122}$$

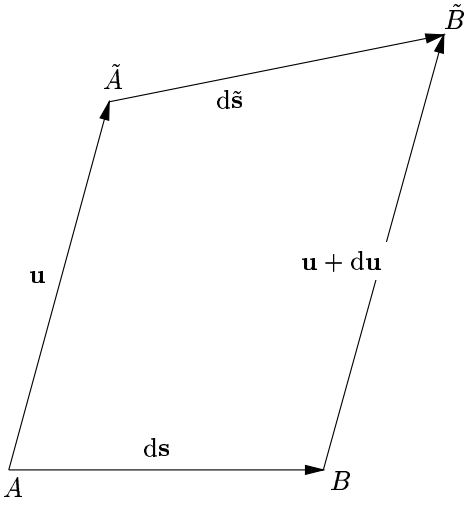

Figure 4.6: Displacement and strain.

During deformation, point A undergoes the displacement $\mathbf{u}$ and moves to $\tilde{A}$, while point B experiences a slightly different displacement $\mathbf{u} + \mathrm{d}\mathbf{u}$ when moving to $\tilde{B}$. If the coordinate system is allowed to undergo the same deformation as the body, the deformed vector $\mathrm{d}\tilde{\mathbf{s}}$ can be written as:

$$\mathrm{d}\tilde{\mathbf{s}} = \tilde{\mathbf{g}}_i dx^i. \tag{4.123}$$

Similarly, the square of the line element $d\tilde{s}$ is:

$$d\tilde{s}^2 = \tilde{g}_{ij} dx^i dx^j \tag{4.124}$$

The degree of deformation is characterized by the difference in the squares of the line elements $d\mathbf{s}$ and $d\tilde{\mathbf{s}}$:

$$d\tilde{s}^2 - ds^2 = (\tilde{g}_{ij} - g_{ij})\, dx^i dx^j. \tag{4.125}$$

Defining

$$\gamma_{ij} = \frac{1}{2}(\tilde{g}_{ij} - g_{ij}), \tag{4.126}$$

Equation (4.125) becomes

$$d\tilde{s}^2 - ds^2 = 2\gamma_{ij} dx^i dx^j. \tag{4.127}$$

The quantities γ_{ij} are the symmetrical components of a covariant tensor which is called the *strain tensor* (Green and Zerna 1968, pag.56) and is referred to the middle surface.
It is possible to express the strain components γ_{ij} in terms of the displacement vector $\mathbf{u}$ by examining the deformation of two adjacent points within a body. From Figure 4.6, the following vector equation can be constructed:

$$\mathrm{d}\tilde{\mathbf{s}} + \mathbf{u} = \mathrm{d}\mathbf{s} + \mathbf{u} + \mathrm{d}\mathbf{u}. \tag{4.128}$$

Using Equation (4.76), the infinitesimal change in displacement, $\mathrm{d}\mathbf{u}$, can be written as:

$$\mathrm{d}\mathbf{u} = u_k|_j \mathbf{g}^k dx^j. \tag{4.129}$$

Substituting Equation (4.129) into Equation (4.128) yields:

$$\mathrm{d}\tilde{\mathbf{s}} = \mathrm{d}\mathbf{s} + u_k|_j \mathbf{g}^k dx^j, \tag{4.130}$$

which allows the deformed line element to be expressed as:

$$\begin{aligned} \mathrm{d}\tilde{\mathbf{s}} \cdot \mathrm{d}\tilde{\mathbf{s}} &= \left(\mathbf{g}_i dx^i + u_k|_i \mathbf{g}^k dx^i\right) \cdot \left(\mathbf{g}_j dx^j + u_l|_j \mathbf{g}^l dx^j\right) \\ &= \left(g_{ij} + u_i|_j + u_j|_i + u^k|_i u_k|_j\right) dx^i dx^j. \end{aligned} \tag{4.131}$$

Through Equations (4.122), (4.125) and (4.128), the above expression simplifies to

$$2\gamma_{ij} dx^i dx^j = \left(u_i|_j + u_j|_i + u^k|_i u_k|_j\right) dx^i dx^j. \tag{4.132}$$

The factors dx^i and dx^j cannot simply be cancelled on both sides since these expressions represent the sums of products containing the factors $\gamma_{11}, \gamma_{12}, \ldots$. However, Equation (4.132) holds for the components of any line element vector $\mathrm{d}\mathbf{s}$. By selecting a line element for which only $dx^1 \neq 0$, it can be shown that (Green and Zerna 1968, pag.57):

$$\gamma_{ij} = \frac{1}{2}\left(u_i|_j + u_j|_i + u^k|_i u_k|_j\right). \tag{4.133}$$

This process may then be repeated for $i, j = 2, 3$. For mixed values of the indices, a line element in the form

$$\mathrm{d}\mathbf{s} = \mathbf{g}_1 dx^1 + \mathbf{g}_2 dx^2, \tag{4.134}$$

is selected and a similar process is adopted to show that Equation (4.133) is valid for all i, j.

The strain-displacement equation defined above is nonlinear as a result of the quadratic term $u^k|_i u_k|_j$. It is based solely on the assumption that the body undergoing deformation is continuous. For small displacements, the strains associated with the quadratic terms can be assumed negligible in comparison to the linear ones thereby reducing Equation (4.133) to:

$$\gamma_{ij} = \frac{1}{2}\left(u_i|_j + u_j|_i\right). \tag{4.135}$$

4.5 The stress tensor

If a three dimensional body is in equilibrium under a system of forces, then the stresses within the body can be studied by considering an infinitesimal area $d\mathbf{A}$ of arbitrary size and orientation (Flügge 1960). At any point within the body, a reference frame and its associated base vectors $\mathbf{g}_i$ may be established. Together with the three curves AB, AC and CB illustrated in Figure 4.7, the base vectors may be used to form the edges of a tetrahedron. The area of the triangle ABC can be computed via the vector cross product:

$$d\mathbf{A} = \frac{1}{2}\mathrm{d}\mathbf{r} \times \mathrm{d}\mathbf{s}. \tag{4.136}$$

Therefore, using $\mathrm{d}\mathbf{r} = \mathrm{d}\mathbf{b} - \mathrm{d}\mathbf{a}$ and $\mathrm{d}\mathbf{s} = \mathrm{d}\mathbf{c} - \mathrm{d}\mathbf{a}$, Equation (4.136) can be

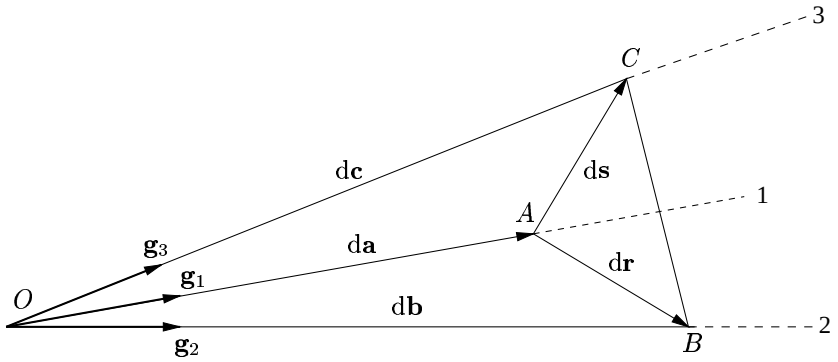

Figure 4.7: Stress definition.

expanded to yield:

$$\begin{aligned} d\mathbf{A} &= \frac{1}{2}\left(\mathrm{d}\mathbf{b} - \mathrm{d}\mathbf{a}\right) \times \left(\mathrm{d}\mathbf{c} - \mathrm{d}\mathbf{a}\right) \\ &= \frac{1}{2}\left(\mathrm{d}\mathbf{b} \times \mathrm{d}\mathbf{c} + \mathrm{d}\mathbf{c} \times \mathrm{d}\mathbf{a} + \mathrm{d}\mathbf{a} \times \mathrm{d}\mathbf{b}\right). \end{aligned} \tag{4.137}$$

The vectors $\mathrm{d}\mathbf{a}, \mathrm{d}\mathbf{b}$ and $\mathrm{d}\mathbf{c}$ have only one non zero component and can be written in the form:

$$\mathrm{d}\mathbf{a} = da^1\mathbf{g}_1, \quad \mathrm{d}\mathbf{b} = db^2\mathbf{g}_2, \quad \mathrm{d}\mathbf{c} = dc^3\mathbf{g}_3. \tag{4.138}$$

Expanding Equation (4.137),

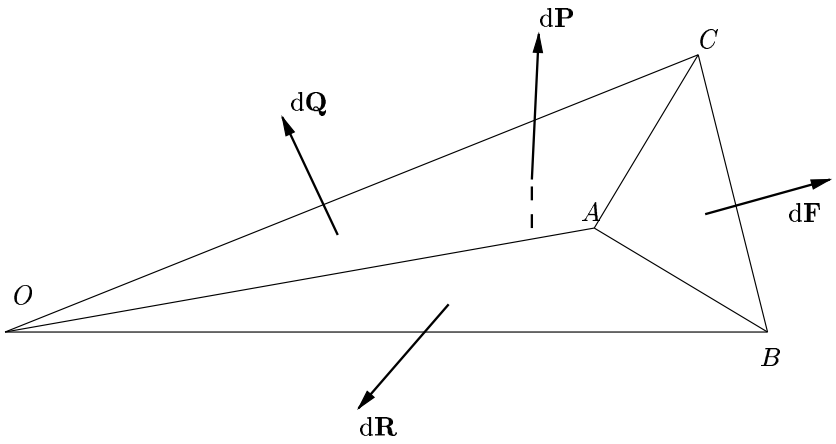

Figure 4.8: Force components.

$$\begin{aligned} d\mathbf{A} &= \frac{1}{2}\left(db^2dc^3 \in_{231} \mathbf{g}^1 + dc^3da^1 \in_{312} \mathbf{g}^2 + da^1db^2 \in_{123} \mathbf{g}^3\right) \\ &= dA_i\mathbf{g}^i, \end{aligned} \tag{4.139}$$

with $dA_1 = \frac{1}{2}db^2dc^3 \in_{231}, dA_2 = \frac{1}{2}dc^3da^1 \in_{312}, dA_3 = \frac{1}{2}da^1db^2 \in_{123}$.
In Equation (4.139), the quantities $\in_{ijk}$ are referred to as the *permutation symbols* and are defined by the following set of rules:

$$\begin{cases} \in_{ijk} = \sqrt{g} & \text{if } i,j,k \text{ is a cyclic sequence,} \\ \in_{ijk} = -\sqrt{g} & \text{if } i,j,k \text{ is an anticyclic sequence,} \\ \in_{ijk} = 0 & \text{if } i,j,k \text{ ia an acyclic sequence.} \end{cases} \tag{4.140}$$

The term g is determined by arranging the nine components of the metric tensor g_{ij} in a square matrix and then calculate its determinant.
Using a similar procedure, it is also possible to compute the areas associated with

the triangles OAB, OAC and OCB:

$$d\mathbf{A}_{OAB} = \frac{1}{2}(\mathrm{d}\mathbf{b} \times \mathrm{d}\mathbf{a}) = \frac{1}{2} db^2 da^1 \in_{213} \mathbf{g}^3 = -d\mathbf{A}_3 \mathbf{g}^3, \quad (4.141a)$$

$$d\mathbf{A}_{OAC} = \frac{1}{2}(\mathrm{d}\mathbf{a} \times \mathrm{d}\mathbf{c}) = \frac{1}{2} da^1 dc^3 \in_{132} \mathbf{g}^2 = -d\mathbf{A}_2 \mathbf{g}^2, \quad (4.141b)$$

$$d\mathbf{A}_{OCB} = \frac{1}{2}(\mathrm{d}\mathbf{c} \times \mathrm{d}\mathbf{b}) = \frac{1}{2} dc^3 db^2 \in_{321} \mathbf{g}^1 = -d\mathbf{A}_1 \mathbf{g}^1. \quad (4.141c)$$

Comparing Equations (4.139) and (4.141a) it is evident that the normal area associated with the sides of the tetrahedron joined at the point O are the covariant components of $d\mathbf{A}$. Having derived these components, the forces $\mathrm{d}\mathbf{P}, \mathrm{d}\mathbf{Q}$ and $\mathrm{d}\mathbf{R}$ may be defined in the form:

$$\mathrm{d}\mathbf{P} = -\sigma^{1j} dA_1 \mathbf{g}_j, \quad (4.142a)$$

$$\mathrm{d}\mathbf{Q} = -\sigma^{2j} dA_2 \mathbf{g}_j, \quad (4.142b)$$

$$\mathrm{d}\mathbf{R} = -\sigma^{3j} dA_3 \mathbf{g}_j. \quad (4.142c)$$

The quantities σ^{ij} are the contravariant components of a symmetric second order tensor called the *stress tensor*. It is important to note that the quantities $\sigma^{1j} dA_1, \sigma^{2j} dA_2$ and $\sigma^{3j} dA_3$ are not exactly forces since $\mathbf{g}_i$ is generally not a dimensionless unit vector (see pag. 160).
From Figure 4.8, the equilibrium equation (Heyman 1977):

$$\mathrm{d}\mathbf{F} = -\mathrm{d}\mathbf{P} - \mathrm{d}\mathbf{Q} - \mathrm{d}\mathbf{R}, \quad (4.143)$$

can be written and combined with Equations (4.142) to yield:

$$\mathrm{d}\mathbf{F} = \left(\sigma^{1j} dA_1 + \sigma^{2j} dA_2 + \sigma^{3j} dA_3\right) \mathbf{g}_j = \sigma^{ij} dA_i \mathbf{g}_j. \quad (4.144)$$

This relationship allows the force components dF^j to be expressed in the form:

$$dF^j = \sigma^{ij} dA_i. \quad (4.145)$$

4.6 The constitutive equations

For an elastic material whose stress-strain behaviour is essentially linear, Hooke's law may be written in the form (Green and Zerna 1968, pag.159):

$$\sigma^{ij} = E^{ijkl} \varepsilon_{kl}, \quad (4.146)$$

where E^{ijkl} is a fourth order tensor referred to as the elastic modulus. This system of equations is applicable to a variety of materials possessing either orthotropic,

isotropic or anisoptropic properties (see Section 3.3).
In the proposed method, it is assumed that the material has isotropic properties, due to the *real* evidence that yarns and material–matrix have a linear elastic isotropic behaviour on their own. As a result, many of the components of the elastic modulus are identical and Equation (4.146) may be written in a more convenient form. To achieve this, the stress-strain properties of an isotropic material expressed with reference to a Cartesian coordinate system are examinated. In matrix form, using Equation (3.16):

$$\begin{Bmatrix} \sigma^{11} \\ \sigma^{22} \\ \sigma^{33} \\ \sigma^{12} \\ \sigma^{23} \\ \sigma^{31} \end{Bmatrix} = \frac{E}{(1+\nu)(1-2\nu)} \begin{bmatrix} (1-\nu) & \nu & \nu & 0 & 0 & 0 \\ \nu & (1-\nu) & \nu & 0 & 0 & 0 \\ \nu & \nu & (1-\nu) & 0 & 0 & 0 \\ 0 & 0 & 0 & (1-2\nu) & 0 & 0 \\ 0 & 0 & 0 & 0 & (1-2\nu) & 0 \\ 0 & 0 & 0 & 0 & 0 & (1-2\nu) \end{bmatrix} \begin{Bmatrix} \varepsilon_{11} \\ \varepsilon_{22} \\ \varepsilon_{33} \\ \varepsilon_{12} \\ \varepsilon_{23} \\ \varepsilon_{31} \end{Bmatrix}, \tag{4.147}$$

where E and ν refer to Young modulus and Poisson's ratio respectively.
By using the symmetric properties associated with the stress and strain tensors it becomes possible to summarize the 81 components of the tensor E^{ijkl} in the following form (Ciarlet 1988):

$$E^{ijkl} = \frac{E\nu}{(1+\nu)(1-2\nu)}\delta^{ij}\delta^{kl} + \frac{E}{2(1+\nu)}(\delta^{ik}\delta^{jl} + \delta^{il}\delta^{jk}). \tag{4.148}$$

Although Equation (4.148) is valid only within a cartesian coordinate system, it can be generalized by replacing the Kronecker deltas with the corresponding components of the metric tensor (Green and Zerna 1968):

$$E^{ijkl} = \frac{E}{2(1+\nu)}\left(\frac{2\nu}{(1-2\nu)}g^{ij}g^{kl} + g^{ik}g^{jl} + g^{il}g^{jk}\right). \tag{4.149}$$

Equation (4.149) can now be combined with Equation (4.146) to yield the constitutive equations for a linear elastic material:

$$\sigma^{ij} = \frac{E}{2(1+\nu)}\left(\frac{2\nu}{(1-2\nu)}g^{ij}g^{lm} + g^{il}g^{jm} + g^{im}g^{jl}\right)\varepsilon_{lm}. \tag{4.150}$$

The inverse relationship can be computed by firstly expressing Equation (4.150) in terms of the mixed components ε^i_j and σ^i_j (Naomis and Lau 1990, pag.38):

$$\sigma^i_j = \frac{E}{(1+\nu)}\left(\varepsilon^i_j + \frac{\nu}{(1-2\nu)}\varepsilon^m_m\delta^i_j\right); \tag{4.151}$$

secondly, an expression for ε^m_m is obtained by letting $i = j$. Equation (4.151) then becomes:

$$\sigma^i_i = \frac{E}{(1+\nu)}\left(\varepsilon^i_i + \frac{3\nu}{(1-2\nu)}\varepsilon^m_m\right) = \frac{E}{(1-2\nu)}\varepsilon^m_m, \tag{4.152}$$

which can be substituted into Equation (4.151) to yield:

$$\varepsilon_j^i = \frac{1}{E}\left[(1+\nu)\sigma_j^i - \nu\sigma_m^m\delta_j^i\right]. \tag{4.153}$$

The application of Equations (4.150) and (4.153) to plane stress systems is of particular importance to the development of a shell theory. When a body is in a state of plane stress, the stresses $\sigma_\alpha^3, \sigma_3^\alpha$ and σ_3^3 are assumed to be zero. Equation (4.153) can therefore be written as:

$$E\varepsilon_\beta^\alpha = (1+\nu)\sigma_\beta^\alpha - \nu\sigma_\xi^\xi\delta_\beta^\alpha, \tag{4.154}$$

$$\varepsilon_3^\alpha = \varepsilon_\alpha^3 = 0, \tag{4.155}$$

$$E\varepsilon_3^3 = -\nu\sigma_\xi^\xi. \tag{4.156}$$

Similarly, the procedure used to invert Equation (4.150) can be applied to the above expression. The following relationship defining the stress-strain properties of an isotropic plane stress material may be developed:

$$\sigma_\beta^\alpha = \frac{E}{(1+\nu)}\left[\varepsilon_\beta^\alpha + \frac{\nu}{(1-\nu)}\varepsilon_\xi^\xi\delta_\beta^\alpha\right]. \tag{4.157}$$

By applying the metric tensor $g^{\alpha\beta}$, the contravariant stress components may be written in the form (Krätzig 1980):

$$\sigma^{\alpha\delta} = \sigma_\gamma^\alpha g^{\gamma\delta}. \tag{4.158}$$

Similarly, the pertinent strain components of the middle surface are expressed in terms of the covariant components of the strain tensor:

$$\varepsilon_\gamma^\alpha = \varepsilon_{\gamma\delta}g^{\alpha\delta}, \tag{4.159}$$

$$\varepsilon_\zeta^\zeta = \varepsilon_{\zeta\delta}g^{\zeta\delta}. \tag{4.160}$$

Combining Equations (4.158), (4.159) and (4.160) yields:

$$\sigma^{\alpha\beta} = \frac{E}{(1-\nu^2)}[(1-\nu)g^{\alpha\gamma}g^{\beta\delta} + \nu g^{\alpha\beta}g^{\gamma\delta}]\varepsilon_{\gamma\delta}, \tag{4.161}$$

which can be written in the form:

$$\boldsymbol{\sigma}^{\alpha\beta} = \{\sigma^{\alpha\alpha} \quad \sigma^{\alpha\beta} \quad \sigma^{\beta\alpha} \quad \sigma^{\beta\beta}\}^T = \boldsymbol{\Sigma}^{\alpha\beta}\boldsymbol{\varepsilon}_{\alpha\beta}, \tag{4.162}$$

where:

$$\boldsymbol{\Sigma}^{\alpha\beta} = \frac{E}{(1-\nu^2)}\,.$$

$$\cdot \begin{bmatrix} g^{11}g^{11} & g^{11}g^{12} \\ g^{11}g^{21} & (1-\nu)g^{11}g^{22} + \nu g^{12}g^{12} \\ g^{21}g^{11} & g^{21}g^{12} \\ (1-\nu)g^{21}g^{21} + \nu g^{11}g^{22} & g^{21}g^{22} \end{bmatrix}$$

$$\begin{bmatrix} g^{12}g^{11} & (1-\nu)g^{12}g^{12} + \nu g^{22}g^{11} \\ g^{12}g^{21} & g^{12}g^{22} \\ (1-\nu)g^{22}g^{11} + \nu g^{21}g^{21} & g^{22}g^{12} \\ g^{22}g^{21} & g^{22}g^{22} \end{bmatrix}, \tag{4.163}$$

and using Equation (4.182b):

$$\begin{bmatrix} g^{11} & g^{12} \\ g^{21} & g^{22} \end{bmatrix} = \begin{bmatrix} \lambda^1_\mu \lambda^1_\nu a^{\mu\nu} & \lambda^1_\mu \lambda^2_\nu a^{\mu\nu} \\ \lambda^2_\mu \lambda^1_\nu a^{\mu\nu} & \lambda^2_\mu \lambda^2_\nu a^{\mu\nu} \end{bmatrix}. \tag{4.164}$$

As an example, really used from a computational point of view in Chapter 5, we consider a two–dimensional skew coordinate system (R, S) (Washizu 1968):

$$x = R + S\cos\alpha \qquad y = S\sin\alpha, \tag{4.165}$$

as shown in Figure 4.9, where α is a constant. Now using Equations (4.40) and

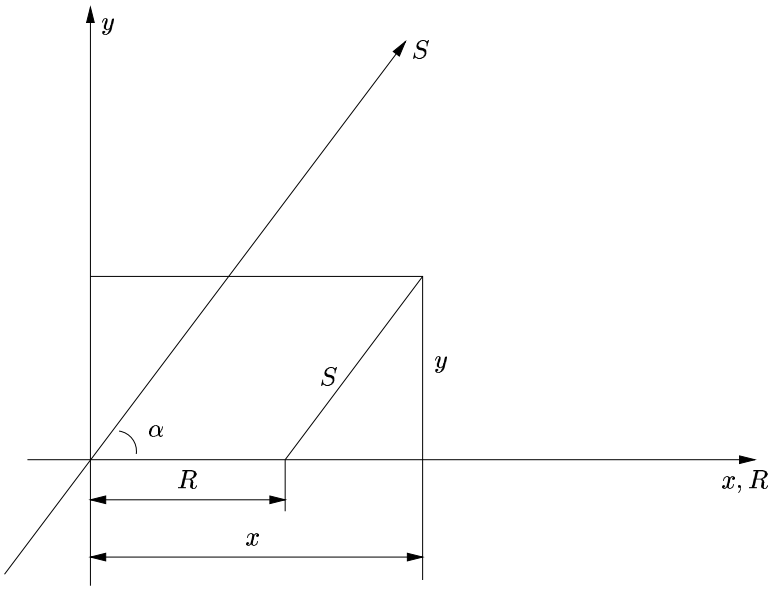

Figure 4.9: Local curvilinear coordinate system (R, S)

(4.43), we can derive the following relations:

$$g_{11} = 1, \quad g_{22} = 1, \quad g_{12} = g_{21} = \cos\alpha, \quad \sqrt{g} = \sin\alpha, \tag{4.166}$$

$$g^{11} = \csc^2\alpha, \quad g^{22} = \csc^2\alpha, \quad g^{12} = g^{21} = -\cos\alpha\csc^2\alpha, \tag{4.167}$$

and applying Equations (4.61) and (4.63) to the stress and strain components, we can write:

$$\varepsilon_{11} = \varepsilon_x, \quad \varepsilon_{22} = \varepsilon_x\cos^2\alpha + \varepsilon_y\sin^2\alpha + \gamma_{xy}\sin\alpha\cos\alpha, \tag{4.168}$$

$$\gamma_{12} = \gamma_{21} = 2\varepsilon_x\cos\alpha + \gamma_{xy}\sin\alpha, \tag{4.169}$$

$$\sigma^{11} = \sigma_x + \sigma_y\cot^2\alpha - 2\tau_{xy}\cot\alpha, \quad \sigma^{22} = \sigma_y\csc^2\alpha, \tag{4.170}$$

$$\sigma^{12} = \sigma^{21} = -\sigma_x\cot\alpha + \tau_{xy}\csc\alpha, \tag{4.171}$$

where 1 refers to the R–direction and 2 to the S–direction. Then, combining the previous equations with the system (4.163), we have the stress–strain relations in the (R, S) coordinate system as follows:

$$\begin{bmatrix}\sigma^{11}\\ \sigma^{22}\\ \sigma^{12}\end{bmatrix} = \frac{E\csc^4\alpha}{(1-\nu^2)}\begin{bmatrix} 1 & \cos^2\alpha + \nu\sin^2\alpha & -\cos\alpha \\ \cos^2\alpha + \nu\sin^2\alpha & 1 & -\cos\alpha \\ -\cos\alpha & -\cos\alpha & \dfrac{1+\cos^2\alpha-\nu\sin^2\alpha}{2}\end{bmatrix}\begin{bmatrix}\varepsilon_{11}\\ \varepsilon_{22}\\ \gamma_{12}\end{bmatrix}. \tag{4.172}$$

4.7 The theory of shells: geometrical relations

A shell structure may be defined as a body consisting of an inner surface, called the middle surface, and two outer surfaces which are parallel to each other. The normal distance from the middle to the outer surfaces are assumed to be the same although they need not be constant. Consider a shell of uniform thickness t as illustrated in Figure 4.10; let $\mathbf{s}$ and $\mathbf{r}$ denote the position vectors of two points A and B which are located at the same coordinates x^α but are separate by a distance z normal to the middle surface, as defined in Section 4.4 and in Table 4.1. From Figure 4.10, the vector equation

$$\mathbf{r} = \mathbf{s} + z\mathbf{a}_3, \tag{4.173}$$

can be written and differentiated to form the expression:

$$\mathbf{r}_{,\alpha} = \mathbf{s}_{,\alpha} + z\mathbf{a}_{3,\alpha} \quad \Longleftarrow \quad \text{(Eq. (4.91))}. \tag{4.174}$$

By using the definition of a base vector introduced in Section 4.3, Equation (4.174) can be expressed as:

$$\mathbf{g}_\alpha = \mathbf{a}_\alpha - zb_\alpha^\beta\mathbf{a}_\beta = \left(\delta_\alpha^\beta - zb_\alpha^\beta\right)\mathbf{a}_\beta. \tag{4.175}$$

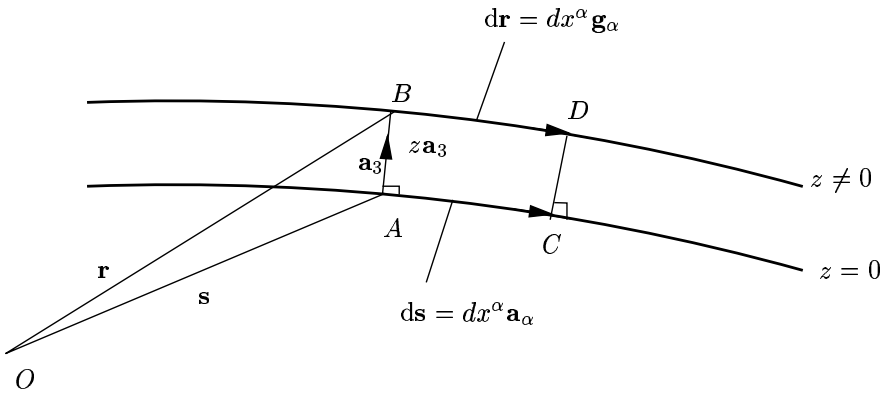

Figure 4.10: Position vector of a point on a shell

The coefficient $\left(\delta_\alpha^\beta - z b_\alpha^\beta\right)$ relates the covariant base vectors associated with the general surface $x^3 = z$ to the middle surface base vectors $\mathbf{a}_\alpha$. It is called the *shift tensor* and is denoted by the symbol μ_α^β (Green and Zerna 1968, pag.374):

$$\mu_\alpha^\beta = \left(\delta_\alpha^\beta - z b_\alpha^\beta\right), \tag{4.176}$$

and Equation (4.175) becomes:

$$\mathbf{g}_\alpha = \mu_\alpha^\beta \mathbf{a}_\beta. \tag{4.177}$$

Similarly, by introducing a tensor λ_α^β, which relates the contravariant base vectors:

$$\mathbf{g}^\beta = \lambda_\alpha^\beta \mathbf{a}^\alpha, \tag{4.178}$$

applying Equations (4.177) and (4.178) to Equation (4.37), yields:

$$\mathbf{g}^\alpha \cdot \mathbf{g}_\beta = \lambda_\gamma^\alpha \mathbf{a}^\gamma \cdot \mu_\beta^\delta \mathbf{a}_\delta = \lambda_\gamma^\alpha \mu_\beta^\gamma, \tag{4.179}$$

from which it can be concluded that:

$$\delta_\beta^\alpha = \lambda_\gamma^\alpha \mu_\beta^\gamma. \tag{4.180}$$

The approach adopted in Section 4.2.3 for the computation of the contravariant components of a metric tensor can also be applied to the above expression. Equation (4.180) represents a system of four equations and if expanded, may be written in the form:

$$\begin{bmatrix} \lambda_\alpha^\alpha & \lambda_\beta^\alpha \\ \lambda_\alpha^\beta & \lambda_\beta^\beta \end{bmatrix} \begin{bmatrix} \mu_\alpha^\alpha & \mu_\beta^\alpha \\ \mu_\alpha^\beta & \mu_\beta^\beta \end{bmatrix} = \begin{bmatrix} 1 & 0 \\ 0 & 1 \end{bmatrix}. \tag{4.181}$$

Having computed the tensor components μ^{α}_{β} and assembled them in the form required by Equation (4.181), λ^{α}_{β} can be computed by simply inverting the matrix containing the shift tensor components μ^{α}_{β}.

Similarly, the metric tensors $g_{\alpha\beta}$ and $g^{\alpha\beta}$ at the point B (see Figure 4.10) may be expressed in terms of the corresponding quantities $a_{\alpha\beta}$ and $a^{\alpha\beta}$ at the point A. Starting with the definition of the metric tensor given by Equation (4.40) and combining it with Equations (4.177) and (4.178):

$$g_{\alpha\beta} = \mathbf{g}_{\alpha} \cdot \mathbf{g}_{\beta} = \mu^{\gamma}_{\alpha}\mathbf{a}_{\gamma} \cdot \mu^{\delta}_{\beta}\mathbf{a}_{\delta} = \mu^{\gamma}_{\alpha}\mu^{\delta}_{\beta}a_{\gamma\delta}, \tag{4.182a}$$

$$g^{\alpha\beta} = \mathbf{g}^{\alpha} \cdot \mathbf{g}^{\beta} = \lambda^{\alpha}_{\gamma}\mathbf{a}^{\gamma} \cdot \lambda^{\beta}_{\delta}\mathbf{a}^{\delta} = \lambda^{\alpha}_{\gamma}\lambda^{\beta}_{\delta}a^{\gamma\delta}. \tag{4.182b}$$

Alternatively, if the product of two base vectors from opposite system, $\mathbf{g}_{\alpha}$ and $\mathbf{a}^{\beta}$, are considered then the shift tensors may be computed from the relationships:

$$\mathbf{g}_{\alpha} \cdot \mathbf{a}^{\beta} = \mu^{\gamma}_{\alpha}\mathbf{a}_{\gamma} \cdot \mathbf{a}^{\beta} = \mu^{\beta}_{\alpha}, \tag{4.183a}$$

$$\mathbf{g}^{\alpha} \cdot \mathbf{a}_{\beta} = \lambda^{\alpha}_{\gamma}\mathbf{a}^{\gamma} \cdot \mathbf{a}_{\beta} = \lambda^{\alpha}_{\beta}. \tag{4.183b}$$

From the definition of the Christoffel symbol given in Section 4.2.5,

$$\overline{\Gamma}^{\gamma}_{\alpha\beta} = \mathbf{g}_{\alpha,\beta} \cdot \mathbf{g}^{\gamma} = \left(\mu^{\delta}_{\alpha}\mathbf{a}_{\delta}\right)_{,\beta} \cdot \lambda^{\gamma}_{\xi}\mathbf{a}^{\xi} = \left(\mu^{\xi}_{\alpha,\beta} + \mu^{\delta}_{\alpha}\Gamma^{\xi}_{\delta\beta}\right)\lambda^{\gamma}_{\xi}. \tag{4.184}$$

However, the planar derivative of the shift tensor is:

$$\mu^{\xi}_{\alpha}\|_{\beta} = \mu^{\xi}_{\alpha,\beta} + \mu^{\delta}_{\alpha}\Gamma^{\xi}_{\delta\beta} - \mu^{\xi}_{\delta}\Gamma^{\delta}_{\alpha\beta}, \tag{4.185}$$

which enables Equation (4.184) to be simplified yielding:

$$\overline{\Gamma}^{\gamma}_{\alpha\beta} = \Gamma^{\gamma}_{\alpha\beta} + \lambda^{\gamma}_{\xi}\mu^{\xi}_{\alpha}\|_{\beta}. \tag{4.186}$$

Similarly, by applying Equations (4.65) and (4.66):

$$\overline{\Gamma}^{3}_{\alpha\beta} = \mathbf{g}_{\alpha,\beta} \cdot \mathbf{g}^{3} = \left(\mu^{\delta}_{\alpha}\mathbf{a}_{\delta}\right)_{,\beta} \cdot \mathbf{a}^{3} = \mu^{\delta}_{\alpha}b_{\delta\beta}, \tag{4.187}$$

$$\overline{\Gamma}^{\alpha}_{3\beta} = \mathbf{g}_{3,\beta} \cdot \mathbf{g}^{\alpha} = -b_{\beta\gamma}\mathbf{a}^{\gamma} \cdot \lambda^{\alpha}_{\delta}\mathbf{a}^{\delta} = -\lambda^{\alpha}_{\delta}b^{\delta}_{\beta}. \tag{4.188}$$

4.7.1 Further kinematics

Figure 4.11 illustrates two points A and B lying within a shell as it undergoes deformation. In the undeformed state, A lies on the shell's middle surface and B lies a distance z from the point A along the normal vector $\mathbf{a}_3$. After the shell undergoes deformation, point A moves to $\tilde{A}$, and point B to $\tilde{B}$. The displacement vector connecting the points B and $\tilde{B}$, can be written as:

$$\mathbf{v} = \mathbf{u} - z\mathbf{a}_3 + \tilde{\mathbf{a}}. \tag{4.189}$$

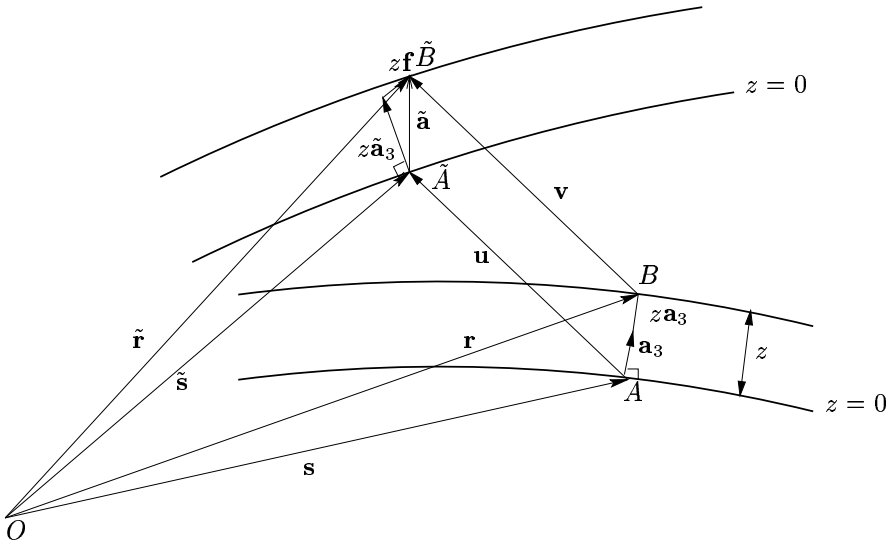

Figure 4.11: Section through a shell before and after deformation.

The vector $\tilde{\mathbf{a}}$ is expressed in the following form:

$$\tilde{\mathbf{a}} = z\tilde{\mathbf{a}}_3 + z\mathbf{f}. \tag{4.190}$$

The components of the vector $\mathbf{f}$ describe a combination of rotational and strech-ing modes which allow the general surface to deform freely. Substituting Equation (4.190) into Equation (4.189), yields:

$$\mathbf{v} = \mathbf{u} + z(\tilde{\mathbf{a}}_3 - \mathbf{a}_3) + z\mathbf{f}. \tag{4.191}$$

Referring to Figure 4.11, the vector equation

$$\tilde{\mathbf{s}} = \mathbf{s} + \mathbf{u}, \tag{4.192}$$

may be written and differentiated with respect to x^3 to yield:

$$\tilde{\mathbf{s}}_{,3} = \mathbf{s}_{,3} + \mathbf{u}_{,3}. \tag{4.193}$$

From Equation (4.35),

$$\mathbf{s}_{,3} = \mathbf{a}_3, \quad \text{and} \quad \tilde{\mathbf{s}}_{,3} = \tilde{\mathbf{a}}_3, \tag{4.194}$$

enabling Equation (4.193) to be written in the form:

$$\tilde{\mathbf{a}}_3 - \mathbf{a}_3 = \mathbf{u}_{,3}. \tag{4.195}$$

For any point on the middle surface, the displacement vector $\mathbf{u}$ can be specified as a function of the coordinates x^α. An expression defining $\mathbf{u}_{,3}$ can therefore be formed using Equation (4.113):

$$\mathbf{u}_{,3} = (u_{\alpha,3} + u_\gamma b^\gamma_\alpha)\,\mathbf{a}^\alpha + u_{3,3}\mathbf{a}^3. \tag{4.196}$$

Substituting the above relationship into Equations (4.195) and (4.191), yields:

$$\mathbf{v} = [u_\alpha + z\,(u_{\alpha,3} + u_\gamma b^\gamma_\alpha + f_\alpha)]\,\mathbf{a}^\alpha + [w + z\,(w_{,3} + f_3)]\,\mathbf{a}^3, \tag{4.197}$$

where $w = u_3$.
Alternatively, the general surface displacement vector $\mathbf{v}$ can be expanded into its normal and inplane components:

$$\mathbf{v} = v_\alpha \mathbf{g}^\alpha + v_3 \mathbf{g}^3. \tag{4.198}$$

The displacement components v_α can be expressed in terms of the middle surface displacement components u_α and f_α by dot multiplying both sides of Equation (4.197) with the base vector $\mathbf{g}_\alpha$:

$$v_\alpha = [u_\delta + z\,(u_{\delta,3} + u_\gamma b^\gamma_\delta + f_\delta)]\,\mathbf{a}^\delta \cdot \mathbf{g}_\alpha. \tag{4.199}$$

This expression can be further simplified through the use of Equation (4.183a):

$$v_\alpha = [u_\delta + z\,(u_{\delta,3} + u_\gamma b^\gamma_\delta + f_\delta)]\,\mu^\delta_\alpha. \tag{4.200}$$

Similarly, the displacement components v_3 are determined by dot multiplying both sides of Equation (4.197) with the base vector $\mathbf{g}^3$:

$$v_3 = w + z\,(w_{,3} + f_3) \tag{4.201}$$

4.7.2 The change in curvature tensor

The change of curvature in a shell's middle surface may be defined as the difference between the curvature before and after deformation. This change is denoted by the tensor k^γ_α and can be expressed in the form (Mason 1980):

$$\kappa^\gamma_\alpha = \tilde{b}^\gamma_\alpha - b^\gamma_\alpha, \tag{4.202}$$

where b^γ_α and $\tilde{b}^\gamma_\alpha$ are the curvature tensors before and after deformation respectively. The covariant components are obtained by applying the metric tensor:

$$\kappa_{\alpha\beta} = \tilde{b}^\gamma_\alpha a_{\gamma\beta} - b_{\alpha\beta}. \tag{4.203}$$

From Equation (4.126) the *middle surface strain tensor* $\varepsilon_{\alpha\beta}$ can be written in the form:

$$\varepsilon_{\alpha\beta} = \frac{1}{2}\left[\tilde{a}_{\alpha\beta} - a_{\alpha\beta}\right]. \tag{4.204}$$

Using the above expression to isolate $a_{\alpha\beta}$ and then substituting into Equation (4.203), yields:

$$\kappa_{\alpha\beta} = \tilde{b}_{\alpha\beta} - b_{\alpha\beta} - 2\tilde{b}^{\gamma}_{\alpha}\varepsilon_{\gamma\beta}. \tag{4.205}$$

The metric tensor for the *deformed middle surface* can be described by the equation:

$$\tilde{a}^{\delta\gamma} = a^{\delta\gamma} - 2\varepsilon^{\delta\gamma}, \tag{4.206}$$

which can be combined with the relationship:

$$\tilde{b}^{\gamma}_{\alpha} = \tilde{b}_{\delta\alpha}\tilde{a}^{\delta\gamma}, \tag{4.207}$$

to yield

$$\tilde{b}^{\gamma}_{\alpha} = \tilde{b}_{\delta\alpha}\left[a^{\delta\gamma} - 2\varepsilon^{\delta\gamma}\right]. \tag{4.208}$$

Multiplying both sides of the above expression by $2\varepsilon_{\gamma\beta}$ and neglecting quadratic terms in strain, the equation

$$2\tilde{b}^{\gamma}_{\alpha}\varepsilon_{\gamma\beta} = 2\tilde{b}_{\delta\alpha}a^{\delta\gamma}\varepsilon_{\gamma\beta}, \tag{4.209}$$

is obtained. The change in curvature tensor can now be expressed in the form:

$$\kappa_{\alpha\beta} = \tilde{b}_{\alpha\beta} - b_{\alpha\beta} - 2\tilde{b}_{\delta\alpha}a^{\delta\gamma}\varepsilon_{\gamma\beta}, \tag{4.210}$$

defining the curvature tensor $\tilde{b}_{\alpha\beta}$ through the use use of Equation (4.102) (Gould 1988, pag.22-27):

$$\tilde{b}_{\alpha\beta} = -\tilde{\mathbf{a}}_{3,\alpha}\cdot\tilde{\mathbf{a}}_{\beta}. \tag{4.211}$$

Differentiating Equation (4.195) with respect to x^{α}, yields:

$$\tilde{\mathbf{a}}_{3,\alpha} = \mathbf{a}_{3,\alpha} + \mathbf{u}_{,3\alpha}\,, \tag{4.212}$$

which can be combined with Equation (4.196) to form:

$$\begin{aligned}\tilde{\mathbf{a}}_{3,\alpha} = \mathbf{a}_{3,\alpha} + \left(u_{\delta,3} + u_{\gamma}b^{\gamma}_{\delta}\right)_{,\alpha}\mathbf{a}^{\delta} + \left(u_{\delta,3} + u_{\gamma}b^{\gamma}_{\delta}\right)\mathbf{a}^{\delta}_{,\alpha} + \\ + w_{,3\alpha}\mathbf{a}^{3} + w_{,3}\mathbf{a}^{3}_{,\alpha}.\end{aligned} \tag{4.213}$$

In addition, Equation (4.192) may be differentiated with respect to x^β to yield:

$$\tilde{\mathbf{a}}_\beta = \mathbf{a}_\beta + \mathbf{u}_{,\beta}. \tag{4.214}$$

The displacement derivative $\mathbf{u}_{,\beta}$, may also be defined using Equation (4.108):

$$\mathbf{u}_{,\beta} = (u_\delta\|_\beta - w b_{\delta\beta})\mathbf{a}^\delta + (w_{,\beta} + u_\gamma b^\gamma_\beta)\mathbf{a}^3. \tag{4.215}$$

Equations (4.213), (4.214) and (4.215) can now be substituted into (4.211) and keeping only the linear terms in displacement, we obtain:

$$\begin{aligned}
-\tilde{b}_{\alpha\beta} &= \left[\mathbf{a}_{3,\alpha} + (u_{\delta,3} + u_\gamma b^\gamma_\delta)_{,\alpha}\,\mathbf{a}^\delta + (u_{\delta,3} + u_\gamma b^\gamma_\delta)\,\mathbf{a}^\delta_{,\alpha} + w_{,3\alpha}\mathbf{a}^3 + w_{,3}\mathbf{a}^3_{,\alpha}\right] \cdot \\
&\qquad \cdot \left[\mathbf{a}_\beta + (u_\rho\|_\beta - w b_{\rho\beta})\,\mathbf{a}^\rho + (w_{,\beta} + u_\xi b^\xi_\beta)\mathbf{a}^3\right] \\
&= -b_{\alpha\beta} + (u_{\beta,3} + u_\gamma b^\gamma_\beta)_{,\alpha} + (u_{\delta,3} + u_\gamma b^\gamma_\delta)\,\mathbf{a}^\delta_{,\alpha}\cdot\mathbf{a}_\beta - w_{,3}b_{\alpha\beta} - \\
&\qquad - (u_\rho\|_\beta - w b_{\rho\beta})\,b^\rho_\alpha \\
&= -b_{\alpha\beta} - (u_\rho\|_\beta - w b_{\rho\beta})\,b^\rho_\alpha + (u_{\beta,3} + u_\gamma b^\gamma_\beta)\|_\alpha - w_{,3}b_{\alpha\beta}.
\end{aligned} \tag{4.216}$$

The above equation is combined with Equation (4.210) to arrive at an expression which describes the change of curvature of the middle surface in terms of the dislacements u_α and w. Once again, only linear terms are retained within the formulation:

$$\kappa_{\alpha\beta} = (u_\rho\|_\beta - w b_{\rho\beta})\,b^\rho_\alpha - (u_{\beta,3} + u_\gamma b^\gamma_\beta)\|_\alpha + w_{,3}\,b_{\alpha\beta} - 2b^\gamma_\alpha\varepsilon_{\gamma\beta}. \tag{4.217}$$

4.7.3 Strain–displacement equations

In Section 4.4 the deformation characteristic of a continuous three dimensional body were examinated. For small displacements, the general strain tensor η_{ij} can be expressed in the form:

$$\eta_{ij} = \frac{1}{2}\left(v_i|_j + v_j|_i\right). \tag{4.218}$$

Aim in this section is to express the general strain components in terms of the middle surface displacement quantities u_α, u_3, f_α and f_3 (Mason 1980). An expression defining the inplane strain $\eta_{\alpha\beta}$ may be obtained by letting the indices $i = \alpha$ and $j = \beta$:

$$\eta_{\alpha\beta} = \frac{1}{2}\left(v_\alpha|_\beta + v_\beta|_\alpha\right). \tag{4.219}$$

The covariant derivative of the displacement components v_α can be derived by combining Equations (4.77), (4.186) and (4.187):

$$\begin{aligned} v_\alpha|_\beta &= v_{\alpha,\beta} - v_\rho \overline{\Gamma}^\rho_{\alpha\beta} - v_3 \overline{\Gamma}^3_{\alpha\beta} \\ &= v_{\alpha,\beta} - v_\rho \Gamma^\rho_{\alpha\beta} - v_\rho \lambda^\rho_\xi \mu^\xi_\alpha \|_\beta - v_3 \mu^\delta_\alpha b_{\delta\beta} \\ &= v_\alpha \|_\beta - v_\rho \lambda^\rho_\xi \mu^\xi_\alpha \|_\beta - v_3 \mu^\delta_\alpha b_{\delta\beta}. \end{aligned} \tag{4.220}$$

For clarity, each term in Equation (4.220) will be considered individually. The quantity $v_\alpha\|_\beta$ is defined by differentiating the inplane displacement vector component v_α:

$$\begin{aligned} v_\alpha\|_\beta &= \left[\left(u_\delta + z\left(u_{\delta,3} + u_\gamma b^\gamma_\delta + f_\delta\right)\right)\mu^\delta_\alpha\right]\|_\beta \\ &= \left[u_\delta + z\left(u_{\delta,3} + u_\gamma b^\gamma_\delta + f_\delta\right)\right]\mu^\delta_\alpha\|_\beta + \\ &+ \left[u_\delta\|_\beta + z\left(u_{\delta,3}\|_\beta + u_\gamma\|_\beta b^\gamma_\delta + u_\gamma b^\gamma_\delta\|_\beta + f_\delta\|_\beta\right)\right]\mu^\delta_\alpha \\ &= u_\delta \mu^\delta_\alpha\|_\beta + u_\delta\|_\beta \mu^\delta_\alpha + z\left[\left(u_{\delta,3} + u_\gamma b^\gamma_\delta + f_\delta\right)\mu^\delta_\alpha\|_\beta + \right. \\ &+ \left.\left(u_{\delta,3}\|_\beta + u_\gamma\|_\beta b^\gamma_\delta + u_\gamma b^\gamma_\delta\|_\beta + f_\delta\|_\beta\right)\mu^\delta_\alpha\right]. \end{aligned} \tag{4.221}$$

Equation (4.180) is combined with Equation (4.200) when expanding the second term of Equation (4.220), obtaining:

$$\begin{aligned} v_\rho \lambda^\rho_\xi \mu^\xi_\alpha\|_\beta &= \left[u_\delta + z\left(u_{\delta,3} + u_\gamma b^\gamma_\delta + f_\delta\right)\right]\mu^\delta_\rho \lambda^\rho_\xi \mu^\xi_\alpha\|_\beta \\ &= \left[u_\delta + z\left(u_{\delta,3} + u_\gamma b^\gamma_\delta + f_\delta\right)\right]\mu^\delta_\alpha\|_\beta, \end{aligned} \tag{4.222}$$

and Equation (4.201) is utilized to form the last term:

$$v_3 \mu^\delta_\alpha b_{\delta\beta} = \left[w + z\left(w_{,3} + f_3\right)\right]\mu^\delta_\alpha b_{\delta\beta}. \tag{4.223}$$

The three Equations (4.221), (4.222) and (4.223) are substituted into Equation (4.220) to form:

$$\begin{aligned} v_\alpha|_\beta = u_\delta\|_\beta \mu^\delta_\alpha - w\mu^\delta_\alpha b_{\delta\beta} + z[u_{\delta,3}\|_\beta + u_\gamma\|_\beta b^\gamma_\delta + u_\gamma b^\gamma_\delta\|_\beta + f_\delta\|_\beta]\mu^\delta_\alpha - \\ - z[w_{,3} + f_3]\mu^\delta_\alpha b_{\delta\beta}. \end{aligned} \tag{4.224}$$

From Equation (4.224), $v_\beta|_\alpha$ is obtained by interchanging the indices α and β. An expression for the general strain tensor $\eta_{\alpha\beta}$ can now be formulated by substituting Equation (4.224) into Equation (4.219):

$$\begin{aligned} 2\eta_{\alpha\beta} &= u_\delta\|_\beta \mu^\delta_\alpha - w\mu^\delta_\alpha b_{\delta\beta} + z[u_{\delta,3}\|_\beta + u_\gamma\|_\beta b^\gamma_\delta + u_\gamma b^\gamma_\delta\|_\beta + f_\delta\|_\beta]\mu^\delta_\alpha + \\ &+ u_\delta\|_\alpha \mu^\delta_\beta - w\mu^\delta_\beta b_{\delta\alpha} + z[u_{\delta,3}\|_\alpha + u_\gamma\|_\alpha b^\gamma_\delta + u_\gamma b^\gamma_\delta\|_\alpha + f_\delta\|_\alpha]\mu^\delta_\beta - \\ &- z[w_{,3} + f_3]\mu^\delta_\alpha b_{\delta\beta} - z[w_{,3} + f_3]\mu^\delta_\beta b_{\delta\alpha}. \end{aligned} \tag{4.225}$$

The relationship describing the strain of the middle surface, denoted by the symbol $\varepsilon_{\alpha\beta}$ (see pag. 186), is obtained by letting $z = 0$:

$$\varepsilon_{\alpha\beta} = \frac{1}{2}[u_\alpha\|_\beta + u_\beta\|_\alpha - 2wb_{\alpha\beta}]. \tag{4.226}$$

This equation can be substituted into Equation (4.217) to yield the following expression for the change in curvature of the middle surface:

$$\kappa_{\alpha\beta} = -u_\gamma\|_\alpha b^\gamma_\beta - u_\beta\|_\gamma b^\gamma_\alpha - u_{\beta,3}\|_\alpha - u_\gamma b^\gamma_\beta\|_\alpha + w_{,3}b_{\alpha\beta} + wb_{\gamma\beta}b^\gamma_\alpha. \tag{4.227}$$

Equations (4.226) and (4.227) are relationships which can be used to simplify the general strain–displacement Equation (4.225). This process begins by considering the difference $2(\eta_{\alpha\beta} - \varepsilon_{\gamma\delta}\mu^\gamma_\alpha\mu^\delta_\beta)$:

$$\begin{aligned}
2(\eta_{\alpha\beta} - \varepsilon_{\gamma\delta}\mu^\gamma_\alpha\mu^\delta_\beta) = {} & \underbrace{u_\delta\|_\beta\mu^\delta_\alpha + u_\delta\|_\alpha\mu^\delta_\beta - u_\gamma\|_\delta\mu^\delta_\beta\mu^\gamma_\alpha - u_\delta\|_\gamma\mu^\gamma_\alpha\mu^\delta_\beta}_{[1]} + \\
& + \underbrace{w(2b_{\gamma\delta}\mu^\gamma_\alpha\mu^\delta_\beta - \mu^\delta_\alpha b_{\delta\beta} - \mu^\delta_\beta b_{\delta\alpha})}_{[2]} + \\
& + \underbrace{z(u_{\delta,3}\|_\beta\mu^\delta_\alpha + u_{\delta,3}\|_\alpha\mu^\delta_\beta + u_\gamma\|_\beta b^\gamma_\delta\mu^\delta_\alpha + u_\gamma\|_\alpha b^\gamma_\delta\mu^\delta_\beta + \\
& \qquad + u_\gamma b^\gamma_\delta\|_\beta\mu^\delta_\alpha + u_\gamma b^\gamma_\delta\|_\alpha\mu^\delta_\beta + f_\delta\|_\beta\mu^\delta_\alpha + f_\delta\|_\alpha\mu^\delta_\beta)}_{[3]} - \\
& - \underbrace{z(w_{,3} + f_3)(\mu^\delta_\alpha b_{\delta\beta} + \mu^\delta_\beta b_{\delta\alpha})}_{[4]}
\end{aligned} \tag{4.228}$$

Next using the definition for μ^β_α given by Equation (4.176), each one of the four designated groups is considered individually. Starting whith group [1]:

$$\begin{aligned}
[1] &= u_\delta\|_\beta(\delta^\delta_\alpha - zb^\delta_\alpha) + u_\delta\|_\alpha(\delta^\delta_\beta - zb^\delta_\beta) - \\
&\quad - u_\gamma\|_\delta(\delta^\delta_\beta\delta^\gamma_\alpha - zb^\gamma_\alpha\delta^\delta_\beta - zb^\delta_\beta\delta^\gamma_\alpha + z^2b^\gamma_\alpha b^\delta_\beta) - \\
&\quad - u_\delta\|_\gamma(\delta^\delta_\beta\delta^\gamma_\alpha - zb^\gamma_\alpha\delta^\delta_\beta - zb^\delta_\beta\delta^\gamma_\alpha + z^2b^\gamma_\alpha b^\delta_\beta) \\
&= z[u_\gamma\|_\delta b^\delta_\beta(\delta^\gamma_\alpha - zb^\gamma_\alpha) + u_\delta\|_\gamma b^\gamma_\alpha(\delta^\delta_\beta - zb^\delta_\beta)] \\
&= zu_\delta\|_\gamma[b^\gamma_\beta\mu^\delta_\alpha + b^\gamma_\alpha\mu^\delta_\beta] \\
&= zu_\delta\|_\gamma b^\gamma_\nu[\delta^\nu_\beta\mu^\delta_\alpha + \delta^\nu_\alpha\mu^\delta_\beta].
\end{aligned}$$

Similarly, group [2] is expanded, term by term in the following way:

$$\begin{aligned}
[2] &= wb_{\gamma\delta}(2\mu^\gamma_\alpha\mu^\delta_\beta - \mu^\delta_\alpha\delta^\gamma_\beta - \mu^\delta_\beta\delta^\gamma_\alpha) = \\
&= wb_{\gamma\delta}(2\delta^\gamma_\alpha\delta^\delta_\beta - 2z\delta^\gamma_\alpha b^\delta_\beta - 2zb^\gamma_\alpha\delta^\delta_\beta + 2z^2 b^\gamma_\alpha b^\delta_\beta - \delta^\gamma_\alpha\delta^\delta_\beta + zb^\delta_\alpha\delta^\gamma_\beta - \\
&- \delta^\gamma_\alpha\delta^\delta_\beta + zb^\delta_\beta\delta^\gamma_\alpha) \\
&= -zw[b_{\gamma\beta}b^\delta_\beta(\delta^\gamma_\alpha - zb^\gamma_\alpha) + b_{\gamma\delta}b^\gamma_\alpha(\delta^\delta_\beta - zb^\delta_\beta)] \\
&= -zwb_{\gamma\beta}[b^\delta_\beta\mu^\gamma_\alpha + b^\delta_\alpha\mu^\gamma_\beta] \\
&= -zwb_{\gamma\delta}b^\delta_\nu[\delta^\nu_\beta\mu^\gamma_\alpha + \delta^\nu_\alpha\mu^\gamma_\beta].
\end{aligned}$$

Examining the third group:

$$\begin{aligned}
[3] &= z[u_{\delta,3}\|_\nu(\delta^\nu_\beta\mu^\delta_\alpha + \delta^\nu_\alpha\mu^\delta_\beta) + u_\gamma\|_\nu b^\gamma_\delta(\delta^\nu_\beta\mu^\delta_\alpha + \delta^\nu_\alpha\mu^\delta_\beta) + \\
&+ u_\gamma b^\gamma_\delta\|_\nu(\delta^\nu_\beta\mu^\delta_\alpha + \delta^\nu_\alpha\mu^\delta_\beta) + f_\delta\|_\nu(\delta^\nu_\beta\mu^\delta_\alpha + \delta^\nu_\alpha\mu^\delta_\beta)] \\
&= z(u_{\delta,3}\|_\nu + u_\gamma\|_\nu b^\gamma_\delta + u_\gamma b^\gamma_\delta\|_\nu + f_\delta\|_\nu)[\delta^\nu_\beta\mu^\delta_\alpha + \delta^\nu_\alpha\mu^\delta_\beta],
\end{aligned}$$

and finally, the fourth group simplifies to:

$$[4] = -z(w_{,3} + f_3)b_{\delta\nu}[\mu^\delta_\alpha\delta^\nu_\beta + \mu^\delta_\beta\delta^\nu_\alpha].$$

Substituting groups [1]–[4] into Equation (4.228) yields:

$$\begin{aligned}
\eta_{\alpha\beta} = \varepsilon_{\delta\nu}\mu^\delta_\alpha\mu^\nu_\beta + \frac{1}{2}z(u_{\delta,3}\|_\nu + u_\gamma\|_\nu b^\gamma_\delta + u_\gamma b^\gamma_\delta\|_\nu + u_\delta\|_\gamma b^\gamma_\nu + \\
+ f_\delta\|_\nu - wb_{\gamma\delta}b^\delta_\nu - (w_{,3} + f_3)b_{\delta\nu})[\mu^\delta_\alpha\delta^\nu_\beta + \mu^\delta_\beta\delta^\nu_\alpha],
\end{aligned} \tag{4.229}$$

which combined with Equation (4.227) becomes:

$$\eta_{\alpha\beta} = \varepsilon_{\delta\nu}\mu^\delta_\alpha\mu^\nu_\beta - \frac{1}{2}z(\kappa_{\delta\nu} + f_3 b_{\delta\nu} - f_\delta\|_\nu)[\mu^\delta_\alpha\delta^\nu_\beta + \mu^\delta_\beta\delta^\nu_\alpha]. \tag{4.230}$$

By introducing the notation (Krätzig 1980, pag.32):

$$\phi_{\delta\nu} = f_3 b_{\delta\nu} - f_\delta\|_\nu, \tag{4.231}$$

Equation (4.230) becomes:

$$\eta_{\alpha\beta} = \varepsilon_{\delta\nu}\mu^\delta_\alpha\mu^\nu_\beta - \frac{1}{2}z(\kappa_{\delta\nu} + \phi_{\delta\nu})[\mu^\delta_\alpha\delta^\nu_\beta + \mu^\delta_\beta\delta^\nu_\alpha]. \tag{4.232}$$

For the strain components $\eta_{\alpha 3}$, the indices i and j in Equation (4.218) are set to α and 3 respectively:

$$\eta_{\alpha 3} = \frac{1}{2}(v_\alpha|_3 + v_3|_\alpha). \tag{4.233}$$

Expressions for the covariant derivatives of the displacement vector $\mathbf{v}$ can be obtained from Equation (4.77). These are simplified using Equations (4.98) and (4.188), enabling the following relationship to be written:

$$\eta_{\alpha 3} = \frac{1}{2}(v_{\alpha,3} + v_{3,\alpha} + 2v_\gamma \lambda^\gamma_\delta b^\delta_\alpha). \tag{4.234}$$

It is possible to express $\eta_{\alpha 3}$ in terms of the middle surface quantities $\mathbf{u}$ and $\mathbf{f}$ by expanding each term individually in Equation (4.234). Differentiating Equation (4.200) with respect to x^3:

$$\begin{aligned} v_{\alpha,3} = &[u_\delta + z(u_{\delta,3} + u_\gamma b^\gamma_\delta + f_\delta)]_{,3}\mu^\delta_\alpha + \\ &+ [u_\delta + z(u_{\delta,3} + u_\gamma b^\gamma_\delta + f_\delta)]\mu^\delta_{\alpha,3}. \end{aligned} \tag{4.235}$$

The thickness of a shell is assumed to be small when compared with the other dimensions of the structure, in particular, with its radius of curvature. Consequently, variations in the curvature tensor along the x^3 axis are assumed to be negligible. Hence the above expression can be simplified to:

$$v_{\alpha,3} = [u_{\delta,3} + z(u_{\delta,33} + u_{\gamma,3} b^\gamma_\delta + f_{\delta,3})]\mu^\delta_\alpha. \tag{4.236}$$

Similarly, Equation (4.201) is differentiated with respect to x^α, to form the expression:

$$v_{3,\alpha} = w_{,\alpha} + z(w_{,3\alpha} + f_{3,\alpha}), \tag{4.237}$$

which can be combined with Equations (4.200), (4.234) and (4.236) to yield:

$$\begin{aligned} 2\eta_{\alpha 3} = &u_{\alpha,3} + 2u_\delta b^\delta_\alpha + w_{,\alpha} + z[2u_\gamma b^\gamma_\delta b^\delta_\alpha + u_{\delta,3} b^\delta_\nu(\delta^\nu_\alpha + \mu^\nu_\alpha) + \\ &+ u_{\delta,33}\mu^\delta_\alpha + w_{,3\alpha} + 2f_\delta b^\delta_\alpha + f_{\delta,3}\mu^\delta_\alpha + f_{3,\alpha}]. \end{aligned} \tag{4.238}$$

The middle surface strain tensor $\varepsilon_{\alpha 3}$ can be easily obtained by letting $z = 0$ in the previous equation::

$$\varepsilon_{\alpha 3} = \frac{1}{2}[u_{\alpha,3} + 2u_\delta b^\delta_\alpha + w_{,\alpha}], \tag{4.239}$$

and using this expression, the strain tensor $\eta_{\alpha 3}$ can be written in the form:

$$\begin{aligned} \eta_{\alpha 3} = &\varepsilon_{\alpha 3} + \frac{1}{2} z[2u_\gamma b^\gamma_\delta b^\delta_\alpha + u_{\delta,3} b^\delta_\nu(\delta^\nu_\alpha + \mu^\nu_\alpha) + \\ &+ u_{\delta,33}\mu^\delta_\alpha + w_{,3\alpha} + 2f_\delta b^\delta_\alpha + f_{\delta,3}\mu^\delta_\alpha + f_{3,\alpha}]. \end{aligned} \tag{4.240}$$

Finally, the strain components η_{33} are formulated by letting $i = j = 3$ in Equation (4.218); this leads to the relationship:

$$\eta_{33} = \varepsilon_{33} + z(w_{,33} + f_{3,3}), \tag{4.241}$$

where:

$$\varepsilon_{33} = w_{,3}. \tag{4.242}$$

Equations (4.232), (4.240) and (4.241) completely describe the kinematic strain–displacement behaviour of a shell structure. Our numerical formulation, introduced in Chapter 5, capable of analysing shells of arbitrary geometry, would therefore need to introduce the equations previously constructed.

Chapter 5

Finite elements for shells and curved members

5.1 A survey of shell finite elements

The development of appropriate methods for the analysis of shell structures is increasingly demanded to ensure the integrity of structural design. In the last three decades there has been a tremendous interest in computational shell mechanics and numerous theoretical models have been developed and applied to various practical circumstances (Yang, Saigal, Masud, and Kapania 2000). Analytical solutions to shell structures are limited in scope and in general no single theory has proven to be general and comprehensive enough for the entire range of applications: arbitrary shapes, general load and support conditions, irregular stiffening, cutouts and many other aspects of practical design. The finite element method has consequently become prominent in the analysis of such shells in view of the ease with which such complexities can be dealt with. Three different approaches to the finite element representation of shell structures can be identified (Hinton and Owen 1984):

1. the first one based on flat triangular or composite–quadrilateral elements;

2. finite elements derived from three–dimensional elements by the use of degeneration methods;

3. stress–resultant–based formulations;

4. incompatible modes approach;

5. enhanced strain approach.

The first numerical study of shell problems involves facetting the shell by plane triangular plate elements, onto which a membrane stiffness is superposed. The results obtained are found to be satisfactory, but depending on the problem, very fine meshes have to be employed. A number of difficulties and shortcoming arise from the application of flat elements to curved shells (Gallagher 1976), such as the presence of discontinuous bending moments, which do not appear in the continuously curved actual structure. Numerous *in–plane* and *bending* element formulations are available, and, in both, conformity was achievable in flat assemblies. Clearly, if the elements are not co–planar conformity will, in general, be violated. Despite these problems, which can be surmounted through various artifices and additional computational effort (Zienkiewicz and Taylor 1991), simple triangular elements have been developed and applied to the nonlinear analysis of shells of arbitrary shape (Qun, Mu, and Wenqi 1998; Qun, Mu, and Wenqi 1999). The problem that remains is to determine if the loss in solution accuracy (as compared with curved elements) is properly balanced by the lower computational cost of these simple elements.
The second approach, originally introduced by Ahmad, Irons, and Zienkiewicz in 1970, discretizes the fundamental equations of 3D–continuum via isoparametric elements with indipendent rotational and displacement degrees of freedom; three dimensional stresses and strains are analysed in a local or global orthogonal cartesian coordinate system and degenerated to shell behaviour by introducing simultaneously physical assumptions at discrete points. The popularity of these elements is due, in part, to their simplicity of formulation that is able to avoid the complexities of fully general shell theories. Numerous modifications and generalizations to non linear (geometrical and material) analysis of the degenerated shell approach can be seen in Ramm (1977), Hughes and Liu (1981a), Hughes and Liu (1981b), Hughes and Cornoy (1983), Dvorkin and Bathe (1984), Hallquist, Benson, and Goudreau (1986) and Liu, Law, and Belytschko (1986). The books by, for example, Bathe (1996), Hughes (1987), and Crisfield (1986), offer comprehensive overviews of the degenerated solids approach and related methodologies which involve some type of reduction to a resultant formulation. Numerous modifications and generalizations of the degenerated shell approach has been done due to the fact that, despite its simple approach, the discretization of a Reissner–Mindlin model is not straightforward both in plates and shells frames. The inclusion of transverse shear strain effect in the finite element models introduce an undesirable numerical effect, the so–called *shear locking* phenomenon. This means that as the thickness of the plate and shell become extremely thin, the shear strain energy predicted by the finite element analysis can be magnified unreasonably even though the average value of the shear strain over the area tends to zero. Finite element schemes for shells problem also suffer of the so–called *membrane locking*: the finite element approximation of the membrane component of the energy is unstable with respect to the thickness

of the shell. The term membrane locking was coined in (Stolarski and Belytschko 1983) where the authors showed that it is related to an inadequate representation of inextensional modes; later Pitkaranta (1992) and Leino and Pitkaranta (1994) have analysed from a mathematical standpoint the membrane locking in a cylindrical shell problem showing that in the standard finite element methods locking occurs especially at low degrees of discretization. Several solutions to avoid the numerical locking have been proposed in the degenerated solid approach:

- mixed formulation (Bathe, Brezzi, and Cho 1989; Brezzi and Bathe 1990; Dvorkin 1995; Bucalem and Bathe 1997);

- reduced integration (Zienkiewicz, Taylor, and Too 1971);

- selective reduced integration (Zienkiewicz, Taylor, and Too 1971; Malkus and Hughes 1978);

- partial reduced selective integration (PRSI) (Chinosi and Lovadina 1994; Chinosi and Lovadina 1995);

- penalty partial reduced selective integration (PPRSI) (Nascimbene 2001).

The third point of view, in shell theories, states that thin bodies are best treated by replacing the general set of three–dimensional governing equations by a set of, in some sense, equivalent equations leading to the construction of shell theories. One of the first achievement in this direction was due to Argyris and Scharpf (1968a) in the development of the SHEBA family of finite elements (Argyris and Scharpf 1968b) and, thereafter, their generalizations (Argyris 1982; Argyris and Tenek 1994a; Argyris and Tenek 1994b). Working along similar lines, Simo and Fox (1989) proposed a stress–resultant–based geometrically exact shell model which is formulated entirely in stress resultants and is essentially equivalent to a one director inextensible Cosserat surface (Bernadou 1996).
It is well known that the presence of incompressibility leads to the so–called *locking* phenomenon in case of a discretization with standard displacement elements. Several methods to circumvent this problem have been developed. Amongst these are the reduced integration techniques (Zienkiewicz, Taylor, and Too 1971) or the mixed methods (Brezzi and Bathe 1990; Nascimbene and Venini 2002). In some approaches rank deficiency of underintegrated elements, which then leads to *hourglassing*, is bypassed by stabilization techniques (Belytschko and Tsay 1983). The method of incompatible modes had been introduced by Wilson, Taylor, Doherty, and Ghaboussi in 1973 as an approach for improving the behaviour of low–order elements in bending–dominated deformation patterns. Taylor, Beresford, and Wilson (1976) corrected the particular form of initial formulation by enforcing the *patch test* satisfaction. Lately, Simo and Rifai (1990) in the linear case and Simo,

Armero, and Taylor (1993) in the non–linear case have developed a family of elements which are based on the Hu–Washizu variational principle. These elements are extension of the incompatible BM6 element developed by Taylor, Beresford, and Wilson.
Several enhanced strain elements have been developed over the last year (Rhiu and Lee 1988; Yeom and Lee 1989; Parish 1990; Rengarajan, Aminpour, and Knight 1995; Ish and Guttal 1997; Kemp, Cho, and Lee 1998). These elements provide a robust tool for numerical simulations in solid mechanics, due to the construction of the elements with enhanced strains.

5.2 An alternative approach for shell finite elements: Based Gauss Mixed Interpolation

Before describing the derivation of the BGMI (Gobetti and Nascimbene 2002), the kinematic of our shell element will be briefly introduced. The element is derived directly from the equations described in Section 4.3, applying two main assumptions:

- *normals* to the middle surface of the shell before and after deformation remain straight;
- the normal stress component (i.e. σ_{33}) is constrained to zero and eliminated from the constitutive equations.

At first, we outline the basic concepts and notations underlying our formulation:

Global Coordinate Set (X, Y, Z): this is a Cartesian coordinate system, in relation to which, nodal coordinates, displacement field, global stiffeness matrix and applied force vector are referred;

Curvilinear Coordinate Set (R, S, T): let R and S be two curvilinear coordinates in the middle plane of the shell and T a linear coordinate in the thickness direction. It is important to point out that the frame (R, S, T) is equal to the *curved* reference $(\theta^1, \theta^2, \theta^3)$ defined by Equations (4.32);

Natural Coordinate System (r, s, t): we assume that (r, s, t) vary between -1 and 1.

The element displacement field can be expressed as:

$$u = u_R + T\theta_S, \tag{5.1a}$$

$$v = v_S - T\theta_R, \tag{5.1b}$$

$$w = w_T, \tag{5.1c}$$

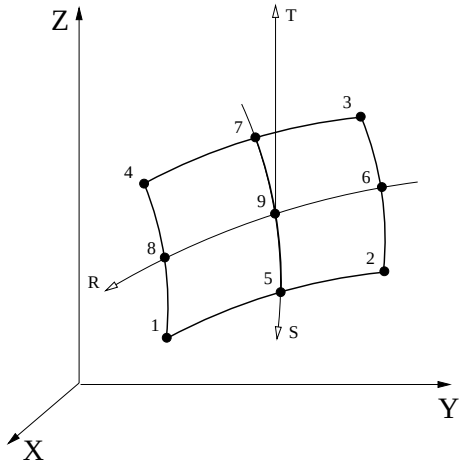

Figure 5.1: Nine–node element in the global and local curvilinear coordinate system.

where u, v and w are the components of the *general surface displacement* vector $\mathbf{v}$ (see Equation (4.189)) and u_R, v_S, w_T, θ_R and θ_S are the components of the *middle surface displacement* vector $\mathbf{u}$ (see Figure 4.6 and Equation (4.192)); both of them are referred to the general curvilinear coordinate system (R, S, T). Now, using Equations (4.126), (4.135) and (4.204), the membrane–bending *general surface* strains ε_{RR} and ε_{SS} and the in/out of plane shear terms γ_{RS}, γ_{RT} and γ_{ST}, can be written as:

$$\varepsilon_{RR} = \frac{\partial u}{\partial R}, \tag{5.2a}$$

$$\varepsilon_{SS} = \frac{\partial v}{\partial S}, \tag{5.2b}$$

$$\gamma_{RS} = \frac{\partial u}{\partial S} + \frac{\partial v}{\partial R}, \tag{5.2c}$$

$$\gamma_{RT} = \frac{\partial u}{\partial T} + \frac{\partial w}{\partial R}, \tag{5.2d}$$

$$\gamma_{ST} = \frac{\partial v}{\partial T} + \frac{\partial w}{\partial S}. \tag{5.2e}$$

Now substituting the kinematic field (5.1) into Equations (5.2), we obtain the general surface strains as a function of the middle surface displacements:

$$\varepsilon_{RR} = \frac{\partial u_R}{\partial R} + T\frac{\partial \theta_S}{\partial R}, \tag{5.3a}$$

$$\varepsilon_{SS} = \frac{\partial v_S}{\partial S} - T\frac{\partial \theta_R}{\partial S}, \tag{5.3b}$$

$$\gamma_{RS} = \frac{\partial u_R}{\partial S} + \frac{\partial v_S}{\partial R} + T\left(\frac{\partial \theta_S}{\partial S} - \frac{\partial \theta_R}{\partial R}\right), \tag{5.3c}$$

$$\gamma_{RT} = \theta_S + \frac{\partial w_T}{\partial R}, \tag{5.3d}$$

$$\gamma_{ST} = -\theta_R + \frac{\partial w_T}{\partial S}, \tag{5.3e}$$

or in matrix form:

$$\begin{bmatrix} \varepsilon_{RR} \\ \varepsilon_{SS} \\ \gamma_{RS} \\ \gamma_{RT} \\ \gamma_{ST} \end{bmatrix} = \begin{bmatrix} \frac{\partial}{\partial R} & 0 & 0 & 0 & T\frac{\partial}{\partial R} \\ 0 & \frac{\partial}{\partial S} & 0 & -T\frac{\partial}{\partial S} & 0 \\ \frac{\partial}{\partial S} & \frac{\partial}{\partial R} & 0 & -T\frac{\partial}{\partial R} & T\frac{\partial}{\partial S} \\ 0 & 0 & \frac{\partial}{\partial R} & 0 & 1 \\ 0 & 0 & \frac{\partial}{\partial S} & -1 & 0 \end{bmatrix} \begin{bmatrix} u_R \\ v_S \\ w_T \\ \theta_R \\ \theta_S \end{bmatrix}. \tag{5.4}$$

We have defined Equations (5.3a) and (5.3b) as *membrane–bending* strain because it contains a coupling of flexural and axial deformation in this model of a curved shell. It is important, at this point, to underline the two coordinate systems used in this analysis: the X, Y, Z system is Cartesian and orthogonal and is used as absolute reference coordinate system; the R, S, T one is curvilinear and not necessarily orthogonal, whose origin is centered in the node placed in the center of the considered element. In particular, the R axis runs from the node 6 towards the node 8, and S from 7 to 5, and T can be obtained as the direction orthogonal to the plane $R - S$ (see Figure 5.1). Nevertheless, for computational reasons we introduce a natural coordinate system (r, s, t) with variables normalized in the range of variation $(-1, 1)$, such that:

$$r = \frac{2}{l_R}R, \qquad s = \frac{2}{l_S}S, \qquad t = \frac{2}{h}T, \tag{5.5}$$

where l_R and l_S are the lenghts of an element along the R and S direction, respectively; and h is the thickness of the shell. The indipendent variables u_R, v_S, w_T, θ_R and θ_S can be expressed with reference to the generalized displacements U, V, W, θ_X, θ_Y and θ_Z of the shell nodes within the (X, Y, Z) global coordinate system, using transformation (4.50) in combination with Equation (4.59):

$$u_R = U\cos\widehat{RX} + V\cos\widehat{RY} + W\cos\widehat{RZ} \tag{5.6a}$$

$$v_S = U\cos\widehat{SX} + V\cos\widehat{SY} + W\cos\widehat{SZ} \tag{5.6b}$$

$$w_T = U\cos\widehat{TX} + V\cos\widehat{TY} + W\cos\widehat{TZ} \tag{5.6c}$$

$$\theta_R = \theta_X\cos\widehat{RX} + \theta_Y\cos\widehat{RY} + \theta_Z\cos\widehat{RZ} \tag{5.6d}$$

$$\theta_S = \theta_X\cos\widehat{SX} + \theta_Y\cos\widehat{SY} + \theta_Z\cos\widehat{SZ} \tag{5.6e}$$

or in matrix form:

$$\begin{bmatrix} u_R \\ v_S \\ w_T \\ \theta_R \\ \theta_S \end{bmatrix} = \begin{bmatrix} \cos\widehat{RX} & \cos\widehat{RY} & \cos\widehat{RZ} & 0 & 0 & 0 \\ \cos\widehat{SX} & \cos\widehat{SY} & \cos\widehat{SZ} & 0 & 0 & 0 \\ \cos\widehat{TX} & \cos\widehat{TY} & \cos\widehat{TZ} & 0 & 0 & 0 \\ 0 & 0 & 0 & \cos\widehat{RX} & \cos\widehat{RY} & \cos\widehat{RZ} \\ 0 & 0 & 0 & \cos\widehat{SX} & \cos\widehat{SY} & \cos\widehat{SZ} \end{bmatrix} \begin{bmatrix} U \\ V \\ W \\ \theta_X \\ \theta_Y \\ \theta_Z \end{bmatrix}. \tag{5.7}$$

Finally, substituting Equation (5.7) in Equation (5.4) we obtain:

$$\begin{aligned} \varepsilon_{RR} = {} & \frac{\partial U}{\partial R}\cos\widehat{RX} + U\frac{\partial\cos\widehat{RX}}{\partial R} + \frac{\partial V}{\partial R}\cos\widehat{RY} + V\frac{\partial\cos\widehat{RY}}{\partial R} + \\ & + \frac{\partial W}{\partial R}\cos\widehat{RZ} + W\frac{\partial\cos\widehat{RZ}}{\partial R} + T\left(\frac{\partial\theta_X}{\partial R}\cos\widehat{SX} + \theta_X\frac{\partial\cos\widehat{SX}}{\partial R} + \right. \\ & \left. + \frac{\partial\theta_Y}{\partial R}\cos\widehat{SY} + \theta_Y\frac{\partial\cos\widehat{SY}}{\partial R} + \frac{\partial\theta_Z}{\partial R}\cos\widehat{SZ} + \theta_Z\frac{\partial\cos\widehat{SZ}}{\partial R}\right), \end{aligned} \tag{5.8}$$

$$\begin{aligned} \varepsilon_{SS} = {} & \frac{\partial U}{\partial S}\cos\widehat{SX} + U\frac{\partial\cos\widehat{SX}}{\partial S} + \frac{\partial V}{\partial S}\cos\widehat{SY} + V\frac{\partial\cos\widehat{SY}}{\partial S} + \\ & + \frac{\partial W}{\partial S}\cos\widehat{SZ} + W\frac{\partial\cos\widehat{SZ}}{\partial S} - T\left(\frac{\partial\theta_X}{\partial S}\cos\widehat{RX} + \theta_X\frac{\partial\cos\widehat{RX}}{\partial S} + \right. \\ & \left. + \frac{\partial\theta_Y}{\partial S}\cos\widehat{RY} + \theta_Y\frac{\partial\cos\widehat{RY}}{\partial S} + \frac{\partial\theta_Z}{\partial S}\cos\widehat{RZ} + \theta_Z\frac{\partial\cos\widehat{RZ}}{\partial S}\right), \end{aligned} \tag{5.9}$$

$$\gamma_{RS} = \frac{\partial U}{\partial S}\cos\widehat{RX} + U\frac{\partial \cos\widehat{RX}}{\partial S} + \frac{\partial V}{\partial S}\cos\widehat{RY} + V\frac{\partial \cos\widehat{RY}}{\partial S} +$$
$$+ \frac{\partial W}{\partial S}\cos\widehat{RZ} + W\frac{\partial \cos\widehat{RZ}}{\partial S} + \frac{\partial U}{\partial R}\cos\widehat{SX} + U\frac{\partial \cos\widehat{SX}}{\partial R} +$$
$$+ \frac{\partial V}{\partial R}\cos\widehat{SY} + V\frac{\partial \cos\widehat{SY}}{\partial R} + \frac{\partial W}{\partial R}\cos\widehat{SZ} + W\frac{\partial \cos\widehat{SZ}}{\partial R} +$$
$$+ T\left(\frac{\partial \theta_X}{\partial S}\cos\widehat{SX} + \theta_X\frac{\partial \cos\widehat{SX}}{\partial S} + \frac{\partial \theta_Y}{\partial S}\cos\widehat{SY} + \theta_Y\frac{\partial \cos\widehat{SY}}{\partial S} +\right.$$
$$+ \frac{\partial \theta_Z}{\partial S}\cos\widehat{SZ} + \theta_Z\frac{\partial \cos\widehat{SZ}}{\partial S} - \frac{\partial \theta_X}{\partial R}\cos\widehat{RX} - \theta_X\frac{\partial \cos\widehat{RX}}{\partial R} -$$
$$\left. - \frac{\partial \theta_Y}{\partial R}\cos\widehat{RY} - \theta_Y\frac{\partial \cos\widehat{RY}}{\partial R} - \frac{\partial \theta_Z}{\partial R}\cos\widehat{RZ} - \theta_Z\frac{\partial \cos\widehat{RZ}}{\partial R}\right), \quad (5.10)$$

$$\gamma_{RT} = \frac{\partial U}{\partial R}\cos\widehat{TX} + U\frac{\partial \cos\widehat{TX}}{\partial R} + \frac{\partial V}{\partial R}\cos\widehat{TY} + V\frac{\partial \cos\widehat{TY}}{\partial R} +$$
$$+ \frac{\partial W}{\partial R}\cos\widehat{TZ} + W\frac{\partial \cos\widehat{TZ}}{\partial R} +$$
$$+ \theta_X\cos\widehat{SX} + \theta_Y\cos\widehat{SY} + \theta_Z\cos\widehat{SZ}, \quad (5.11)$$

$$\gamma_{ST} = \frac{\partial U}{\partial S}\cos\widehat{TX} + U\frac{\partial \cos\widehat{TX}}{\partial S} + \frac{\partial V}{\partial S}\cos\widehat{TY} + V\frac{\partial \cos\widehat{TY}}{\partial S} +$$
$$+ \frac{\partial W}{\partial S}\cos\widehat{TZ} + W\frac{\partial \cos\widehat{TZ}}{\partial S} -$$
$$- \theta_X\cos\widehat{RX} - \theta_Y\cos\widehat{RY} - \theta_Z\cos\widehat{RZ}. \quad (5.12)$$

In Equation (5.7), the terms $\cos\widehat{RX}$, $\cos\widehat{RY}$, $\cos\widehat{RZ}$, $\cos\widehat{SX}$, $\cos\widehat{SY}$, $\cos\widehat{SZ}$, $\cos\widehat{TX}$, $\cos\widehat{TY}$ and $\cos\widehat{TZ}$, are needed to permit the transformation between the (R,S,T) and (X,Y,Z) coordinate systems, as defined by Equations (4.50) and (4.59).

5.2.1 Discretization

As is well known the isoparametric approach (Crisfield 1986) states that the same approximated functions modelling the displacement field have to be used to describe the shape of the field itself. First of all, the formulation adopted herein permits the introduction of identical discretizing functions for both transversal displacement and rotation of a section. Moreover, having in mind the curvilinear shape of the element which is going to be formulated, the use of the same functions describing the axial displacement seems to be suitable, so the following relations hold for a nine node elements:

$$U = \sum_{i=1}^{9} N_i u_i, \qquad \theta_X = \sum_{i=1}^{9} N_i \theta_{Xi}, \tag{5.13}$$

$$V = \sum_{i=1}^{9} N_i v_i, \qquad \theta_Y = \sum_{i=1}^{9} N_i \theta_{Yi}, \tag{5.14}$$

$$W = \sum_{i=1}^{9} N_i w_i, \qquad \theta_Z = \sum_{i=1}^{9} N_i \theta_{Zi},, \tag{5.15}$$

where $N_i (i = 1, 2, .., 9)$ are the shape functions, all second order polynomials for nine–node element:

$$N_i = [rr_i(1 + rr_i)/2 + (1 - r^2)(1 - r_i^2)][ss_i(1 + ss_i)/2 + (1 - s^2)(1 - s_i^2)] \tag{5.16}$$

The expressions (5.16) can also be used to describe the geometry of the middle surface of the shell, within the frame of the isoparametric approach:

$$\begin{bmatrix} X \\ Y \\ Z \end{bmatrix}_{\text{mid}} = \sum_{i=1}^{9} N_i(r, s) \begin{bmatrix} X_i \\ Y_i \\ Z_i \end{bmatrix}_{\text{mid}} . \tag{5.17}$$

In Equations (5.17), the shape functions N_i were assumed to be dependent just on the variables r and s. With a small change in their definition it is also possible to introduce the dependence on a third indipendent variable t through the thickness:

$$N_{i\text{top}} = \frac{1}{2}(1 + t)N_i, \quad N_{i\text{bottom}} = \frac{1}{2}(1 - t)N_i, \quad i = 1, \ldots, 9. \tag{5.18}$$

The use of this local coordinate system facilitates the evaluation of the matrices related to the discretized problem in terms of the global coordinates X, Y and Z, simply following the strategy stated by the isoparametric approach; therefore, the *general surface coordinates* can be written:

$$\begin{bmatrix} X \\ Y \\ Z \end{bmatrix} = \sum_{i=1}^{9} N_{i\text{top}}(r, s, t) \begin{bmatrix} X_i \\ Y_i \\ Z_i \end{bmatrix}_{\text{top}} + \sum_{i=1}^{9} N_{i\text{bottom}}(r, s, t) \begin{bmatrix} X_i \\ Y_i \\ Z_i \end{bmatrix}_{\text{bottom}} , \tag{5.19}$$

where:

$$X_{i\text{top}} = X_i + \frac{h}{2}\cos\widehat{TX}_i, \tag{5.20a}$$

$$X_{i\text{bottom}} = X_i - \frac{h}{2}\cos\widehat{TX}_i, \tag{5.20b}$$

$$Y_{i\text{top}} = Y_i + \frac{h}{2}\cos\widehat{TY}_i, \tag{5.20c}$$

$$Y_{i\text{bottom}} = Y_i - \frac{h}{2}\cos\widehat{TY}_i, \tag{5.20d}$$

$$Z_{i\text{top}} = Z_i + \frac{h}{2}\cos\widehat{TZ}_i, \tag{5.20e}$$

$$Z_{i\text{bottom}} = Z_i - \frac{h}{2}\cos\widehat{TZ}_i. \tag{5.20f}$$

Obviously, the introduction of the coordinate t in the formulas governing the phenomenon is only a first step towards a more complex formulation of the model, such as that of layered materials or of piezoelectric shells (Gobetti, Venini, and Nascimbene 2002) or of material of which a known initial stress distribution throughout the thickness has to be taken into account; furthermore, the introduction of the through–thickness integration via t coordinate, makes easy the evaluation of the Jacobian matrix:

$$\mathbf{J} = \begin{bmatrix} \dfrac{\partial X}{\partial r} & \dfrac{\partial Y}{\partial r} & \dfrac{\partial Z}{\partial r} \\ \dfrac{\partial X}{\partial s} & \dfrac{\partial Y}{\partial s} & \dfrac{\partial Z}{\partial s} \\ \dfrac{\partial X}{\partial t} & \dfrac{\partial Y}{\partial t} & \dfrac{\partial Z}{\partial t} \end{bmatrix}. \tag{5.21}$$

The substitution of Equations (5.13)–(5.15) and (5.5) into Equations (5.8)–(5.12), gives unsatisfactory results from several points of view:

$$\begin{aligned} \varepsilon_{RR} = \sum_{i=1}^{9} \Bigg\{ & \left(\frac{\partial N_i}{\partial r}\cos\widehat{RX}_i + N_i \frac{\partial \cos\widehat{RX}}{\partial r}\bigg|_i \right) U_i + \left(\frac{\partial N_i}{\partial r}\cos\widehat{RY}_i + N_i \frac{\partial \cos\widehat{RY}}{\partial r}\bigg|_i \right) V_i + \\ & + \left(\frac{\partial N_i}{\partial r}\cos\widehat{RZ}_i + N_i \frac{\partial \cos\widehat{RZ}}{\partial r}\bigg|_i \right) W_i + \Bigg[\left(\frac{\partial N_i}{\partial r}\cos\widehat{SX}_i + N_i \frac{\partial \cos\widehat{SX}}{\partial r}\bigg|_i \right) \theta_{X\,i} + \\ & + \left(\frac{\partial N_i}{\partial r}\cos\widehat{SY}_i + N_i \frac{\partial \cos\widehat{SY}}{\partial r}\bigg|_i \right) \theta_{Y\,i} + \left(\frac{\partial N_i}{\partial r}\cos\widehat{SZ}_i + N_i \frac{\partial \cos\widehat{SZ}}{\partial r}\bigg|_i \right) \theta_{Z\,i} \Bigg] t\frac{h}{2} \Bigg\} \frac{2}{l_R}, \end{aligned} \tag{5.22}$$

$$\varepsilon_{SS} = \sum_{i=1}^{9} \left\{ \left(\frac{\partial N_i}{\partial s} \cos \widehat{SX}_i + N_i \frac{\partial \cos \widehat{SX}}{\partial s}\bigg|_i \right) U_i + \left(\frac{\partial N_i}{\partial s} \cos \widehat{SY}_i + N_i \frac{\partial \cos \widehat{SY}}{\partial s}\bigg|_i \right) V_i + \right.$$
$$+ \left(\frac{\partial N_i}{\partial s} \cos \widehat{SZ}_i + N_i \frac{\partial \cos \widehat{SZ}}{\partial s}\bigg|_i \right) W_i - \left[\left(\frac{\partial N_i}{\partial s} \cos \widehat{RX}_i + N_i \frac{\partial \cos \widehat{RX}}{\partial s}\bigg|_i \right) \theta_{X\,i} + \right.$$
$$\left. \left. + \left(\frac{\partial N_i}{\partial s} \cos \widehat{RY}_i + N_i \frac{\partial \cos \widehat{RY}}{\partial s}\bigg|_i \right) \theta_{Y\,i} + \left(\frac{\partial N_i}{\partial s} \cos \widehat{RZ}_i + N_i \frac{\partial \cos \widehat{RZ}}{\partial s}\bigg|_i \right) \theta_{Z\,i} \right] t \frac{h}{2} \right\} \frac{2}{l_S}, \quad (5.23)$$

$$\gamma_{RS} = \sum_{i=1}^{9} \left[\left(\frac{\partial N_i}{\partial s} \frac{2}{l_S} \cos \widehat{RX}_i + \frac{\partial N_i}{\partial r} \frac{2}{l_R} \cos \widehat{SX}_i + N_i \left(\frac{2}{l_S} \frac{\partial \cos \widehat{RX}}{\partial s}\bigg|_i + \frac{2}{l_R} \frac{\partial \cos \widehat{SX}}{\partial r}\bigg|_i \right) \right) U_i + \right.$$
$$+ \left(\frac{\partial N_i}{\partial s} \frac{2}{l_S} \cos \widehat{RY}_i + \frac{\partial N_i}{\partial r} \frac{2}{l_R} \cos \widehat{SY}_i + N_i \left(\frac{2}{l_S} \frac{\partial \cos \widehat{RY}}{\partial s}\bigg|_i + \frac{2}{l_R} \frac{\partial \cos \widehat{SY}}{\partial r}\bigg|_i \right) \right) V_i +$$
$$+ \left(\frac{\partial N_i}{\partial s} \frac{2}{l_S} \cos \widehat{RZ}_i + \frac{\partial N_i}{\partial r} \frac{2}{l_R} \cos \widehat{SZ}_i + N_i \left(\frac{2}{l_S} \frac{\partial \cos \widehat{RZ}}{\partial s}\bigg|_i + \frac{2}{l_R} \frac{\partial \cos \widehat{SZ}}{\partial r}\bigg|_i \right) \right) W_i +$$
$$+ \left(\frac{\partial N_i}{\partial s} \frac{2}{l_S} \cos \widehat{SX}_i - \frac{\partial N_i}{\partial r} \frac{2}{l_R} \cos \widehat{RX}_i + N_i \left(\frac{2}{l_S} \frac{\partial \cos \widehat{SX}}{\partial s}\bigg|_i - \frac{2}{l_R} \frac{\partial \cos \widehat{RX}}{\partial r}\bigg|_i \right) \right) t \frac{h}{2} \theta_{X\,i} +$$
$$+ \left(\frac{\partial N_i}{\partial s} \frac{2}{l_S} \cos \widehat{SY}_i - \frac{\partial N_i}{\partial r} \frac{2}{l_R} \cos \widehat{RY}_i + N_i \left(\frac{2}{l_S} \frac{\partial \cos \widehat{SY}}{\partial s}\bigg|_i - \frac{2}{l_R} \frac{\partial \cos \widehat{RY}}{\partial r}\bigg|_i \right) \right) t \frac{h}{2} \theta_{Y\,i} +$$
$$\left. + \left(\frac{\partial N_i}{\partial s} \frac{2}{l_S} \cos \widehat{SZ}_i - \frac{\partial N_i}{\partial r} \frac{2}{l_R} \cos \widehat{RZ}_i + N_i \left(\frac{2}{l_S} \frac{\partial \cos \widehat{SZ}}{\partial s}\bigg|_i - \frac{2}{l_R} \frac{\partial \cos \widehat{RZ}}{\partial r}\bigg|_i \right) \right) t \frac{h}{2} \theta_{Z\,i} \right], \quad (5.24)$$

$$\gamma_{RT} = \sum_{i=1}^{9} \left\{ \left[\left(\frac{\partial N_i}{\partial r} \cos \widehat{TX}_i + N_i \frac{\partial \cos \widehat{TX}}{\partial r}\bigg|_i \right) U_i + \left(\frac{\partial N_i}{\partial r} \cos \widehat{TY}_i + N_i \frac{\partial \cos \widehat{TY}}{\partial r}\bigg|_i \right) V_i + \right.\right.$$
$$\left. + \left(\frac{\partial N_i}{\partial r} \cos \widehat{TZ}_i + N_i \frac{\partial \cos \widehat{TZ}}{\partial r}\bigg|_i \right) W_i \right] \frac{2}{l_R} + N_i \cos \widehat{SX}_i \theta_{X\,i} + N_i \cos \widehat{SY}_i \theta_{Y\,i} +$$
$$\left. + N_i \cos \widehat{SZ}_i \theta_{Z\,i} \right\}, \quad (5.25)$$

$$\gamma_{ST} = \sum_{i=1}^{9} \left\{ \left[\left(\frac{\partial N_i}{\partial s} \cos \widehat{TX}_i + N_i \frac{\partial \cos \widehat{TX}}{\partial s}\bigg|_i \right) U_i + \left(\frac{\partial N_i}{\partial s} \cos \widehat{TY}_i + N_i \frac{\partial \cos \widehat{TY}}{\partial s}\bigg|_i \right) V_i + \right.\right.$$
$$\left. + \left(\frac{\partial N_i}{\partial s} \cos \widehat{TZ}_i + N_i \frac{\partial \cos \widehat{TZ}}{\partial s}\bigg|_i \right) W_i \right] \frac{2}{l_S} - N_i \cos \widehat{RX}_i \theta_{X\,i} - N_i \cos \widehat{RY}_i \theta_{Y\,i} -$$
$$\left. - N_i \cos \widehat{RZ}_i \theta_{Z\,i} \right\}. \quad (5.26)$$

First of all the tangential coefficients $\gamma_{RS}, \gamma_{RT}, \gamma_{ST}$ have a more refined definition in terms of the basic variables of the discretization because they are described by

a higher order polynomial than the strain rate of deformation ε_{RR} and ε_{SS}. This fact produces an incorrect estimation of the shear deformation in comparison with the strain due to membrane and bending. This is particularly evident at the lower thickness limit ($h \to 0$) because of the different rate of velocity shown by the two different contributions to the global deformation energy (respectively bending and shear types as shown in Equations (5.140) and (5.141) for the monodimensional problem), as they tend zero together with the thickness. Our procedure provides a solution scheme the main advantage of which is its compatibility with the exact solution whatever the choice of integration scheme, regardless the number of nodes employed in describing the element. The incorrect evaluation of the two components of the strain energy seems to be ascribed, as suggested by some heuristic improvement known as reduced integration schemes, to a too high polynomials degree of the function shaping the tensor components (5.22)–(5.26). Looking back to the difficulties related to the non pertinent choice of the polynomials degree, this procedure follows the strategy of decreasing the γ and ε polynomials order (second order for our nine–node element) by means of new, suitable shape functions. Let us introduce:

$$\gamma^*_{RS} = N^*_1\gamma^*_{RS1} + N^*_2\gamma^*_{RS2} + N^*_3\gamma^*_{RS3} + N^*_4\gamma^*_{RS4} \tag{5.27a}$$

$$\gamma^*_{RT} = N^*_1\gamma^*_{RT1} + N^*_2\gamma^*_{RT2} + N^*_3\gamma^*_{RT3} + N^*_4\gamma^*_{RT4} \tag{5.27b}$$

$$\gamma^*_{ST} = N^*_1\gamma^*_{ST1} + N^*_2\gamma^*_{ST2} + N^*_3\gamma^*_{ST3} + N^*_4\gamma^*_{ST4} \tag{5.27c}$$

$$\varepsilon^*_{RR} = N^*_1\varepsilon^*_{RR1} + N^*_2\varepsilon^*_{RR2} + N^*_3\varepsilon^*_{RR3} + N^*_4\varepsilon^*_{RR4} \tag{5.27d}$$

$$\varepsilon^*_{SS} = N^*_1\varepsilon^*_{SS1} + N^*_2\varepsilon^*_{SS2} + N^*_3\varepsilon^*_{SS3} + N^*_4\varepsilon^*_{SS4} \tag{5.27e}$$

or in matrix form:

$$\gamma^*_{RS} = \begin{bmatrix} N^*_1 & N^*_2 & N^*_3 & N^*_4 \end{bmatrix} \begin{bmatrix} \gamma^*_{RS1} \\ \gamma^*_{RS2} \\ \gamma^*_{RS3} \\ \gamma^*_{RS4} \end{bmatrix} = \mathbf{N}^*\boldsymbol{\gamma}^*_{RS}, \tag{5.28}$$

$$\gamma^*_{RT} = \begin{bmatrix} N^*_1 & N^*_2 & N^*_3 & N^*_4 \end{bmatrix} \begin{bmatrix} \gamma^*_{RT1} \\ \gamma^*_{RT2} \\ \gamma^*_{RT3} \\ \gamma^*_{RT4} \end{bmatrix} = \mathbf{N}^*\boldsymbol{\gamma}^*_{RT}, \tag{5.29}$$

$$\gamma^*_{ST} = \begin{bmatrix} N^*_1 & N^*_2 & N^*_3 & N^*_4 \end{bmatrix} \begin{bmatrix} \gamma^*_{ST1} \\ \gamma^*_{ST2} \\ \gamma^*_{ST3} \\ \gamma^*_{ST4} \end{bmatrix} = \mathbf{N}^* \boldsymbol{\gamma}^*_{ST}, \tag{5.30}$$

$$\varepsilon^*_{RR} = \begin{bmatrix} N^*_1 & N^*_2 & N^*_3 & N^*_4 \end{bmatrix} \begin{bmatrix} \varepsilon^*_{RR1} \\ \varepsilon^*_{RR2} \\ \varepsilon^*_{RR3} \\ \varepsilon^*_{RR4} \end{bmatrix} = \mathbf{N}^* \boldsymbol{\varepsilon}^*_{RR}, \tag{5.31}$$

$$\varepsilon^*_{SS} = \begin{bmatrix} N^*_1 & N^*_2 & N^*_3 & N^*_4 \end{bmatrix} \begin{bmatrix} \varepsilon^*_{SS1} \\ \varepsilon^*_{SS2} \\ \varepsilon^*_{SS3} \\ \varepsilon^*_{SS4} \end{bmatrix} = \mathbf{N}^* \boldsymbol{\varepsilon}^*_{SS}, \tag{5.32}$$

where a new set of shape functions is defined for a nine–node element:

$$\begin{aligned} N^*_1 &= \frac{3}{4}\left(\frac{\sqrt{3}}{3} - r\right) \cdot \left(\frac{\sqrt{3}}{3} - s\right), \qquad N^*_2 = \frac{3}{4}\left(\frac{\sqrt{3}}{3} - r\right) \cdot \left(\frac{\sqrt{3}}{3} + s\right), \\ N^*_3 &= \frac{3}{4}\left(\frac{\sqrt{3}}{3} + r\right) \cdot \left(\frac{\sqrt{3}}{3} - s\right), \qquad N^*_4 = \frac{3}{4}\left(\frac{\sqrt{3}}{3} + r\right) \cdot \left(\frac{\sqrt{3}}{3} + s\right), \end{aligned} \tag{5.33}$$

one degree lower and defined at the four Gauss points, which exactly integrate the flexural strain energy. The use of Equations (5.27) now give for γ and ε a contrasting definition because γ and ε were previously defined in a slightly different way in Equations (5.8)–(5.12). This incoherence can be removed by imposing the coincidence of the *new* shear–polynomials (5.28)–(5.30) with the *old* ones (5.24)–(5.26); and the coincidence of the two *new* membrane/bending–polynomials (5.31) and (5.32) with the *old* ones (5.22) and (5.23), at a number of selected points. To this purpose the Gauss integration points have proved to be very efficient. Here is developed the nine–node case. Referring to the Equations (5.28) and (5.24) we have:

$$\gamma^*_{RS}\Big|_{\overline{r},\overline{s}=\pm\frac{\sqrt{3}}{3}} = \gamma_{RS}\Big|_{\overline{r},\overline{s}=\pm\frac{\sqrt{3}}{3}} \Rightarrow$$

$$
\begin{aligned}
&\gamma^*_{RS1} = \\
&\sum_{i=1}^{9}\Bigg[\left(\left.\frac{\partial N_i}{\partial s}\right|_{\overline{r},\,\overline{s}=\left(-\frac{\sqrt{3}}{3},-\frac{\sqrt{3}}{3}\right)}\frac{2}{l_S}\cos\widehat{RX}_i+\left.\frac{\partial N_i}{\partial r}\right|_{\overline{r},\,\overline{s}}\frac{2}{l_R}\cos\widehat{SX}_i+N_i|_{\overline{r},\overline{s}}\left(\frac{2}{l_S}\left.\frac{\partial\cos\widehat{RX}}{\partial s}\right|_i+\frac{2}{l_R}\left.\frac{\partial\cos\widehat{SX}}{\partial r}\right|_i\right)\right)U_i+\\
&+\left(\left.\frac{\partial N_i}{\partial s}\right|_{\overline{r},\,\overline{s}}\frac{2}{l_S}\cos\widehat{RY}_i+\left.\frac{\partial N_i}{\partial r}\right|_{\overline{r},\,\overline{s}}\frac{2}{l_R}\cos\widehat{SY}_i+N_i|_{\overline{r},\overline{s}}\left(\frac{2}{l_S}\left.\frac{\partial\cos\widehat{RY}}{\partial s}\right|_i+\frac{2}{l_R}\left.\frac{\partial\cos\widehat{SY}}{\partial r}\right|_i\right)\right)V_i+\\
&+\left(\left.\frac{\partial N_i}{\partial s}\right|_{\overline{r},\,\overline{s}}\frac{2}{l_S}\cos\widehat{RZ}_i+\left.\frac{\partial N_i}{\partial r}\right|_{\overline{r},\,\overline{s}}\frac{2}{l_R}\cos\widehat{SZ}_i+N_i|_{\overline{r},\overline{s}}\left(\frac{2}{l_S}\left.\frac{\partial\cos\widehat{RZ}}{\partial s}\right|_i+\frac{2}{l_R}\left.\frac{\partial\cos\widehat{SZ}}{\partial r}\right|_i\right)\right)W_i+\\
&+\left(\left.\frac{\partial N_i}{\partial s}\right|_{\overline{r},\,\overline{s}}\frac{2}{l_S}\cos\widehat{SX}_i-\left.\frac{\partial N_i}{\partial r}\right|_{\overline{r},\,\overline{s}}\frac{2}{l_R}\cos\widehat{RX}_i+N_i|_{\overline{r},\overline{s}}\left(\frac{2}{l_S}\left.\frac{\partial\cos\widehat{SX}}{\partial s}\right|_i-\frac{2}{l_R}\left.\frac{\partial\cos\widehat{RX}}{\partial r}\right|_i\right)\right)t\frac{h}{2}\theta_{Xi}+\\
&+\left(\left.\frac{\partial N_i}{\partial s}\right|_{\overline{r},\,\overline{s}}\frac{2}{l_S}\cos\widehat{SY}_i-\left.\frac{\partial N_i}{\partial r}\right|_{\overline{r},\,\overline{s}}\frac{2}{l_R}\cos\widehat{RY}_i+N_i|_{\overline{r},\overline{s}}\left(\frac{2}{l_S}\left.\frac{\partial\cos\widehat{SY}}{\partial s}\right|_i-\frac{2}{l_R}\left.\frac{\partial\cos\widehat{RY}}{\partial r}\right|_i\right)\right)t\frac{h}{2}\theta_{Yi}+\\
&+\left(\left.\frac{\partial N_i}{\partial s}\right|_{\overline{r},\,\overline{s}}\frac{2}{l_S}\cos\widehat{SZ}_i-\left.\frac{\partial N_i}{\partial r}\right|_{\overline{r},\,\overline{s}}\frac{2}{l_R}\cos\widehat{RZ}_i+N_i|_{\overline{r},\overline{s}}\left(\frac{2}{l_S}\left.\frac{\partial\cos\widehat{SZ}}{\partial s}\right|_i-\frac{2}{l_R}\left.\frac{\partial\cos\widehat{RZ}}{\partial r}\right|_i\right)\right)t\frac{h}{2}\theta_{Zi}\Bigg]
\end{aligned}
$$

$$
\gamma^*_{RS2}\Longrightarrow\overline{r}=-\frac{\sqrt{3}}{3}\qquad\overline{s}=+\frac{\sqrt{3}}{3}
$$

$$
\gamma^*_{RS3}\Longrightarrow\overline{r}=+\frac{\sqrt{3}}{3}\qquad\overline{s}=-\frac{\sqrt{3}}{3}
$$

$$
\gamma^*_{RS4}\Longrightarrow\overline{r}=+\frac{\sqrt{3}}{3}\qquad\overline{s}=+\frac{\sqrt{3}}{3}
$$

$$
\Downarrow
$$

$$
\begin{bmatrix}\gamma^*_{RS1}\\ \gamma^*_{RS2}\\ \gamma^*_{RS3}\\ \gamma^*_{RS4}\end{bmatrix}=\boldsymbol{\gamma}^*_{RS}=\overline{\mathbf{B}}\mathbf{U},\tag{5.34}
$$

and referring to the Equations (5.29) and (5.25), (5.30) and (5.26), (5.31) and (5.22), (5.32) and (5.23), we can write:

$$
\left.\gamma^*_{RT}\right|_{\overline{r},\overline{s}=\pm\frac{\sqrt{3}}{3}}=\left.\gamma_{RT}\right|_{\overline{r},\overline{s}=\pm\frac{\sqrt{3}}{3}}\Rightarrow\boldsymbol{\gamma}^*_{RT}=\overline{\mathbf{B}}'\mathbf{U},\tag{5.35}
$$

$$\gamma^*_{ST}\Big|_{\overline{r},\overline{s}=\pm\frac{\sqrt{3}}{3}} = \gamma_{ST}\Big|_{\overline{r},\overline{s}=\pm\frac{\sqrt{3}}{3}} \Rightarrow \boldsymbol{\gamma}^*_{ST} = \overline{\mathbf{B}}''\mathbf{U}, \tag{5.36}$$

$$\varepsilon^*_{RR}\Big|_{\overline{r},\overline{s}=\pm\frac{\sqrt{3}}{3}} = \varepsilon_{RR}\Big|_{\overline{r},\overline{s}=\pm\frac{\sqrt{3}}{3}} \Rightarrow \boldsymbol{\varepsilon}^*_{RR} = \overline{\mathbf{B}}'''\mathbf{U}, \tag{5.37}$$

$$\varepsilon^*_{SS}\Big|_{\overline{r},\overline{s}=\pm\frac{\sqrt{3}}{3}} = \varepsilon_{RR}\Big|_{\overline{r},\overline{s}=\pm\frac{\sqrt{3}}{3}} \Rightarrow \boldsymbol{\varepsilon}^*_{SS} = \overline{\mathbf{B}}''''\mathbf{U}, \tag{5.38}$$

where $\mathbf{U} = [U_1\ V_1\ W_1\ \theta_{X1}\ \theta_{Y1}\ \theta_{Z1} \ldots U_9\ V_9\ W_9\ \theta_{X9}\ \theta_{Y9}\ \theta_{Z9}]^T$ is the nodal displacement vector in the global reference system. The final result is:

$$\gamma^*_{RS} = \begin{bmatrix} N^*_1 & N^*_2 & N^*_3 & N^*_4 \end{bmatrix} \overset{4\times 54}{\overline{\mathbf{B}}}\ \mathbf{U} = \overset{1\times 54}{\overline{\overline{\mathbf{B}}}}\ \mathbf{U}, \tag{5.39}$$

$$\gamma^*_{RT} = \begin{bmatrix} N^*_1 & N^*_2 & N^*_3 & N^*_4 \end{bmatrix} \overset{4\times 54}{\overline{\mathbf{B}}'}\ \mathbf{U} = \overset{1\times 54}{\overline{\overline{\mathbf{B}}}'}\ \mathbf{U}, \tag{5.40}$$

$$\gamma^*_{ST} = \begin{bmatrix} N^*_1 & N^*_2 & N^*_3 & N^*_4 \end{bmatrix} \overset{4\times 54}{\overline{\mathbf{B}}''}\ \mathbf{U} = \overset{1\times 54}{\overline{\overline{\mathbf{B}}}''}\ \mathbf{U}, \tag{5.41}$$

$$\varepsilon^*_{RR} = \begin{bmatrix} N^*_1 & N^*_2 & N^*_3 & N^*_4 \end{bmatrix} \overset{4\times 54}{\overline{\mathbf{B}}'''}\ \mathbf{U} = \overset{1\times 54}{\overline{\overline{\mathbf{B}}}'''}\ \mathbf{U}, \tag{5.42}$$

$$\varepsilon^*_{SS} = \begin{bmatrix} N^*_1 & N^*_2 & N^*_3 & N^*_4 \end{bmatrix} \overset{4\times 54}{\overline{\mathbf{B}}''''}\ \mathbf{U} = \overset{1\times 54}{\overline{\overline{\mathbf{B}}}''''}\ \mathbf{U}. \tag{5.43}$$

Now we can write:

$$\begin{bmatrix} \varepsilon^*_{RR} \\ \varepsilon^*_{SS} \\ \gamma^*_{RS} \\ \gamma^*_{RT} \\ \gamma^*_{ST} \end{bmatrix} = \mathbf{B}\mathbf{U} = \begin{bmatrix} \overline{\overline{\mathbf{B}}}''' \\ \overline{\overline{\mathbf{B}}}'''' \\ \overline{\overline{\mathbf{B}}} \\ \overline{\overline{\mathbf{B}}}' \\ \overline{\overline{\mathbf{B}}}'' \end{bmatrix} \mathbf{U}, \tag{5.44}$$

where the $\mathbf{B}(5 \times 54)$ has the following expression:

$$\mathbf{B} = \begin{bmatrix} B(1) & B(2) & B(3) & B(4) & B(5) & B(6) & \cdots \\ B(7) & B(8) & B(9) & B(10) & B(11) & B(12) & \cdots \\ B(13) & B(14) & B(15) & B(16) & B(17) & B(18) & \cdots \\ B(19) & B(20) & B(21) & B(22) & B(23) & B(24) & \cdots \\ B(25) & B(26) & B(27) & B(28) & B(29) & B(30) & \cdots \end{bmatrix}, \tag{5.45}$$

and the $B(i), (i = 1, \ldots, 54)$ terms can be written, only for the first node, in this way:

$$\begin{aligned} B(1) = \Bigg\{ & \left(\left. \frac{\partial N_1}{\partial r} \right|_{\overline{r}=-\frac{\sqrt{3}}{3}, \overline{s}=-\frac{\sqrt{3}}{3}} \cos \widehat{RX}_1 + N_1 \left|_{\overline{r}=-\frac{\sqrt{3}}{3}, \overline{s}=-\frac{\sqrt{3}}{3}} \right. \left. \frac{\partial \cos \widehat{RX}}{\partial r} \right|_1 \right) N_1^* |_G + \\ & + \left(\left. \frac{\partial N_1}{\partial r} \right|_{\overline{r}=-\frac{\sqrt{3}}{3}, \overline{s}=\frac{\sqrt{3}}{3}} \cos \widehat{RX}_1 + N_1 \left|_{\overline{r}=-\frac{\sqrt{3}}{3}, \overline{s}=\frac{\sqrt{3}}{3}} \right. \left. \frac{\partial \cos \widehat{RX}}{\partial r} \right|_1 \right) N_2^* |_G + \\ & + \left(\left. \frac{\partial N_1}{\partial r} \right|_{\overline{r}=\frac{\sqrt{3}}{3}, \overline{s}=-\frac{\sqrt{3}}{3}} \cos \widehat{RX}_1 + N_1 \left|_{\overline{r}=\frac{\sqrt{3}}{3}, \overline{s}=-\frac{\sqrt{3}}{3}} \right. \left. \frac{\partial \cos \widehat{RX}}{\partial r} \right|_1 \right) N_3^* |_G + \\ & + \left(\left. \frac{\partial N_1}{\partial r} \right|_{\overline{r}=\frac{\sqrt{3}}{3}, \overline{s}=\frac{\sqrt{3}}{3}} \cos \widehat{RX}_1 + N_1 \left|_{\overline{r}=\frac{\sqrt{3}}{3}, \overline{s}=\frac{\sqrt{3}}{3}} \right. \left. \frac{\partial \cos \widehat{RX}}{\partial r} \right|_1 \right) N_4^* |_G \Bigg\} \frac{2}{l_R} \end{aligned} \tag{5.46}$$

$$\begin{aligned} B(2) = \Bigg\{ & \left(\left. \frac{\partial N_1}{\partial r} \right|_{\overline{r}=-\frac{\sqrt{3}}{3}, \overline{s}=-\frac{\sqrt{3}}{3}} \cos \widehat{RY}_1 + N_1 \left|_{\overline{r}=-\frac{\sqrt{3}}{3}, \overline{s}=-\frac{\sqrt{3}}{3}} \right. \left. \frac{\partial \cos \widehat{RY}}{\partial r} \right|_1 \right) N_1^* |_G + \\ & + \left(\left. \frac{\partial N_1}{\partial r} \right|_{\overline{r}=-\frac{\sqrt{3}}{3}, \overline{s}=\frac{\sqrt{3}}{3}} \cos \widehat{RY}_1 + N_1 \left|_{\overline{r}=-\frac{\sqrt{3}}{3}, \overline{s}=\frac{\sqrt{3}}{3}} \right. \left. \frac{\partial \cos \widehat{RY}}{\partial r} \right|_1 \right) N_2^* |_G + \\ & + \left(\left. \frac{\partial N_1}{\partial r} \right|_{\overline{r}=\frac{\sqrt{3}}{3}, \overline{s}=-\frac{\sqrt{3}}{3}} \cos \widehat{RY}_1 + N_1 \left|_{\overline{r}=\frac{\sqrt{3}}{3}, \overline{s}=-\frac{\sqrt{3}}{3}} \right. \left. \frac{\partial \cos \widehat{RY}}{\partial r} \right|_1 \right) N_3^* |_G + \\ & + \left(\left. \frac{\partial N_1}{\partial r} \right|_{\overline{r}=\frac{\sqrt{3}}{3}, \overline{s}=\frac{\sqrt{3}}{3}} \cos \widehat{RY}_1 + N_1 \left|_{\overline{r}=\frac{\sqrt{3}}{3}, \overline{s}=\frac{\sqrt{3}}{3}} \right. \left. \frac{\partial \cos \widehat{RY}}{\partial r} \right|_1 \right) N_4^* |_G \Bigg\} \frac{2}{l_R} \end{aligned} \tag{5.47}$$

$$\begin{aligned} B(3) = \Bigg\{ & \left(\left. \frac{\partial N_1}{\partial r} \right|_{\overline{r}=-\frac{\sqrt{3}}{3}, \overline{s}=-\frac{\sqrt{3}}{3}} \cos \widehat{RZ}_1 + N_1 \left|_{\overline{r}=-\frac{\sqrt{3}}{3}, \overline{s}=-\frac{\sqrt{3}}{3}} \right. \left. \frac{\partial \cos \widehat{RZ}}{\partial r} \right|_1 \right) N_1^* |_G + \\ & + \left(\left. \frac{\partial N_1}{\partial r} \right|_{\overline{r}=-\frac{\sqrt{3}}{3}, \overline{s}=\frac{\sqrt{3}}{3}} \cos \widehat{RZ}_1 + N_1 \left|_{\overline{r}=-\frac{\sqrt{3}}{3}, \overline{s}=\frac{\sqrt{3}}{3}} \right. \left. \frac{\partial \cos \widehat{RZ}}{\partial r} \right|_1 \right) N_2^* |_G + \\ & + \left(\left. \frac{\partial N_1}{\partial r} \right|_{\overline{r}=\frac{\sqrt{3}}{3}, \overline{s}=-\frac{\sqrt{3}}{3}} \cos \widehat{RZ}_1 + N_1 \left|_{\overline{r}=\frac{\sqrt{3}}{3}, \overline{s}=-\frac{\sqrt{3}}{3}} \right. \left. \frac{\partial \cos \widehat{RZ}}{\partial r} \right|_1 \right) N_3^* |_G + \\ & + \left(\left. \frac{\partial N_1}{\partial r} \right|_{\overline{r}=\frac{\sqrt{3}}{3}, \overline{s}=\frac{\sqrt{3}}{3}} \cos \widehat{RZ}_1 + N_1 \left|_{\overline{r}=\frac{\sqrt{3}}{3}, \overline{s}=\frac{\sqrt{3}}{3}} \right. \left. \frac{\partial \cos \widehat{RZ}}{\partial r} \right|_1 \right) N_4^* |_G \Bigg\} \frac{2}{l_R} \end{aligned} \tag{5.48}$$

$$B(4) = \left\{ \left(\left.\frac{\partial N_1}{\partial r}\right|_{\overline{r}=-\frac{\sqrt{3}}{3},\overline{s}=-\frac{\sqrt{3}}{3}} \cos\widehat{SX}_1 + N_1 \left|_{\overline{r}=-\frac{\sqrt{3}}{3},\overline{s}=-\frac{\sqrt{3}}{3}} \frac{\partial \cos\widehat{SX}}{\partial r}\right|_1 \right) N_1^*|_G + \right.$$
$$+ \left(\left.\frac{\partial N_1}{\partial r}\right|_{\overline{r}=-\frac{\sqrt{3}}{3},\overline{s}=\frac{\sqrt{3}}{3}} \cos\widehat{SX}_1 + N_1 \left|_{\overline{r}=-\frac{\sqrt{3}}{3},\overline{s}=\frac{\sqrt{3}}{3}} \frac{\partial \cos\widehat{SX}}{\partial r}\right|_1 \right) N_2^*|_G +$$
$$+ \left(\left.\frac{\partial N_1}{\partial r}\right|_{\overline{r}=\frac{\sqrt{3}}{3},\overline{s}=-\frac{\sqrt{3}}{3}} \cos\widehat{SX}_1 + N_1 \left|_{\overline{r}=\frac{\sqrt{3}}{3},\overline{s}=-\frac{\sqrt{3}}{3}} \frac{\partial \cos\widehat{SX}}{\partial r}\right|_1 \right) N_3^*|_G +$$
$$\left. + \left(\left.\frac{\partial N_1}{\partial r}\right|_{\overline{r}=\frac{\sqrt{3}}{3},\overline{s}=\frac{\sqrt{3}}{3}} \cos\widehat{SX}_1 + N_1 \left|_{\overline{r}=\frac{\sqrt{3}}{3},\overline{s}=\frac{\sqrt{3}}{3}} \frac{\partial \cos\widehat{SX}}{\partial r}\right|_1 \right) N_4^*|_G \right\} \frac{th}{l_R} \quad (5.49)$$

$$B(5) = \left\{ \left(\left.\frac{\partial N_1}{\partial r}\right|_{\overline{r}=-\frac{\sqrt{3}}{3},\overline{s}=-\frac{\sqrt{3}}{3}} \cos\widehat{SY}_1 + N_1 \left|_{\overline{r}=-\frac{\sqrt{3}}{3},\overline{s}=-\frac{\sqrt{3}}{3}} \frac{\partial \cos\widehat{SY}}{\partial r}\right|_1 \right) N_1^*|_G + \right.$$
$$+ \left(\left.\frac{\partial N_1}{\partial r}\right|_{\overline{r}=-\frac{\sqrt{3}}{3},\overline{s}=\frac{\sqrt{3}}{3}} \cos\widehat{SY}_1 + N_1 \left|_{\overline{r}=-\frac{\sqrt{3}}{3},\overline{s}=\frac{\sqrt{3}}{3}} \frac{\partial \cos\widehat{SY}}{\partial r}\right|_1 \right) N_2^*|_G +$$
$$+ \left(\left.\frac{\partial N_1}{\partial r}\right|_{\overline{r}=\frac{\sqrt{3}}{3},\overline{s}=-\frac{\sqrt{3}}{3}} \cos\widehat{SY}_1 + N_1 \left|_{\overline{r}=\frac{\sqrt{3}}{3},\overline{s}=-\frac{\sqrt{3}}{3}} \frac{\partial \cos\widehat{SY}}{\partial r}\right|_1 \right) N_3^*|_G +$$
$$\left. + \left(\left.\frac{\partial N_1}{\partial r}\right|_{\overline{r}=\frac{\sqrt{3}}{3},\overline{s}=\frac{\sqrt{3}}{3}} \cos\widehat{SY}_1 + N_1 \left|_{\overline{r}=\frac{\sqrt{3}}{3},\overline{s}=\frac{\sqrt{3}}{3}} \frac{\partial \cos\widehat{SY}}{\partial r}\right|_1 \right) N_4^*|_G \right\} \frac{th}{l_R} \quad (5.50)$$

$$B(6) = \left\{ \left(\left.\frac{\partial N_1}{\partial r}\right|_{\overline{r}=-\frac{\sqrt{3}}{3},\overline{s}=-\frac{\sqrt{3}}{3}} \cos\widehat{SZ}_1 + N_1 \left|_{\overline{r}=-\frac{\sqrt{3}}{3},\overline{s}=-\frac{\sqrt{3}}{3}} \frac{\partial \cos\widehat{SZ}}{\partial r}\right|_1 \right) N_1^*|_G + \right.$$
$$+ \left(\left.\frac{\partial N_1}{\partial r}\right|_{\overline{r}=-\frac{\sqrt{3}}{3},\overline{s}=\frac{\sqrt{3}}{3}} \cos\widehat{SZ}_1 + N_1 \left|_{\overline{r}=-\frac{\sqrt{3}}{3},\overline{s}=\frac{\sqrt{3}}{3}} \frac{\partial \cos\widehat{SZ}}{\partial r}\right|_1 \right) N_2^*|_G +$$
$$+ \left(\left.\frac{\partial N_1}{\partial r}\right|_{\overline{r}=\frac{\sqrt{3}}{3},\overline{s}=-\frac{\sqrt{3}}{3}} \cos\widehat{SZ}_1 + N_1 \left|_{\overline{r}=\frac{\sqrt{3}}{3},\overline{s}=-\frac{\sqrt{3}}{3}} \frac{\partial \cos\widehat{SZ}}{\partial r}\right|_1 \right) N_3^*|_G +$$
$$\left. + \left(\left.\frac{\partial N_1}{\partial r}\right|_{\overline{r}=\frac{\sqrt{3}}{3},\overline{s}=\frac{\sqrt{3}}{3}} \cos\widehat{SZ}_1 + N_1 \left|_{\overline{r}=\frac{\sqrt{3}}{3},\overline{s}=\frac{\sqrt{3}}{3}} \frac{\partial \cos\widehat{SZ}}{\partial r}\right|_1 \right) N_4^*|_G \right\} \frac{th}{l_R} \quad (5.51)$$

$$B(7) = \left\{ \left(\left. \frac{\partial N_1}{\partial s} \right|_{\overline{r}=-\frac{\sqrt{3}}{3},\overline{s}=-\frac{\sqrt{3}}{3}} \cos\widehat{SX}_1 + N_1 \left|_{\overline{r}=-\frac{\sqrt{3}}{3},\overline{s}=-\frac{\sqrt{3}}{3}} \frac{\partial \cos\widehat{SX}}{\partial s}\right|_1 \right) N_1^*|_G + \right.$$
$$+ \left(\left. \frac{\partial N_1}{\partial s} \right|_{\overline{r}=-\frac{\sqrt{3}}{3},\overline{s}=\frac{\sqrt{3}}{3}} \cos\widehat{SX}_1 + N_1 \left|_{\overline{r}=-\frac{\sqrt{3}}{3},\overline{s}=\frac{\sqrt{3}}{3}} \frac{\partial \cos\widehat{SX}}{\partial s}\right|_1 \right) N_2^*|_G +$$
$$+ \left(\left. \frac{\partial N_1}{\partial s} \right|_{\overline{r}=\frac{\sqrt{3}}{3},\overline{s}=-\frac{\sqrt{3}}{3}} \cos\widehat{SX}_1 + N_1 \left|_{\overline{r}=\frac{\sqrt{3}}{3},\overline{s}=-\frac{\sqrt{3}}{3}} \frac{\partial \cos\widehat{SX}}{\partial s}\right|_1 \right) N_3^*|_G +$$
$$\left. + \left(\left. \frac{\partial N_1}{\partial s} \right|_{\overline{r}=\frac{\sqrt{3}}{3},\overline{s}=\frac{\sqrt{3}}{3}} \cos\widehat{SX}_1 + N_1 \left|_{\overline{r}=\frac{\sqrt{3}}{3},\overline{s}=\frac{\sqrt{3}}{3}} \frac{\partial \cos\widehat{SX}}{\partial s}\right|_1 \right) N_4^*|_G \right\} \frac{2}{l_S} \quad (5.52)$$

$$B(8) = \left\{ \left(\left. \frac{\partial N_1}{\partial s} \right|_{\overline{r}=-\frac{\sqrt{3}}{3},\overline{s}=-\frac{\sqrt{3}}{3}} \cos\widehat{SY}_1 + N_1 \left|_{\overline{r}=-\frac{\sqrt{3}}{3},\overline{s}=-\frac{\sqrt{3}}{3}} \frac{\partial \cos\widehat{SY}}{\partial s}\right|_1 \right) N_1^*|_G + \right.$$
$$+ \left(\left. \frac{\partial N_1}{\partial s} \right|_{\overline{r}=-\frac{\sqrt{3}}{3},\overline{s}=\frac{\sqrt{3}}{3}} \cos\widehat{SY}_1 + N_1 \left|_{\overline{r}=-\frac{\sqrt{3}}{3},\overline{s}=\frac{\sqrt{3}}{3}} \frac{\partial \cos\widehat{SY}}{\partial s}\right|_1 \right) N_2^*|_G +$$
$$+ \left(\left. \frac{\partial N_1}{\partial s} \right|_{\overline{r}=\frac{\sqrt{3}}{3},\overline{s}=-\frac{\sqrt{3}}{3}} \cos\widehat{SY}_1 + N_1 \left|_{\overline{r}=\frac{\sqrt{3}}{3},\overline{s}=-\frac{\sqrt{3}}{3}} \frac{\partial \cos\widehat{SY}}{\partial s}\right|_1 \right) N_3^*|_G +$$
$$\left. + \left(\left. \frac{\partial N_1}{\partial s} \right|_{\overline{r}=\frac{\sqrt{3}}{3},\overline{s}=\frac{\sqrt{3}}{3}} \cos\widehat{SY}_1 + N_1 \left|_{\overline{r}=\frac{\sqrt{3}}{3},\overline{s}=\frac{\sqrt{3}}{3}} \frac{\partial \cos\widehat{SY}}{\partial s}\right|_1 \right) N_4^*|_G \right\} \frac{2}{l_S} \quad (5.53)$$

$$B(9) = \left\{ \left(\left. \frac{\partial N_1}{\partial s} \right|_{\overline{r}=-\frac{\sqrt{3}}{3},\overline{s}=-\frac{\sqrt{3}}{3}} \cos\widehat{SZ}_1 + N_1 \left|_{\overline{r}=-\frac{\sqrt{3}}{3},\overline{s}=-\frac{\sqrt{3}}{3}} \frac{\partial \cos\widehat{SZ}}{\partial s}\right|_1 \right) N_1^*|_G + \right.$$
$$+ \left(\left. \frac{\partial N_1}{\partial s} \right|_{\overline{r}=-\frac{\sqrt{3}}{3},\overline{s}=\frac{\sqrt{3}}{3}} \cos\widehat{SZ}_1 + N_1 \left|_{\overline{r}=-\frac{\sqrt{3}}{3},\overline{s}=\frac{\sqrt{3}}{3}} \frac{\partial \cos\widehat{SZ}}{\partial s}\right|_1 \right) N_2^*|_{PG} +$$
$$+ \left(\left. \frac{\partial N_1}{\partial s} \right|_{\overline{r}=\frac{\sqrt{3}}{3},\overline{s}=-\frac{\sqrt{3}}{3}} \cos\widehat{SZ}_1 + N_1 \left|_{\overline{r}=\frac{\sqrt{3}}{3},\overline{s}=-\frac{\sqrt{3}}{3}} \frac{\partial \cos\widehat{SZ}}{\partial s}\right|_1 \right) N_3^*|_G +$$
$$\left. + \left(\left. \frac{\partial N_1}{\partial s} \right|_{\overline{r}=\frac{\sqrt{3}}{3},\overline{s}=\frac{\sqrt{3}}{3}} \cos\widehat{SZ}_1 + N_1 \left|_{\overline{r}=\frac{\sqrt{3}}{3},\overline{s}=\frac{\sqrt{3}}{3}} \frac{\partial \cos\widehat{SZ}}{\partial s}\right|_1 \right) N_4^*|_G \right\} \frac{2}{l_S} \quad (5.54)$$

$$B(10) = -\left\{ \left(\left.\frac{\partial N_1}{\partial s}\right|_{\overline{r}=-\frac{\sqrt{3}}{3},\overline{s}=-\frac{\sqrt{3}}{3}} \cos\widehat{RX}_1 + N_1 \left|_{\overline{r}=-\frac{\sqrt{3}}{3},\overline{s}=-\frac{\sqrt{3}}{3}} \frac{\partial \cos\widehat{RX}}{\partial s}\right|_1 \right) N_1^*|_G + \right.$$
$$+ \left(\left.\frac{\partial N_1}{\partial s}\right|_{\overline{r}=-\frac{\sqrt{3}}{3},\overline{s}=\frac{\sqrt{3}}{3}} \cos\widehat{RX}_1 + N_1 \left|_{\overline{r}=-\frac{\sqrt{3}}{3},\overline{s}=\frac{\sqrt{3}}{3}} \frac{\partial \cos\widehat{RX}}{\partial s}\right|_1 \right) N_2^*|_G +$$
$$+ \left(\left.\frac{\partial N_1}{\partial s}\right|_{\overline{r}=\frac{\sqrt{3}}{3},\overline{s}=-\frac{\sqrt{3}}{3}} \cos\widehat{RX}_1 + N_1 \left|_{\overline{r}=\frac{\sqrt{3}}{3},\overline{s}=-\frac{\sqrt{3}}{3}} \frac{\partial \cos\widehat{RX}}{\partial s}\right|_1 \right) N_3^*|_G +$$
$$\left. + \left(\left.\frac{\partial N_1}{\partial s}\right|_{\overline{r}=\frac{\sqrt{3}}{3},\overline{s}=\frac{\sqrt{3}}{3}} \cos\widehat{RX}_1 + N_1 \left|_{\overline{r}=\frac{\sqrt{3}}{3},\overline{s}=\frac{\sqrt{3}}{3}} \frac{\partial \cos\widehat{RX}}{\partial s}\right|_1 \right) N_4^*|_G \right\} \frac{th}{l_S} \quad (5.55)$$

$$B(11) = -\left\{ \left(\left.\frac{\partial N_1}{\partial s}\right|_{\overline{r}=-\frac{\sqrt{3}}{3},\overline{s}=-\frac{\sqrt{3}}{3}} \cos\widehat{RY}_1 + N_1 \left|_{\overline{r}=-\frac{\sqrt{3}}{3},\overline{s}=-\frac{\sqrt{3}}{3}} \frac{\partial \cos\widehat{RY}}{\partial s}\right|_1 \right) N_1^*|_G + \right.$$
$$+ \left(\left.\frac{\partial N_1}{\partial s}\right|_{\overline{r}=-\frac{\sqrt{3}}{3},\overline{s}=\frac{\sqrt{3}}{3}} \cos\widehat{RY}_1 + N_1 \left|_{\overline{r}=-\frac{\sqrt{3}}{3},\overline{s}=\frac{\sqrt{3}}{3}} \frac{\partial \cos\widehat{RY}}{\partial s}\right|_1 \right) N_2^*|_G +$$
$$+ \left(\left.\frac{\partial N_1}{\partial s}\right|_{\overline{r}=\frac{\sqrt{3}}{3},\overline{s}=-\frac{\sqrt{3}}{3}} \cos\widehat{RY}_1 + N_1 \left|_{\overline{r}=\frac{\sqrt{3}}{3},\overline{s}=-\frac{\sqrt{3}}{3}} \frac{\partial \cos\widehat{RY}}{\partial s}\right|_1 \right) N_3^*|_G +$$
$$\left. + \left(\left.\frac{\partial N_1}{\partial s}\right|_{\overline{r}=\frac{\sqrt{3}}{3},\overline{s}=\frac{\sqrt{3}}{3}} \cos\widehat{RY}_1 + N_1 \left|_{\overline{r}=\frac{\sqrt{3}}{3},\overline{s}=\frac{\sqrt{3}}{3}} \frac{\partial \cos\widehat{RY}}{\partial s}\right|_1 \right) N_4^*|_G \right\} \frac{th}{l_S} \quad (5.56)$$

$$B(12) = -\left\{ \left(\left.\frac{\partial N_1}{\partial s}\right|_{\overline{r}=-\frac{\sqrt{3}}{3},\overline{s}=-\frac{\sqrt{3}}{3}} \cos\widehat{RZ}_1 + N_1 \left|_{\overline{r}=-\frac{\sqrt{3}}{3},\overline{s}=-\frac{\sqrt{3}}{3}} \frac{\partial \cos\widehat{RZ}}{\partial s}\right|_1 \right) N_1^*|_G + \right.$$
$$+ \left(\left.\frac{\partial N_1}{\partial s}\right|_{\overline{r}=-\frac{\sqrt{3}}{3},\overline{s}=\frac{\sqrt{3}}{3}} \cos\widehat{RZ}_1 + N_1 \left|_{\overline{r}=-\frac{\sqrt{3}}{3},\overline{s}=\frac{\sqrt{3}}{3}} \frac{\partial \cos\widehat{RZ}}{\partial s}\right|_1 \right) N_2^*|_G +$$
$$+ \left(\left.\frac{\partial N_1}{\partial s}\right|_{\overline{r}=\frac{\sqrt{3}}{3},\overline{s}=-\frac{\sqrt{3}}{3}} \cos\widehat{RZ}_1 + N_1 \left|_{\overline{r}=\frac{\sqrt{3}}{3},\overline{s}=-\frac{\sqrt{3}}{3}} \frac{\partial \cos\widehat{RZ}}{\partial s}\right|_1 \right) N_3^*|_G +$$
$$\left. + \left(\left.\frac{\partial N_1}{\partial s}\right|_{\overline{r}=\frac{\sqrt{3}}{3},\overline{s}=\frac{\sqrt{3}}{3}} \cos\widehat{RZ}_1 + N_1 \left|_{\overline{r}=\frac{\sqrt{3}}{3},\overline{s}=\frac{\sqrt{3}}{3}} \frac{\partial \cos\widehat{RZ}}{\partial s}\right|_1 \right) N_4^*|_G \right\} \frac{th}{l_S} \quad (5.57)$$

$$
\begin{aligned}
B\,(13) = & \left[\left(\frac{\partial N_1}{\partial r}\bigg|_{\overline{r}=-\frac{\sqrt{3}}{3},\overline{s}=-\frac{\sqrt{3}}{3}} \cos\widehat{SX}_1 + N_1\bigg|_{\overline{r}=-\frac{\sqrt{3}}{3},\overline{s}=-\frac{\sqrt{3}}{3}} \frac{\partial\cos\widehat{SX}}{\partial r}\bigg|_1 \right)\frac{2}{l_R} + \right. \\
& \left. + \left(\frac{\partial N_1}{\partial s}\bigg|_{\overline{r}=-\frac{\sqrt{3}}{3},\overline{s}=-\frac{\sqrt{3}}{3}} \cos\widehat{RX}_1 + N_1\bigg|_{\overline{r}=-\frac{\sqrt{3}}{3},\overline{s}=-\frac{\sqrt{3}}{3}} \frac{\partial\cos\widehat{RX}}{\partial s}\bigg|_1 \right)\frac{2}{l_S} \right] N_1^*|_G + \\
& + \left[\left(\frac{\partial N_1}{\partial r}\bigg|_{\overline{r}=-\frac{\sqrt{3}}{3},\overline{s}=\frac{\sqrt{3}}{3}} \cos\widehat{SX}_1 + N_1\bigg|_{\overline{r}=-\frac{\sqrt{3}}{3},\overline{s}=\frac{\sqrt{3}}{3}} \frac{\partial\cos\widehat{SX}}{\partial r}\bigg|_1 \right)\frac{2}{l_R} + \right. \\
& \left. + \left(\frac{\partial N_1}{\partial s}\bigg|_{\overline{r}=-\frac{\sqrt{3}}{3},\overline{s}=\frac{\sqrt{3}}{3}} \cos\widehat{RX}_1 + N_1\bigg|_{\overline{r}=-\frac{\sqrt{3}}{3},\overline{s}=\frac{\sqrt{3}}{3}} \frac{\partial\cos\widehat{RX}}{\partial s}\bigg|_1 \right)\frac{2}{l_S} \right] N_2^*|_G + \\
& + \left[\left(\frac{\partial N_1}{\partial r}\bigg|_{\overline{r}=\frac{\sqrt{3}}{3},\overline{s}=-\frac{\sqrt{3}}{3}} \cos\hat{SX}_1 + N_1\bigg|_{\overline{r}=\frac{\sqrt{3}}{3},\overline{s}=-\frac{\sqrt{3}}{3}} \frac{\partial\cos\widehat{SX}}{\partial r}\bigg|_1 \right)\frac{2}{l_R} + \right. \\
& \left. + \left(\frac{\partial N_1}{\partial s}\bigg|_{\overline{r}=\frac{\sqrt{3}}{3},\overline{s}=-\frac{\sqrt{3}}{3}} \cos\widehat{RX}_1 + N_1\bigg|_{\overline{r}=\frac{\sqrt{3}}{3},\overline{s}=-\frac{\sqrt{3}}{3}} \frac{\partial\cos\widehat{RX}}{\partial s}\bigg|_1 \right)\frac{2}{l_S} \right] N_3^*|_G + \\
& + \left[\left(\frac{\partial N_1}{\partial r}\bigg|_{\overline{r}=\frac{\sqrt{3}}{3},\overline{s}=\frac{\sqrt{3}}{3}} \cos\widehat{SX}_1 + N_1\bigg|_{\overline{r}=\frac{\sqrt{3}}{3},\overline{s}=\frac{\sqrt{3}}{3}} \frac{\partial\cos\widehat{SX}}{\partial r}\bigg|_1 \right)\frac{2}{l_R} + \right. \\
& \left. + \left(\frac{\partial N_1}{\partial s}\bigg|_{\overline{r}=\frac{\sqrt{3}}{3},\overline{s}=\frac{\sqrt{3}}{3}} \cos\widehat{RX}_1 + N_1\bigg|_{\overline{r}=\frac{\sqrt{3}}{3},\overline{s}=\frac{\sqrt{3}}{3}} \frac{\partial\cos\widehat{RX}}{\partial s}\bigg|_1 \right)\frac{2}{l_S} \right] N_4^*|_G \qquad (5.58)
\end{aligned}
$$

$$
\begin{aligned}
B\,(14) = & \left[\left(\frac{\partial N_1}{\partial r}\bigg|_{\overline{r}=-\frac{\sqrt{3}}{3},\overline{s}=-\frac{\sqrt{3}}{3}} \cos\widehat{SY}_1 + N_1\bigg|_{\overline{r}=-\frac{\sqrt{3}}{3},\overline{s}=-\frac{\sqrt{3}}{3}} \frac{\partial\cos\widehat{SY}}{\partial r}\bigg|_1 \right)\frac{2}{l_R} + \right. \\
& \left. + \left(\frac{\partial N_1}{\partial s}\bigg|_{\overline{r}=-\frac{\sqrt{3}}{3},\overline{s}=-\frac{\sqrt{3}}{3}} \cos\widehat{RY}_1 + N_1\bigg|_{\overline{r}=-\frac{\sqrt{3}}{3},\overline{s}=-\frac{\sqrt{3}}{3}} \frac{\partial\cos\widehat{RY}}{\partial s}\bigg|_1 \right)\frac{2}{l_S} \right] N_1^*|_G + \\
& + \left[\left(\frac{\partial N_1}{\partial r}\bigg|_{\overline{r}=-\frac{\sqrt{3}}{3},\overline{s}=\frac{\sqrt{3}}{3}} \cos\widehat{SY}_1 + N_1\bigg|_{\overline{r}=-\frac{\sqrt{3}}{3},\overline{s}=\frac{\sqrt{3}}{3}} \frac{\partial\cos\widehat{SY}}{\partial r}\bigg|_1 \right)\frac{2}{l_R} + \right. \\
& \left. + \left(\frac{\partial N_1}{\partial s}\bigg|_{\overline{r}=-\frac{\sqrt{3}}{3},\overline{s}=\frac{\sqrt{3}}{3}} \cos\widehat{RY}_1 + N_1\bigg|_{\overline{r}=-\frac{\sqrt{3}}{3},\overline{s}=\frac{\sqrt{3}}{3}} \frac{\partial\cos\widehat{RY}}{\partial s}\bigg|_1 \right)\frac{2}{l_S} \right] N_2^*|_G + \\
& + \left[\left(\frac{\partial N_1}{\partial r}\bigg|_{\overline{r}=\frac{\sqrt{3}}{3},\overline{s}=-\frac{\sqrt{3}}{3}} \cos\widehat{SY}_1 + N_1\bigg|_{\overline{r}=\frac{\sqrt{3}}{3},\overline{s}=-\frac{\sqrt{3}}{3}} \frac{\partial\cos\widehat{SY}}{\partial r}\bigg|_1 \right)\frac{2}{l_R} + \right. \\
& \left. + \left(\frac{\partial N_1}{\partial s}\bigg|_{\overline{r}=\frac{\sqrt{3}}{3},\overline{s}=-\frac{\sqrt{3}}{3}} \cos\widehat{RY}_1 + N_1\bigg|_{\overline{r}=\frac{\sqrt{3}}{3},\overline{s}=-\frac{\sqrt{3}}{3}} \frac{\partial\cos\widehat{RY}}{\partial s}\bigg|_1 \right)\frac{2}{l_S} \right] N_3^*|_G + \\
& + \left[\left(\frac{\partial N_1}{\partial r}\bigg|_{\overline{r}=\frac{\sqrt{3}}{3},\overline{s}=\frac{\sqrt{3}}{3}} \cos\widehat{SY}_1 + N_1\bigg|_{\overline{r}=\frac{\sqrt{3}}{3},\overline{s}=\frac{\sqrt{3}}{3}} \frac{\partial\cos\widehat{SY}}{\partial r}\bigg|_1 \right)\frac{2}{l_R} + \right. \\
& \left. + \left(\frac{\partial N_1}{\partial s}\bigg|_{\overline{r}=\frac{\sqrt{3}}{3},\overline{s}=\frac{\sqrt{3}}{3}} \cos\widehat{RY}_1 + N_1\bigg|_{\overline{r}=\frac{\sqrt{3}}{3},\overline{s}=\frac{\sqrt{3}}{3}} \frac{\partial\cos\widehat{RY}}{\partial s}\bigg|_1 \right)\frac{2}{l_S} \right] N_4^*|_G \qquad (5.59)
\end{aligned}
$$

$$B\,(15) = \left[\left(\left.\frac{\partial N_1}{\partial r}\right|_{\overline{r}=-\frac{\sqrt{3}}{3},\overline{s}=-\frac{\sqrt{3}}{3}} \cos\widehat{SZ}_1 + N_1 \left|_{\overline{r}=-\frac{\sqrt{3}}{3},\overline{s}=-\frac{\sqrt{3}}{3}} \frac{\partial \cos\widehat{SZ}}{\partial r}\right|_1 \right) \frac{2}{l_R} + \right.$$
$$+ \left(\left.\frac{\partial N_1}{\partial s}\right|_{\overline{r}=-\frac{\sqrt{3}}{3},\overline{s}=-\frac{\sqrt{3}}{3}} \cos\widehat{RZ}_1 + N_1 \left|_{\overline{r}=-\frac{\sqrt{3}}{3},\overline{s}=-\frac{\sqrt{3}}{3}} \frac{\partial \cos\widehat{RZ}}{\partial s}\right|_1 \right) \left.\frac{2}{l_S}\right] N_1^*|_G +$$
$$+ \left[\left(\left.\frac{\partial N_1}{\partial r}\right|_{\overline{r}=-\frac{\sqrt{3}}{3},\overline{s}=\frac{\sqrt{3}}{3}} \cos\widehat{SZ}_1 + N_1 \left|_{\overline{r}=-\frac{\sqrt{3}}{3},\overline{s}=\frac{\sqrt{3}}{3}} \frac{\partial \cos\widehat{SZ}}{\partial r}\right|_1 \right) \frac{2}{l_R} + \right.$$
$$+ \left(\left.\frac{\partial N_1}{\partial s}\right|_{\overline{r}=-\frac{\sqrt{3}}{3},\overline{s}=\frac{\sqrt{3}}{3}} \cos\widehat{RZ}_1 + N_1 \left|_{\overline{r}=-\frac{\sqrt{3}}{3},\overline{s}=\frac{\sqrt{3}}{3}} \frac{\partial \cos\widehat{RZ}}{\partial s}\right|_1 \right) \left.\frac{2}{l_S}\right] N_2^*|_G +$$
$$+ \left[\left(\left.\frac{\partial N_1}{\partial r}\right|_{\overline{r}=\frac{\sqrt{3}}{3},\overline{s}=-\frac{\sqrt{3}}{3}} \cos\widehat{SZ}_1 + N_1 \left|_{\overline{r}=\frac{\sqrt{3}}{3},\overline{s}=-\frac{\sqrt{3}}{3}} \frac{\partial \cos\widehat{SZ}}{\partial r}\right|_1 \right) \frac{2}{l_R} + \right.$$
$$+ \left(\left.\frac{\partial N_1}{\partial s}\right|_{\overline{r}=\frac{\sqrt{3}}{3},\overline{s}=-\frac{\sqrt{3}}{3}} \cos\widehat{RZ}_1 + N_1 \left|_{\overline{r}=\frac{\sqrt{3}}{3},\overline{s}=-\frac{\sqrt{3}}{3}} \frac{\partial \cos\widehat{RZ}}{\partial s}\right|_1 \right) \left.\frac{2}{l_S}\right] N_3^*|_G +$$
$$+ \left[\left(\left.\frac{\partial N_1}{\partial r}\right|_{\overline{r}=\frac{\sqrt{3}}{3},\overline{s}=\frac{\sqrt{3}}{3}} \cos\widehat{SZ}_1 + N_1 \left|_{\overline{r}=\frac{\sqrt{3}}{3},\overline{s}=\frac{\sqrt{3}}{3}} \frac{\partial \cos\widehat{SZ}}{\partial r}\right|_1 \right) \frac{2}{l_R} + \right.$$
$$\left. + \left(\left.\frac{\partial N_1}{\partial s}\right|_{\overline{r}=\frac{\sqrt{3}}{3},\overline{s}=\frac{\sqrt{3}}{3}} \cos\widehat{RZ}_1 + N_1 \left|_{\overline{r}=\frac{\sqrt{3}}{3},\overline{s}=\frac{\sqrt{3}}{3}} \frac{\partial \cos\widehat{RZ}}{\partial s}\right|_1 \right) \left.\frac{2}{l_S}\right] N_4^*|_G \qquad (5.60)$$

$$B\,(16) = \left[- \left(\left.\frac{\partial N_1}{\partial r}\right|_{\overline{r}=-\frac{\sqrt{3}}{3},\overline{s}=-\frac{\sqrt{3}}{3}} \cos\widehat{RX}_1 + N_1 \left|_{\overline{r}=-\frac{\sqrt{3}}{3},\overline{s}=-\frac{\sqrt{3}}{3}} \frac{\partial \cos\widehat{RX}}{\partial r}\right|_1 \right) \frac{th}{l_R} + \right.$$
$$+ \left(\left.\frac{\partial N_1}{\partial s}\right|_{\overline{r}=-\frac{\sqrt{3}}{3},\overline{s}=-\frac{\sqrt{3}}{3}} \cos\widehat{SX}_1 + N_1 \left|_{\overline{r}=-\frac{\sqrt{3}}{3},\overline{s}=-\frac{\sqrt{3}}{3}} \frac{\partial \cos\widehat{SX}}{\partial s}\right|_1 \right) \left.\frac{th}{l_S}\right] N_1^*|_G +$$
$$+ \left[- \left(\left.\frac{\partial N_1}{\partial r}\right|_{\overline{r}=-\frac{\sqrt{3}}{3},\overline{s}=\frac{\sqrt{3}}{3}} \cos\widehat{RX}_1 + N_1 \left|_{\overline{r}=-\frac{\sqrt{3}}{3},\overline{s}=\frac{\sqrt{3}}{3}} \frac{\partial \cos\widehat{RX}}{\partial r}\right|_1 \right) \frac{th}{l_R} + \right.$$
$$+ \left(\left.\frac{\partial N_1}{\partial s}\right|_{\overline{r}=-\frac{\sqrt{3}}{3},\overline{s}=\frac{\sqrt{3}}{3}} \cos\widehat{SX}_1 + N_1 \left|_{\overline{r}=-\frac{\sqrt{3}}{3},\overline{s}=\frac{\sqrt{3}}{3}} \frac{\partial \cos\widehat{SX}}{\partial s}\right|_1 \right) \left.\frac{th}{l_S}\right] N_2^*|_G +$$
$$+ \left[- \left(\left.\frac{\partial N_1}{\partial r}\right|_{\overline{r}=\frac{\sqrt{3}}{3},\overline{s}=-\frac{\sqrt{3}}{3}} \cos\widehat{RX}_1 + N_1 \left|_{\overline{r}=\frac{\sqrt{3}}{3},\overline{s}=-\frac{\sqrt{3}}{3}} \frac{\partial \cos\widehat{RX}}{\partial r}\right|_1 \right) \frac{th}{l_R} + \right.$$
$$+ \left(\left.\frac{\partial N_1}{\partial s}\right|_{\overline{r}=\frac{\sqrt{3}}{3},\overline{s}=-\frac{\sqrt{3}}{3}} \cos\widehat{SX}_1 + N_1 \left|_{\overline{r}=\frac{\sqrt{3}}{3},\overline{s}=-\frac{\sqrt{3}}{3}} \frac{\partial \cos\widehat{SX}}{\partial s}\right|_1 \right) \left.\frac{th}{l_S}\right] N_3^*|_G +$$
$$+ \left[- \left(\left.\frac{\partial N_1}{\partial r}\right|_{\overline{r}=\frac{\sqrt{3}}{3},\overline{s}=\frac{\sqrt{3}}{3}} \cos\widehat{RX}_1 + N_1 \left|_{\overline{r}=\frac{\sqrt{3}}{3},\overline{s}=\frac{\sqrt{3}}{3}} \frac{\partial \cos\widehat{RX}}{\partial r}\right|_1 \right) \frac{th}{l_R} + \right.$$
$$\left. + \left(\left.\frac{\partial N_1}{\partial s}\right|_{\overline{r}=\frac{\sqrt{3}}{3},\overline{s}=\frac{\sqrt{3}}{3}} \cos\widehat{SX}_1 + N_1 \left|_{\overline{r}=\frac{\sqrt{3}}{3},\overline{s}=\frac{\sqrt{3}}{3}} \frac{\partial \cos\widehat{SX}}{\partial s}\right|_1 \right) \left.\frac{th}{l_S}\right] N_4^*|_G \qquad (5.61)$$

$$
\begin{aligned}
B\left(17\right) = & \left[- \left(\left. \frac{\partial N_1}{\partial r} \right|_{\overline{r}=-\frac{\sqrt{3}}{3},\overline{s}=-\frac{\sqrt{3}}{3}} \cos \widehat{RY}_1 + N_1 \left|_{\overline{r}=-\frac{\sqrt{3}}{3},\overline{s}=-\frac{\sqrt{3}}{3}} \right. \frac{\partial \cos \widehat{RY}}{\partial r} \right|_1 \right) \frac{th}{l_R} + \right. \\
& \left. + \left(\left. \frac{\partial N_1}{\partial s} \right|_{\overline{r}=-\frac{\sqrt{3}}{3},\overline{s}=-\frac{\sqrt{3}}{3}} \cos \widehat{SY}_1 + N_1 \left|_{\overline{r}=-\frac{\sqrt{3}}{3},\overline{s}=-\frac{\sqrt{3}}{3}} \right. \frac{\partial \cos \widehat{SY}}{\partial s} \right|_1 \right) \frac{th}{l_S} \right] N_1^* \big|_G + \\
& + \left[- \left(\left. \frac{\partial N_1}{\partial r} \right|_{\overline{r}=-\frac{\sqrt{3}}{3},\overline{s}=\frac{\sqrt{3}}{3}} \cos \widehat{RY}_1 + N_1 \left|_{\overline{r}=-\frac{\sqrt{3}}{3},\overline{s}=\frac{\sqrt{3}}{3}} \right. \frac{\partial \cos \widehat{RY}}{\partial r} \right|_1 \right) \frac{th}{l_R} + \right. \\
& \left. + \left(\left. \frac{\partial N_1}{\partial s} \right|_{\overline{r}=-\frac{\sqrt{3}}{3},\overline{s}=\frac{\sqrt{3}}{3}} \cos \widehat{SY}_1 + N_1 \left|_{\overline{r}=-\frac{\sqrt{3}}{3},\overline{s}=\frac{\sqrt{3}}{3}} \right. \frac{\partial \cos \widehat{SY}}{\partial s} \right|_1 \right) \frac{th}{l_S} \right] N_2^* \big|_G + \\
& + \left[- \left(\left. \frac{\partial N_1}{\partial r} \right|_{\overline{r}=\frac{\sqrt{3}}{3},\overline{s}=-\frac{\sqrt{3}}{3}} \cos \widehat{RY}_1 + N_1 \left|_{\overline{r}=\frac{\sqrt{3}}{3},\overline{s}=-\frac{\sqrt{3}}{3}} \right. \frac{\partial \cos \widehat{RY}}{\partial r} \right|_1 \right) \frac{th}{l_R} + \right. \\
& \left. + \left(\left. \frac{\partial N_1}{\partial s} \right|_{\overline{r}=\frac{\sqrt{3}}{3},\overline{s}=-\frac{\sqrt{3}}{3}} \cos \widehat{SY}_1 + N_1 \left|_{\overline{r}=\frac{\sqrt{3}}{3},\overline{s}=-\frac{\sqrt{3}}{3}} \right. \frac{\partial \cos \widehat{SY}}{\partial s} \right|_1 \right) \frac{th}{l_S} \right] N_3^* \big|_G + \\
& + \left[- \left(\left. \frac{\partial N_1}{\partial r} \right|_{\overline{r}=\frac{\sqrt{3}}{3},\overline{s}=\frac{\sqrt{3}}{3}} \cos \widehat{RY}_1 + N_1 \left|_{\overline{r}=\frac{\sqrt{3}}{3},\overline{s}=\frac{\sqrt{3}}{3}} \right. \frac{\partial \cos \widehat{RY}}{\partial r} \right|_1 \right) \frac{th}{l_R} + \right. \\
& \left. \left. + \left(\left. \frac{\partial N_1}{\partial s} \right|_{\overline{r}=\frac{\sqrt{3}}{3},\overline{s}=\frac{\sqrt{3}}{3}} \cos \widehat{SY}_1 + N_1 \left|_{\overline{r}=\frac{\sqrt{3}}{3},\overline{s}=\frac{\sqrt{3}}{3}} \right. \frac{\partial \cos \widehat{SY}}{\partial s} \right|_1 \right) \frac{th}{l_S} \right] N_4^* \big|_G \right. \qquad (5.62)
\end{aligned}
$$

$$
\begin{aligned}
B\left(18\right) = & \left[- \left(\left. \frac{\partial N_1}{\partial r} \right|_{\overline{r}=-\frac{\sqrt{3}}{3},\overline{s}=-\frac{\sqrt{3}}{3}} \cos \widehat{RZ}_1 + N_1 \left|_{\overline{r}=-\frac{\sqrt{3}}{3},\overline{s}=-\frac{\sqrt{3}}{3}} \right. \frac{\partial \cos \widehat{RZ}}{\partial r} \right|_1 \right) \frac{th}{l_R} + \right. \\
& \left. + \left(\left. \frac{\partial N_1}{\partial s} \right|_{\overline{r}=-\frac{\sqrt{3}}{3},\overline{s}=-\frac{\sqrt{3}}{3}} \cos \widehat{SZ}_1 + N_1 \left|_{\overline{r}=-\frac{\sqrt{3}}{3},\overline{s}=-\frac{\sqrt{3}}{3}} \right. \frac{\partial \cos \widehat{SZ}}{\partial s} \right|_1 \right) \frac{th}{l_S} \right] N_1^* \big|_G + \\
& + \left[- \left(\left. \frac{\partial N_1}{\partial r} \right|_{\overline{r}=-\frac{\sqrt{3}}{3},\overline{s}=\frac{\sqrt{3}}{3}} \cos \widehat{RZ}_1 + N_1 \left|_{\overline{r}=-\frac{\sqrt{3}}{3},\overline{s}=\frac{\sqrt{3}}{3}} \right. \frac{\partial \cos \widehat{RZ}}{\partial r} \right|_1 \right) \frac{th}{l_R} + \right. \\
& \left. + \left(\left. \frac{\partial N_1}{\partial s} \right|_{\overline{r}=-\frac{\sqrt{3}}{3},\overline{s}=\frac{\sqrt{3}}{3}} \cos \widehat{SZ}_1 + N_1 \left|_{\overline{r}=-\frac{\sqrt{3}}{3},\overline{s}=\frac{\sqrt{3}}{3}} \right. \frac{\partial \cos \widehat{SZ}}{\partial s} \right|_1 \right) \frac{th}{l_S} \right] N_2^* \big|_G + \\
& + \left[- \left(\left. \frac{\partial N_1}{\partial r} \right|_{\overline{r}=\frac{\sqrt{3}}{3},\overline{s}=-\frac{\sqrt{3}}{3}} \cos \widehat{RZ}_1 + N_1 \left|_{\overline{r}=\frac{\sqrt{3}}{3},\overline{s}=-\frac{\sqrt{3}}{3}} \right. \frac{\partial \cos \widehat{RZ}}{\partial r} \right|_1 \right) \frac{th}{l_R} + \right. \\
& \left. + \left(\left. \frac{\partial N_1}{\partial s} \right|_{\overline{r}=\frac{\sqrt{3}}{3},\overline{s}=-\frac{\sqrt{3}}{3}} \cos \widehat{SZ}_1 + N_1 \left|_{\overline{r}=\frac{\sqrt{3}}{3},\overline{s}=-\frac{\sqrt{3}}{3}} \right. \frac{\partial \cos \widehat{SZ}}{\partial s} \right|_1 \right) \frac{th}{l_S} \right] N_3^* \big|_G + \\
& + \left[- \left(\left. \frac{\partial N_1}{\partial r} \right|_{\overline{r}=\frac{\sqrt{3}}{3},\overline{s}=\frac{\sqrt{3}}{3}} \cos \widehat{RZ}_1 + N_1 \left|_{\overline{r}=\frac{\sqrt{3}}{3},\overline{s}=\frac{\sqrt{3}}{3}} \right. \frac{\partial \cos \widehat{RZ}}{\partial r} \right|_1 \right) \frac{th}{l_R} + \right. \\
& \left. \left. + \left(\left. \frac{\partial N_1}{\partial s} \right|_{\overline{r}=\frac{\sqrt{3}}{3},\overline{s}=\frac{\sqrt{3}}{3}} \cos \widehat{SZ}_1 + N_1 \left|_{\overline{r}=\frac{\sqrt{3}}{3},\overline{s}=\frac{\sqrt{3}}{3}} \right. \frac{\partial \cos \widehat{SZ}}{\partial s} \right|_1 \right) \frac{th}{l_S} + \right] N_4^* \big|_G \right. \qquad (5.63)
\end{aligned}
$$

$$B\,(19) = \left\{ \left(\left.\frac{\partial N_1}{\partial r}\right|_{\overline{r}=-\frac{\sqrt{3}}{3},\overline{s}=-\frac{\sqrt{3}}{3}} \cos\widehat{TX}_1 + N_1\left|_{\overline{r}=-\frac{\sqrt{3}}{3},\overline{s}=-\frac{\sqrt{3}}{3}} \frac{\partial\cos\widehat{TX}}{\partial r}\right|_1 \right) N_1^*|_G + \right.$$
$$+ \left(\left.\frac{\partial N_1}{\partial r}\right|_{\overline{r}=-\frac{\sqrt{3}}{3},\overline{s}=\frac{\sqrt{3}}{3}} \cos\widehat{TX}_1 + N_1\left|_{\overline{r}=-\frac{\sqrt{3}}{3},\overline{s}=\frac{\sqrt{3}}{3}} \frac{\partial\cos\widehat{TX}}{\partial r}\right|_1 \right) N_2^*|_G +$$
$$+ \left(\left.\frac{\partial N_1}{\partial r}\right|_{\overline{r}=\frac{\sqrt{3}}{3},\overline{s}=-\frac{\sqrt{3}}{3}} \cos\widehat{TX}_1 + N_1\left|_{\overline{r}=\frac{\sqrt{3}}{3},\overline{s}=-\frac{\sqrt{3}}{3}} \frac{\partial\cos\widehat{TX}}{\partial r}\right|_1 \right) N_3^*|_G +$$
$$\left. + \left(\left.\frac{\partial N_1}{\partial r}\right|_{\overline{r}=\frac{\sqrt{3}}{3},\overline{s}=\frac{\sqrt{3}}{3}} \cos\widehat{TX}_1 + N_1\left|_{\overline{r}=\frac{\sqrt{3}}{3},\overline{s}=\frac{\sqrt{3}}{3}} \frac{\partial\cos\widehat{TX}}{\partial r}\right|_1 \right) N_4^*|_G \right\} \frac{2}{l_R} \qquad (5.64)$$

$$B\,(20) = \left\{ \left(\left.\frac{\partial N_1}{\partial r}\right|_{\overline{r}=-\frac{\sqrt{3}}{3},\overline{s}=-\frac{\sqrt{3}}{3}} \cos\widehat{TY}_1 + N_1\left|_{\overline{r}=-\frac{\sqrt{3}}{3},\overline{s}=-\frac{\sqrt{3}}{3}} \frac{\partial\cos\widehat{TY}}{\partial r}\right|_1 \right) N_1^*|_G + \right.$$
$$+ \left(\left.\frac{\partial N_1}{\partial r}\right|_{\overline{r}=-\frac{\sqrt{3}}{3},\overline{s}=\frac{\sqrt{3}}{3}} \cos\widehat{TY}_1 + N_1\left|_{\overline{r}=-\frac{\sqrt{3}}{3},\overline{s}=\frac{\sqrt{3}}{3}} \frac{\partial\cos\widehat{TY}}{\partial r}\right|_1 \right) N_2^*|_G +$$
$$+ \left(\left.\frac{\partial N_1}{\partial r}\right|_{\overline{r}=\frac{\sqrt{3}}{3},\overline{s}=-\frac{\sqrt{3}}{3}} \cos\widehat{TY}_1 + N_1\left|_{\overline{r}=\frac{\sqrt{3}}{3},\overline{s}=-\frac{\sqrt{3}}{3}} \frac{\partial\cos\widehat{TY}}{\partial r}\right|_1 \right) N_3^*|_G +$$
$$\left. + \left(\left.\frac{\partial N_1}{\partial r}\right|_{\overline{r}=\frac{\sqrt{3}}{3},\overline{s}=\frac{\sqrt{3}}{3}} \cos\widehat{TY}_1 + N_1\left|_{\overline{r}=\frac{\sqrt{3}}{3},\overline{s}=\frac{\sqrt{3}}{3}} \frac{\partial\cos\widehat{TY}}{\partial r}\right|_1 \right) N_4^*|_G \right\} \frac{2}{l_R} \qquad (5.65)$$

$$B\,(21) = \left\{ \left(\left.\frac{\partial N_1}{\partial r}\right|_{\overline{r}=-\frac{\sqrt{3}}{3},\overline{s}=-\frac{\sqrt{3}}{3}} \cos\widehat{TZ}_1 + N_1\left|_{\overline{r}=-\frac{\sqrt{3}}{3},\overline{s}=-\frac{\sqrt{3}}{3}} \frac{\partial\cos\widehat{TZ}}{\partial r}\right|_1 \right) N_1^*|_G + \right.$$
$$+ \left(\left.\frac{\partial N_1}{\partial r}\right|_{\overline{r}=-\frac{\sqrt{3}}{3},\overline{s}=\frac{\sqrt{3}}{3}} \cos\widehat{TZ}_1 + N_1\left|_{\overline{r}=-\frac{\sqrt{3}}{3},\overline{s}=\frac{\sqrt{3}}{3}} \frac{\partial\cos\widehat{TZ}}{\partial r}\right|_1 \right) N_2^*|_G +$$
$$+ \left(\left.\frac{\partial N_1}{\partial r}\right|_{\overline{r}=\frac{\sqrt{3}}{3},\overline{s}=-\frac{\sqrt{3}}{3}} \cos\widehat{TZ}_1 + N_1\left|_{\overline{r}=\frac{\sqrt{3}}{3},\overline{s}=-\frac{\sqrt{3}}{3}} \frac{\partial\cos\widehat{TZ}}{\partial r}\right|_1 \right) N_3^*|_G +$$
$$\left. + \left(\left.\frac{\partial N_1}{\partial r}\right|_{\overline{r}=\frac{\sqrt{3}}{3},\overline{s}=\frac{\sqrt{3}}{3}} \cos\widehat{TZ}_1 + N_1\left|_{\overline{r}=\frac{\sqrt{3}}{3},\overline{s}=\frac{\sqrt{3}}{3}} \frac{\partial\cos\widehat{TZ}}{\partial r}\right|_1 \right) N_4^*|_G \right\} \frac{2}{l_R} \qquad (5.66)$$

$$B\,(22) = \left(N_1|_{\overline{r}=-\frac{\sqrt{3}}{3},\overline{s}=-\frac{\sqrt{3}}{3}} \cos\widehat{SX}_1 \right) N_1^*|_G + \left(N_1|_{\overline{r}=-\frac{\sqrt{3}}{3},\overline{s}=\frac{\sqrt{3}}{3}} \cos\widehat{SX}_1 \right) N_2^*|_G +$$
$$+ \left(N_1|_{\overline{r}=\frac{\sqrt{3}}{3},\overline{s}=-\frac{\sqrt{3}}{3}} \cos\widehat{SX}_1 \right) N_3^*|_G + \left(N_1|_{\overline{r}=\frac{\sqrt{3}}{3},\overline{s}=\frac{\sqrt{3}}{3}} \cos\widehat{SX}_1 \right) N_4^*|_G \qquad (5.67)$$

$$B\,(23) = \left(N_1|_{\overline{r}=-\frac{\sqrt{3}}{3},\overline{s}=-\frac{\sqrt{3}}{3}} \cos\widehat{SY}_1 \right) N_1^*|_G + \left(N_1|_{\overline{r}=-\frac{\sqrt{3}}{3},\overline{s}=\frac{\sqrt{3}}{3}} \cos\widehat{SY}_1 \right) N_2^*|_G +$$
$$+ \left(N_1|_{\overline{r}=\frac{\sqrt{3}}{3},\overline{s}=-\frac{\sqrt{3}}{3}} \cos\widehat{SY}_1 \right) N_3^*|_G + \left(N_1|_{\overline{r}=\frac{\sqrt{3}}{3},\overline{s}=\frac{\sqrt{3}}{3}} \cos\widehat{SY}_1 \right) N_4^*|_G \qquad (5.68)$$

$$B(24) = \left(N_1|_{\overline{r}=-\frac{\sqrt{3}}{3},\overline{s}=-\frac{\sqrt{3}}{3}} \cos\widehat{SZ}_1\right) N_1^*|_G + \left(N_1|_{\overline{r}=-\frac{\sqrt{3}}{3},\overline{s}=\frac{\sqrt{3}}{3}} \cos\widehat{SZ}_1\right) N_2^*|_G +$$
$$+ \left(N_1|_{\overline{r}=\frac{\sqrt{3}}{3},\overline{s}=-\frac{\sqrt{3}}{3}} \cos\widehat{SZ}_1\right) N_3^*|_G + \left(N_1|_{\overline{r}=\frac{\sqrt{3}}{3},\overline{s}=\frac{\sqrt{3}}{3}} \cos\widehat{SZ}_1\right) N_4^*|_G \quad (5.69)$$

$$B(25) = \left\{ \left(\left.\frac{\partial N_1}{\partial s}\right|_{\overline{r}=-\frac{\sqrt{3}}{3},\overline{s}=-\frac{\sqrt{3}}{3}} \cos\widehat{TX}_1 + N_1 \left|_{\overline{r}=-\frac{\sqrt{3}}{3},\overline{s}=-\frac{\sqrt{3}}{3}} \frac{\partial \cos\widehat{TX}}{\partial s}\right|_1 \right) N_1^*|_G + \right.$$
$$+ \left(\left.\frac{\partial N_1}{\partial s}\right|_{\overline{r}=-\frac{\sqrt{3}}{3},\overline{s}=\frac{\sqrt{3}}{3}} \cos\widehat{TX}_1 + N_1 \left|_{\overline{r}=-\frac{\sqrt{3}}{3},\overline{s}=\frac{\sqrt{3}}{3}} \frac{\partial \cos\widehat{TX}}{\partial s}\right|_1 \right) N_2^*|_G +$$
$$+ \left(\left.\frac{\partial N_1}{\partial s}\right|_{\overline{r}=\frac{\sqrt{3}}{3},\overline{s}=-\frac{\sqrt{3}}{3}} \cos\widehat{TX}_1 + N_1 \left|_{\overline{r}=\frac{\sqrt{3}}{3},\overline{s}=-\frac{\sqrt{3}}{3}} \frac{\partial \cos\widehat{TX}}{\partial s}\right|_1 \right) N_3^*|_G +$$
$$\left. + \left(\left.\frac{\partial N_1}{\partial s}\right|_{\overline{r}=\frac{\sqrt{3}}{3},\overline{s}=\frac{\sqrt{3}}{3}} \cos\widehat{TX}_1 + N_1 \left|_{\overline{r}=\frac{\sqrt{3}}{3},\overline{s}=\frac{\sqrt{3}}{3}} \frac{\partial \cos\widehat{TX}}{\partial s}\right|_1 \right) N_4^*|_G \right\} \frac{2}{l_S} \quad (5.70)$$

$$B(26) = \left\{ \left(\left.\frac{\partial N_1}{\partial s}\right|_{\overline{r}=-\frac{\sqrt{3}}{3},\overline{s}=-\frac{\sqrt{3}}{3}} \cos\widehat{TY}_1 + N_1 \left|_{\overline{r}=-\frac{\sqrt{3}}{3},\overline{s}=-\frac{\sqrt{3}}{3}} \frac{\partial \cos\widehat{TY}}{\partial s}\right|_1 \right) N_1^*|_G + \right.$$
$$+ \left(\left.\frac{\partial N_1}{\partial s}\right|_{\overline{r}=-\frac{\sqrt{3}}{3},\overline{s}=\frac{\sqrt{3}}{3}} \cos\widehat{TY}_1 + N_1 \left|_{\overline{r}=-\frac{\sqrt{3}}{3},\overline{s}=\frac{\sqrt{3}}{3}} \frac{\partial \cos\widehat{TY}}{\partial s}\right|_1 \right) N_2^*|_G +$$
$$+ \left(\left.\frac{\partial N_1}{\partial s}\right|_{\overline{r}=\frac{\sqrt{3}}{3},\overline{s}=-\frac{\sqrt{3}}{3}} \cos\widehat{TY}_1 + N_1 \left|_{\overline{r}=\frac{\sqrt{3}}{3},\overline{s}=-\frac{\sqrt{3}}{3}} \frac{\partial \cos\widehat{TY}}{\partial s}\right|_1 \right) N_3^*|_G +$$
$$\left. + \left(\left.\frac{\partial N_1}{\partial s}\right|_{\overline{r}=\frac{\sqrt{3}}{3},\overline{s}=\frac{\sqrt{3}}{3}} \cos\widehat{TY}_1 + N_1 \left|_{\overline{r}=\frac{\sqrt{3}}{3},\overline{s}=\frac{\sqrt{3}}{3}} \frac{\partial \cos\widehat{TY}}{\partial s}\right|_1 \right) N_4^*|_G \right\} \frac{2}{l_S} \quad (5.71)$$

$$B(27) = \left\{ \left(\left.\frac{\partial N_1}{\partial s}\right|_{\overline{r}=-\frac{\sqrt{3}}{3},\overline{s}=-\frac{\sqrt{3}}{3}} \cos\widehat{TZ}_1 + N_1 \left|_{\overline{r}=-\frac{\sqrt{3}}{3},\overline{s}=-\frac{\sqrt{3}}{3}} \frac{\partial \cos\widehat{TZ}}{\partial s}\right|_1 \right) N_1^*|_G + \right.$$
$$+ \left(\left.\frac{\partial N_1}{\partial s}\right|_{\overline{r}=-\frac{\sqrt{3}}{3},\overline{s}=\frac{\sqrt{3}}{3}} \cos\widehat{TZ}_1 + N_1 \left|_{\overline{r}=-\frac{\sqrt{3}}{3},\overline{s}=\frac{\sqrt{3}}{3}} \frac{\partial \cos\widehat{TZ}}{\partial s}\right|_1 \right) N_2^*|_G +$$
$$+ \left(\left.\frac{\partial N_1}{\partial s}\right|_{\overline{r}=\frac{\sqrt{3}}{3},\overline{s}=-\frac{\sqrt{3}}{3}} \cos\widehat{TZ}_1 + N_1 \left|_{\overline{r}=\frac{\sqrt{3}}{3},\overline{s}=-\frac{\sqrt{3}}{3}} \frac{\partial \cos\widehat{TZ}}{\partial s}\right|_1 \right) N_3^*|_G +$$
$$\left. + \left(\left.\frac{\partial N_1}{\partial s}\right|_{\overline{r}=\frac{\sqrt{3}}{3},\overline{s}=\frac{\sqrt{3}}{3}} \cos\widehat{TZ}_1 + N_1 \left|_{\overline{r}=\frac{\sqrt{3}}{3},\overline{s}=\frac{\sqrt{3}}{3}} \frac{\partial \cos\widehat{TZ}}{\partial s}\right|_1 \right) N_4^*|_G \right\} \frac{2}{l_S} \quad (5.72)$$

$$B(28) = -\left(N_1|_{\overline{r}=-\frac{\sqrt{3}}{3},\overline{s}=-\frac{\sqrt{3}}{3}} \cos\widehat{RX}_1\right) N_1^*|_G - \left(N_1|_{\overline{r}=-\frac{\sqrt{3}}{3},\overline{s}=\frac{\sqrt{3}}{3}} \cos\widehat{RX}_1\right) N_2^*|_G -$$
$$- \left(N_1|_{\overline{r}=\frac{\sqrt{3}}{3},\overline{s}=-\frac{\sqrt{3}}{3}} \cos\widehat{RX}_1\right) N_3^*|_G - \left(N_1|_{\overline{r}=\frac{\sqrt{3}}{3},\overline{s}=\frac{\sqrt{3}}{3}} \cos\widehat{RX}_1\right) N_4^*|_G \quad (5.73)$$

$$B\,(29) = -\left(N_1|_{\overline{r}=-\frac{\sqrt{3}}{3},\overline{s}=-\frac{\sqrt{3}}{3}}\cos\widehat{RY}_1\right)N_1^*|_G - \left(N_1|_{\overline{r}=-\frac{\sqrt{3}}{3},\overline{s}=\frac{\sqrt{3}}{3}}\cos\widehat{RY}_1\right)N_2^*|_G -$$
$$-\left(N_1|_{\overline{r}=\frac{\sqrt{3}}{3},\overline{s}=-\frac{\sqrt{3}}{3}}\cos\widehat{RY}_1\right)N_3^*|_G - \left(N_1|_{\overline{r}=\frac{\sqrt{3}}{3},\overline{s}=\frac{\sqrt{3}}{3}}\cos\widehat{RY}_1\right)N_4^*|_G \quad (5.74)$$

$$B\,(30) = -\left(N_1|_{\overline{r}=-\frac{\sqrt{3}}{3},\overline{s}=-\frac{\sqrt{3}}{3}}\cos\widehat{RZ}_1\right)N_1^*|_G - \left(N_1|_{\overline{r}=-\frac{\sqrt{3}}{3},\overline{s}=\frac{\sqrt{3}}{3}}\cos\widehat{RZ}_1\right)N_2^*|_G -$$
$$-\left(N_1|_{\overline{r}=\frac{\sqrt{3}}{3},\overline{s}=-\frac{\sqrt{3}}{3}}\cos\widehat{RZ}_1\right)N_3^*|_G - \left(N_1|_{\overline{r}=\frac{\sqrt{3}}{3},\overline{s}=\frac{\sqrt{3}}{3}}\cos\widehat{RZ}_1\right)N_4^*|_G \quad (5.75)$$

The tangent stiffness matrix $\mathbf{K}$ can be obtained using the local definition for the strains and constitutive matrices as:

$$\int_V \mathbf{B}^t\mathbf{D}\mathbf{B}dV, \quad (5.76)$$

where $dV = |\mathbf{J}|drdsdt$ and $\mathbf{J}, \mathbf{B}$ and $\mathbf{D}$ are given by Equations (5.21), (5.45) and (5.109), respectively. The numerical solutions, in Section 5.2.3, are all obtained using 3×3 exact integration in (r, s)–direction in Equation (5.76), and 2, 4, 6, 8, 10 or 12 Newton–Cotes points in t direction.

5.2.2 Surface geometry

In Equations (5.46)–(5.75) the *cosinus* terms depend on the then present state of equilibrium via the corresponding nodal cartesian coordinate $(X_i, Y_i, Z_i, i = 1, 2, 3)$. The equations used to describe the middle surface geometry, may be derived from expression (4.30), in terms of a position vector emanating from the origin of the global reference system (X, Y, Z):

$$\mathbf{r} = X\hat{\boldsymbol{\imath}}_1 + Y\hat{\boldsymbol{\imath}}_2 + Z\hat{\boldsymbol{\imath}}_3, \quad (5.77)$$

in which $\hat{\boldsymbol{\imath}}_1$, $\hat{\boldsymbol{\imath}}_2$ and $\hat{\boldsymbol{\imath}}_3$ are unit vectors along the X, Y and Z axes, respectively, and X, Y and Z are given by Equation (5.17). The covariant components of the tangent vector to the middle surface, are given by Equation (4.91):

$$\frac{\partial \mathbf{r}}{\partial R} = \mathbf{r}_{,R}, \quad \frac{\partial \mathbf{r}}{\partial S} = \mathbf{r}_{,S}, \quad (5.78)$$

these are vectors tangent to R and S coordinate lines, respectively. Defining the Lamè parameters A and B using Equation (4.89):

$$A^2 = \mathbf{r}_{,R} \cdot \mathbf{r}_{,R}, \quad B^2 = \mathbf{r}_{,S} \cdot \mathbf{r}_{,S}, \quad (5.79)$$

the unit tangent and normal vectors are given by Equations (4.91) and (4.92), respectively:

$$\mathbf{t}_R = \frac{\mathbf{r}_{,R}}{A} = \begin{bmatrix} \cos\widehat{RX} \\ \cos\widehat{RY} \\ \cos\widehat{RZ} \end{bmatrix}, \qquad \mathbf{t}_S = \frac{\mathbf{r}_{,S}}{B} = \begin{bmatrix} \cos\widehat{SX} \\ \cos\widehat{SY} \\ \cos\widehat{SZ} \end{bmatrix}, \tag{5.80}$$

$$\mathbf{t}_T = \mathbf{t}_R \times \mathbf{t}_S = \frac{\mathbf{r}_{,R} \times \mathbf{r}_{,S}}{A \cdot B} = \begin{bmatrix} \cos\widehat{TX} \\ \cos\widehat{TY} \\ \cos\widehat{TZ} \end{bmatrix}. \tag{5.81}$$

Using Equations (5.78) and (5.79) in combination with the expressions (5.17), we can write the explicit form of the cosinus terms fot the i^{th}–node of our nine node element:

$$\cos\widehat{RX}_i = \frac{E_i}{\sqrt{E_i^2 + F_i^2 + G_i^2}}, \tag{5.82a}$$

$$\cos\widehat{RY}_i = \frac{F_i}{\sqrt{E_i^2 + F_i^2 + G_i^2}}, \tag{5.82b}$$

$$\cos\widehat{RZ}_i = \frac{G_i}{\sqrt{E_i^2 + F_i^2 + G_i^2}}, \tag{5.82c}$$

$$\cos\widehat{SX}_i = \frac{E_i'}{\sqrt{E_i'^2 + F_i'^2 + G_i'^2}}, \tag{5.82d}$$

$$\cos\widehat{SY}_i = \frac{F_i'}{\sqrt{E_i'^2 + F_i'^2 + G_i'^2}}, \tag{5.82e}$$

$$\cos\widehat{SZ}_i = \frac{G_i'}{\sqrt{E_i'^2 + F_i'^2 + G_i'^2}}, \tag{5.82f}$$

$$\cos\widehat{TX}_i = \cos\widehat{RY}_i \cos\widehat{SZ}_i - \cos\widehat{SY}_i \cos\widehat{RZ}_i, \tag{5.82g}$$

$$\cos\widehat{TY}_i = \cos\widehat{RZ}_i \cos\widehat{SX}_i - \cos\widehat{RX}_i \cos\widehat{SZ}_i, \tag{5.82h}$$

$$\cos\widehat{TZ}_i = \cos\widehat{RX}_i \cos\widehat{SY}_i - \cos\widehat{RY}_i \cos\widehat{SX}_i, \tag{5.82i}$$

where:

$$E_i = \sum_{i=1}^{9} \frac{\partial N_i}{\partial r}\bigg|_i X_i, \quad F_i = \sum_{i=1}^{9} \frac{\partial N_i}{\partial r}\bigg|_i Y_i, \quad G_i = \sum_{i=1}^{9} \frac{\partial N_i}{\partial r}\bigg|_i Z_i, \tag{5.83}$$

$$E_i' = \sum_{i=1}^{9} \frac{\partial N_i}{\partial s}\bigg|_i X_i, \quad F_i' = \sum_{i=1}^{9} \frac{\partial N_i}{\partial s}\bigg|_i Y_i, \quad G_i' = \sum_{i=1}^{9} \frac{\partial N_i}{\partial s}\bigg|_i Z_i. \tag{5.84}$$

5.2.3 Some numerical examples

The shells studied to verify the method proposed in the previous sections, are:

- a cylinder with point load;
- a vault;
- a hemisphere;

the few of which we have an analytical solution in literature (Timoshenko 1940) and (Bernadou 1996).

5.2.3.1 The cylinder

The cylinder we have analyzed is a tube with radius $R = 300$, lenght $L = 600$ and is subject to two radial loads $P = 1$ which are opposite diametrically (Figure 5.2(a)). The ends of the cylinder are constrained by a diaphragm so that $U = V = 0$. More, we have set $D = Es^3/12(1-\nu^2)$ with $E = 3 \cdot 10^6$ and $\nu = 0.3$. We have to remember that those adimensional parameters which have to be included into the model, are: $R/s \equiv L/h = 100$ or $s/R \equiv h/L = 0.01$. In order to simplify the mesh creation and to reduce the size of dates, we have used the cylinder symmetry by studying only an octave of it. The Table 5.1 shows the good convergence in terms of displacements as well as stresses with BGMI in comparison to the selective and reduced integration. Furthermore Figure 5.3 shows the displacement field and the stress–through–thickness behaviour under the pinched load.

Table 5.1: Comparison of values by changing the finite element model.

Nodes per element	Number of elements	Integration type	W	n_x	n_y
9	3×3	3×3	0.0016836	123.34	90.173
		3×2	0.15541	391.84	417.27
		2×2	0.20923	289.64	351.07
		BGMI	0.18130	363.53	450.83
		Exact value	0.1825	620	520

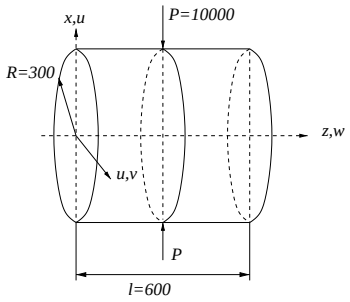

(a)

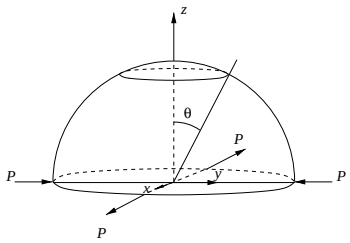

(b)

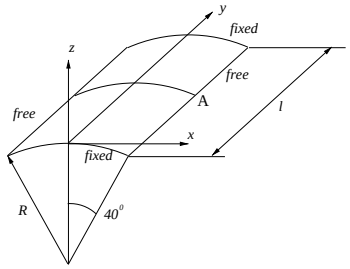

(c)

Figure 5.2: Some numerical examples.

5.2.3.2 The vault

Another application of the code has been made on a vault having a lenght $L = 50$ and thickness $s = 0.25$, subject to a unitary dead load. (Figure 5.2(c)). We have set $E = 4.32 \cdot 10^8$ and $\nu = 0.0$; in this case the parameters which have to be included into the BGMI are: $s/R \equiv h/L = 0.001$ or $R/s \equiv L/h = 100$. In the cylinder, studied in the previous section, the shear locking prevails, on the contrary, the vault is a kind problem where the shear deformation energy is much lower with respect to the membrane one, and so it is dominated by the membrane locking. In Table 5.2 we show the convergence of the displacement patter also with very few elements in the mesh.

Table 5.2: Displacement pattern for the vault problem.

Nodes per element	Number of elements	Integration type	W	CPU seconds
9	3×3	3×3	0.00049992	5.11
		3×2	0.00052161	5.17
		2×2	0.00087434	4.79
		BGMI	0.00084472	5.66
		Exact value	0.00084	

5.2.3.3 The hemisphere

The last analyzed structure is an hemisphere simmetrically loaded with a radius $R = 10$ and thickness $s = 0.04$. We have set $E = 6.825 \cdot 10^7$ and $\nu = 0.3$ and $R/s \equiv L/h = 250$. When the surface is not perforated ($\theta = 0$) in literature we can find that the theoretical value of the displacement of the loaded nodes is 92.24. This kind of problem is dominated by the membrane locking, as well as shear loacking. In this case the surface has a double curvature. The 9 nodes element becomes singular by using the reduced integration, while with the selective one it is stiff and converges slowly; with BGMI we obtain exactly the theoretical value.

An efficient nine node element devoid of shear and membrane locking, even in the extreme limit, has been proposed. The results of the test problems solved show

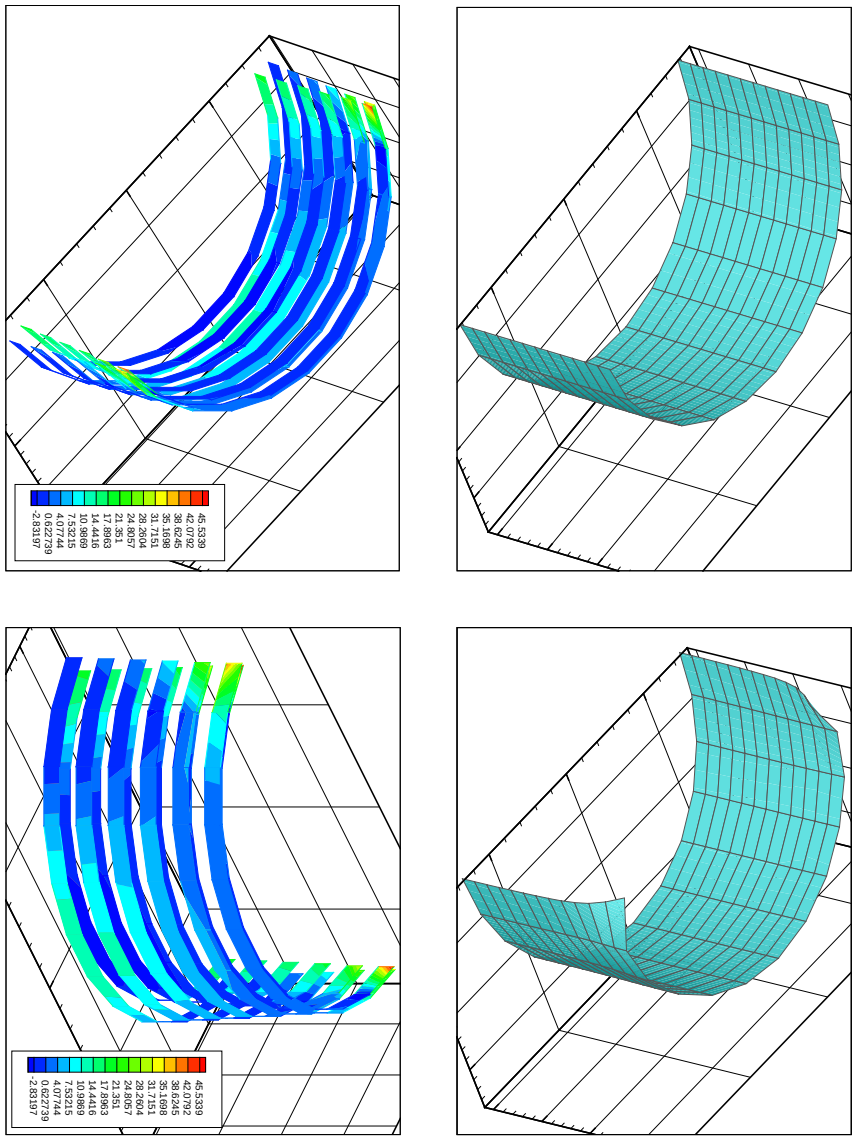

Figure 5.3: Analysis of the pinched cylinder.

that the proposed element not only has a good convergence at the thin limit but also yield accurate predictions even with coarse mesh.

5.2.4 Geometric nonlinear formulations (small strains)

The main topic of this section is to formulate an incremental analysis: being known the configuration at time (load level) t we search for the configuration at time (load level) $t+\Delta t$ (Onate and Oliver 1986). For this purpose we make use of the Update Lagrangian Formulation (UL), but, at first we prefer to introduce the basics of the Total Lagrangian Formulation (TL).

5.2.4.1 Total Lagrangian Formulation

For the equilibrium configuration at time $t+\Delta t$, the Principle of Virtual Work (Bathe 1996), states:

$$\int_{^0V} {}^{t+\Delta t}_{\ 0}\mathbf{S} : \delta \left({}^{t+\Delta t}_{\ 0}\varepsilon \right) {}^0dV = {}^{t+\Delta t}\mathfrak{R}. \tag{5.85}$$

In the above we have use Bathe's notation (Bathe 1996, pag.523) and:

- ${}^t_0\mathbf{S}$ is the 2$^{\text{nd}}$ *Piola–Kirchhoff stress tensor*, corresponding to the t–configuration and referred to the configuration at time $t = 0$ (undeformed) (Marsden and Hughes 1983). It should be remembered that ${}^t_0\mathbf{S}$ is the *pull–back of the Kirchhoff stress tensor* ${}^t\boldsymbol{\tau}$ from the t–configuration to the configuration at $t = 0$ (Bonet and Wood 1997, pag.63).

Defining a coordinate system in the t–configuration (spatial configuration), with coordinates $({}^tx^i; i = 1, 2, 3)$, we can write:

$${}^t\boldsymbol{\tau} = {}^t\tau^{ij}\ {}^t\mathbf{g}_i\, {}^t\mathbf{g}_j, \tag{5.86}$$

where:

$${}^t\tau^{ij} = \frac{{}^0\rho}{{}^t\rho}\, {}^t\sigma^{ij} \tag{5.87}$$

and $\mathbf{g}_i$ are the covariant base vectors obtained from Equation (4.35).

- ${}^0\rho$ and ${}^t\rho$: densities in the $t = 0$ and t–configuration respectively.
- ${}^t\sigma^{ij}$: contravariant components of the *Cauchy stress tensor* in the spatial configuration.

The coordinate system (X, Y, Z), previously introduced (pag. 196), in the $t = 0$ configuration (reference configuration), can be renamed in indicial notation $(X^I; I = 1, 2, 3)$, in order to write:

$$ {}^t_0\mathbf{S} = {}^t_0S^{IJ}\ \mathbf{G}_I\mathbf{G}_J, \tag{5.88} $$

where $\mathbf{G}_I$ are the covariant base vectors referred to the reference configuration. Using the standard notation of manifold analysis (Berger and Gostiaux 1988):

$$ {}^t_0S^{IJ} = \left({}^t_0F^{-1}\right)^I_i\ {}^t\tau^{ij}\ \left({}^t_0F^{-1}\right)^J_j, \tag{5.89} $$

where:

$$ {}^t_0F^i_I = \frac{\partial^t x^i}{\partial X^I}, \tag{5.90} $$

is the mixed components of the *deformation gradient tensor* (Malvern 1969).

- ${}^t_0\boldsymbol{\varepsilon}$: *Green–Lagrange strain tensor*, corresponding to the t–configuration and referred to the configuration at time $t = 0$ (Bathe 1996). Defining in the spatial configuration the *Almansi strain tensor* ${}^t\mathbf{e}$ (Malvern 1969) we can write:

$$ {}^t_0\varepsilon_{IJ} = \left({}^t_0F\right)^i_I\ {}^te_{ij}\ \left({}^t_0F\right)^j_J. \tag{5.91} $$

- ${}^t\mathfrak{R}$: virtual work of the external loads acting in the t–configuration.

We will now develop the incremental equations working in the *element natural coordinate system* (r, s, t) (the convective system introduced at pag. 196), where we introduce the following notations:

- ${}^t\tilde{\mathbf{g}}_i$: covariant base vectors in the spatial configuration (natural system);
- $\tilde{\mathbf{G}}_i$: covariant base vectors in the reference configuration (natural system).

In the spatial configuration:

$$ {}^t\boldsymbol{\sigma} = {}^t\tilde{\sigma}^{ij}\ {}^t\tilde{\mathbf{g}}_i\,{}^t\tilde{\mathbf{g}}_j, \tag{5.92} $$

$$ {}^t\boldsymbol{\tau} = {}^t\tilde{\tau}^{ij}\ {}^t\tilde{\mathbf{g}}_i\,{}^t\tilde{\mathbf{g}}_j, \tag{5.93} $$

$$ {}^t\mathbf{e} = {}^t\tilde{e}^{ij}\ {}^t\tilde{\mathbf{g}}_i\,{}^t\tilde{\mathbf{g}}_j, \tag{5.94} $$

and in the reference configuration:

$$ {}^t_0\mathbf{S} = {}^t_0\tilde{S}^{IJ}\ {}^t\tilde{\mathbf{G}}_I\,{}^t\tilde{\mathbf{G}}_J, \tag{5.95} $$

$$ {}^t_0\boldsymbol{\varepsilon} = {}^t_0\tilde{\varepsilon}_{IJ}\ {}^t\tilde{\mathbf{G}}^I\ {}^t\tilde{\mathbf{G}}^J. \tag{5.96} $$

It is worth pointing out that (Fung 1965):

$$ {}^{t}_{0}\tilde{S}^{IJ} = {}^{t}_{0}\tilde{\tau}^{ij}, \tag{5.97} $$

$$ {}^{t}_{0}\tilde{\varepsilon}_{IJ} = {}^{t}_{0}\tilde{e}^{ij}, \tag{5.98} $$

for $I = i$ and $J = j$.
For the incremental step from the t–configuration to the $(t + \Delta t)$–configuration:

$$ {}^{t+\Delta t}_{0}\tilde{S}^{IJ} = {}^{t}_{0}\tilde{S}^{IJ} + \underbrace{{}_{0}\tilde{S}^{IJ}}_{\text{increment}}, \tag{5.99} $$

$$ {}^{t+\Delta t}_{0}\tilde{\varepsilon}_{IJ} = {}^{t}_{0}\tilde{\varepsilon}_{IJ} + \underbrace{{}_{0}\tilde{\varepsilon}_{IJ}}_{\text{increment}}, \tag{5.100} $$

$$ {}_{0}\tilde{\varepsilon}_{IJ} = \underbrace{{}_{0}\tilde{e}_{IJ}}_{\text{linear terms}} + \underbrace{{}_{0}\tilde{\eta}_{IJ}}_{\text{nonlinear terms}} \tag{5.101} $$

For linearizing the step, we use:

$$ {}_{0}\tilde{S}^{IJ} = {}_{0}\tilde{C}^{IJKL}\,{}_{0}\tilde{e}_{KL}, \tag{5.102} $$

$$ \delta_0\tilde{\varepsilon}_{IJ} = \delta_0\tilde{e}_{IJ}. \tag{5.103} $$

In Equation (5.102) ${}_{0}\tilde{\mathbf{C}}$ is the tangent constitutive tensor in the reference configuration.
Hence, the *linearized incremental equations* are:

$$ \int_{{}_0V} {}_{0}\tilde{C}^{IJKL}\,{}_{0}\tilde{e}_{KL}\delta\left({}_{0}\tilde{e}_{IJ}\right){}^{0}dV + \int_{{}_0V} {}^{t}_{0}\tilde{S}^{IJ}\delta\left({}_{0}\tilde{\eta}_{IJ}\right){}^{0}dV = $$

$$ = {}^{t+\Delta t}\mathfrak{R} - \int_{{}_0V} {}^{t}_{0}\tilde{S}^{IJ}\delta\left({}_{0}\tilde{e}_{IJ}\right){}^{0}dV. \tag{5.104} $$

As it is well known, the $(t + \Delta t)$–configuration is determined using the above equation in an iterative scheme. For our element we interpolate the incremental displacement and rotations using Equations (5.13)–(5.15); the in–layer incremental strains are derived from the displacement interpolations using Equation (5.44). In this way, from expression (5.104), an equation of the form:

$$ \left({}^{t}_{0}\mathbf{K}_{\mathrm{L}} + {}^{t}_{0}\mathbf{K}_{\mathrm{NL}}\right)\mathbf{U} = {}^{t+\Delta t}\mathbf{R} - {}^{t}_{0}\mathbf{F}, \tag{5.105} $$

is obtained for the linearized incremental step. In Equation (5.105) we have:

- ${}^{t}_{0}\mathbf{K}_{\mathrm{L}}$: linear stiffness matrix;
- ${}^{t}_{0}\mathbf{K}_{\mathrm{NL}}$: nonlinear stiffness matrix;

- $\mathbf{U}$: vector of generalized incremental displacements;
- ${}^{t+\Delta t}\mathbf{R}$: vector of nodal forces equivalent (in the sense of the Principle of Virtual Work) to the external loads acting at $(t + \Delta t)$;
- ${}^{t}_{0}\mathbf{F}$: vector of nodal forces equivalent to the stresses acting at time t.

The solution of Equation (5.105) provides a linearized approximation to the step from t to $(t + \Delta t)$. An iterative scheme (Bathe and Cimento 1980) is used until the following equation:

$$ {}^{t+\Delta t}\mathbf{R} - {}^{t+\Delta t}_{0}\mathbf{F} = \mathbf{0}, \tag{5.106} $$

is satisfied within certain computational tolerances.

5.2.4.2 Update Lagrangian Formulation

In the Update Lagrangian description all static and kinematic variables are referred to the configuration at time t. This implies that the reference configuration is conveniently updated after each displacement increment solution has been found. However, the basic steps for deriving the finite element formulation do not differ much from those followed for the Total Lagrangian description. Moreover, all the relevant finite element matrices can be easily deduced from those obtained in previous sections simply taking into account the following:

1. all derivatives appearing in the expressions of the strain matrices (5.45) are now with respect to the coordinates at time t;
2. the Jacobian matrix (5.21) contains the derivatives of the coordinates of the configuration at time t with respect to the natural coordinates;
3. the initial displacement effect is automatically taken into account by updating the reference configuration;
4. the volume and surface of the shell correspond to the actual values in the configuration t;
5. the 2^{nd} Piola–Kirchhoff stresses $\mathbf{S}$ are referred to the configuration at time t and, thus, become identical to the Cauchy (true) stress $\boldsymbol{\sigma}$. The Cauchy stresses are updated after each new displacement increment has been found, and then they are appropriately transformed to the *next reference configuration*;
6. a final point should be said about the constitutive equation to be used. It can be shown that both the Updated and Total Lagrangian formulation give the

same results if the coefficients of the constitutive matrix in both formulation are related by the expressions:

$$ {}_tC^{ijkl} = \frac{\partial x^i}{\partial X^I}\frac{\partial x^j}{\partial X^J}\frac{\partial x^k}{\partial X^K}\frac{\partial x^l}{\partial X^L}\,{}_0C^{IJKL}, \tag{5.107} $$

where, as usual, indexes 0 and t refer to the initial configuration and the configuration at time t, respectively. Moreover, it can be proved (Bathe 1996) that for small strain conditions in a UL formulation, Equation (5.107) gives approximately:

$$ {}_tC^{ijkl} \approx {}_0\tilde{C}^{IJKL} = \text{Equation (4.172)}. \tag{5.108} $$

In our formulation, the stress–strain relation can be written, using Equations (4.172) and (5.108), in the following way:

$$ \begin{bmatrix} \sigma^{RR} \\ \sigma^{SS} \\ \sigma^{RS} \\ \sigma^{RT} \\ \sigma^{ST} \end{bmatrix} = \frac{E\csc^4\alpha}{(1-\nu^2)} \begin{bmatrix} 1 & \cos^2\alpha+\nu\sin^2\alpha & -\cos\alpha & 0 & 0 \\ \cos^2\alpha+\nu\sin^2\alpha & 1 & -\cos\alpha & 0 & 0 \\ -\cos\alpha & -\cos\alpha & \dfrac{1+\cos^2\alpha-\nu\sin^2\alpha}{2} & 0 & 0 \\ 0 & 0 & 0 & G & 0 \\ 0 & 0 & 0 & 0 & G \end{bmatrix} \begin{bmatrix} \varepsilon_{RR} \\ \varepsilon_{SS} \\ \gamma_{RS} \\ \gamma_{RT} \\ \gamma_{ST} \end{bmatrix}. \tag{5.109} $$

5.3 A monodimensional application of BGMI

5.3.1 A survey of arch finite elements

The development of finite elements for curved structural members has received a lot of attention in recent years (Petrov and Géradin 1998). The main interest of the arch element is that it would be able to form a simple case of a more general curved shell.

Classical curved low order displacement–based isoparametric finite elements, when used to model thin and deep–shallow shear–flexible arches, show a critical behaviour of two kinds (Stolarski and Belytschko 1983): firstly, there is excessively stiff behaviour (called shear–locking) due to overestimating the shear strain energy over its bending counterpart; secondly, inextensional or nearly inextensional deformations are poorly represented, thus resulting in an inability of an element to bend without stretching (membrane–locking).

In recent years a wide range of researches have been proposed for the development of suitable and efficient finite element models for the analysis of thin curved structures. Among them the following are worth mentioning: selective–reduced integration (Zienkiewicz, Taylor, and Too 1971; Pawsey and Clough 1971; Fried 1973; Hughes, Taylor, and Kanoknukulchai 1977; Pugh, Hinton, and Zienkiewicz

1978; Noor and Peters 1981; Pandian, AppaRao, and Chandra 1989), which is widely used for eliminating higher–order components in strain distributions. Unfortunately, these methods may lead to undesirable "mechanism" with zero–energy modes, due to a low rank stiffness matrix. Furthermore, they may be accompanied by a deterioration of membrane–bending coupling (Stolarski and Belytschko 1983), which is one of the essential features of a curved element; it is also of interest to underline that the convergence is not achieved "from below" and is not monotonic because reduced integration does not always ensure variational correctness. In the Discrete Kirchhoff's theory (Wemper, Oden, and Kross 1968; Batoz, Bathe, and Ho 1980; Batoz 1982), to obtain the behaviour of thin finite element, constraints of zero transverse shear strains are imposed at a discrete number of points.
The earliest attempts to idealize curved thin structures, free of membrane locking, attributed at first to an unsatisfactory description by lower–order isoparametric elements of the unstressed rigid–body modes in a strain–free problem, led Dawe (Dawe 1974a; Dawe 1974b) and Ashwell (Ashwell and Gallagher 1976) to overcome the problem by using high–order independent polynomial representation (quintic–quintic) or by incorporating trigonometric displacement fields. Meck in 1980 showed that failures, which have been observed when using classical polynomial functions for curved elements, were not due to the neglect of rigid–body motions, but due to the lack of coupling between normal and tangential displacements in which the order of interpolation for the deflection is one order lower than that for the tangential displacement. The C^1 element proposed by Ashwell, Sabir, and Roberts in 1971, with constant strain and linear bending, is a good alternative to the use of higher order polynomial representation.
In the field consistency approach (Prathap and Bhashyam 1982; Prathap and Viswanath 1983; Prathap 1985b; Prathap 1985a; Babu and Prathap 1986; Prathap and Babu 1986; Prathap and Naganarayana 1990; Prathap and Shashirekha 1993), that ensures a variationally correct and orthogonally consistent strain field by a reconstitution technique, all "spurious" shear constraints are identified and then rejected using a field consistent redistribution strategy applied to shape functions. More recently Lee, Koo, and Choi (1996) proposed a modified Babu and Prathap's element (Babu and Prathap 1986) using the separation of transverse displacement into bending and shear deflection, developing a particular shear strain constant and linear curvature element consistent in membrane field. Relaxation of penalty constraints (membrane and shear) at the element level, proposed by Tessler and Hughes in 1983 and slightly modified by Tessler and Spiridigliozzi in 1986, yielded constant strain two–node element using a particular anisoparametric formulation with a non–uniform order of kinematic interpolation scheme.
Recently, Shi and Voyiadjis, using a quasi–conforming element technique (Atluri 1983), presented a shear–flexible two–node arch/beam finite element with linear bending assumed strain, derived not so easily by the weak form of strain–

displacement relations; good and accurate results are obtained by Lee and Sin using to start with, a three–node element based on curvature and then reduced, by a transformation matrix between nodal curvature and nodal displacements, into a two–node configuration.
More recently, the material finite element, proposed by Raveendranath, Singh, and Pradhan (1999), starting from cubic radial displacement and then using the element equilibrium equations, derives a coupled displacement field (with quartic tangetial displacement and section rotation) in which the shape functions contain coefficients involving material properties of the element (Raveendranath, Singh, and Rao 2001).
In another way, a considerably large number of hybrid elements (Spilker and Munir 1980), with consistent transverse shear stress distributions, and variational mixed methods based on Hellinger–Reissner or Hu–Washizu principles have been published to study locking phenomena and some of them have been considered effective devices to overcome such difficulty (Noor and Peters 1981; Bathe and Dvorkin 1985; Reddy and Volpi 1992; Bathe 1996). Even if, in view of the equivalence between reduced–selective integration techniques and mixed finite element (Malkus and Hughes 1978), in some cases of beams and flat plates, some mixed models exhibit membrane and shear locking.
It is curious to emphasize that, in some cases, an idealization of curved members with straight line beam elements achieves acceptable accuracy with many fewer elements (Kikuchi 1982; Yamamoto and Ohtsubo 1982; Kikuchi and Tanizawa 1984) in comparison with the above–mentioned elements.
More recently steps have been developed in the direction of meshless methods to solve classical locking problems with finite element methods (Liu and Donning 1998) in the field of shear–deformable curved beams and plates.
All the above approaches have been successfully applied to reduce locking with different type of "tricks", achieving in some cases, good levels of accuracy, in spite of more complex mathematical formulations and computational effort, leading to a hard introduction in a general purpose finite element programmes and an unlikely extension to non–linear formulations. Aim of this section is the development of simple three–node (9 degrees of freedom) and five–node (15 degrees of freedom) curved shear–flexible beam elements, which should be able to satisfy the following requirements:

1. the element should be able to avoid membrane and shear locking and violent stress oscillations in the thin limit;

2. the element should be applicable to any arch's shape (shallow–deep);

3. accurate geometry modelling;

4. the element should not contain any zero energy modes or mechanisms;

5. the theory should not be formulated using correction numerical factors;

6. the element should possess a fast and monotonic convergence;

7. numerical efficiency.

The main features of this element lies in the Based–Gauss–Mixed–Interpolation (BGMI) (Gobetti and Nascimbene 2001) of the normal/tangential generalized displacements and of the transverse shear/membrane strains. The functions shaping the displacement field are the classical one, on the contrary, because of the presence in the model of shear, the component of the transverse shear strain is shaped by means of suitable functions defined over Gauss integration points. Furthermore we have incorporated the possibility of a layered arch and generic form of transverse section to take into account composite material and initial self–stresses. The formulation is applied to a great number of problems to verify the concept employed and its capabilities of the analysis.

5.3.2 The arch finite element with BGMI

5.3.2.1 Basic equations

Herein, we follow exactly the same strategy presented in Section 5.2 concerning the shell element.
Let $\widehat{ab}$ represent an infinitely small element cut from a curved structural beam element by one pair of planes normal to the middle axis of the arch. Taking the curvilinear coordinates axes R tangent at middle line and S normal, as shown in Figure 5.4, we denote by r_S the radius of curvature in the (R, S) plane. The thickness of the arch, which is assumed constant, is denoted by h. As a consequence of deformation the element dR will take a new configuration $\widetilde{dR}$ due to:

- membrane strain ε_R;

- shear strain γ;

- change of the angle θ_R between tangent directions before and after deformation.

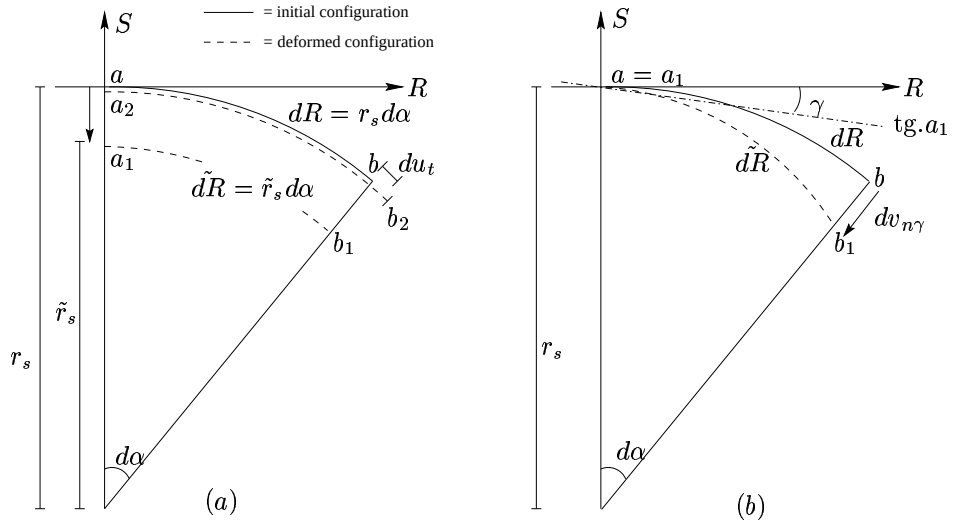

Figure 5.4: Membrane strain (a); shear strain (b).

These three strain measures may be expressed in terms of the tangential and normal displacements u_t and v_n respectively, and their derivatives:

$$\varepsilon_R = \frac{\widetilde{dR} - dR}{dR} = \frac{du_t}{dR} + \frac{v_n}{r_S} \qquad \Leftarrow \text{Fig.5.4}(a), \tag{5.110}$$

$$\gamma = \frac{dv_{n\gamma}}{dR} \qquad \Leftarrow \text{Fig.5.4}(b), \tag{5.111}$$

$$\theta_R = -\frac{u_t}{r_S} + \frac{dv_{n\theta_R}}{dR} \qquad \Leftarrow \text{Fig.5.5}(a), \tag{5.112}$$

$$\chi = \frac{d\theta_R}{dR} \qquad \Leftarrow \text{Fig.5.5}(b), \tag{5.113}$$

and, according to the fact that $dv_n = dv_{n\gamma} + dv_{n\theta_R}$ we obtain, substituting this relation into Equations (5.111) and (5.112), a new espression for shear strain that reads:

$$\gamma = \frac{dv_n}{dR} - \frac{u_t}{r_S} - \theta_R. \tag{5.114}$$

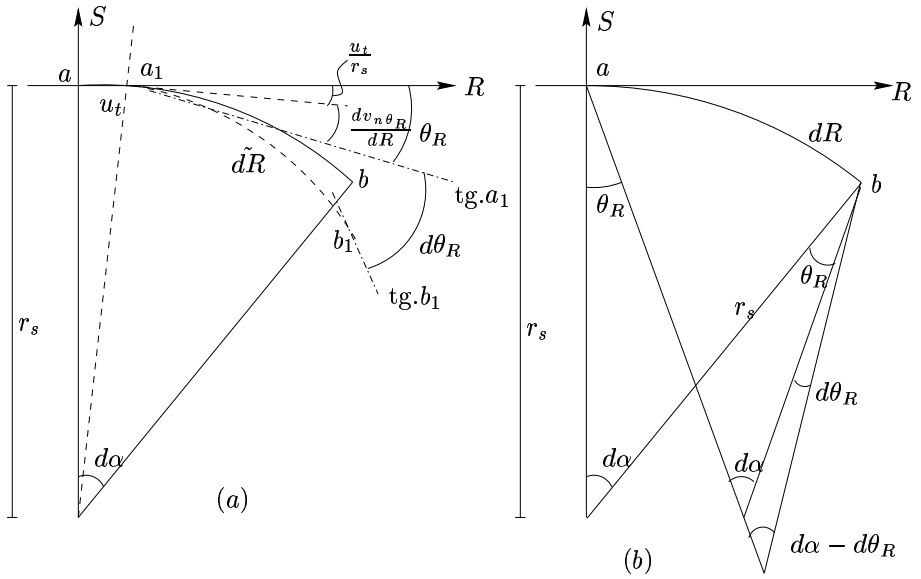

Figure 5.5: Section rotation (a); curvature (b).

With reference to Figure 5.7, the unit membrane elongation of a thin lamina at a distance S from the middle surface is:

$$\varepsilon = \frac{r_S}{r_S + S}\left(\varepsilon_R - S\chi\right) = \left[\frac{1}{1 + \frac{S}{r_S}}\right]\left(\varepsilon_R - S\chi\right). \tag{5.115}$$

In our formulation the thickness h of the arch will always be assumed small in comparison to radii of curvature: in such a case the quantity S/r_S can be neglected in comparison with unity and we are able to rewrite Equation (5.115):

$$\varepsilon = \varepsilon_R - S\chi. \tag{5.116}$$

Furthermore, taking into account the last hypothesis ($r_S \gg 1$) applied to the shear strain (5.114) and substituting relations (5.110) and (5.113) in Equation (5.116), the membrane–bending strain ε_{RR} and shear strain γ_{RS} of the arch element of length l are given by the strain–displacement relations:

$$\varepsilon_{RR} = \frac{\partial u_t}{\partial R} - S\frac{\partial \theta_R}{\partial R}, \tag{5.117}$$

$$\gamma_{RS} = \frac{\partial v_n}{\partial R} - \theta_R, \tag{5.118}$$

or in matrix form:

$$\begin{bmatrix} \varepsilon_{RR} \\ \gamma_{RS} \end{bmatrix} = \begin{bmatrix} \dfrac{\partial}{\partial R} & 0 & -S\dfrac{\partial}{\partial R} \\ 0 & \dfrac{\partial}{\partial R} & -1 \end{bmatrix} \begin{bmatrix} u_t \\ v_n \\ \theta_R \end{bmatrix}, \tag{5.119}$$

where u_t and v_n denote respectively the tangential and normal displacements, and θ_R the section rotation of the centroid of the section. We have defined Equation (5.117) as *membrane–bending* strain because it contains a coupling of flexural and axial deformation in this model of a curved beam. The main assumption underlying the present formulation states that the cross section of the curved beam will remain plane during each loading step. In the elastic–isotropic range, a formulation has been herein developed, which takes into account a cross section conceived as a set of strips in order to permit the analysis of generic cross–sections (see Figure 5.7). Every strip is identified by two different sets of nodal points along its border lines as we have depicted in Figure 5.7. These nodes define an intrinsic curvilinear coordinate system (R, S) having the origin at the centroid of the strip, the principal ones lying on the baricentral line of the strip along the element length l of the beam and supporting the curvilinear intrinsic axis R. A secondary group of nodes establishes the shape of the cross sections of the arch and hence a S straight axis normal to the previous ones by the right hand rule through the thickness h of the strip. For computational reasons we introduce a natural coordinate system (r, s) with variables normalized in the range of variation $(-1, 1)$, such that:

$$r = \frac{2}{l}R, \qquad \text{and} \qquad s = \frac{2}{h}S. \tag{5.120}$$

The indipendent variables u_t, v_n and θ_R can be expressed with reference to the generalized displacements u, v and θ of the arch nodes (centroids of an assigned number of cross sections along the element axis) within the (x, y) global coordinates system:

$$u_t = u\cos\widehat{Rx} + v\cos\widehat{Ry}, \tag{5.121}$$

$$v_n = -u\cos\widehat{Ry} + v\cos\widehat{Rx}, \tag{5.122}$$

$$\theta_R = \theta, \tag{5.123}$$

or in matrix form:

$$\begin{bmatrix} u_t \\ v_n \\ \theta_R \end{bmatrix} = \begin{bmatrix} \cos\widehat{Rx} & \cos\widehat{Ry} & 0 \\ -\cos\widehat{Ry} & \cos\widehat{Rx} & 0 \\ 0 & 0 & 1 \end{bmatrix} \begin{bmatrix} u \\ v \\ \theta \end{bmatrix}. \tag{5.124}$$

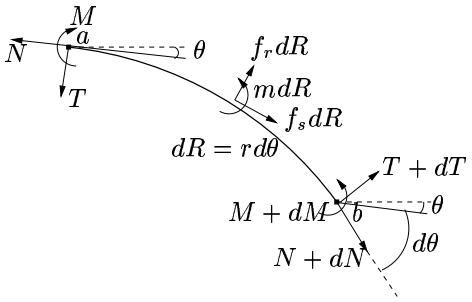

Figure 5.6: Static variable in a curved beam.

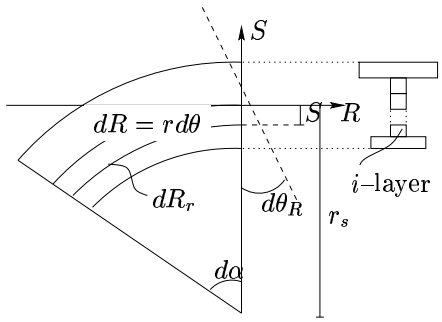

Figure 5.7: Section geometry.

Finally, substituting Equation (5.124) in Equation (5.119) we obtain:

$$\varepsilon_{RR} = -S\frac{\partial\theta}{\partial R} + \left[\frac{\partial u}{\partial R}\cos\widehat{Rx} + u\frac{\partial\cos\widehat{Rx}}{\partial R} + \frac{\partial v}{\partial R}\cos\widehat{Ry} + v\frac{\partial\cos\widehat{Ry}}{\partial R}\right], \quad (5.125)$$

$$\gamma_{RS} = \left[-\theta - \frac{\partial u}{\partial R}\cos\widehat{Ry} - u\frac{\partial\cos\widehat{Ry}}{\partial R} + \frac{\partial v}{\partial R}\cos\widehat{Rx} + v\frac{\partial\cos\widehat{Rx}}{\partial R}\right]. \quad (5.126)$$

In Equations (5.124), (5.125) and (5.126) the terms $\cos\widehat{Rx}$ and $\cos\widehat{Ry}$ are needed to permit the orthogonal transformation between the (R, S) and (x, y) coordinate system.

5.3.2.2 Principle of virtual work

Figure 5.6 depicts an infinitely small portion of the centerline arch element $\widehat{ab} = dR$ loaded by a transversal f_R, tangential f_S loads per unit length and a moment m. Stress resultants are the axial forces N, transverse shear T and bending moments M at sections a and b of the arch. We adopt sign conventions so that the six resultants as shown in Figure 5.6 are positive. The equilibrium equations of forces and moments are written as follows:

$$N + dN - N\cos d\theta + T\sin d\theta + f_S dR = 0, \quad (5.127)$$

$$T + dT - N\sin d\theta - T\cos d\theta + f_R dR = 0, \quad (5.128)$$

$$M + dM - M + T dR\cos d\theta + m dR = 0. \quad (5.129)$$

Now using the following hyphotesis:

$$\cos d\theta \cong 1, \qquad \sin d\theta \cong d\theta, \qquad dR = r_S d\theta, \quad (5.130)$$

we obtain:

$$\frac{dN}{dR} + \frac{T}{r_S} + f_S = 0, \tag{5.131}$$

$$\frac{dT}{dR} - \frac{N}{r_S} + f_R = 0, \tag{5.132}$$

$$\frac{dM}{dR} + T + m = 0. \tag{5.133}$$

Consider infinitesimal virtual displacements from the equilibrium configuration, with components $\delta u_t, \delta v_n$ and $\delta\theta_R$ function of the R variable. Thus, the virtual strains and rotations associated with the infinitesimal virtual displacement distribution, reads:

$$\delta\varepsilon_R = \frac{d\delta u_t}{dR} + \frac{\delta v_n}{r_S}, \tag{5.134}$$

$$\delta\gamma = \frac{d\delta v_n}{dR} - \frac{\delta u_t}{r_S} - \delta\theta_R, \tag{5.135}$$

$$\delta\chi = \frac{d\delta\theta_R}{dR}. \tag{5.136}$$

For the equilibrium configuration the virtual work due to external loads and generalized internal nodal loads, may be written as:

$$\delta W^{ext} = \int_R (f_S\delta u_t + f_R\delta v_n + m\delta\theta_R)dR + |N\delta u_t + T\delta v_n + M\delta\theta_R|_0^R, \tag{5.137}$$

The second term in Equation (5.137) can be rewritten:

$$\int_0^R \left[\frac{d(N\delta u_t)}{dR} + \frac{d(T\delta v_n)}{dR} + \frac{d(M\delta\theta_R)}{dR}\right] dR = \int_0^R \left[\frac{dN}{dR}\delta u_t + N\delta\frac{(du_t)}{dR} + \frac{dT}{dR}\delta v_n + T\delta\frac{(dv_n)}{dR} + \frac{dM}{dR}\delta\theta_R + M\delta\frac{(d\theta_R)}{dR}\right] dR. \tag{5.138}$$

Now we use Equation (5.138) into (5.137) and obtain:

$$\delta W^{ext} = \int_R \left[\left(\frac{dN}{dR} + f_S\right)\delta u_t + \left(\frac{dT}{dR} + f_R\right)\delta v_n + \left(\frac{dM}{dR} + m\right)\delta\theta_R + N\frac{d\delta u_t}{dR} + T\frac{d\delta v_n}{dR} + M\frac{d\delta\theta_R}{dR}\right] dR, \tag{5.139}$$

and using equilibrium relations (5.131)–(5.133) with regard of (5.134)–(5.136):

$$\delta W^{ext} = \int_R (\overset{\text{membrane}}{\overset{\uparrow}{N\delta\varepsilon_R}} + \underset{\text{shear}}{\underset{\downarrow}{T\delta\gamma}} + \overset{\text{bending}}{\overset{\uparrow}{M\delta\chi}})dR, \tag{5.140}$$

and the kinematic variables conjugate to N, T and M are ε_R, γ and χ. The coefficients in the variational form of the virtual work (5.140) are usually connected by the following inequalities:

$$E > Gk >> Eh^2, \tag{5.141}$$

which state that these parameters act, when a curved beam becomes thin ($h/R \to 0$), as penalty constraints on the membrane and shear energy terms. Most of the strain energy in a thick beam goes into shear deformation, whereas in a thin beam, most energy goes into bending strain. Shear locking appears in a formulation which is not able to represent a state of zero shear in the thin limit independent of the mesh size. In a thin limit the coefficient for the shear is h and the coefficient of the bending term is of order h^3, so the first one becomes much larger than the latter as $h \to 0$. In a curved structure membrane action comes from the coupling of bending and membrane deformation. Membrane locking appears when this coupling is inconsistent (Stolarski and Belytschko 1982) and the interpolation functions are not able to describe a state of inextensional bending.

5.3.2.3 Discretization

As is well known the isoparametric approach (Crisfield 1986) states that the same approximated functions modelling the displacement field have to be used to describe the shape of the field itself. First of all, the formulation adopted herein permits the introduction of identical discretizing functions for both transversal displacement and rotation of a section. Moreover, having in mind the curvilinear shape of the element which is going to be formulated, the use of the same functions describing the axial displacement seems to be suitable, so the following relations hold for a three and five node elements:

$$u = \sum_{i=1}^{3 \text{ or } 5} N_i u_i, \tag{5.142}$$

$$v = \sum_{i=1}^{3 \text{ or } 5} N_i v_i, \tag{5.143}$$

$$\theta = \sum_{i=1}^{3 \text{ or } 5} N_i \theta_i, \tag{5.144}$$

where $N_i (i = 1, 2, 3 \text{ or } 5)$ are the shape functions, all second order polynomials for three–node element:

$$N_1 = \frac{1}{2}(1-r) - N_3, \qquad N_2 = \frac{1}{2}(1+r) - N_3, \qquad N_3 = (1-r^2), \tag{5.145}$$

and for a five–node element:

$$N_1' = \frac{1}{2}(1-r) - \frac{1}{2}N_3 + r(1-r^2)\left(\frac{1}{2}-r\right) + \frac{1}{3}r(1-r^2)\left(\frac{1}{2}+r\right), \tag{5.146}$$

$$N_2' = \frac{1}{2}(1+r) - \frac{1}{2}N_3 - r(1-r^2)\left(\frac{1}{2}+r\right) - \frac{1}{3}r(1-r^2)\left(\frac{1}{2}-r\right), \tag{5.147}$$

$$N_3' = (1-r^2) + 2r(1-r^2)\left(\frac{1}{2}-r\right) - 2r(1-r^2)\left(\frac{1}{2}+r\right), \tag{5.148}$$

$$N_4' = -\frac{8}{3}r(1-r^2)\left(\frac{1}{2}-r\right), \tag{5.149}$$

$$N_5' = \frac{8}{3}r(1-r^2)\left(\frac{1}{2}+r\right). \tag{5.150}$$

The expressions (5.145) and (5.146)–(5.150) can also be used to describe the geometry of the straight or of the curvilinear beam element, within the frame of the isoparametric approach. The substitution of Equations (5.120) and (5.142) to (5.145) or (5.150) into Equations (5.125) and (5.126) gives unsatisfactory results from several points of view:

$$\begin{aligned}\varepsilon_{RR} = \sum_{i=1}^{3 \text{ or } 5} \Bigg[&\left(\frac{\partial N_i}{\partial R} u_i \cos\widehat{Rx}_i + N_i u_i \frac{\partial \cos\widehat{Rx}_i}{\partial R}\right) + \\ &+ \left(\frac{\partial N_i}{\partial R} v_i \cos\widehat{Ry}_i + N_i v_i \frac{\partial \cos\widehat{Ry}_i}{\partial R}\right) - s_i \frac{h}{2}\frac{\partial N_i}{\partial R}\theta_i \Bigg],\end{aligned} \tag{5.151}$$

$$\begin{aligned}\gamma_{RS} = \sum_{i=1}^{3 \text{ or } 5} \Bigg[&\left(-\frac{\partial N_i}{\partial R} u_i \cos\widehat{Ry}_i - N_i u_i \frac{\partial \cos\widehat{Ry}_i}{\partial R}\right) + \\ &+ \left(\frac{\partial N_i}{\partial R} v_i \cos\widehat{Rx}_i + N_i v_i \frac{\partial \cos\widehat{Rx}_i}{\partial R}\right) - \theta_i N_i \Bigg].\end{aligned} \tag{5.152}$$

First of all the tangential coefficient γ_{RS} has a more refined definition in terms of the basic variables of the discretization because it is described by a higher order polynomial than the strain rate of deformation ε_{RR}. This fact produces an incorrect estimation of the shear deformation in comparison with the strain due to bending. This is particularly evident at the lower thickness limit $(h/R \to 0)$

because of the different rate of velocity shown by the two different contributions to the global deformation energy (respectively bending and shear types as shown in Equation (5.140)), as they tend zero together with the thickness. Our procedure provides a solution scheme the main advantage of which is its compatibility with the exact solution whatever the choice of integration scheme, regardless the number of nodes employed in describing the element.
The incorrect evaluation of the two components of the strain energy seems to be ascribed, as suggested by some heuristic improvement known as reduced integration schemes, to a too high polynomials degree of the function shaping the tensor components (5.151) and (5.152). Looking back to the difficulties related to the non pertinent choice of the polynomials degree, this procedure follows the strategy of decreasing the γ_{RS} and ε_{RR} polynomials order (first order in this three–node element and second order in five–node element) by means of new, suitable shape functions. Let us introduce:

$$\begin{cases} \gamma^*_{RS} &= N^*_1\gamma^*_{RS1} + N^*_2\gamma^*_{RS2} \\ \varepsilon^*_{RR} &= N^*_1\varepsilon^*_{RR1} + N^*_2\varepsilon^*_{RR2} \end{cases} \Leftarrow \text{three-node,} \tag{5.153}$$

$$\begin{cases} \gamma^\circ_{RS} &= N^\circ_1\gamma^\circ_{RS1} + N^\circ_2\gamma^\circ_{RS2} + N^\circ_3\gamma^\circ_{RS3} + N^\circ_4\gamma^\circ_{RS4} \\ \varepsilon^\circ_{RR} &= N^\circ_1\varepsilon^\circ_{RR1} + N^\circ_2\varepsilon^\circ_{RR2} + N^\circ_3\varepsilon^\circ_{RR3} + N^\circ_4\varepsilon^\circ_{RR4} \end{cases} \Leftarrow \text{five–node.} \tag{5.154}$$

or in matrix form:

$$\gamma^*_{RS} = \begin{bmatrix} N^*_1 & N^*_2 \end{bmatrix} \begin{bmatrix} \gamma^*_{RS1} \\ \gamma^*_{RS2} \end{bmatrix} = \mathbf{N}^*\boldsymbol{\gamma}^* \qquad \varepsilon^*_{RR} = \begin{bmatrix} N^*_1 & N^*_2 \end{bmatrix} \begin{bmatrix} \varepsilon^*_{RR1} \\ \varepsilon^*_{RR2} \end{bmatrix} = \mathbf{N}^*\boldsymbol{\varepsilon}^* \tag{5.155}$$

$$\gamma^\circ_{RS} = \begin{bmatrix} N^\circ_1 & N^\circ_2 & N^\circ_3 & N^\circ_4 \end{bmatrix} \begin{bmatrix} \gamma^\circ_{RS1} \\ \gamma^\circ_{RS2} \\ \gamma^\circ_{RS3} \\ \gamma^\circ_{RS4} \end{bmatrix} = \mathbf{N}^\circ\boldsymbol{\gamma}^\circ, \tag{5.156a}$$

$$\varepsilon^\circ_{RR} = \begin{bmatrix} N^\circ_1 & N^\circ_2 & N^\circ_3 & N^\circ_4 \end{bmatrix} \begin{bmatrix} \varepsilon^\circ_{RR1} \\ \varepsilon^\circ_{RR2} \\ \varepsilon^\circ_{RR3} \\ \varepsilon^\circ_{RR4} \end{bmatrix} = \mathbf{N}^\circ\boldsymbol{\varepsilon}^\circ, \tag{5.156b}$$

where a new set of shape functions is defined for a three–node element:

$$N^*_1 = \frac{3}{2\sqrt{3}}\left(\frac{\sqrt{3}}{3} - r\right), \qquad \text{and} \qquad N^*_2 = \frac{3}{2\sqrt{3}}\left(\frac{\sqrt{3}}{3} + r\right), \tag{5.157}$$

and for five–node:

$$N_1^\circ = -\frac{15-2\sqrt{30}}{\sqrt{30}}\left(\frac{1}{2}-\frac{1}{2}\sqrt{\frac{35}{15+2\sqrt{30}}}r\right)\left(\frac{1}{2}-\frac{1}{2}\sqrt{\frac{35}{15+2\sqrt{30}}}r\right)\left(\frac{1}{2}+\frac{1}{2}\sqrt{\frac{35}{15+2\sqrt{30}}}r\right), \tag{5.158}$$

$$N_2^\circ = -\frac{15-2\sqrt{30}}{\sqrt{30}}\left(\frac{1}{2}+\frac{1}{2}\sqrt{\frac{35}{15+2\sqrt{30}}}r\right)\left(\frac{1}{2}-\frac{1}{2}\sqrt{\frac{35}{15+2\sqrt{30}}}r\right)\left(\frac{1}{2}+\frac{1}{2}\sqrt{\frac{35}{15+2\sqrt{30}}}r\right), \tag{5.159}$$

$$N_3^\circ = +\frac{15+2\sqrt{30}}{\sqrt{30}}\left(\frac{1}{2}+\frac{1}{2}\sqrt{\frac{35}{15+2\sqrt{30}}}r\right)\left(\frac{1}{2}-\frac{1}{2}\sqrt{\frac{35}{15+2\sqrt{30}}}r\right)\left(\frac{1}{2}-\frac{1}{2}\sqrt{\frac{35}{15+2\sqrt{30}}}r\right), \tag{5.160}$$

$$N_4^\circ = +\frac{15+2\sqrt{30}}{\sqrt{30}}\left(\frac{1}{2}+\frac{1}{2}\sqrt{\frac{35}{15+2\sqrt{30}}}r\right)\left(\frac{1}{2}+\frac{1}{2}\sqrt{\frac{35}{15+2\sqrt{30}}}r\right)\left(\frac{1}{2}-\frac{1}{2}\sqrt{\frac{35}{15+2\sqrt{30}}}r\right), \tag{5.161}$$

one degree lower and defined at the two and four Gauss points, which exactly integrate the flexural strain energy. The use of Equations (5.153) or (5.154) now gives for γ_{RS} and ε_{RR} a contrasting definition because γ_{RS} and ε_{RR} were previously defined in a slightly different way in Equations (5.126) and (5.125). This incoherence can be removed by imposing the coincidence of the two shear–polynomials $(5.155)_1$ or (5.156a) and (5.152); and the coincidence of the two membrane–polynomials $(5.155)_2$ or relation (5.156b) and (5.151) at a number of selected points. To this purpose the Gauss integration points have proved to be very efficient. Here is developed the three–node case; we can write the expression for a five–node in a straightforward manner. Referring to the Equations (5.120), (5.152) and $(5.155)_1$ we have:

$$\gamma^*_{RS}\Big|_{r=\pm\frac{\sqrt{3}}{3}} = \gamma_{RS}\Big|_{r=\pm\frac{\sqrt{3}}{3}} \Rightarrow \tag{5.162}$$

$$[N_1^*\gamma_{RS1}^* + N_2^*\gamma_{RS2}^*]\Big|_{r=-\frac{\sqrt{3}}{3}} =$$
$$= \sum_{i=1}^{3}\left\{\left[\left(-\frac{\partial N_i}{\partial r}\Big|_{r=-\frac{\sqrt{3}}{3}} u_i\cos\widehat{Ry}_i - N_i\Big|_{r=-\frac{\sqrt{3}}{3}} u_i\frac{\partial\cos\widehat{Ry}_i}{\partial r}\right) + \right.\right.$$
$$\left.\left. + \left(\frac{\partial N_i}{\partial r}\Big|_{r=-\frac{\sqrt{3}}{3}} v_i\cos\widehat{Rx}_i + N_i\Big|_{r=-\frac{\sqrt{3}}{3}} v_i\frac{\partial\cos\widehat{Rx}_i}{\partial r}\right)\right]\frac{2}{l} - \theta_i N_i\Big|_{r=-\frac{\sqrt{3}}{3}}\right\}, \tag{5.163}$$

$$[N_1^*\gamma_{RS1}^* + N_2^*\gamma_{RS2}^*]\Big|_{r=+\frac{\sqrt{3}}{3}} =$$
$$= \sum_{i=1}^{3}\left\{\left[\left(-\frac{\partial N_i}{\partial r}\Big|_{r=+\frac{\sqrt{3}}{3}} u_i\cos\widehat{Ry}_i - N_i\Big|_{r=+\frac{\sqrt{3}}{3}} u_i\frac{\partial\cos\widehat{Ry}_i}{\partial r}\right) + \right.\right.$$
$$\left.\left. + \left(\frac{\partial N_i}{\partial r}\Big|_{r=+\frac{\sqrt{3}}{3}} v_i\cos\widehat{Rx}_i + N_i\Big|_{r=+\frac{\sqrt{3}}{3}} v_i\frac{\partial\cos\widehat{Rx}_i}{\partial r}\right)\right]\frac{2}{l} - \theta_i N_i\Big|_{r=+\frac{\sqrt{3}}{3}}\right\}, \tag{5.164}$$

$$\Downarrow$$

$$\begin{bmatrix}\gamma_{RS1}^*\\ \gamma_{RS2}^*\end{bmatrix} = \boldsymbol{\gamma}^* = \overline{\mathbf{B}}\mathbf{U}, \tag{5.165}$$

and referring to the Equations (5.120), (5.151) and $(5.155)_2$ we have:

$$\varepsilon_{RR}^*\Big|_{r=\pm\frac{\sqrt{3}}{3}} = \varepsilon_{RR}\Big|_{r=\pm\frac{\sqrt{3}}{3}} \Rightarrow \boldsymbol{\varepsilon}^* = \overline{\mathbf{B}}'\mathbf{U}, \tag{5.166}$$

where $\mathbf{U} = [u_1\ v_1\ \theta_1 \cdots u_3\ v_3\ \theta_3]^T$ is the nodal displacement vector in the global reference system. The final result is:

$$\gamma_{RS}^* = \begin{bmatrix}N_1^* & N_2^*\end{bmatrix}\overset{2\times 9}{\overline{\mathbf{B}}}\ \mathbf{U} = \overset{1\times 9}{\overline{\overline{\mathbf{B}}}}\ \mathbf{U}. \tag{5.167}$$

$$\varepsilon_{RR}^* = \begin{bmatrix}N_1^* & N_2^*\end{bmatrix}\overset{2\times 9}{\overline{\mathbf{B}}'}\ \mathbf{U} = \overset{1\times 9}{\overline{\overline{\mathbf{B}}}'}\ \mathbf{U}. \tag{5.168}$$

Now we can write:

$$\left[\begin{array}{c} \varepsilon^*_{RR} \\ \gamma^*_{RS} \end{array} \right] = \mathbf{BU} = \left[\begin{array}{c} \overset{1\times 9}{\uparrow} \\ \overline{\overline{\mathbf{B}}}'' \\ \dots \\ \underset{\downarrow}{1\times 9} \\ \overline{\overline{\mathbf{B}}} \end{array} \right] \mathbf{U}, \tag{5.169}$$

where:

$$\overline{\overline{\mathbf{B}}}''(i=1,4,7) = \left[\left(\left.\frac{\partial N_j}{\partial r}\right|_{r=-\frac{\sqrt{3}}{3}} \cos\widehat{Rx}_j + N_j \left|_{r=-\frac{\sqrt{3}}{3}} \frac{\partial \cos\widehat{Rx}_j}{\partial r} \right.\right) N_1^* \Big|_{G.} + \right.$$
$$\left. + \left(\left.\frac{\partial N_j}{\partial r}\right|_{r=+\frac{\sqrt{3}}{3}} \cos\widehat{Rx}_j + N_j \left|_{r=+\frac{\sqrt{3}}{3}} \frac{\partial \cos\widehat{Rx}_j}{\partial r} \right.\right) N_2^* \Big|_{G.} \right] \frac{2}{l} \qquad j=1,2,3 \tag{5.170}$$

$$\overline{\overline{\mathbf{B}}}''(i=2,5,8) = \left[\left(\left.\frac{\partial N_j}{\partial r}\right|_{r=-\frac{\sqrt{3}}{3}} \cos\widehat{Ry}_j + N_j \left|_{r=-\frac{\sqrt{3}}{3}} \frac{\partial \cos\widehat{Ry}_j}{\partial r} \right.\right) N_1^* \Big|_{G.} + \right.$$
$$\left. + \left(\left.\frac{\partial N_j}{\partial r}\right|_{r=+\frac{\sqrt{3}}{3}} \cos\widehat{Ry}_j + N_j \left|_{r=+\frac{\sqrt{3}}{3}} \frac{\partial \cos\widehat{Ry}_j}{\partial r} \right.\right) N_2^* \Big|_{G.} \right] \frac{2}{l} \qquad j=1,2,3 \tag{5.171}$$

$$\overline{\overline{\mathbf{B}}}''(i=3,6,9) = -\left[\left.\frac{\partial N_j}{\partial r}\right|_{r=-\frac{\sqrt{3}}{3}} N_1^* \Big|_{G.} + \left.\frac{\partial N_j}{\partial r}\right|_{r=+\frac{\sqrt{3}}{3}} N_2^* \Big|_{G.} \right] \frac{2}{l} s_j \frac{h}{2} \qquad j=1,2,3 \tag{5.172}$$

$$\overline{\overline{\mathbf{B}}}(i=1,4,7) = \left[\left(-\left.\frac{\partial N_j}{\partial r}\right|_{r=-\frac{\sqrt{3}}{3}} \cos\widehat{Ry}_j - N_j \left|_{r=-\frac{\sqrt{3}}{3}} \frac{\partial \cos\widehat{Ry}_j}{\partial r} \right.\right) N_1^* \Big|_{G.} + \right.$$
$$\left. + \left(-\left.\frac{\partial N_j}{\partial r}\right|_{r=+\frac{\sqrt{3}}{3}} \cos\widehat{Ry}_j - N_j \left|_{r=+\frac{\sqrt{3}}{3}} \frac{\partial \cos\widehat{Ry}_j}{\partial r} \right.\right) N_2^* \Big|_{G.} \right] \frac{2}{l} \qquad j=1,2,3 \tag{5.173}$$

$$\overline{\overline{\mathbf{B}}}(i=2,5,8)=\left[\left(\left.\frac{\partial N_j}{\partial r}\right|_{r=-\frac{\sqrt{3}}{3}}\cos\widehat{Rx}_j+N_j\left|_{r=-\frac{\sqrt{3}}{3}}\right.\frac{\partial\cos\widehat{Rx}_j}{\partial r}\right)N_1^*\Big|_{G.}+\right.$$
$$\left.+\left(\left.\frac{\partial N_j}{\partial r}\right|_{r=+\frac{\sqrt{3}}{3}}\cos\widehat{Rx}_j+N_j\left|_{r=+\frac{\sqrt{3}}{3}}\right.\frac{\partial\cos\widehat{Rx}_j}{\partial r}\right)N_2^*\Big|_{G.}\right]\frac{2}{l}\qquad j=1,2,3 \tag{5.174}$$

$$\overline{\overline{\mathbf{B}}}(i=3,6,9)=-N_j\left|_{r=-\frac{\sqrt{3}}{3}}\right.N_1^*\Big|_{G.}-N_j\left|_{r=+\frac{\sqrt{3}}{3}}\right.N_2^*\Big|_{G.}\qquad j=1,2,3. \tag{5.175}$$

where we have defined with the subscript $G.$ the actual Gauss point depending on the exact integration scheme.

5.3.2.4 Middle line geometry

In the Equations (5.170)–(5.175) the functions of the R variable $\cos\widehat{Rx}$ and $\cos\widehat{Ry}$ depend on the then present state of equilibrium via the corresponding nodal cartesian coordinate $(x_i, y_i, i=1,2,3)$. The equation used to describe the middle line, may be written in terms of a position vector emanating from the origin of the global reference system (x,y):

$$\mathbf{r}=x\mathbf{u}+y\mathbf{v}, \tag{5.176}$$

in which $\mathbf{u}$ and $\mathbf{v}$ are unit vectors along the x and y axes, respectively. The derivative of $\mathbf{r}$ with respect to the curvilinear coordinates is considered:

$$\frac{\partial\mathbf{r}}{\partial R}=\mathbf{r}_{,R}, \tag{5.177}$$

this is a vector tangent to R coordinate line. Defining the Lamè parameter A:

$$A^2=\mathbf{r}_{,R}\cdot\mathbf{r}_{,R}, \tag{5.178}$$

the unit tangent vector is:

$$\mathbf{t}_R=\begin{bmatrix}\cos\widehat{Rx}\\ \cos\widehat{Ry}\end{bmatrix}=\frac{\mathbf{r}_{,R}}{A}=\begin{bmatrix}\dfrac{E}{\sqrt{E^2+F^2}}\\ \dfrac{F}{\sqrt{E^2+F^2}}\end{bmatrix} \tag{5.179}$$

where:

$$E=\sum_{i=1}^{3\text{ or }5}\frac{\partial N_i}{\partial r}x_i, \tag{5.180}$$

$$F=\sum_{i=1}^{3\text{ or }5}\frac{\partial N_i}{\partial r}y_i. \tag{5.181}$$

Moreover in previous calculations the shape functions N_i were assumed to be dependent solely on the variable r. With a small change in their definition it is possible explicitly to introduce their dependence on a second indipendent variable s through the thickness:

$$N_{\text{top}\,i} = N_i\left(\frac{1}{2}(1+s)\right) \qquad \text{and} \qquad N_{\text{bottom}\,i} = N_i\left(\frac{1}{2}(1-s)\right). \tag{5.182}$$

The dependence on variable r and s of the shape functions thus introduced, gives two great advantages even if produces an increase in the consumption of computer time. The use of two local coordinates facilitates the evaluation of the matrices related to the discretized problem in terms of the global coordinates x and y, simply following the strategy stated by the isoparametric approach:

$$\begin{bmatrix} x \\ y \end{bmatrix} = \sum_{i=1}^{3 \text{ or } 5} N_{\text{top}\,i}(r,s) \begin{bmatrix} x_i \\ y_i \end{bmatrix}_{\text{top}} + \sum_{i=1}^{3 \text{ or } 5} N_{\text{bottom}\,i}(r,s) \begin{bmatrix} x_i \\ y_i \end{bmatrix}_{\text{bottom}}. \tag{5.183}$$

On the other hand the introduction of the coordinate s in the formulas governing the phenomenon is only a first step towards a more complex formulation of the model, which is invoked by several problems involving particular aspects of curved beam analysis, such as that of layered materials or of material of which a known initial stress distribution throughout the thickness has to be taken into account. From this point of view the portion of the area which corresponds to the beam has to be divided into strips parallel to the axis of the beam (Figure 5.7) so that in each strip the numerical evaluation of the then present mechanical properties may be performed indipendently, the only relationship between them being the compatibility of the displacement through the thickness.

5.3.2.5 Constitutive law and stiffness matrix

For an elastic isotropic material, the stress vector is related to the strain vector as follows:

$$\begin{bmatrix} \sigma_{RR} \\ \tau_{RS} \end{bmatrix} = \begin{bmatrix} E & 0 \\ 0 & G \end{bmatrix} \begin{bmatrix} \varepsilon_{RR} \\ \gamma_{RS} \end{bmatrix}, \tag{5.184}$$

or in compact form:

$$\boldsymbol{\sigma} = \mathbf{D}\boldsymbol{\varepsilon}, \tag{5.185}$$

where instead of $\boldsymbol{\varepsilon}$ we use $\boldsymbol{\varepsilon}^*$ for a three–node and $\boldsymbol{\varepsilon}^\circ$ for a five–node.

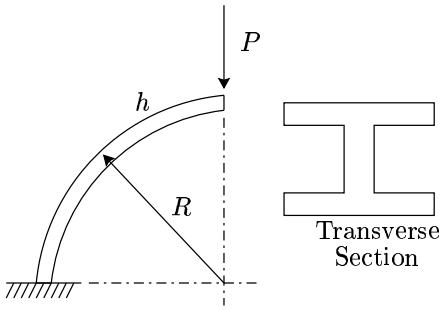

Figure 5.8: A quarter–circular cantilever ring.

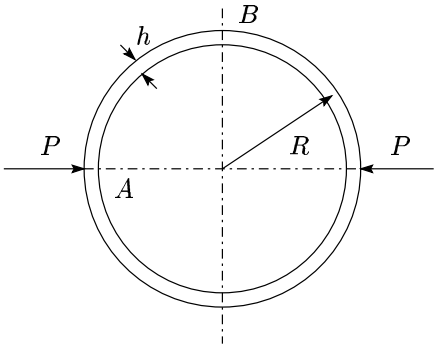

Figure 5.9: A pinched ring.

5.3.3 Some numerical examples

Here we introduce three typical examples of the shear–membrane locking, frequently used to test the capability and effectiveness of the element developed. The geometrical dimensions and the physical material parameters employed for the test problems are in consistent units; shear coorection factor $k = 5/6$ is used in Equations (5.186)–(5.190).

5.3.3.1 Test case 1: a quarter–circular cantilever ring

The quarter–circular cantilever ring (Figure 5.8) is subjected to a radial point load at the free end. This moderately deep arch configuration has been idealized using one and two three node elements; Table 5.3 shows that the results of the present analysis compare very well with the Castigliano's solutions for radial displacement (w_{ex}), tangential displacement (u_{ex}) and section rotation (θ_{ex}):

$$w_{ex} = -\left(\frac{\pi PR^3}{4EI} + \frac{\pi PR}{4GAk} + \frac{\pi PR}{4EA}\right), \tag{5.186}$$

$$u_{ex} = \frac{PR^3}{2EI} - \frac{PR}{2GAk} - \frac{PR}{2EA}, \tag{5.187}$$

$$\theta_{ex} = \frac{PR^2}{EI}. \tag{5.188}$$

Furthermore Table 5.3 shows the convergence with respect to mesh size (number of elements used) and the patterns for fixed mesh and variable slenderness ratio R/h. The element yields accurate solution over the entire range of slenderness ratio (R/h) avoiding any deterioration in the performance at the lower thickness value $R/h \to 100000$. We have obtained these results for a three–node element

using 4–Gauss points in r–direction which exactly integrates flexural energy term, 2–Gauss points in s–direction. Here we haven't reported the solutions using one five–node element because the ratio between exact and f.e.m. solution is, with R/h between 100 and 100000, exactly equal one.

Table 5.3: Comparison of finite element solutions, using 3 node element, for tip response of the quarter ring with Castigliano's solutions; finite element solution normalized w.r.t. the exact solution.

$\frac{R}{h}$	One–element model			Two–element model		
	w_{fem}/w_{ex}	θ_{fem}/θ_{ex}	u_{fem}/u_{ex}	w_{fem}/w_{ex}	θ_{fem}/θ_{ex}	u_{fem}/u_{ex}
10	0.940692	0.987419	0.944102	0.996925	1.000012	1.000121
20	0.939445	0.986392	0.940256	0.995470	0.999128	0.996967
50	0.939095	0.986104	0.939183	0.995062	0.998797	0.995807
100	0.939045	0.986063	0.939030	0.995003	0.998750	0.995641
200	0.939032	0.986053	0.938992	0.994989	0.998738	0.995600
500	0.939028	0.986050	0.938981	0.994985	0.998734	0.995588
1000	0.939028	0.986049	0.938979	0.994984	0.998734	0.995586
5000	0.939028	0.986049	0.938979	0.994984	0.998733	0.995585
10000	0.939028	0.986049	0.938979	0.994984	0.998733	0.995585
100000	0.939028	0.986049	0.938979	0.994984	0.998733	0.995585

5.3.3.2 Test case 2: a pinched ring

Figure 5.9 shows the details of a ring pinched by two identical and diametrically opposite forces P. This problem is the best example to demonstrate the behaviour of the elements in a deep arch configuration, and it is widely used by researchers to assess the performance of curved beam elements. Only one quadrant AB of the ring is modelled with appropriate symmetric boundary conditions. Castigliano's energy theorem yields the following responses for the problem:

$$w_A = -\left(\frac{PR^3(\pi^2-8)}{8\pi EI} + \frac{\pi PR}{8GAk} + \frac{\pi PR}{8EA}\right), \tag{5.189}$$

$$u_B = \frac{PR^3(4-\pi)}{4\pi EI} + \frac{PR}{4GAk} - \frac{PR}{4EA}. \tag{5.190}$$

Table 5.4 shows the displacement response of the pinched ring modelled by two and four three–node elements and using one five–node element. Whether using a three–node element or a five–node element, full–exact gaussian quadrature rules are employed for evaluating stiffness matrix. Excellent results are observed

Table 5.4: Analysis of a pinched ring using two and four three–node elements model and one five–node element model; the results are normalized w.r.t. the exact solution based on Castigliano's theorem.

	Three–node element				**Five–node element**	
$\frac{R}{h}$	Two–element model		Four–element model		One–element model	
	w_{fem}/w_{ex}	u_{fem}/u_{ex}	w_{fem}/w_{ex}	u_{fem}/u_{ex}	w_{fem}/w_{ex}	u_{fem}/u_{ex}
10	0.984584	0.992341	0.999157	1.000034	1.001103	1.002148
20	0.984366	0.991725	0.999012	0.999680	1.000600	1.001503
50	0.984304	0.991552	0.998971	0.999494	1.000600	1.000900
100	0.984296	0.991527	0.998966	0.999468	1.000600	1.000900
200	0.984293	0.991521	0.998964	0.999461	1.000600	1.000900
500	0.984293	0.991519	0.998964	0.999459	1.000590	1.000900
1000	0.984293	0.991519	0.998964	0.999459	1.000590	1.000900
5000	0.984293	0.991519	0.998964	0.999459	1.000590	1.000900
10000	0.984293	0.991519	0.998964	0.999459	1.000590	1.000900
100000	0.984293	0.991519	0.998964	0.999459	1.000590	1.000900

throughout all the thickness range from thick to thin to very thin. The capability and effectiveness of the element BGMI is quite remarkable considering that the responses are obtained with only one and two element models in the very thin cases with shear and membrane locking completely eliminated.

5.3.3.3 Test case 3: a thin arch under a moment discontinuity.

Figure 5.10 shows the details of a simply supported thin arch subjected to a concentrated moment M at the middle of the span. The central displacement by the Castigliano's theorem can be calculated explicitly, but are very complex, so

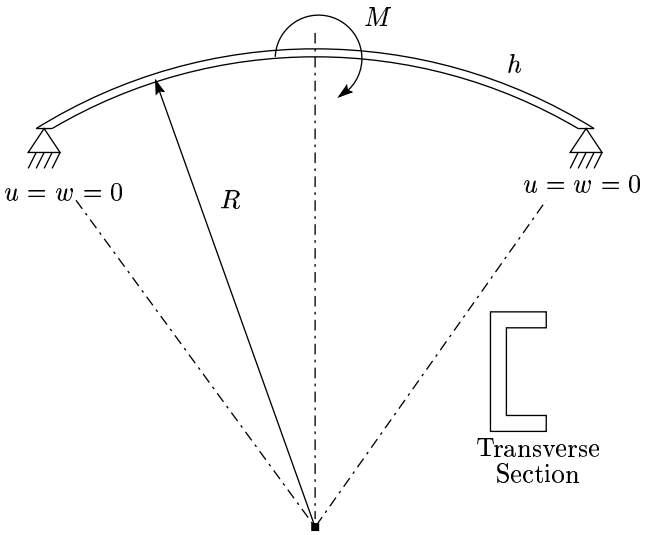

Figure 5.10: A simply supported arch with a central moment load.

we use a simple case of the Euler beam when it is very thin:

$$w_{ex} = 0, \tag{5.191}$$

$$u_{ex} = -\frac{20(\sqrt{2}-1) - \pi(4-\sqrt{2})}{16}\frac{MR^2}{EI}, \tag{5.192}$$

$$\theta_{ex} = \frac{3-\sqrt{2}+\pi}{4}\frac{MR}{EI} \tag{5.193}$$

Table 5.5 shows the convergence behaviour of the finite element solution normalized with the analytical solutions. These studies indicate that the two type of elements yield very accurate predictions. The values are in very good agreement with the exact solution given by Equations (5.192) and (5.193) over the entire arc length.

Two simple and efficient three and five node elements devoid of shear and membrane locking, even in the extreme thin limit, have been proposed. The results of the test problems solved show that the proposed elements not only have good convergence in thin like cable element but also yield accurate predictions even with coarse meshes. As it can be argued by the previous formulation is quite straightforward the extension to the three–dimensional problem. By coupling this *cable* element with the membrane one, we will be able to model the sail as a textile

Table 5.5: Comparison of finite element solution for central displacement of a thin simply supported arch w.r.t. the exact solution based on Equations (5.192) and (5.193).

	Three–node element				**Five–node element**	
$\frac{R}{h}$	Two–element model		Four–element model		Two–element model	
	θ_{fem}/θ_{ex}	u_{fem}/u_{ex}	θ_{fem}/θ_{ex}	u_{fem}/u_{ex}	θ_{fem}/θ_{ex}	u_{fem}/u_{ex}
100	0.988	1.012	0.999	1.000	1.000	0.999
200	0.988	1.012	0.999	1.000	1.000	0.999
500	0.988	1.012	0.999	1.000	1.000	0.999
1000	0.988	1.012	0.999	1.000	1.000	0.999
5000	0.988	1.012	0.999	1.000	1.000	0.999
10000	0.988	1.012	0.999	1.000	1.000	0.999
100000	0.988	1.012	0.999	1.000	1.000	0.999

composite structure as we have seen in Section 3.6.3 and as we are going to see in Chapter 6.

Chapter 6

Conclusions and numerical results

6.1 Sail shape

In this last chapter, we present the three–dimensional structural behaviour of the optimized sail of Section 3.6.3 under a given wind–load.
A sail is a tensile structure hoisted on the rig of a yacht, inflated by wind pressure. Our first objective was the aerodynamic optimization of the sail in order to obtain the maximum thrust force for a given load distribution. The next step was to model the sail as a textile composite and to obtain the optimum distribution of the fibers in the material matrix.
Then, a fluid–structure interaction problem occurs (LeMaître, Huberson, and De-Cursi 1999): the sail shape depends on the aerodynamic loading, which itself depends upon the shape. A first way for solving this aero–elastic problem is to subdivide it into two parts (Schoop 1990). On one hand, we have to solve the equilibrium shape under a given pressure: a flow field is given and a configuration of the sail is computed (structural step) (Muttin 1991). On the other hand we have to compute the wind pressure for a given shape: a new external flow is then computed by taking into account the new configuration of the sail (aerodynamic step) (Schoop and Bessert 2001). This leads to a new external flow, a new geometry of the sail and so on: the sequence of structural/aerodynamic steps is repeated until some stopping condition is satisfied.
The aim of this last chapter is to solve the *structural* sail problem. We consider the sail as a textile flexible structure, already optimized from an aerodynamic and fiber–distribution point of view, submitted to an aerodynamic forces resulting from a given flow field. So, only the resulting aerodynamic forces are computed as a part of a fluid–structure interaction problem. The effects of the changes of the geometry on the flow are not considered here.

The very flexible behaviour of sails leads to large displacement analysis of very thin structure (LeMaître, DeCursi, and Huberson 1998). Due to large displacement, our model is geometrically non–linear, and since deformations in modern sails remain low, constitutive laws of the material can be consider as linear (LeDret and Raoult 1995). We emphasize on a consequence of the capability of the sail to undergo large displacements without significant deformations.
From the initial geometry (Figure 6.1) we have computed the equilibrium configuration for the opposite field of external loads (close–hauled course). This computation case, defined by Charvet and Huberson (1998) as a *tack*, proves the great capabilities of our *string–membrane network model* which can support a large displacement field and find the final equilibrium configuration (Figure 6.4) even if the initial (given) shape is far from the solution. A few intermediate configurations, extracted from the iterative procedure, are plotted in Figures 6.2 and 6.3. The stress pattern is presented in Figures 6.5 and 6.6.

The future development of the sail models, should be the inclusion in the iterative procedure of the aerodynamic step coupled opportunily with the structural step. Furthermore all actual and future models should be improved on real cases that will require experimental data and measurements in real sailing conditions.

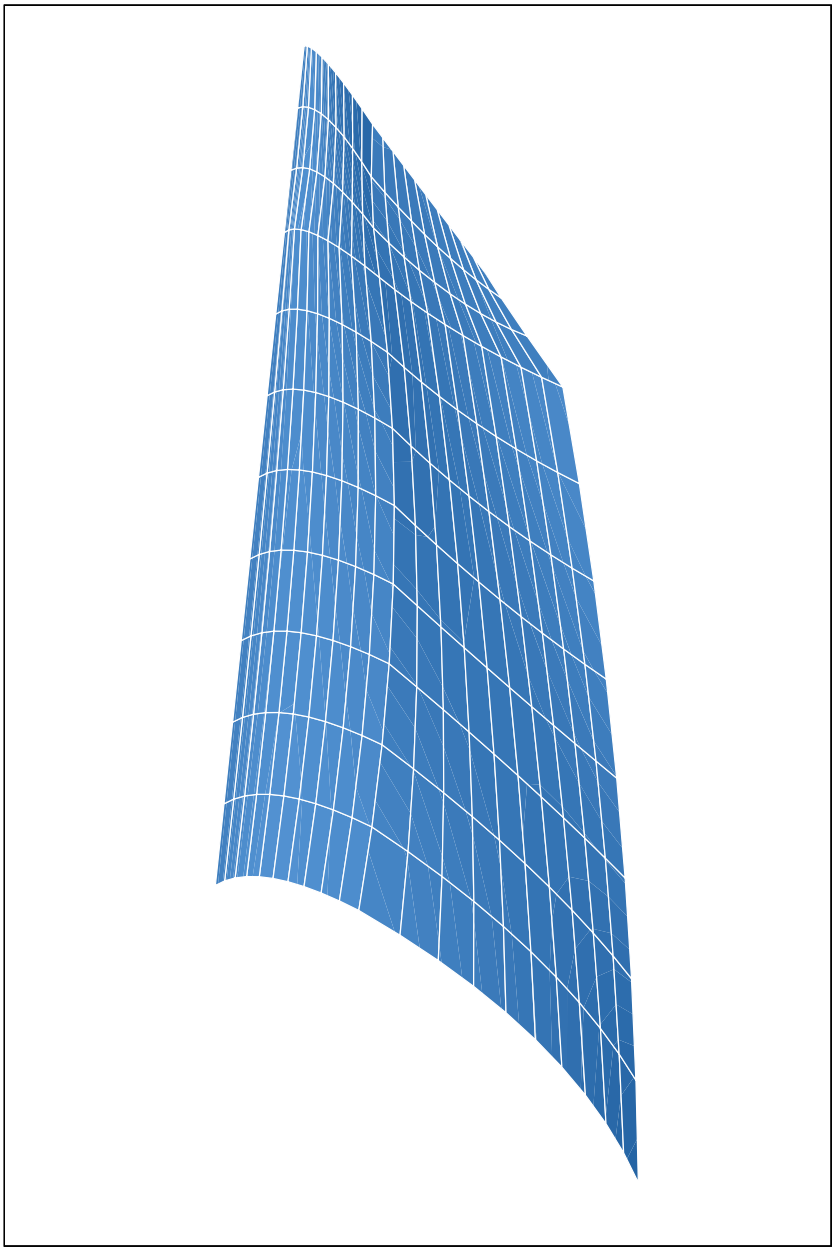

Figure 6.1: Initial undeformed configuration.

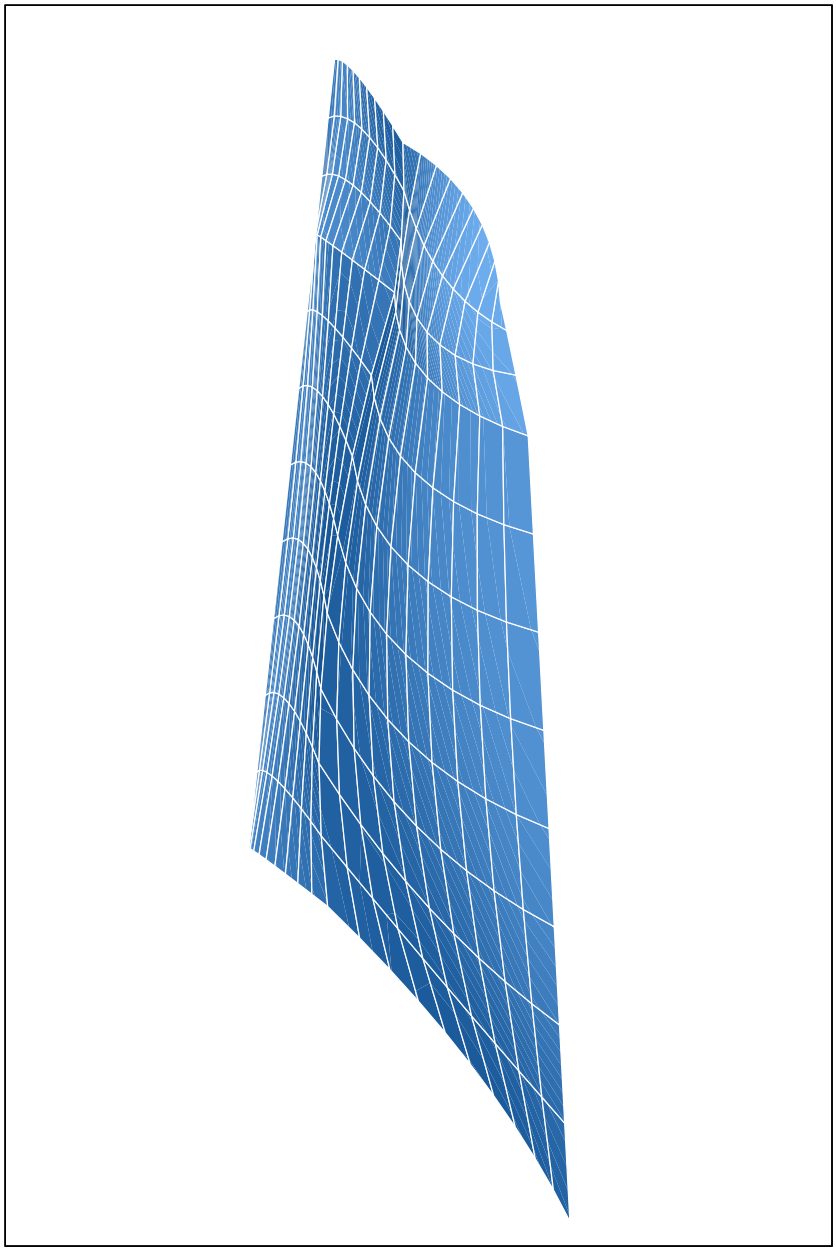

Figure 6.2: First intermediate configuration.

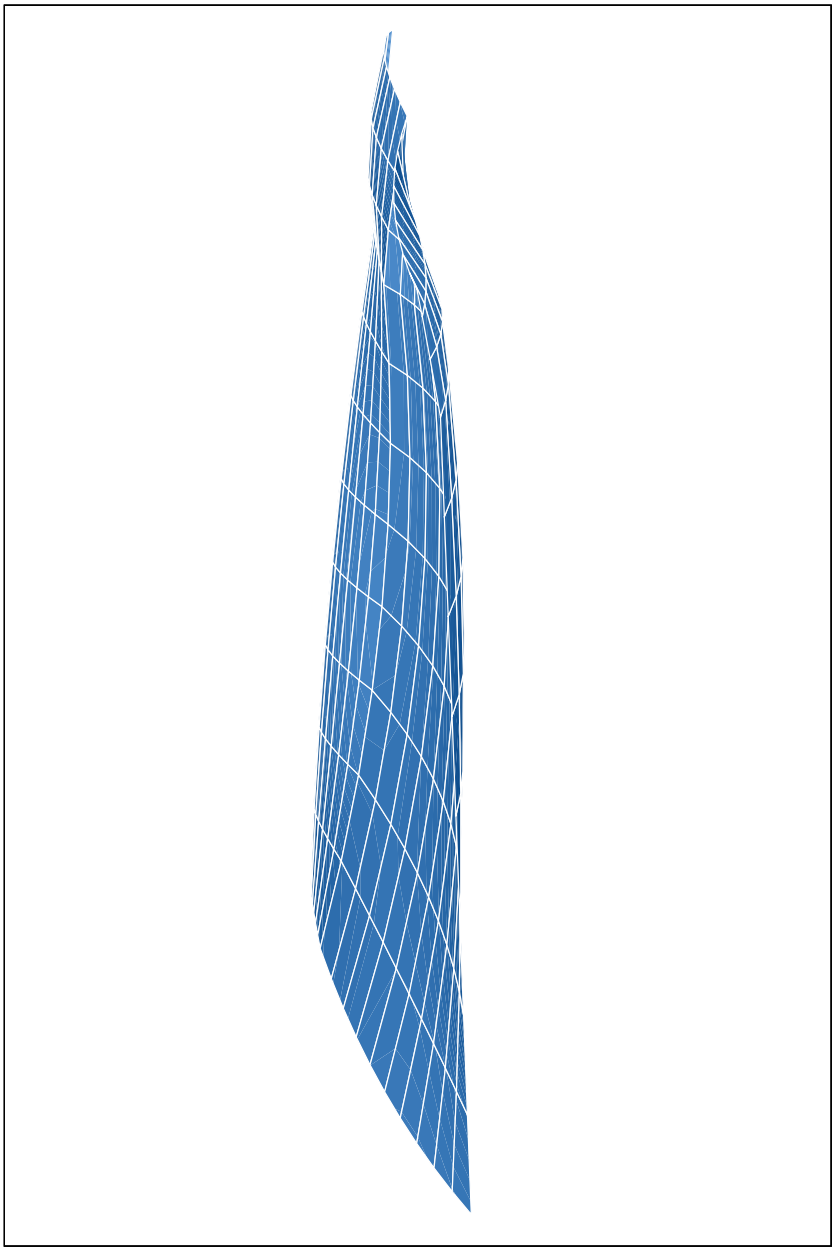

Figure 6.3: Second intermediate configuration.

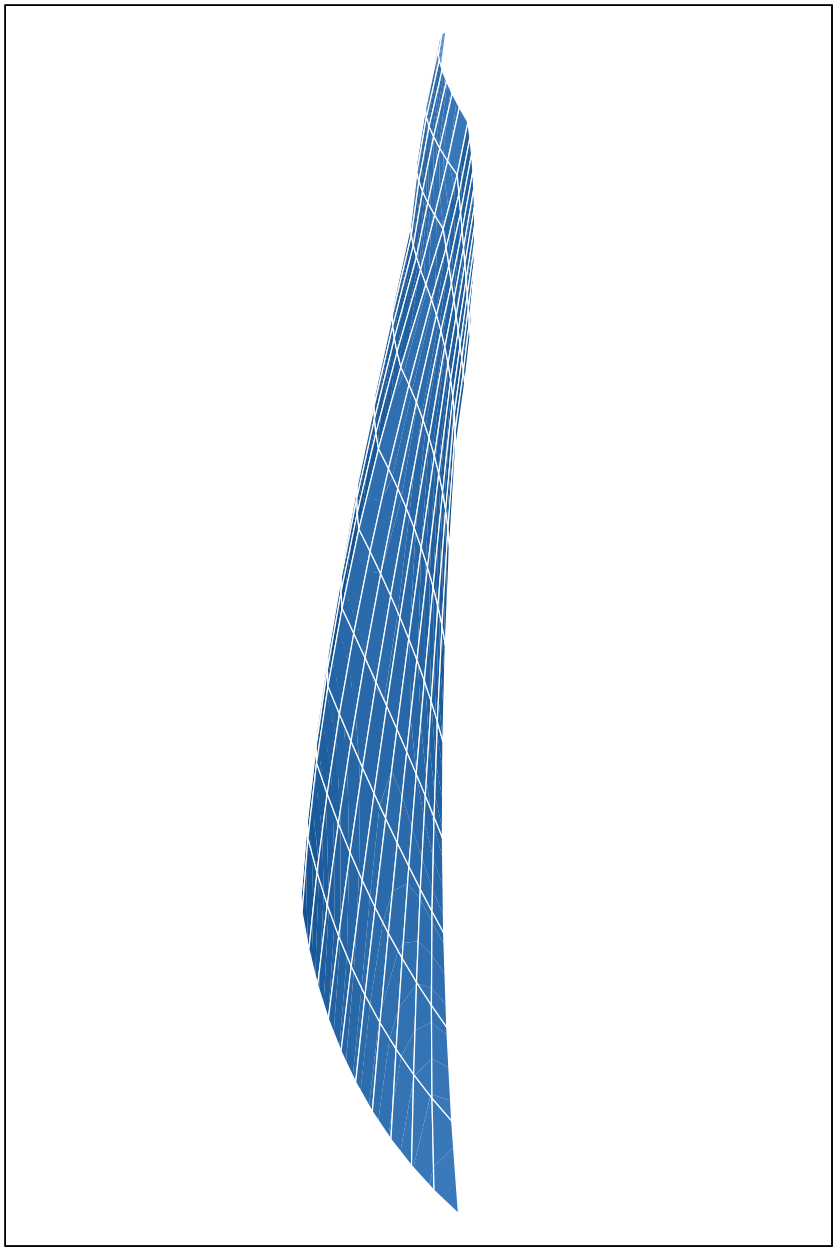

Figure 6.4: Final shape.

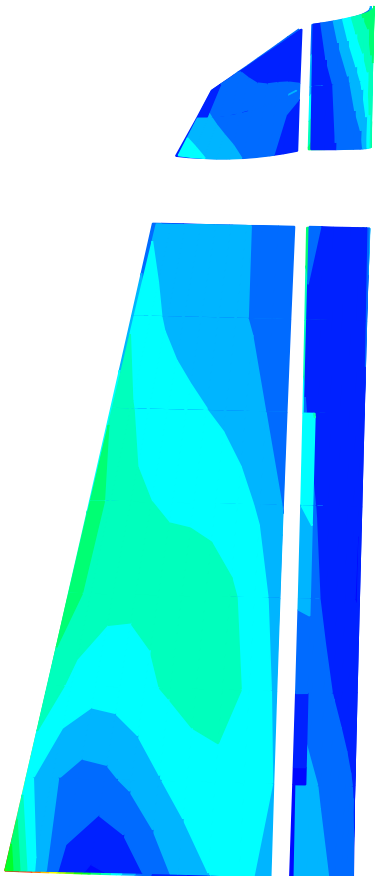

Figure 6.5: Final shape stress distribution.

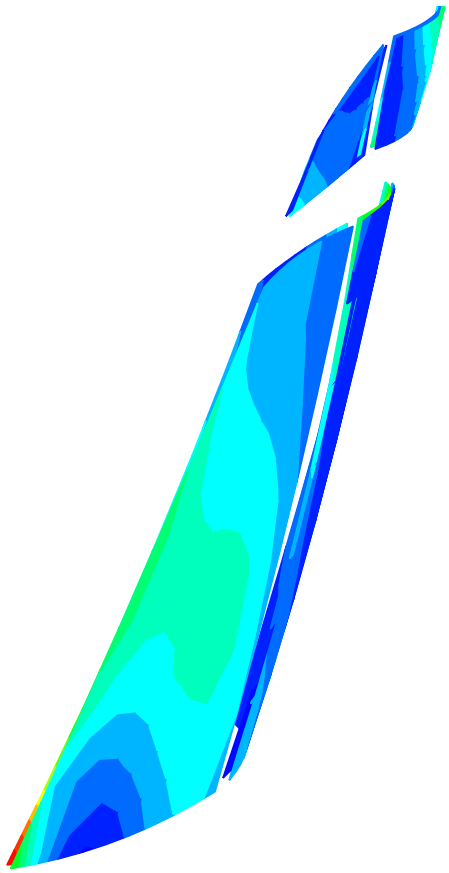

Figure 6.6: Final shape stress distribution (three–dimensional view).

References

Ahmad, S., B. M. Irons, and O. C. Zienkiewicz (1970). Analysis of thick and thin shell structures by curved elements. *Int. J. Numer. Meth. Engng. 2*, 419–451.

Argyris, J. H. (1982). An excursion into large rotations. *Comput. Methods Appl. Mech. Engrg. 32*, 85–155.

Argyris, J. H. and D. W. Scharpf (1968a). The sheba family of shell elements for the matrix displacement method. Part I. natural definition of geometry and strains. *Journal of the Royal Aeronautical Society 72*, 873–878.

Argyris, J. H. and D. W. Scharpf (1968b). The sheba family of shell elements for the matrix displacement method. Part II. interpolation scheme and stiffness matrix. *Journal of the Royal Aeronautical Society 72*, 878–883.

Argyris, J. H. and L. Tenek (1994a). High–temperature bending, buckling and post–buckling of laminated composite plates using the natural mode method. *Comput. Methods Appl. Mech. Engrg. 117*, 105–142.

Argyris, J. H. and L. Tenek (1994b). Linear and geometrically nonlinear bending of isotropic and multilayered composite plates by the natural mode method. *Comput. Methods Appl. Mech. Engrg. 113*, 207–251.

Ashley, H. and M. Landahl (1965). *Aerodynamics of Wings and Bodies*. New York: Dover Publications, Inc.

Ashwell, D. G. and R. H. Gallagher (1976). *Finite Elements for Thin Shells and Curved Members*. London: John Wiley & Sons.

Ashwell, D. G., A. B. Sabir, and T. M. Roberts (1971). Further study in the application of curved finite element to circular arches. *Int. J. Mech. Sci. 13*, 507–517.

Atluri (1983). *Hybrid and Mixed Finite Element Methods*. New York: Wiley.

Babu, C. R. and G. Prathap (1986). A linear thick curved beam element. *Int. J. Numer. Meth. Engng. 23*, 1313–1328.

Babuska, I. (1974). Solution of problems with interfaces and singularities. In C. deBoor (Ed.), *Mathematical Aspects of Finite Elements in Partial Differential Equations*, New York, pp. 213–227. Academic Press.

Bakhvalov, N. and G. Panasenko (1990). *Homogenization: averaging processes in periodic media*, Volume 36 of *Mathematics and its application*. Dordrecht: Kluwer Academic Publisher.

Banichuk, N. V. (1981). Optimization problems for elastic anisotropic bodies. *Arch. Mech. 33*(6), 347–363.

Batchelor, G. K. (1967). *An Introduction to Fluid Mechanics*. Cambridge: Cambridge University Press.

Bathe, K.-J. (1996). *Finite element procedures*. Englewood Cliffs: Prentice Hall.

Bathe, K.-J., F. Brezzi, and S. W. Cho (1989). The MITC7 and MITC9 plate bending elements. *Comput. Struct. 32*(3), 797–814.

Bathe, K.-J. and A. P. Cimento (1980). Some practical procedures for the solution of nonlinear finite element equations. *Comp. Meth. Appl. Mechs. Eng. 22*, 59–85.

Bathe, K.-J. and E. N. Dvorkin (1985). A four–node plate bending element based on Mindlin/Reissner plate theory and a mixed interpolation. *Int. J. Numer. Meth. Engng. 21*, 367–383.

Batoz, J. L. (1982). An explicit formulation for an efficient triangular plate–bending element. *Int. J. Numer. Meth. Engng. 18*, 1077–1089.

Batoz, J. L., K.-J. Bathe, and L. W. Ho (1980). A study of three–node triangular plate–bending elements. *Int. J. Numer. Meth. Engng. 15*, 1771–1812.

Belytschko, T. and C. Tsay (1983). A stabilization procedure for the quadrilateral plate element with one–point quadrature. *Int. J. Numer. Meth. Engng. 19*, 405–419.

Bendsøe, M. P. (1996). *Optimization of Structural Topology, Shape, and Material*. New York: Springer.

Bendsøe, M. P., A. Diaz, and N. Kikuchi (1993). Topology and generalized layout optimization of elastic structures. In M. P. Bendsøe and C. A. Soares (Eds.), *Topology Design of Structures*, Dordrecht, pp. 159–205. Kluwer Academic Publisher.

Bensoussan, A., J. L. Lions, and G. Papanicolaou (1978). *Asymptotic analysis for periodic structures*. Amsterdam: North–Holland.

Berger, M. and B. Gostiaux (1988). *Differential geometry: manifolds, curves, and surfaces*. New York: Springer Verlag.

Bernadou, M. (1996). *Finite element methods for thin shell problems.* New York: John Wiley & Sons.

Bisplinghoff, R. L., H. Ashley, and R. L. Halfman (1955). *Aeroelasticity.* New York: Dover Publications, Inc.

Bogdanovich, A. E. (1993). Three–dimensional analysis of anisotropic spatially reinforced structures. *Composites Manufacturing 4*(4), 173–186.

Bogdanovich, A. E. and B. P. Deepak (1997). Three–dimensional analysis of thick composite plates with multiple layers. *Composites Part B 28*, 345–357.

Bogdanovich, A. E. and C. M. Pastore (1996). Material–smart analysis of textile–reinforced structures. *Composites Science and Technology 56*, 291–309.

Bonet, J. and R. D. Wood (1997). *Nonlinear continuum mechanics for finite element analysis.* Cambridge: Cambridge University Press.

Borri, A. and E. Speranzini (1993). Multicriteria optimization of laminated composite material structures. *Meccanica 28*, 233–238.

Brank, B. and E. Carrera (2000). Multilayered shell finite element with interlaminar continuous shear stresses: a refinement of the Reissner–Mindlin formulation. *International Journal for Numerical Methods in Engineering 48*, 843–874.

Brezzi, F. and K.-J. Bathe (1990). Mixed-interpolated elements for Reissner-Mindlin plates. *Int. J. Numer. Meth. Engng. 28*, 1787–1801.

Bucalem, M. L. and K.-J. Bathe (1997). Finite element analysis of shell structures. *Archives of Computational Methods in Engineering 4*(1), 3–61.

Carvelli, V. and C. Poggi (2001). A homogenization procedure for the numerical analysis of woven fabric composites. *Composites Part A 32*, 1425–1432.

Cebeci, T. (1999). *An Engineering Approach to the Calculation of Aerodynamic Flows.* New York: Springer Verlag.

Chao, W. C. and J. N. Reddy (1984). Analysis of laminated composite shells using a degenerated 3-d element. *International Journal for Numerical Methods in Engineering 20*, 1991–2007.

Chapman, C. and J. Whitcomb (1995). Effect of assumed tow architecture on predicted moduli and stresses in plain weave composites. *Journal of Composite Materials 29*(16), 2134–2159.

Charvet, T. and S. Huberson (1998). Numerical calculation of the flow around sails. *European Journal of Mechanics, B/Fluids 11*, 599–610.

Chinosi, C. and C. Lovadina (1994). Mixed finite elements for Reissner–Mindlin plate model. In M. Papadrakakis and B. H. V. Topping (Eds.), *Advances in Finite Element Techniques*, Berlin, pp. 33–38. CST.

Chinosi, C. and C. Lovadina (1995). Numerical analisys of some mixed finite elements methods for Reissner-Mindlin plates. *Computational Mechanics 16*, 33–44.

Ciarlet, P. G. (1988). *Mathematical elasticity: three dimensional elasticity*, Volume 1. Amsterdam: Elsevier Science.

Ciarlet, P. G. (2000). *Mathematical elasticity: theory of shells*, Volume 3. Amsterdam: Elsevier Science.

Claughton, A. R., J. F. Wellicome, and R. A. Shenoi (1998). *Sailing Yacht Design: Theory*. Edinburgh: Addison Wesley Longman Limited.

Correia, V. M. F., M. A. A. Gomes, A. Suleman, C. M. M. Soares, and C. A. M. Soares (2000). Modelling and design of adaptive composite structures. *Comp. Meth. Appl. Mechs. Eng. 185*, 325–346.

Correia, V. M. F., C. M. M. Soares, and C. A. M. Soares (2001). Refined models for the optimal design of adaptive structures using simulated annealing. *Composites Structures 54*, 161–167.

Crisfield, M. A. (1986). *Finite elements and solution procedures for structural analysis Vol.1:linear analysis*. Swansea: Pineridge Press.

DalMaso, G. and L. Modica (1986). Nonlinear stochastic homogenization and ergodic theory. *Journal für die reine und angewandte Mathematik 368*, 28–42.

D'Amato, E. (2001). Finite element modeling of textile composites. *Composite Structures 54*, 467–475.

Daniel, I. M. and O. Ishai (1994). *Engineering Mechanics of Composite Materials*. New York: Oxford University Press, Inc.

Dawe, D. J. (1974a). Curved finite elements for the analysis of shallow and deep arches. *Comput. Struct. 4*, 559–580.

Dawe, D. J. (1974b). Numerical studies using circular arch finite elements. *Comput. Struct. 4*, 729–740.

Day, A. H. (1996). Sail optimisation for maximal speed. *Journal of Wind Engineering and Industrial Aerodynamics 63*, 131–154.

DeGiorgi, E. (1975). Sulla convergenza di alcune successioni di integrali del tipo dell'area. *Rendiconti di Mat. 8*, 277–294.

DeGiorgi, E. (1983). G–operators and Γ–convergence. In *Proceedings of the International Congress of Mathematicians*, Warsazwa, pp. 1175–1191. PWN Polish Scientific Publishers and North Holland.

DeGiorgi, E. and S. Spagnolo (1973). Sulla convergenza degli integrali dell'energia per operatori ellittici del secondo ordine. *Boll. Un. Mat. It. 8*, 391–411.

Diana, G., S. DePonte, M. Falco, and A. Zasso (1998). A new large wind tunnel for civil–environmental and aeronautical applications. *Journal of Wind Engineering and Industrial Aerodynamics 74*, 553–565.

Ding, Y. (1987). Optimum design of sandwich constructions. *Comput. Struct. 25*(1), 51–68.

DoCarmo, M. P. (1976). *Differential geometry of curves and surfaces*. Englewood Cliffs: Prentice–Hall.

Dvorkin, E. N. (1995). Nonlinear analysis of shells using the MITC formulation. *Archives of Computational Methods in Engineering 2*(2), 1–50.

Dvorkin, E. N. and K.-J. Bathe (1984). A continuum mechanics based four–node shell element for general non–linear analysis. *Engineering Computations 1*, 77–88.

Dyrbye, C. and S. O. Hansen (1997). *Wind loads on structures*. New York: John Wiley & Sons, Inc.

Eschenauer, H., N. Olhoff, and W. Schnell (1997). *Applied Structural Mechanics*. New York: Springer Verlag.

Eschenauer, H. A. and N. Olhoff (2001). Topology optimization of continuum structures: a review. *Appl. Mech. Rev. 54*(4), 331–390.

Fallow, J. B. (1996). America's cup sail design. *Journal of Wind Engineering and Industrial Aerodynamics 63*, 183–192.

Fish, J. and S. Markolefas (1992). The s–version of the finite element method for multilayer laminates. *International Journal for Numerical Methods in Engineering 33*, 1081–1105.

Flay, R. G. J., N. J. Locke, and G. D. Mallinson (1996). Model tests of twisted flow wind tunnel designs for testing yacht sails. *Journal of Wind Engineering and Industrial Aerodynamics 63*, 155–169.

Fletcher, R. (1987). *Practical Methods of Optimization* (Second ed.). London: John Wiley & Sons.

Fleury, C. (1989). Conlin: an efficient dual optimizer based on convex approximation concepts. *Structural Optimization 1*, 81–89.

Fleury, C. and V. Braibant (1986). Structural optimization: a new dual method using mixed variables. *Int. J. Numer. Meth. Engng. 23*, 409–428.

Flügge, W. (1960). *Stresses in shells*. Berlin: Springer Verlag.

Fried, I. (1973). Shear in C^0 and C^1 bending finite elements. *Int. J. Solids Structures 9*, 449–460.

Fujita, A., H. Hamada, and Z. Maekawa (1993). Tensile properties of carbon fiber triaxial woven fabric composites. *Journal of Composite Materials 27*(15), 1428–1442.

Fujita, A., Z. Maekawa, H. Hamada, and A. Yokoyama (1992). Mechanical behaviour and fracture mechanism in flat braided composites. Part 1: braided flat bar. *Journal of Reinforced Plastics and Composites 11*, 600–617.

Fukunaga, H. and G. N. Vanderplaats (1991). Stiffness optimization of orthotropic laminated composites using lamination parameters. *AIAA J. 29*(4), 641–646.

Fung, Y. C. (1965). *Foundations of Solid Mechanics*. Englewood Cliffs, New Jersey: Prentice–Hall.

Gallagher, R. H. (1976). Problems and progress in thin shell finite element analysis. In D. G. Ashwell and R. H. Gallagher (Eds.), *Finite elements for thin shells and curved members*, London, pp. 1–14. John Wiley & Sons.

Garrett, R. (1990). *Fisica della Vela: La simmetria tra aerodinamica e idrodinamica nel movimento di un'imbarcazione*. Bologna: Zanichelli.

Glauert, H. (1926). *The Elements of Aerofoil and Airscrew Theory* (Second ed.). Cambridge: Cambridge University Press.

Glènans (1975). *Corso di Navigazione dei Glènans* (Mursia ed.). Glènans.

Gobetti, A. and R. Nascimbene (2001). Elasto–plastic, nonlinear analysis of a locking–free shear/flexible curved beam element. In *Proceedings of the European Conference on Computational Mechanics, ECCM*.

Gobetti, A. and R. Nascimbene (2002). Development of a new locking–free curved shell element. In *Proceedings of the Fifth World Congress on Computational Mechanics, WCCM–V*.

Gobetti, A., P. Venini, and R. Nascimbene (2002). Finite element analysis of membrane structures including active piezoelectric devices. In *Proceedings of the Third World Conference on Structural Control, WCSC*.

Gould, P. L. (1988). *Analysis of shells and plates*. New York: Springer Verlag.

Gowayed, Y. A. (1997). The effect of voids on the elastic properties of textile reinforced composites. *Journal of Composites Technology & Research 19*(3), 168–173.

Gowayed, Y. A. and J.-C. Hwang (1995). Thermal conductivity of composite materials made from plain weaves and 3-d weaves. *Composites Engineering 5*(9), 1177–1186.

Gowayed, Y. A., J.-C. Hwang, and D. Chapman (1995). Thermal conductivity of textile composites with arbitrary preform structures. *Journal of Composites Technology & Research 17*(1), 56–62.

Gowayed, Y. A., C. Pastore, and C. S. Howarth (1996). Modification and application of a unit cell continuum model to predict the elastic properties of textile composites. *Composites Part A 27*, 149–155.

Green, A. E. and W. Zerna (1968). *Theoretical Elasticity*. London: Oxford University Press.

Guermond, J. L. (1989). Collocation methods and lifting–surfaces. *European Journal of Mechanics, B/Fluids 8*(4), 283–305.

Gürdal, Z., R. T. Haftka, and P. Hajela (1999). *Design and Optimization of Laminated Composite Materials*. New York: John Wiley & Sons, Inc.

Haan, S. I., P. G. Charalambides, and M. Suri (2001). A specialized finite element for the study of woven composites. *Computational Mechanics 27*, 445–462.

Hallquist, J. O., D. J. Benson, and G. L. Goudreau (1986). Implementation of a modified Hughes–Liu shell into a fully vectorized explicit finite element code. In P. Bergan (Ed.), *Finite element methods for nonlinear problems*, Berlin, pp. 283–297. Springer Verlag.

Hashin, Z. (1983). Analysis of composite materials – a survey. *Journal of Applied Mechanics 50*, 481–505.

Heyman, J. (1977). *Equilibrium of shell structures*. Oxford: Oxford University Press.

Hinton, E. and D. R. J. Owen (1984). *Finite element software for plates and shells*. Swansea: Pineridge.

Hu, J. L. and J. G. Teng (1996). Computational fabric mechanics: present status and future trends. *Finite Elements in Analysis and Design 21*, 225–237.

Hughes, T. J. R. (1987). *The finite element method*. Englewood Cliffs: Prentice–Hall.

Hughes, T. J. R. and E. Cornoy (1983). Nonlinear finite element shell formulation accounting for large membrane strains. *Comput. Methods Appl. Mech. Engrg. 39*, 69–82.

Hughes, T. J. R. and W. K. Liu (1981a). Nonlinear finite element analysis of shells: Part I. three–dimensional shells. *Comput. Methods Appl. Mech. Engrg. 26*, 331–362.

Hughes, T. J. R. and W. K. Liu (1981b). Nonlinear finite element analysis of shells: Part II. two–dimensional shells. *Comput. Methods Appl. Mech. Engrg. 27*, 167–181.

Hughes, T. J. R., R. L. Taylor, and W. Kanoknukulchai (1977). A simple and efficient finite element for plate bending. *Int. J. Numer. Meth. Engng. 11*, 1529–1543.

Hull, D. (1981). *An introduction to composite materials*. New York: Cambridge University Press.

Ish, J. and R. Guttal (1997). On the assumed strain formulation with selective polynomial order enrichment for p–version shells. *Comput. Struct. 63*(5), 899–913.

Jara-Almonte, C. C. and C. E. Knight (1988). The specified boundary stiffness/force SBSF method for finite element subregion analysis. *International Journal for Numerical Mrthods in Engineering 26*, 1567–1578.

Jones, R. M. (1975). *Mechanics of Composite Materials*. New York: Mc Graw–Hill.

Jones, R. T. (1950). The spanwise distribution of lift for minimum induced drag of wings having a given lift and a given bending moment. *NACA Tech. Note 2249*, 1–14.

Kalidindi, S. R. and A. Abusafieh (1996). Longitudinal and transverse moduli and strengths of low angle 3-D braided composites. *Journal of Composite Materials 30*(8), 885–905.

Kalidindi, S. R. and E. Franco (1997). Numerical evaluation of isostrain and weighted–average models for elastic moduli of three–dimensional composites. *Composites Science and Technology 57*, 293–305.

Kartevelishvili, V. M. and V. V. Kobelev (1984). Rational schemes for reinforcing laminar plates from composite materials. *P. M. M. 48*(1), 68–88.

Kemp, B. L., C. Cho, and S. W. Lee (1998). A four–node solid shell element formulation with assumed strain. *Int. J. Numer. Meth. Engng. 43*, 909–924.

Kere, P. and J. Koski (2001). Multicriterion stacking sequence optimization scheme for composite laminates subjected to multiple loading conditions. *Composites Structures 54*, 225–229.

Kikuchi, F. (1982). Accuracy of some finite element models for arch problems. *Comput. Methods Appl. Mech. Engrg. 35*, 315–345.

Kikuchi, F. and K. Tanizawa (1984). Accuracy and locking–free property of the beam element approximation for arch problems. *Comput. Struct. 19*, 103–110.

Kirsch, U. (1990). On the relationship between optimum structural topologies and geometries. *Struct. Optim. 2*, 39–45.

Klein, A. and S. P. Viswanathan (1973). Minimum induced drag of wings with given lift and root–bending moment. *Journal of Applied Mathematics and Physics (ZAMP) 24*, 886–892.

Kohn, R. V. and G. Strang (1986). Optimal design in elasticity and plasticity. *Num. Meths. Eng. 22*, 183–188.

Koiter, W. T. (1959). A consistent first approximation in the general theory of thin elastic shells. In W. T. Koiter (Ed.), *IUTAM: Proceedings of the Symposium on the Theory of Thin Elastic Shells*, Amsterdam, pp. 12–33. North–Holland Publishing Company.

Kozlov, S. (1980). Averaging of random operators. *Math. USSR Sbornik 37*, 167–180.

Krätzig, W. B. (1980). Introduction to general shell theory. In W. Olszak (Ed.), *Thin Shell Theory, new trends and applications*, Udine, pp. 4–61. CISM.

Krog, L. A. and N. Olhoff (1997). Topology and reinforcement layout optimization of disk, plate, and shell structures. In G. I. N. Rozvany (Ed.), *Topology optimization in structural mechanics*, Udine, pp. 237–322. CISM.

Kuritz, S. P. and C. Fleury (1989). Mixed variable structural optimization using convex linearization techniques. *Eng. Opt. 15*, 27–41.

Lanchester, F. W. (1907). *Aerodynamic*. Berlin: Verlag.

LeDret, H. and A. Raoult (1995). The nonlinear membrane model as variational limit of nonlinear three–dimensional elasticity. *J. Math. Pures Appl. 74*, 549–578.

Lee, P.-G. and H.-C. Sin (1994). Locking–free curved beam element based on curvature. *Int. J. Numer. Meth. Engng. 37*, 989–1007.

Lee, S.-S., J. S. Koo, and J. M. Choi (1996). Development of a new curved beam element with shear effect. *Engineering Computations 13*, 9–25.

Leino, Y. and J. Pitkaranta (1994). On the membrane locking of $h - p$ finite elemets in a cylindrical shell problem. *Int. J. Numer. Meth. Engng. 37*, 1053–1070.

LeMaître, O., E. S. DeCursi, and S. Huberson (1998). Large displacement analysis for ideally flexible sails. *European Journal of Mechanics, A/Solids 17*(4), 619–636.

LeMaître, O., S. Huberson, and E. S. DeCursi (1999). Unsteady model of sail and flow interaction. *Journal of Fluids and Structures 13*, 37–59.

Liu, W. K. and B. M. Donning (1998). Meshless methods for shear–deformable beams and plates. *Comput. Methods Appl. Mech. Engrg. 151*, 47–71.

Liu, W. K., E. S. Law, and Y. Belytschko (1986). Resultant–stress degenerated–shell element. *Comput. Methods Appl. Mech. Engrg. 55*, 259–300.

Lomov, S. V., G. Huysmans, Y. Luo, R. S. Parnas, A. Prodromou, I. Verpoest, and F. R. Phelan (2001). Textile composites: modelling strategies. *Composites Part A 32*, 1379–1394.

Malkus, D. S. and T. J. R. Hughes (1978). Mixed finite element methods–reduced and selective integration techniques: a unification of concepts. *Comput. Methods Appl. Mech. Engrg. 15*, 63–81.

Mallick, P. K. (1988). *Fiber–Reinforced Composites: Materials, Manufacturing and Design*. New York: Marcel Dekker, Inc.

Malvern, L. E. (1969). *Introduction to the Mechanics of a Continuous Medium*. Englewood Cliffs, New Jersey: Prentice–Hall.

Marchaj, C. A. (1964). *Sailing theory and practice*. New York: Dodd, Mead and Company.

Marchaj, C. A. (1979). *Aero–Hydrodynamics of Sailing*. London: Adlard Coles Nautical.

Marchaj, C. A. (1990). *Sail Performance: Techniques to Maximize Sail Power*. Camden: International Marine.

Marsden, J. E. and T. J. R. Hughes (1983). *Mathematical foundations of elasticity*. New York: Dover Publications.

Mason, J. (1980). *Variational, incremental and energy methods in solid mechanics and shell theory*. New York: Elsevier Scientific Publishing Company.

Masters, J. E., R. L. Foye, C. M. Pastore, and Y. A. Gowayed (1993). Mechanical properties of triaxially braided composites: experimental and analytical results. *Journal of Composites Technology & Research 15*(2), 112–122.

Maxwell, J. C. (1881). *A treatise on electricity and magnetism*. Oxford: Clarendon Press.

McIlhagger, R., B. J. Hill, D. Brown, and L. Limmer (1995). Construction and analysis of three–dimensional woven composite materials. *Composites Engineering 5*(9), 1187–1197.

Meck, H. R. (1980). An accurate polynomial displacement function for finite ring elements. *Comput. Struct. 11*, 265–269.

Milgram, J. H. (1968). The analytical design of yacht sails. *Trans. SNAME 74*, 118–160.

Mróz, Z. (1986). Variational approach to shape sensitivity analysis and optimal design. In J. A. Bennet and M. E. Botkin (Eds.), *General Motors Symposium on the Optimum Shape: Automated Structural Design*, New York, pp. 79–110. Plenum Press.

Muc, A. and W. Gurba (2001). Genetic algorithms and finite element analysis in optimization of composite structures. *Composites Structures 54*, 275–281.

Munk, M. M. (1923a). General theory of thin wing sections. *NACA Rep. 142*, 243–261.

Munk, M. M. (1923b). The minimum induced drag of aerofoils. *NACA Rep. 121*, 373–390.

Munk, M. M. (1923c). Some new aerodynamical relations. *NACA Rep. 121*, 129–141.

Murat, F. and L. Tartar (1985). Optimality conditions and homogenization. In A. Marino (Ed.), *Nonlinear Variational Problems*, Boston, pp. 1–8. Pitman.

Muttin, F. (1991). Structural analysis of sails. *European Journal of Mechanics, A/Solids 10*(5), 517–534.

Nagendra, S., R. T. Haftka, and Z. Gürdal (1993). Design of a blade stiffened composite panel by a genetic algorithm. In *Proceedings of 34^{th} Structures, Structural Dynamics and Materials Conference*, La Jolla, CA.

Naik, N. K. and R. Kuchibhotla (2002). Analytical study of strength and failure behaviour of plain weave fabric composites made of twisted yarn. *Composites Part A 33*, 697–708.

Naomis, S. and P. C. M. Lau (1990). Computational tensor analysis of shell structures. In C. A. Brebbia and S. A. Orszag (Eds.), *Lecture Notes in Engineering*, New York. Springer Verlag.

Nascimbene, R. (2001). Partial reduced selective integration applied to shell elements. In *AIMETA '01*.

Nascimbene, R. and P. Venini (2002). A new locking–free equilibrium mixed element for plane elasticity with continuous displacement interpolation. *Comput. Methods Appl. Mech. Engrg. 191*, 1843–1860.

Nguyen, V. H., J. J. Strodiot, and C. Fleury (1987). A mathematical convergence analysis of the convex linearization method for engineering design optimization. *Eng. Opt. 11*, 195–216.

Noor, A. K. and J. M. Peters (1981). Mixed models and reduced/selective integration displacement models for nonlinear analysis of curved beams. *Int. J. Numer. Meth. Engng. 17*, 615–631.

Norman, T. L., P. Allison, J. W. Baldwin, B. K. Gracias, and D. Seesdorf (1993). Effect of tow alignment on the mechanical performance of 3D woven textile composites. *Composites Manufacturing 4*(4), 209–215.

Norman, T. L., C. Anglin, and D. Gaskin (1996). Strength and damage mechanism of notched two–domensional braided textile composites and tape equivalents under tension. *Journal of Composites Technology & Research 18*(1), 38–46.

Norman, T. L., C. Anglin, D. Gaskin, and M. Patrick (1996). Normal stress distribution of notched 2D triaxial braided textile composites and tape equivalents under tension. *Journal of Composite Materials 30*(5), 589–602.

Offshore Racing Council (2002). *A handicapping system for cruising/racing yachts* (International Measurement System ed.). Offshore Racing Council.

Olhoff, N., K. A. Lurie, A. V. Cherkaev, and A. Fedorov (1981). Sliding regimes of anisotropy in optimal design of vibrating plates. *Int. J. Solids Struct. 17*(10), 931–948.

Onate, E. and J. Oliver (1986). A finite element formulation for the geometrically non linear analysis of shells. In T. J. R. Hughes and E. Hinton (Eds.), *Finite Element Methods for Plate and Shell Structures. Volume 2: Formulations and Algorithms*, Swansea, pp. 83–101. Pineridge Press.

Pandian, N., T. V. S. R. AppaRao, and S. Chandra (1989). Studies on performance of curved beam finite elements for analysis of thin arches. *Comput. Struct. 31*, 997–1002.

Parish, H. (1990). An investigation of a finite rotation four node assumed strain shell element. *Int. J. Numer. Meth. Engng. 30*, 127–150.

Pastore, C. M., A. E. Bogdanovich, and Y. A. Gowayed (1993). Applications of a meso–volume–based analysis for textile composite structures. *Composites Engineering 3*(2), 181–194.

Pastore, C. M. and Y. A. Gowayed (1994). A self–consistent fabric geometry model: modification and application of a fabric geometry model to predict the elastic properties of textile composites. *Journal of Composites Technology & Research 16*(1), 32–36.

Pawsey, S. F. and R. W. Clough (1971). Improved numerical integration of thick shell finite elements. *Int. J. Numer. Meth. Engng. 3*, 575–586.

Petrov, E. and M. Géradin (1998). Finite element theory for curved and twisted beams based on exact solutions for three–dimensional solids, Part I/II. *Comput. Methods Appl. Mech. Engrg. 165*, 43–127.

Pitkaranta, J. (1992). The problem of membrane locking in finite element analysis of cylindrical shells. *Numer. Math. 61*, 523–542.

Poisson, S. (1822). *Second mémoire sur la théorie du magnétisme*, Volume 5. Mem. Acad. France.

Prandtl, L. (1952). *Essentials of Fluid Dynamics with Applications to Hydraulics, Aeronautics, Metereology and other Subjects*. London: Blackie & Sons Limited.

Prandtl, L. and O. G. Tietjens (1934). *Applied Hydro- and Aeromechanics*. New York: Dover Publications, Inc.

Prathap, G. (1985a). An additional stiffness parameter measure of error of the second kind in the finite element method. *Int. J. Numer. Meth. Engng. 21*, 1001–1012.

Prathap, G. (1985b). The curved beam/deep arch/finite ring element revisited. *Int. J. Numer. Meth. Engng. 21*, 389–407.

Prathap, G. and C. R. Babu (1986). An isoparametric quadratic thick curved beam element. *Int. J. Numer. Meth. Engng. 23*, 1583–1600.

Prathap, G. and G. R. Bhashyam (1982). Reduced integration and the shear–flexible beam element. *Int. J. Numer. Meth. Engng. 18*, 195–210.

Prathap, G. and B. P. Naganarayana (1990). Analysis of locking and stress oscillations in a general curved beam element. *Int. J. Numer. Meth. Engng. 30*, 177–200.

Prathap, G. and B. R. Shashirekha (1993). Variationally correct assumed strain field for the simple curved beam element. *Comput. Struct. 47*, 1071–1073.

Prathap, G. and S. Viswanath (1983). An optimally integrated four–node quadrilateral plate bending element. *Int. J. Numer. Meth. Engng. 19*, 831–840.

Pugh, E. D. L., E. Hinton, and O. C. Zienkiewicz (1978). A study of quadrilateral plate bending elements with 'reduced' integration. *Int. J. Numer. Meth. Engng. 12*, 1059–1079.

Qun, Z., L. Mu, and K. Wenqi (1998). Geometric non–linear analysis of space shell structures using generalized conforming flat shell elements—for space shell structures. *Commun. Numer. Meth. Engng. 14*, 941–957.

Qun, Z., L. Mu, and K. Wenqi (1999). Application of the generalized conforming flat shell element to geometrical non–linear analysis for composite stiffened shell structures. *Commun. Numer. Meth. Engng. 15*, 399–412.

Ramm, E. (1977). A plate/shell element for large deflection and rotations. In K.-J. Bathe, J. T. Oden, and W. Wunderlich (Eds.), *Formulation and computational algorithms in finite element analysis*, Cambridge. MIT Press.

Rauch, J. and M. Taylor (1975). Potential and scattering theory on wildly perturbed domains. *J. Funct. Anal. 18*, 27–59.

Raveendranath, P., G. Singh, and B. Pradhan (1999). A two–node locking–free shear flexible curved beam element. *Int. J. Numer. Meth. Engng. 44*, 265–280.

Raveendranath, P., G. Singh, and G. V. Rao (2001). A three–noded shear–flexible curved beam element based on coupled displacement field interpolation. *Int. J. Numer. Meth. Engng. 51*, 85–101.

Rayleigh, J. W. (1892). On the influence of obstacles arranged in rectangular order upon the properties of a medium. *Phil. Mag. 32*, 481–491.

Reddy, B. D. and M. B. Volpi (1992). Mixed finite element methods for the circular arch problem. *Comput. Methods Appl. Mech. Engrg. 97*, 125–145.

Reddy, J. N. (1984a). *Energy and variational methods in applied mechanics*. New York: John Wiley & Sons.

Reddy, J. N. (1984b). A simple higher–order theory for laminated composite plates. *Journal of Applied Mechanics 51*, 745–752.

Reddy, J. N. (1989). On refined computational models of composite laminates. *International Journal for Numerical Methods in Engineering 27*, 361–382.

Reddy, J. N. (1990). On refined theories of composite laminates. *Meccanica 25*, 230–238.

Reddy, J. N. (1997). *Mechanics of Laminated Composite Plates – Theory and Analysis*. New York: CRC Press, Inc.

Reddy, J. N. and M. L. Rasmussen (1982a). *Advanced engineering analysis*. New York: John Wiley & Sons.

Reddy, J. N. and M. L. Rasmussen (1982b). *Advanced Engineering Analysis*. New York: John Wiley & Sons, Inc.

Reddy, J. N. and D. H. Robbins (1994). Theories and computational models for composite laminates. *Appl. Mech. Rev. 47*(6), 147–169.

Rengarajan, G., M. A. Aminpour, and N. F. Knight (1995). Improved assumed–stress hybrid shell element with drilling degrees of freedom for linear stress buckling and free vibration analyses. *Int. J. Numer. Meth. Engng. 38*, 1917–1943.

Rhiu, J. J. and S. W. Lee (1988). A sixteen node shell element with a matrix stabilization scheme. *Computational Mechanics 3*, 99–113.

Richards, P. J., A. Johnson, and A. Stanton (2001). America's cup downwind sails–vertical wings or horizontal parachutes? *Journal of Wind Engineering and Industrial Aerodynamics 89*, 1565–1577.

Roberts, O. T. P. (1995). An explanation of ancient windward sailing–some other considerations. *The International Journal of Nautical Archeology 24*(4), 307–315.

Rovati, M. and A. Taliercio (1990). Optimal orientation of the symmetry axes of orthotropic 3–D materials. In *Proceedings of the International Conference on Engineering Optimization in Design Processes*, Karlsruhe.

Rovati, M., A. Taliercio, and C. Cinquini (1991). On maximum stiffness of orthotropic shells. In S. Hernandez and C. A. Brebbia (Eds.), *Optimization of Structural Systems and Industrial Applications*, Southampton, Boston, pp. 597–604. Computational Mechanics Publications.

Rozvany, G. I. N., M. P. Bendsøe, and U. Kirsch (1995). Layout optimization of structures. *Applied Mechanics Reviews 48*, 41–119.

SacchiLandriani, G. and M. Rovati (1989). Optimal limit design of fiber reinforced orthotropib bodies. In *Proceedings of the Course on Computer Aided Optimal Design of Structures, COMETT*, Pavia.

Schlichting, H. (1979). *Boundary–Layer Theory*. New York: Mc Graw–Hill.

Schmit, L. A. and B. Farshi (1977). Optimum design of laminated fibre composite plates. *Int. J. Numer. Meth. Engng. 11*, 623–640.

Schoop, H. (1990). Structural and aerodynamic theory of sails. *European Journal of Mechanics, A/Solids 9*(1), 37–52.

Schoop, H. and N. Bessert (2001). Instationary aeroelastic computation of yacht sails. *Int. J. Numer. Meth. Engng. 52*, 787–803.

Sherman, F. S. (1990). *Viscous Flow*. New York: Mc Graw–Hill.

Shi, G. and G. Z. Voyiadjis (1991). Simple and efficient shear flexible two–node arch/beam and four–node cylindrical shell/plate finite elements. *Int. J. Numer. Meth. Engng. 31*, 759–776.

Sidhu, R. M. J. S., R. C. Averill, M. Riaz, and F. Pourboghrat (2001). Finite element analysis of textile composite preform stamping. *Composite Structures 52*, 483–497.

Simiu, E. and R. H. Scanlan (1986). *Wind effects on structures* (Second ed.). New York: John Wiley & Sons, Inc.

Simo, J. C., F. Armero, and R. L. Taylor (1993). Improved versions of assumed enhanced strain tri–linear elements for 3D finite deformation problems. *Comput. Methods Appl. Mech. Engrg. 110*, 359–386.

Simo, J. C. and D. D. Fox (1989). On a stress resultant geometrically exact shell model. part i: formulation and optimal parametrization. *Comput. Methods Appl. Mech. Engrg. 72*, 267–304.

Simo, J. C. and M. S. Rifai (1990). A class of mixed assumed strain method of incompatible modes. *Int. J. Numer. Meth. Engng. 29*, 1595–1638.

Sneyd, A. D. and T. Sugimoto (1997). The influence of a yacht's heeling stability on optimum sail design. *Fluid Dynamic Research 19*, 47–63.

Spagnolo, S. (1968). Sulla convergenza di soluzioni di equazioni paraboliche ed ellettiche. *Ann. Sc. Norm. Sup. Pisa 22*, 577–597.

Sparenberg, J. A. (1984). *Elements of hydrodynamic propulsion.* Netherlands: Martinus Nijhoff Publishers.

Sparenberg, J. A. and A. K. Wiersma (1976). On the maximum thrust of sails by sailing close to wind. *Journal of Ship Research 20*(2), 98–106.

Spilker, R. L. and N. I. Munir (1980). A hybrid–stress quadratic serendipity displacement Mindlin plate bending element. *Comput. Struct. 12*, 11–21.

Steven, G. P., Q. Li, and Y. M. Xie (2000). Evolutionary topology and shape design for general physical field problems. *Computational Mechanics 26*, 129–139.

Stolarski, H. and T. Belytschko (1982). Membrane locking and reduced integration for curved elements. *J. Appl. Mech. 49*, 172–177.

Stolarski, H. and T. Belytschko (1983). Shear and membrane locking in curved C^0 elements. *Comput. Methods Appl. Mech. Engrg. 41*, 279–296.

Sugimoto, T. (1993). A first course in optimum design of yacht sails. *Fluid Dynamic Research 11*, 153–170.

Sugimoto, T. (1995). Optimum sail design for small heel and weak wind shear conditions. *Fluid Dynamic Research 15*, 75–88.

Sugimoto, T. (1999). A method for optimizing sail design. *Sports Engineering 2*, 35–48.

Sun, C. T., J. D. Achenbach, and G. Herrmann (1968). Continuum theory for a laminated medium. *Journal of Applied Mechanics 68*, 467–475.

Svanberg, K. (1987). The method of moving asymptotes – a new method for structural optimization. *Int. J. Numer. Meth. Engng. 24*, 359–373.

Tan, P., L. Tong, and G. P. Steven (1997). Modelling for predicting the mechanical properties of textile composites–A review. *Composites Part A 28*, 903–922.

Tanner, T. (1967). The application of lifting line theory to an upright bermudan mainsail. *J. R. Aeronaut. Soc. 71*, 553–558.

Tartar, L. (1986). Remarks on homogenization. In J. L. Ericksen (Ed.), *Homogenization and effective moduli of materials and media*, New York, pp. 228–246. Springer.

Taylor, R. L., P. J. Beresford, and E. L. Wilson (1976). A non–conforming element for stress analysis. *Int. J. Numer. Meth. Engng. 10*, 1211–1219.

Tessler, A. and T. J. R. Hughes (1983). An improved treatment of transverse shear in the Mindlin–type four–node quadrilateral element. *Comput. Methods Appl. Mech. Engrg. 39*, 311–335.

Tessler, A. and L. Spiridigliozzi (1986). Curved beam elements with penalty relaxation. *Int. J. Numer. Meth. Engng. 23*, 2245–2262.

Thwaites, B. (1960). *Incompressible aerodynamics: An Account of the Theory and Observation of the Steady Flow of Incompressible Fluid past Aerofoils, Wings and Other Bodies*. New York: Dover Publications, Inc.

Tilley, A. (1994). Sailing to windward in the ancient mediterranean. *The International Journal of Nautical Archeology 23*(4), 309–313.

Timoshenko, S. (1940). *Theory of plates and shells*. London: McGraw-Hill.

Topping, B. H. V. and M. Papadrakis (1994). *Advances in Structural Optimization*. Edinburgh: CIVIL–COMP Ltd.

Tricomi, F. G. (1957). *Integral Equations*. New York: Interscience Publishers, Inc.

Ubertini, F. (1994). Vento e strutture: problemi di interazione. Master's thesis, University of Bologna.

Vaidyanathan, R. and Y. A. Gowayed (1996). Optimization of elastic properties in the design of textile composites. *Polymer Composites 17*(2), 305–311.

Vanderplaats, G. N. and T. A. Weisshaar (1989). Optimum design of composite structures. *Int. J. Numer. Meth. Engng. 27*, 437–448.

Vinh, N. X. (1993). *Flight Mechanics of High–Performance Aircraft*. Cambridge University Press.

Wang, Z. Y., E. J. Plate, M. Rau, and R. Keiser (1996). Scale effects in wind tunnel modelling. *Journal of Wind Engineering and Industrial Aerodynamics 61*, 113–130.

Washizu, K. (1968). *Variational methods in elasticity and plasticity*. Oxford: Pergamon Press.

Watkins, R. I. and A. J. Morris (1987). A multicriteria objective function optimization scheme for laminated composites for use in multilevel structural optimization schemes. *Comp. Meth. Appl. Mechs. Eng. 60*, 233–251.

Weissinger, J. (1947). The lift distribution of swept–back wings. *NACA Tech. Memorandum 1120*, 1–51.

Weissinger, J. (1949). Über eine erweiterung der prandtlechen theorie der tragenden linie. *Math. Nachr 2*, 46–109.

Wemper, G., J. T. Oden, and D. Kross (1968). Finite element analysis of thin shells. *Proc. ASCE, J. Eng. Mech. Div. 94*, 1273–1294.

Whidden, T. and M. Levitt (1993). *L'arte e la Scienza delle Vele*. Milano: Mursia.

Whitcomb, J. (1991). Iterative global/local finite element analysis. *Computer & Structures 40*(4), 1027–1031.

Whitcomb, J., G. Kondagunta, and K. Woo (1995). Boundary effects in woven composites. *Journal of Composite Materials 29*(4), 507–524.

Whitcomb, J., J. Noh, and C. Chapman (1999). Evaluation of various approximate analyses for plain weave composites. *Journal of Composite Materials 33*(21), 1958–1980.

Whitcomb, J. and K. Srirengan (1996). Effect of various approximations on predicted progressive failure in plain weave composites. *Composite Structures 34*, 13–20.

Whitcomb, J., K. Srirengan, and C. Chapman (1995). Evaluation of homogenization for global/local stress analysis of textile composites. *Composite Structures 31*, 137–149.

Whitcomb, J. and K. Woo (1994). Enhanced direct stiffness method for finite element analysis of textile composites. *Composite Structures 28*, 385–390.

Whitcomb, J., K. Woo, and S. Gundapaneni (1994). Macro finite element for analysis of textile composites. *Journal of Composite Materials 28*(7), 607–618.

Wiersma, A. K. (1978). On the profit of optimizing the fin–keel of a yacht sailing close to wind. *Journal of Engineering Mathematics 12*(4), 357–364.

Wiersma, A. K. (1979). On the optimization of the thrust of a yacht sailing to windward. *Journal of Engineering Mathematics 13*(4), 289–316.

Wilson, E. L., R. L. Taylor, W. P. Doherty, and J. Ghaboussi (1973). Incompatible displacement models. In S. J. Fenves, N. Perrone, A. R. Robinson, and W. C. Schnobrich (Eds.), *Numerical and Computer Models in Structural Mechanics*, New York, pp. 43–57. Academic Press.

Wohlfahrt, M. (1988). The extended lifting line theory for systems of sails. In V. Boffi and H. Neunzert (Eds.), *Proceedings of the Third German–Italian Symposium: Application of Mathematics in Industry and Technology*, Stuttgart, pp. 77–96. B. G. Teubner.

Woo, K. and J. Whitcomb (1994). Global/local finite element analysis for textile composites. *Journal of Composite Materials 28*(14), 1305–1321.

Woo, K. and J. Whitcomb (1996). Three-dimensional failure analysis of plain weave textile composites using a global/local finite element method. *Journal of Composite Materials 30*(9), 984–1003.

Wood, C. J. and S. H. Tan (1978). Towards an optimum yacht sail. *J. Fluid Mech 85*(3), 459–477.

Yamamoto, Y. and H. Ohtsubo (1982). A qualitative accuracy consideration on arch elements. *Int. J. Numer. Meth. Engng. 18*, 1179–1195.

Yang, H. T. Y., S. Saigal, A. Masud, and R. K. Kapania (2000). A survey of recent shell finite elements. *Int. J. Numer. Meth. Engng. 47*, 101–127.

Yang, R. J. and M. E. Botkin (1986). The relationship between the variational approach and the implicit differentiation approach to shape design sensitivities. In J. A. Bennet and M. E. Botkin (Eds.), *General Motors Symposium on the Optimum Shape: Automated Structural Design*, New York, pp. 61–77. Plenum Press.

Yeom, C. H. and S. W. Lee (1989). An assumed strain finite element model for large deformation composite shells. *Int. J. Numer. Meth. Engng. 28*, 1749–1768.

Yushanov, S. P. and A. E. Bogdanovich (1998a). Analytical probabilistic modeling of initial failure and reliability of laminated composite structures. *Int. J. Solids Structures 35*(7), 665–685.

Yushanov, S. P. and A. E. Bogdanovich (1998b). Stochastic theory of composite materials with random waviness of the reinforcement. *Int. J. Solids Structures 35*(22), 2901–2930.

Zhang, W. H. and C. Fleury (1994). Recent advances in convex approximation methods for structural optimization. *Advances in Structural Optimization 24*, 83–90.

Zienkiewicz, O. C. and R. L. Taylor (1991). *The finite element method, Vol. I–II*. London: McGraw Hill.

Zienkiewicz, O. C., R. L. Taylor, and J. M. Too (1971). Reduced integration technique in general analysis of plates and shells. *Int. J. Numer. Meth. Engng. 3*, 275–290.

Appendix A

Yacht's Nomenclature

A.1 Sail and hull terminology

First–time sailors are faced with a lot of unfamiliar material. The centuries–old terminology can be bewindering, and at times it may indeed seem as if we are learning a new language as we incorporate these words.

abaft the beam behind a perpendicular line extending out from the middle of the boat;

abeam a direction at right angles to the centerline of the boat;

aft toward the stern of the boat; to move aft is to move back;

ahead the front of the boat; toward the front of the boat;

alee the side away from the direction of the wind;

anemometer an instrument for measuring wind speed;

aspect ratio (AR) the ratio between the foot length and the luff length of a sail;

astern in the direction of, or behind, the stern;

backstay a wire mast support, leading aft to the deck or another mast;

ballast heavy material placed in the bottom of a boat to give stability;

batten a short flexible strips of wood, plastic or fiberglass commonly inserted in the mainsail to support the aft portion, or roach, so that it will not curl, to keep it taut (see Figure A.1);

beam the greatest width of the boat, usually in the middle;

beat to go to windward in a sailboat by sailing alternate legs, with the wind first on one side and then on the other

beating sailing against the wind by tacking;

beaufort scale a table of wind velocity;

boom the bar to which the bottom, or foot, of the sail is attached; a spar extending from a mast to hold the outstretched bottom of a sail;

boom vang a system used to hold the boom down, particularly when boat is sailing downwind, so that the mainsail area facing the wind is kept to a maximum;

bow the front, or forward end, of a boat;

cabin an enclosed compartment in a ship, used as shelter or living quarters;

cabin sole the bottom surface of the enclosed space under the deck of a boat;

center of effort (CE) a theoretical point on a boat's sail plan that represents the focus or center of the total forces of wind on the

sails;

clew the lower after corner of a sail, where the foot meets the leech (see Figure A.1);

close–hauled sailing close to the wind with sails pulled in (see Figure 1.21(b));

course the direction in which a ship is steering in making her way from point to point during a voyage or the angle of the boat in sailing against the wind (see Figure 1.4);

deck covering of the interior of a boat, like floors in a building;

displacement the weight, in tons, of the water displaced by the boat and its equipment;

downwind sailing in the same direction as the wind;

draft the amount of vertical distance from a boats waterline to the bottom of its keel;

drift the leeway, or movement of the boat, when not under power, or when being pushed sideways while under power;

fall off to head a boat away from the direction of the wind;

foot the lower edge (bottom) of the sail (see Figure A.1);

fore the front part of a ship; in the direction of or toward the bow;

fore–and–aft sail sail set in a fore–and–aft line; not square–rigged;

foremast the mast nearest the bow of a ship;

foresail the forward sail;

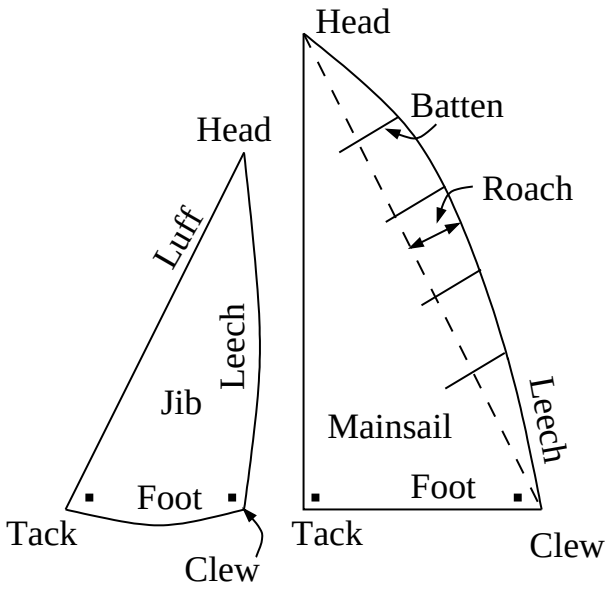

Figure A.1: Parts of the sail.

gale a range of winds from 28 to 47 knots;

genoa also known as *genny*, usually the biggest jib on the boat; a headsail that extends from bow to behind the mast;

head the forward part of a boat, including the bow and adjacent area; the uppermost corner of a triangular sail (see Figure A.1);

headsail a sail forward of the mast;

heel the leeward lean of the boat caused by the winds action on the sails;

helm the device, usually a tiller or wheel attached or connected to the rudder, by which a boat is steered;

hull the body of the boat;

hull speed the maximum speed a hull can achieve without planning;

jib a foresail, usually the foremost sail (see Figure A.1);

keel the fixed underwater fin on the hull which helps provide stability and prevents the boat from slipping sideways; usually ballasted, for stability and lateral resistance;

knot a measurement of speed;

leech the after edge of a fore–and–aft sail (see Figure A.1);

leeward downwind;

leeway sideways drift of a boat;

luff the leading, or forward, edge of a fore–and–aft sail; when this edge shakes in the wind, the sail is luffing (see Figure A.1);

LWL length of a boat at the waterline;

mainsail the main sail of the sail boat set off the mast and main boom (see Figure A.1);

mast the vertical spar or pole supporting boom and sails;

masthead the top of the mast;

offshore away from the shore;

offwind any point of sailing away from the wind;

onboard on the boat;

onshore toward the shore;

pitch plunging of a vessel fore and aft (see Figure A.2);

port the left side of a boat, looking toward the bow;

port tack when the wind comes over the port side of a boat, and the sails are on the starboard side;

reaching sailing a course that is neither close–hauled or downwind; sailing on a tack with the wind roughly abeam; any point of sailing between close–hauled and running;

rig arrangements of masts and sails;

rigging collectively, all the ropes and chains used to support and work the masts, yards, booms and sails of a vessel;

roach the curved leech of a sail (see Figure A.1);

rudder plate hinged to the stern of the vessel used to steer the boat by turning the wheel;

running (to run downwind) going with the wind, downwind sailing (see Figure 1.21);

sloop a boat with a single mast set forward;

spar another term for mast;

spinnaker large, light foresail set forward of the mainsail when running before the wind;

starboard the right side of the boat, facing the bow;

starboard tack sailing with the wind coming from the starboard side, the sails on the port;

stern the afterpart of the boat;

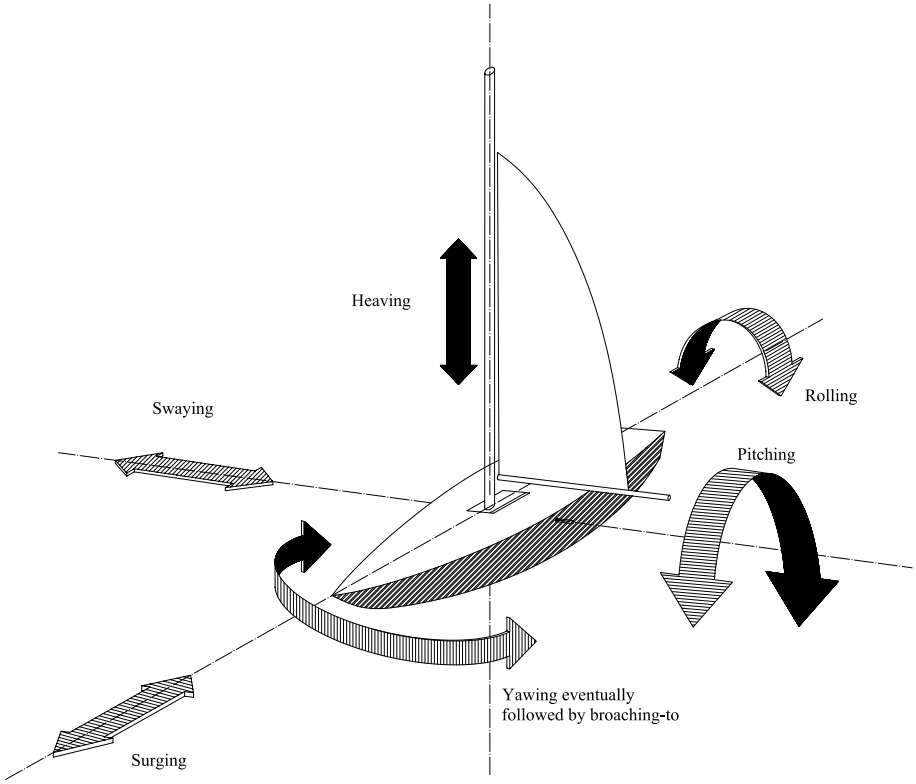

Figure A.2: Six degrees of freedom of a yacht.

tack	to sail to windward by alternating courses, staying as close to the wind as possible; to zigzag into the wind;
tacking	working the windward close–hauled;
tack of a sail	forward lower corner of a sail (see Figure A.1);
trim	to adjust angle of the sails to accord with the wind;
true wind	wind direction without taking into account the motion of the boat;
yaw	to turn from side to side (see Figure A.2);
windward	upwind, toward the wind.

Appendix B

Coordinate systems

B.1 Derivatives of vectors in rotating reference frames

We wish to examine the rate of change of a vector as it is perceived by two observers, each in a different reference frame rotating with respect to one another. Let us denote the nonrotating system by (x, y, z) and the rotating reference frame by $(\bar{x}, \bar{y}, \bar{z})$. Let $\boldsymbol{\omega}$ denote the angular rotation of the barred system with respect to the unbarred system. In the nonrotating system the basis vectors $(\mathbf{e}_1, \mathbf{e}_2, \mathbf{e}_3)$ do not change with time. In the rotating system the basis vectors $(\bar{\mathbf{e}}_1, \bar{\mathbf{e}}_2, \bar{\mathbf{e}}_3)$ are rotating with the angular velocity $\boldsymbol{\omega}$. The time derivatives now can be written as:

- for a nonrotating system:
$$\mathbf{A} = A_i \mathbf{e}_i$$
$$\frac{d\mathbf{A}}{dt} = \frac{dA_i}{dt}\mathbf{e}_i$$

- for rotating system:
$$\mathbf{A} = \bar{A}_i \bar{\mathbf{e}}_i$$
$$\frac{d\mathbf{A}}{dt} = \frac{d\bar{A}_i}{dt}\bar{\mathbf{e}}_i + \bar{A}_i \frac{d\bar{\mathbf{e}}_i}{dt}$$

The rate of change $d\bar{\mathbf{e}}_i/dt$ is given by:

$$\frac{d\bar{\mathbf{e}}_i}{dt} = \boldsymbol{\omega} \times \bar{\mathbf{e}}_i, \tag{B.1.1}$$

because the change is brought about by a rigid–body rotation. To an observer in the rotating frame, however, the basis vectors appear to be constant. Thus we

write:

$$\frac{d\bar{A}_i}{dt}\bar{\mathbf{e}}_i \equiv \left(\frac{d\mathbf{A}}{dt}\right)_{\text{rot}}. \tag{B.1.2}$$

The relationship of the time derivatives in the two frames is thus given by:

$$\begin{aligned}\left(\frac{d\mathbf{A}}{dt}\right)_{\text{nonrot}} &= \left(\frac{d\mathbf{A}}{dt}\right)_{\text{rot}} + \bar{A}_i(\boldsymbol{\omega}\times\bar{\mathbf{e}}_i)\\ &= \left(\frac{d\mathbf{A}}{dt}\right)_{\text{rot}} + \boldsymbol{\omega}\times\mathbf{A}.\end{aligned} \tag{B.1.3}$$

Consider now the velocity vector as an example. Let the two frames of reference have the same origin. Then the position vector is given by $\mathbf{r} = \bar{\mathbf{r}}$. It follows that:

$$\left(\frac{d\mathbf{r}}{dt}\right)_{\text{nonrot}} = \left(\frac{d\mathbf{r}}{dt}\right)_{\text{rot}} + \boldsymbol{\omega}\times\mathbf{r}. \tag{B.1.4}$$

The first term on the right side of Equation (B.1.4) is the velocity of a point as it is perceived by an observer in the rotating system. Thus we write:

$$(\mathbf{V})_{\text{nonrot}} = (\mathbf{V})_{\text{rot}} + \boldsymbol{\omega}\times\mathbf{r}. \tag{B.1.5}$$

If the term $(\mathbf{V})_{\text{rot}}$ is zero, then the point in question is fixed with respect to the rotating system, and the Equation (B.1.5) reduces to the expression of a rotating rigid body. The acceleration in the two systems can be obtained by applying the operator

$$\left(\frac{d}{dt}\right)_{\text{nonrot}} = \left(\frac{d}{dt}\right)_{\text{rot}} + \boldsymbol{\omega}\times \tag{B.1.6}$$

to the Equation (B.1.4). We get

$$\begin{aligned}\left(\frac{d^2\mathbf{r}}{dt^2}\right)_{\text{nonrot}} &= \frac{d}{dt}\left(\frac{d\mathbf{r}}{dt}\right)_{\text{rot}} + \frac{d}{dt}(\boldsymbol{\omega}\times\mathbf{r})\\ &= \frac{d}{dt}\left(\frac{d\mathbf{r}}{dt}\right)_{\text{rot}} + \boldsymbol{\omega}\times\frac{d\mathbf{r}}{dt} + \frac{d\boldsymbol{\omega}}{dt}\times\mathbf{r}\\ &= \left(\frac{d^2\mathbf{r}}{dt^2}\right)_{\text{rot}} + \boldsymbol{\omega}\times\left(\frac{d\mathbf{r}}{dt}\right)_{\text{rot}} + \boldsymbol{\omega}\times\left[\left(\frac{d\mathbf{r}}{dt}\right)_{\text{rot}} + \boldsymbol{\omega}\times\mathbf{r}\right] + \frac{d\boldsymbol{\omega}}{dt}\times\mathbf{r},\end{aligned}$$

or finally:

$$= \left(\frac{d^2\mathbf{r}}{dt^2}\right)_{\text{rot}} + 2\boldsymbol{\omega}\times\left(\frac{d\mathbf{r}}{dt}\right)_{\text{rot}} + \boldsymbol{\omega}\times(\boldsymbol{\omega}\times\mathbf{r}) + \frac{d\boldsymbol{\omega}}{dt}\times\mathbf{r}. \tag{B.1.7}$$

Thus the acceleration in the nonrotating frame is made up of four parts:

$\left(\frac{d^2\mathbf{r}}{dt^2}\right)_{\mathbf{rot}}$ acceleration relative to rotating reference frame;

$2\boldsymbol{\omega} \times \left(\frac{d\mathbf{r}}{dt}\right)_{\mathbf{rot}}$ Coriolis acceleration;

$\boldsymbol{\omega} \times (\boldsymbol{\omega} \times \mathbf{r})$ centripetal (or negative centrifugal) acceleration;

$\frac{d\boldsymbol{\omega}}{dt} \times \mathbf{r}$ angular acceleration.

If the origin of the rotating frame of reference is different from that of the fixed frame of reference, we have (Reddy and Rasmussen 1982b):

$$\left(\frac{d^2\mathbf{r}}{dt^2}\right)_{\text{nonrot}} = \frac{d^2\mathbf{R}}{dt^2} + \left(\frac{d^2\mathbf{r}}{dt^2}\right)_{\text{rot}} + 2\boldsymbol{\omega} \times \left(\frac{d\mathbf{r}}{dt}\right)_{\text{rot}} + \boldsymbol{\omega} \times (\boldsymbol{\omega} \times \mathbf{r}) + \frac{d\boldsymbol{\omega}}{dt} \times \mathbf{r} \tag{B.1.8}$$

where $\mathbf{R}$ is the position vector of the origin of the rotating frame of reference with respect to the nonrotating frame of reference, and $d^2\mathbf{R}/dt^2$ is the absolute acceleration of the origin of the rotating frame of reference. If we regard the result obtained in Equation (B.1.7), in the context of the Newton's second law, which must be written as $\mathbf{F} = \mathbf{ma}$ in an inertial or nonrotating reference frame, we have:

$$\begin{aligned}\mathbf{F} &= m\left(\frac{d^2\mathbf{r}}{dt^2}\right)_{\text{nonrot}} \\ &= m\left(\frac{d^2\mathbf{r}}{dt^2}\right)_{\text{rot}} + \underbrace{2m\boldsymbol{\omega} \times \left(\frac{d\mathbf{r}}{dt}\right)_{\text{rot}}}_{\text{Coriolis force}} + \overbrace{m\boldsymbol{\omega} \times (\boldsymbol{\omega} \times \mathbf{r})}^{\text{centrifugal force}} + m\frac{d\boldsymbol{\omega}}{dt} \times \mathbf{r}.\end{aligned} \tag{B.1.9}$$

Appendix C

Beaufort scale of wind speed

In the next page we present the Beaufort scale of wind speed.

Beaufort Number	Seaman's Description of Wind	Terms used in US Weather Bureau Forecast	Wind Speed		Approximate pressure in pounds per feet^2
			knots	meters	
0	Calm	Light	Less than 1	Less than 0.3	Less than 0.01
1	Light air		1÷3	0.3÷1.5	0.01÷0.06
2	Light Breeze		4÷6	1.6÷3.3	0.06÷0.2
3	Gentle Breeze	Gentle	7÷10	3.4÷5.4	0.2÷0.4
4	Moderate Breeze	Moderate	11÷16	5.5÷8.0	0.4÷1.0
5	Fresh Breeze	Fresh	17÷21	8.1÷10.7	1.0÷2.0
6	Strong Breeze	Strong	22÷27	10.8÷13.8	2.0÷3.0
7	Moderate Gale (High Wind)		28÷33	13.9÷17.1	3.0÷4.0
8	Fresh Gale	Gale	34÷40	17.2÷20.7	4.0÷6.0
9	Strong Gale		41÷47	20.8÷24.4	6.0÷9.0
10	Whole Gale (Heavy Gale)	Whole Gale	48÷55	24.5÷28.3	9.0÷12.0
11	Storm		56÷65	28.4÷33.5	12.0÷16.0
12	Hurricane	Hurricane	Above 65	Above 33.6	Above 16.0